Development of an Experimentally Validated Non-linear Viscoelastic Viscoplastic Model for a Novel Fuel Cell Membrane Material

Jessica Anne May

Dissertation submitted to the faculty of the Virginia Polytechnic Institute and State University in partial fulfillment of the requirements for the degree of

Doctor of Philosophy
In
Mechanical Engineering

Michael W. Ellis, Chair
Scott W. Case
David A. Dillard
Yeh-Hung Lai
Robert L. West

2/7/2014
Blacksburg, VA

Keywords: proton exchange membrane, polymer, non-linear viscoelastic, viscoplastic, constitutive model, finite element analysis

Development of an Experimentally Validated Non-linear Viscoelastic Viscoplastic Model for a Novel Fuel Cell Membrane Material

Jessica Anne May

ABSTRACT

The proton exchange membrane (PEM) is a key component in proton exchange membrane fuel cells (PEMFCs). During standard fuel cell operation, the PEM degrades due to cyclic hygrothermal loads, resulting in performance loss or total failure. Improvement of current PEM materials and development of cheaper, more durable materials is essential to the commercialization of PEMFC technology, which may provide an attractive alternative energy source for transportation.

This dissertation investigates a new PEM material which is a blend of sulfonated perfluorocyclobutane (PFCB) and polyvinylidene fluoride (PVDF). Hereafter referred to as PFCB/PVDF, this polymer blend was developed by General Motors Company™ as a potential replacement for the current benchmark PEM, the DuPont™ product Nafion®. The PFCB/PVDF blend is less costly to manufacture than standard PEM materials and investigations into its long-term mechanical durability are ongoing.

Specifically, this document discusses the experimental and analytical work performed in the material characterization, constitutive expression development, and implementation of that expression into uniaxial and biaxial finite element geometries. Extension of the model to time-varying temperature and moisture conditions is also explored.

The uniaxial finite element model uses a non-linear viscoelastic viscoplastic (NLVE-VP) constitutive expression with parameters determined from uniaxial creep and recovery experiments at a single environmental condition. Validation tests show that this model accurately predicts results from uniaxial tension experiments, such as stress relaxation, force ramp, and multistep creep and recovery, to stresses of 8 MPa and strains approaching 15%, which is the maximum hygrothermal strain expected in an operating fuel cell.

The biaxial finite element model combines the NLVE-VP constitutive expression with the geometry of a pressure-loaded blister experiment, which better approximates fuel cell membrane constraints. Results from the biaxial model are compared to experimental results. The model accurately predicts strain in the blister test but predicts stresses that differ from those estimated from blister curvature.

Additionally, it is found that both the non-linear viscoelastic and viscoplastic parameters are functions of the operating environment. Future experimental work is needed to characterize that dependence before the constitutive model is used to simulate the response of the PFCB/PVDF blend to fuel cell operating conditions.

Acknowledgements

I would like to express my gratitude to my advisor, Dr. Ellis, for his great patience with me during the path to this degree. Over the six years I worked with him, I learned incredible lessons in engineering, research, and life skills that don't come from reading textbooks. I would also like to thank the other members of my committee and our supporters from General Motors Company for their input and suggestions, for being flexible to meet with me and discuss the various challenging aspects of this project. My fellow students in the lab and on the General Motors project made the long days (and nights) in lab pass more quickly and less painfully – thank you Ashley, Nathan, Chase, Keith, Junbo, Angela, Brad, Lei, Katherine, Jeremy, Karthik, Zhou, Bladimir, Isaac, Scott... Many thanks to the Chinn and Newcomb families for hosting me during my trips back to Blacksburg, for asking, commiserating and genuinely caring about my research and lab work. Thanks also to my family – Dad, Mom, Rebecca and Rachel (future Hokie class of 2019!) – for teaching me the importance of education and keeping me sane during my time in higher education. And finally, a huge thanks to Nathan May. I can't express my gratitude to you for all your help over the past several years, from technical expertise to comic relief and now loving husband. Thank you all so much!

Table of Contents

List of Figures

List of Tables

List of Symbols

Symbol	Description
A	viscoplastic parameter
A_T	viscoplastic parameter A as a function of temperature
A_λ	viscoplastic parameter A as a function of water content
A'	viscoplastic parameter A as a function of temperature and water content
a_{TH}	hygrothermal shift factor
a_σ	stress shift factor
B	material property: bulk compliance
b	viscoplastic parameter governing stress dependence
c	viscoplastic parameter governing time dependence
D	material property: compliance
E	material property: modulus
e	deviatoric strain
exp	exponential function
g_i	non-linear viscoelastic parameters
J	material property: shear compliance
K	material property: bulk modulus
$\pounds$	Laplace transform
p	pressure applied during blister test
q	hereditary component of non-linear viscoelastic constitutive expression
R	radius of curvature of blister
s	deviatoric stress
S	compliance matrix
T	temperature
t	thickness or time
t_{eff}	effective time used in viscoplastic strain hardening calculation
α	CTE: coefficient of thermal expansion
β	CHE: coefficient of hygral expansion
Δ	represents the difference in two values
ε	strain
$\bar{\varepsilon}^P$	equivalent plastic strain
η	viscosity
λ	water content
ν	Poisson's ratio
ρ	dummy variable for time integration
σ	stress
$\bar{\sigma}$	octahedral shear stress
τ	characteristic time
φ	reduced time
NLVE	abbreviation for 'non-linear viscoelastic'
VP	abbreviation for 'viscoplastic'

1. Introduction

In the search for alternative energy sources for transportation, proton exchange membrane fuel cells have been explored as devices for converting the energy in chemical bonds to electricity for use in propulsion systems. Proton exchange membrane, or polymer electrolyte membrane, fuel cells (PEMFCs) operate at lower temperatures than other fuel cell types so they are better suited for the intermittent demand of vehicle drive cycles. However, at the moment, PEMFC vehicles are not competitive with traditional internal combustion vehicles in terms of simultaneous low cost and acceptable lifetime. Research into fuel cell components has helped to reduce projected costs from $275/kW in 2002 to $47/kW in 2012, but that total cost is still greater than the DOE target of $30/kW in 2015 [1]. The average lifespan of a fuel cell has also increased to around 2500 hours under standard drive cycle conditions [2], but still falls short of the 2015 DOE target of 5000 hours that would begin to make fuel cells a viable alternative to gasoline engines.

Although many components of a fuel cell are known to degrade over time, one of the most critical is the proton exchange membrane. This membrane separates the reactants – hydrogen and oxygen – and transports the H^+ ions (protons) released by the electrochemical reaction in which hydrogen is oxidized to protons and electrons. The vehicle drive cycle results in changing temperatures and moisture in the membrane, which is very sensitive to both. When unconstrained, the membrane swells when warm and/or moist and contracts when cool and/or dry. However, the mechanical constraints imposed on the membrane by the bipolar plates of the fuel cell restrict the dimensional changes, so compressive and tensile stresses result in the membrane. Over time, many cycles of temperature and/or moisture change may cause the membrane to thin in regions with high residual tensile stresses. If the membrane thins sufficiently or develops a hole, it can no longer separate the reactants, which are then able to interact directly. In this case, the reaction between hydrogen and oxygen is no longer electrochemical; it is now a combustion reaction and the electrons that would have been released and recaptured during the electrochemical reaction are not available for use in the external circuit. Therefore, the performance of the fuel cell drops or fails completely. Moreover, the heat from the combustion reaction can lead to further membrane damage.

New materials are being developed and studied to find cheaper and more durable proton exchange membranes. Experimental characterization is necessary to compare various membranes, but a full experimental analysis may be prohibitively time consuming or expensive. To this end, numerical models can be very useful. For example, if the response of a new material to a 3,000 hour load profile is desired, it may be much more efficient to characterize that material with a limited set of experiments and then run a numerical analysis of the 3,000 hour load cycle with the experimentally determined properties. Models are also useful for analyzing the effects of different operating conditions and start-up/shut-down processes.

Finite Element Analysis (FEA) is an excellent tool for performing this type of numerical analysis. A finite element analysis consists of a ‘physical’ model representing the geometry and constraints of the system to be analyzed and a constitutive model to relate deformations and forces in the material. It is the aim

of this research to develop, implement and validate a constitutive model in a finite element program that would allow numerical analysis of PEM materials during hygrothermal cycling in fuel cell devices.

Fuel Cell Components and Operation

The PEM is just one component in the complex system that makes up an operating fuel cell. During operation, the PEM is sandwiched between catalyst layers to form a membrane electrode assembly (MEA). The MEA is sandwiched between gas diffusion layers (GDL) and clamped between conductive plates with channels cut into them (bipolar plates) to allow hydrogen and air/oxygen to flow over the MEA. The power required to operate a vehicle is much greater than what a single cell can produce, so multiple cells are used together in series or parallel to obtain the desired voltage and current for vehicle operation. This collection of individual cells is called the 'stack'.

The stack itself is part of a larger system called the 'plant'. The plant contains the components necessary for storing and delivering fuels to the stack, receiving power from the stack, and managing the water and heat produced during fuel cell operation. The temperature of the stack and the amount of water produced increase as more power is demanded, and the mechanical and electrochemical properties of PEM materials are often highly sensitive to moisture and temperature, so thermal and moisture management is extremely important for the fuel cell to operate efficiently. Additionally, the channels through which the gaseous fuels are supplied to the gas diffusion layers and the pore structure within the GDL are often quite small. Improper water management may result in liquid water blocking part or all of a reactant pathway, which then disrupts reactant delivery to the portion of the cell 'downstream' of the blockage.

Additional components are necessary to interface the plant with standard vehicle systems, such as the drive train and user comfort devices like radio and air conditioning. Most manufacturers couple the power management system of the fuel cell with the braking system and a battery to take advantage of energy available from regenerative braking.

Because this research is focused on the PEM, it is useful to consider the components and processes directly around the PEM in more detail. In Figure 1-1, the far left is the anode side of a cell and the far right is the cathode. The leftmost component is a bipolar flow plate. Humidified hydrogen gas flows through the channels on the anode plate. The gas is constrained on three sides by the walls of the channel, and on the fourth side is in contact with a gas diffusion layer. Some of the gas passes through this layer where it encounters a layer of catalyst.

The most common catalyst in PEMFCs is carbon-supported platinum. Several techniques are used to incorporate the platinum catalyst layer into the MEA. Often the catalyst is applied to the GDL to form a gas diffusion electrode (GDE), although sometimes it is applied directly to the PEM. Regardless, the layer to the right of the anode catalyst in Figure 1-1 is the PEM. On the other side of the PEM are another catalyst layer, gas diffusion layer and bipolar plate. Oxygen or an air mixture flows through the channels on the cathode bipolar plate.

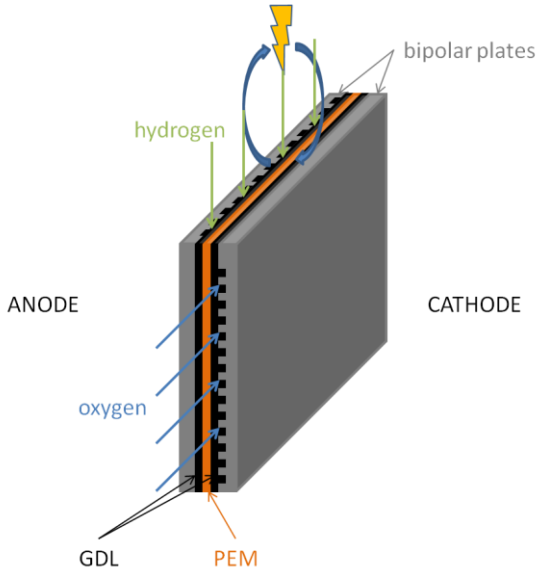

Figure 1-1. Illustration of a single cell PEM assembly.

Because the reactants are different on the anode and cathode, the reactions are also different. On the anode, hydrogen is oxidized such that the electrons are carried through the anode plate to the external circuit which drives the vehicle and the protons are released into the PEM and carried to the cathode. At the cathode, the electrons pass through the cathode plate and participate in an oxygen reduction reaction, which forms water.

The primary functions of the PEM are to conduct protons from the anode to the cathode, prevent electrons from moving from anode to cathode through the PEM directly, and separate the fuel cell reactants, hydrogen and oxygen. Failure in any of these areas reduces fuel cell performance and may ultimately lead to complete cell failure.

1.1. Proton Exchange Membrane Materials

As mentioned previously, current PEM materials, such as Nafion[1], contribute to the high cost of PEMFCs and are often a limiting factor in fuel cell operating lifetime. For this reason, research is being conducted into the improvement of existing materials and the development of new ones. Most of these materials are polymers with ionic functionality that allows the movement of protons from anode to cathode. Additionally, the membranes are often very thin, often significantly less than 100 microns, to reduce protonic resistance. Although thin membranes improve the electrochemical response of the fuel cell, they are more susceptible to chemical and mechanical damage. Thus, a key component in the development of new membrane materials is the balance between mechanical integrity, resistance to chemical attack, and good proton conductivity.

An interesting behavior of polymeric materials is that their mechanical properties are often noticeably time dependent. This arises from conformation changes of the individual polymer chains which occur

[1] Nafion® and DuPont™ are registered trademarks of the E. I. du Pont de Numours and Company or its affiliates. For visual clarity, the copyright symbols are not included with each reference to these names.

when the polymer is subjected to stress. Mechanical degradation occurs due to this rearrangement and localized thinning may develop because of the stress state a PEM experiences during fuel cell operation. This aspect of mechanical behavior is important to include in any numerical material model.

1.2. Constitutive Expressions

Constitutive expressions are essentially transfer functions which relate an output on a system to an input. The constitutive expressions used in the present analysis will describe relevant material behaviors. For PEMs in operating fuel cell environments, it is important to include not only time dependent mechanical properties, but also the effect that varying moisture levels and temperatures have on the magnitude and time dependence of those mechanical properties.

Mechanical constitutive expressions relate stresses and strains. Materials which are time dependent and the constitutive expressions used to describe their behavior are called 'viscoelastic'. These expressions result in time dependent strain under a constant stress, or time dependent stress under a constant strain, for example. Some viscoelastic materials will very nearly return to their initial dimensions if allowed to recover long enough after unloading; these are called viscoelastic solids. Viscoelastic fluids, on the other hand, will never return to their initial dimensions because some of the deformation is inelastic (unrecoverable) rather than elastic. Constitutive expressions for both types of materials exist and may be useful for modeling the behavior of PEMs.

Sometimes the stress and strain in a material are linearly related to each other. That is, the mechanical properties are independent of stress and strain, so if the applied strain (stress) is doubled, so is the resulting stress (strain). However, not all materials exhibit this behavior. Constitutive expressions which incorporate stress or strain dependent mechanical properties are said to capture 'material non-linearity'. Many constitutive expressions exist for describing the behavior of these non-linear materials.

Geometric non-linearity may also be relevant to fuel cell models. This type of non-linearity is not related to the material, but instead arises from the definition of strain used in material models. The familiar definition of strain, where the change in length of a material segment is divided by the initial length of that segment, is a linear approximation of the strain tensor. It is generally applicable if the strains are less than 5-7%. For PEMs, strain resulting from free hygral expansion of operating fuel cell conditions reach or exceed these strains [3]. For analyses which deal with larger strains, the true definition of strain should be used. Similarly, the definition of stress as force divided by the initial area over which it is applied neglects the changes in material dimension due to large strains. For geometrically non-linear analyses, care must be taken to use proper stress and strain definitions. In the present analysis, the Cauchy stress and Almansi-Hamel strain tensor are used to properly account for geometric non-linearity.

1.3. Finite Element Models

Constitutive models can be used independently to calculate material response to uniform loading conditions in the absence of geometric effects. However, if the effects of sample geometry or non-uniform or dynamic loading conditions are of interest, a more advanced technique is needed to address these factors. One popular technique is the use of finite element models. In a finite element model, a geometric representation of a system is developed in one, two or three dimensions. Constitutive

relationships are assigned to the geometry and boundary conditions and loads are applied. The model is usually discretized into a number of subdomains and the forces, displacements, etc., at all subdomains are determined, sometimes through iterative solutions. This type of analysis gives the researcher insight into the stress and strain profiles that occur within a system due to non-uniform sample geometries and load applications.

Geometric models may be 1D, 2D, or 3D. 1D models are used to approximate very simple behavior. For instance, in a uniaxial experiment, a 1D model could be used to simulate the axial strain which develops from an axial stress application.

2D models are a little more sophisticated, but require information about material behavior in both dimensions. For isotropic materials, the behavior is identical in all dimensions, but not all materials are isotropic and this assumption must be used carefully. A 2D geometry would provide simulations of the axial and (in-plane) transverse strains resulting from an axial stress load.

3D models result in simulations of material response in all three material directions. For the case in which a sample is subjected to an axial stress, a 3D geometry would calculate the strain response in the axial direction and both transverse directions (in-plane and out-of-plane). Again, in order for such a simulation to be useful, knowledge of the material behavior in all dimensions is essential.

For any finite element geometry, a wide array of constitutive expressions may be used. Many commercial finite element codes have a collection of ready-to-use constitutive expressions for which the user must simply define values for various material properties. However, not all materials are well described by one of these 'standard' constitutive expressions, so most codes also allow the user to define their own constitutive behavior to be used in conjunction with the geometric model.

In all cases, a finite element model should be subjected to experimental validation. Although part of the benefit of finite element models is the ability to simulate conditions which are difficult or impossible to impose experimentally, it is important to provide evidence that the model is applicable to the system it is attempting to describe.

1.4. Research Objectives

An experimentally validated finite element model can be of great use in the development and evaluation of new PEMs, which decrease cost and improve operating lifetime, thus aiding in commercialization of fuel cell technology. The aim of this research is to develop such a model.

The material on which this research is focused is a new PEM under development by General Motors Company. This research was carried out by individuals at both General Motors Company and Virginia Tech; hereafter this group will be referred to as the 'GM/VT research group'. The material of interest is a blend of the block copolymer perfluorocyclobutane and polyvinylidene diflouride (PFCB/PVDF). Experiments on this material demonstrate that in the temperature and relative humidities anticipated during fuel cell operation, the stresses and strains that develop are large enough to require the use of non-linear analytical techniques. Therefore, the objectives of this research are as follows:

- Perform uniaxial tensile experiments necessary to characterize the mechanical behavior of the novel PEM material at conditions relevant to fuel cell operation.
- Select a constitutive expression capable of describing the material behavior at conditions relevant to fuel cell operation.
- Determine parameter values for the selected constitutive expression.
- Implement the constitutive expression in a uniaxial finite element geometry.
- Validate the finite element model with additional uniaxial experiments.

Because the PEM in an operating fuel cell is biaxially constrained, the finite element model should also be applicable to biaxial loads. Therefore, the following objectives are established for biaxial modeling:

- Extend the uniaxial finite element model to a biaxial geometry and load condition.
- Establish the time dependent Poisson's ratio for the material.
- Validate the biaxial finite element model with experiments.

Finally, the temperature and moisture in a fuel cell are not constant during operation. Ideally, a finite element model of a fuel cell material should simulate the response of the PEM to changing temperature and moisture levels. The need to describe this behavior results in the following objectives:

- Extend the finite element model to accept time-varying temperature and moisture profiles.
- Compare the finite element results to experiments with changing temperature and moisture.

This dissertation describes the work undertaken to achieve these objectives and to establish an experimentally validated model for the PFCB/PVDF membrane. This first chapter has provided a brief overview of important considerations in the development of a finite element model with an appropriate mechanical constitutive expression. The second chapter will review relevant literature on fuel cell damage mechanisms, current PEM materials, constitutive expressions and finite element models of fuel cell membranes. Chapter 3 will describe the experiments performed to characterize the PEM, develop the uniaxial constitutive model and validate the uniaxial and biaxial finite element models. Chapter 4 will present the analytical approaches used to develop the constitutive expression and implement it in the finite element models. The fifth chapter will present results for the uniaxial and biaxial models and describe an approach for extending the model to time-varying temperature and moisture profiles. Finally, Chapter 6 will summarize the work and discuss key conclusions which can be drawn from the analysis.

2. Literature Review

This literature review covers publications which relate to degradation in an operating fuel cell, the characteristic behavior of ionomers which are used as PEMs, PEM characterization techniques, constitutive expressions used to model PEM mechanical behavior, and examples of finite element analyses which use mechanical constitutive models to simulate PEM behavior in an operating fuel cell environment.

2.1. Fuel Cell Degradation

During operation, a unit fuel cell converts the energy in chemical bonds into electricity. Humidified hydrogen gas flows on the anode side of the membrane electrode assembly. This gas diffuses through the GDL and reacts at the catalyst layer, separating into protons and electrons. The electrons are conducted via the bipolar plates to an electrical circuit to drive the vehicle and the protons pass through the proton exchange membrane to the cathode side of the cell. At the cathode, humidified air or oxygen flows through the gas channels and passes to the surface of the membrane via another GDL. At the interface of the GDL and the membrane on the cathode is another catalyst layer. Here, electrons are again conducted via a bipolar plate through the GDL to the catalyst layer, where they react with the protons and oxygen to form water. This is the basic operation of a fuel cell, and the various components which play roles in this operation are all susceptible to degradation as a result of the operating conditions. These degradation mechanisms, especially those associated with the PEM, are discussed below.

2.1.1. Component Degradation

Each component of the fuel cell assembly can compromise the system life, leading to inadequate durability. Although some are much more durable than others, it is still possible for degradation in any component to affect overall cell efficiency. System degradation can be divided into four categories: ohmic, activation, mass transport and fuel efficiency losses [4]. Ohmic losses are related to how effectively the PEM transports protons and the GDL and bipolar plates transport electrons. Activation losses are characterized by a decrease in the rate of electrochemical reaction on the electrodes. Mass transport losses occur when fuel concentration on the electrode surface is too low, and fuel efficiency losses occur when the PEM is not able to properly isolate the anode and cathode, which results in wasting fuel rather than utilizing it to power the external circuit. Isolation failures may occur through reactant gas crossover or electrical shorting. The following paragraphs briefly describe the degradation mechanisms associated with the components of a fuel cell.

Bipolar Plates. Although the bipolar plates are one of the more durable components in a fuel cell, they may still be susceptible to degradation. Oxidation is a concern for metal bipolar plates, especially stainless steel plates at the anode. This increases the contact resistance between the bipolar plate and the GDL, which contributes to ohmic losses [4], [5], [6], [7], [8], [9], [10], [11]. Graphite and graphite-polymer plates are not affected by corrosion under normal operating conditions [7], [8], [9], [12]. In addition to increasing contact resistance, corrosion of the bipolar plates is a concern because metal ions released may contaminate the PEM, reducing proton conductivity [4], [7], [8].

Gas Diffusion Layer. The gas diffusion layer (GDL) must be able to deliver fuel to the electrode surface, manage the amount of water present at the electrode, and conduct electrons from the electrode to the bipolar plate [4], [7], [13]. Mass transport losses occur if the GDL does not properly perform these functions, either because there is not enough fuel reaching the electrode to support the electrochemical reaction, or the reaction sites are flooded with water due to poor water management [4]. Most GDLs are carbon paper or carbon cloth treated to assist with electron transport and so that the surface is hydrophobic to aid in water management [4] , [7], [14]. Performance losses result if the GDL loses its conductive capability because of carbon oxidation or degradation of the treatment [4], [7], [15], [16], [17], [18].

Catalyst Layer. The primary degradation mechanism of the catalyst layer is the loss of electrochemically active surface area (ECSA or EASA) [4], [7], [11], [13], [19], [20], [21], [22], [23]. As the electrochemical reaction proceeds, the platinum catalyst is often found to agglomerate into particles larger than the initial dispersion [20], [21]. This results in a decrease of platinum surface area, which is essentially ECSA. Similarly, catalyst particles tend to migrate into the PEM or to the interface of the PEM and the electrode [21], [24]. Catalyst particles may also become contaminated by impurities in the reactant supply or the product of incomplete electrochemical reactions. These include hydrocarbons, carbon monoxide, sulfur compounds, ammonia, metallic ions, and others [11] , [13], [25], [26], [27]. Because the catalyst has a stronger affinity for these contaminants than hydrogen, sites which bond the contaminants no longer participate in the electrochemical reaction.

Proton Exchange Membrane. Degradation of the PEM may be divided into three categories: thermal, chemical and mechanical. Although there is often a compounding effect between the mechanisms, they will be considered separately here for convenience.

The most common PEM material, Nafion, is resistant to thermal degradation in the current operating temperature range of fuel cells. However, the design of the plant is improved at higher operating temperatures because the heat rejected from the stack can be used for other applications (e.g cogeneration in stationary systems) and because the catalyst is less susceptible to poisoning at higher temperatures. Unfortunately, Nafion begins to experience thermal degradation through the loss of sulfonate groups above 200˚C [28]. Because the sulfonate groups are responsible for proton conduction, this results in an irreversible loss of performance.

Like the catalyst layer, the ionomer is susceptible to ionic contamination as a form of chemical degradation [4], [7], [11], [13], [17], [28], [29]. These contaminants block sulfonate groups which would conduct protons, leading to an ohmic loss in performance. The sulfonate groups are also responsible for keeping the membrane hydrated, so ionic contamination dehydrates the PEM, further decreasing proton conductivity. Some chemicals attack the PEM and cause it to degrade physically; peroxides attack the conductive side chains and cause the ionomer to leach fluorine ions [11], [13], [30]. Other chemicals attack the main chain of the ionomer, decreasing the mechanical strength of the PEM.

Mechanical degradation may also occur through cracks, tears, pinholes, and punctures, leading to electrical shorts or allowing reactant gases to pass through the membrane and react directly [7], [13],

[28]. Some of these are introduced into the PEM during assembly of the cell. For instance, if fibers in the GDL pierce the PEM, shorting may occur between the anode and the cathode through the conductive fiber. Careful assembly and quality control of GDL materials can mostly eliminate initial mechanical defects. However, research has shown that the PEM thins during fuel cell operation, partly from material loss due to chemical attack, as mentioned above, but also due to moisture cycling without any chemical reaction in the cell [13], [31], [32], [33], [34]. The issue with mechanical degradation from thinning is gas crossover. Not only does this result in a loss of cell power since the electrons released during the reaction aren't conducted through the bipolar plates, but a direct reaction between hydrogen and oxygen results in extremely high temperatures. This leads to thermal degradation in areas around that region, which in turn increases the area of the degraded region [11].

It is also common for degradation mechanisms to interact and have compounding effects. This has already been illustrated in terms of membrane thinning, which may be accelerated through thermal or chemical means. The compounding effect may also include multiple component of the cell. For instance, corrosion of the bipolar plates weakens the plates and decreases their conductivity but may also lead to contamination of the PEM with metal ions, which decreases the proton conductivity of the membrane and therefore lowers operating efficiency.

2.1.2. Drive Cycles

The DOE target for transportation fuel cell lifetime is 5000 operating hours, roughly equivalent to 10 years of operation for a standard internal combustion engine (150,000 miles) [35]. However, it is important to remember that the *kind* of miles make a difference, not just the number. Degradation of PEMFC components can often be linked to specific operating conditions. For instance, increased operating temperature is correlated with shorter lifetimes, as are open circuit voltage and RH cycling conditions [13]. In stop-and-go traffic a fuel cell vehicle will be subjected to voltage and RH cycles, so experiments under these conditions can be useful in collecting lifetime data for fuel cell assemblies made from various materials.

Protocols exist for what are termed 'accelerated stress tests' (AST) [36]. The goal of these experiments is to subject the fuel cell stack to the harshest conditions anticipated during standard operation in order to estimate lifetime quickly, rather than having to wait a full 5000 hours for lifetime and performance data. In the context of developing a mechanical model for PEM behavior during fuel cell operation, the primary damage mechanism of interest is thinning in the absence of a chemical reaction. The source of purely mechanically induced thinning is the time dependent properties of the PEM materials, as will be discussed in the following section.

2.2. Characteristic Behavior of Ionomers

The PEM materials most commonly used for hydrogen fuel cells are ionomer membranes. An ionomer is a polymer with ionic functionality. That is, the membrane consists of many entangled polymer strands which interact with charge-carrying particles. Much of the mechanical behavior of PEM materials is determined or influenced by the microstructure, so this discussion will tie macroscopically observed behavior to microscopic sources. The most common PEM is Nafion. Because of the widespread use of

this polymer and the similarity between it and other PEM materials, it will be used as the primary example of material behavior.

2.2.1. Mechanical Behavior

Nafion is a perfluorosulfonic acid membrane. It has a hydrophobic polytetrafluoroethylene main chain or backbone with hydrophilic sulfonic acid side chains, as illustrated in Figure 2-1. The backbone gives Nafion its strength, while the side chains provide the ionic functionality and network mobility. A Nafion membrane consists of many entangled backbone/side chain strands. When tension is applied to the membrane, the strands attempt to remove the internal stress by stretching and/or rearranging. Because the side chains are shorter than the main chains, it is easier for them to change positions. However, the main chains are also of different lengths and may have large or small entanglement density. The statistical distribution of chain lengths and entanglements gives rise to the time-dependent mechanical properties observed in Nafion membranes. Short chains and low density entanglements relax, or rearrange, quickly, while long chains or high density entanglements take much longer [37].

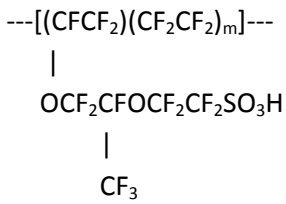

Figure 2-1. Nafion chemical structure [38].

When a load is applied to a membrane, several forms of deformation may take place. These can be characterized by how quickly after load application they occur and whether they remain after the load is removed. First, consider a deformation which occurs instantaneously upon the application of any load, and instantaneously disappears, or recovers, once that load is removed. This deformation is called elastic and rises from stretching between the bonds in the main and side chains. Contrast this with a deformation which increases with time under load, but recovers given enough time after removal of the load. This is a viscoelastic deformation and is due to the changing configuration of the polymer chains driven by the applied load. Chemical or physical crosslinks between chains provide the restoring force which results in polymer chains returning to their original configuration after load removal. Finally, deformations which do not recover are called inelastic or plastic. These may be instantaneous or time dependent, and are generally related to chains breaking or slipping past each other. Time dependent inelastic deformations are sometimes called 'viscoplastic', implying that the deformation changes with time under load (visco-) but does not recover after load removal (-plastic), although this behavior could also be described as simply 'viscous'.

2.2.2. Environmental Effects

The environment at which the material is being used affects its mechanical response. For instance, consider the effect of the coefficient of thermal expansion on a microscopic level. There will be more distance between chains at a higher temperature; this increase in free volume increases chain mobility, allowing changes in conformation to occur more rapidly at high temperatures than at low temperatures.

In general, moisture in the membranes has an analogous effect, and the chains move farther apart to accommodate additional water molecules at higher humidities.

The effect of water on the membrane properties, however, can be complicated. Research has shown that not all water in Nafion interacts with the polymer chains in the same way. Instead, water in the membrane is partitioned three ways: tightly bound, loosely bound, and free water. The parameter used to express water content in sulfonic-acid based PEMs is lambda (λ), which is defined as the number of water molecules per sulfonic acid site in the material. For low lambda values, all water is tightly bound in the groups of sulfonic acid. This water does not freeze even at extremely low temperatures. The next category, loosely bound water, may freeze and is relatively mobile between sulfonic acid sites. Free water is very mobile and is thought to move between sulfonic acid groups through established channels in a well-hydrated membrane [38].

For some materials, a temperature change affects all time-dependent characteristics uniformly [39], [40]. Further, for some PEM materials, this assumption is applicable over the temperature range used in fuel cells. This allows researchers to use a technique called the Time Temperature Superposition Principle (TTSP) to simplify the expression of mechanical behavior over a range of times and temperatures. Essentially, an experiment which gives a material property at a particular temperature, modulus for instance, from 10 to 10,000 seconds, can be shifted along the time axis to express that same property at another temperature. By performing the same experiment at various temperatures and recording the horizontal shift factors necessary to make the curves fall into a single line, called the master curve, information about the material response at very long or very short times can be obtained much more easily than performing experiments at those times [31], [37], [41], [42]. Because moisture influences the free volume of the polymer similarly to temperature, the Time Moisture Superposition Principle (TMSP) can often be applied to the same materials. In this case, the shift factors are a function of moisture rather than temperature. If the two techniques can be applied simultaneously, it is called the Time Temperature Moisture Superposition Principle (TTMSP).

The thermal and hygral (moisture) history of a material may also influence the mechanical properties [43]. Extreme hygral or thermal loads may swell or shrink the membrane in such a manner that it will not recover under standard conditions. For instance, if a Nafion membrane is conditioned under high temperature and very low relative humidity, nearly all of the water that is usually bound to the ionic groups may be drawn out. Additionally, the channels by which water molecules move in and out of the membrane may collapse. In this case, even once the membrane is returned to standard room conditions, it will not re-hydrate to the previous moisture level observed prior to the treatment. This will lead to significantly different experimental results when comparing treated and untreated materials. Because of phenomena like this, it may be important to know the history of PEM specimens before performing comparative analyses [44].

Polymers may also exhibit inconsistent mechanical properties if physical aging occurs. This phenomenon is similar to the history effect just described in that it results in a modified molecular structure. Physical aging is the process of chain rearrangement which takes place when a material is not in its equilibrium molecular configuration. In some environments, this is a rapid process. For instance, higher

temperatures increase the free volume available chain motion, so the equilibrium configuration may be reached quickly. However, if the environmental temperature is significantly less than the material's glass transition temperature (at which long-range segmental motion becomes significant), there is very little room for the chains to rearrange themselves. In this case, physical aging is a slow process. If samples from a single batch of slowly aging material are tested several months or years apart, the difference in the experimental results may be significant because of the changes in molecular arrangement due to physical aging [37].

2.2.3. Proton Conductivity

In addition to mechanical properties, the conductivity of a PEM is also extremely important to fuel cell operation. Nafion and other PEMs are known to have better conductivities when hydrated. The partitioning of water within Nafion results in clusters of water molecules associated with the sulfonic acid sites. Various hypotheses have been proposed for the exact mechanism by which protons move through the membrane. Currently it is thought that protons move through the breaking and forming of hydrogen bonds between water molecules attached to the sulfonic acid sites at elevated hydration levels; this is known at the Grotthus or hopping mechanism. At low hydration levels, it is thought that the vehicular mechanism dominates, in which water molecules carrying protons diffuse through the membrane [45].

2.2.4. Survey of Materials Explored as PEMs

Overall, there are several key characteristics of an effective and viable PEM material. At fuel cell conditions, good proton conductivity is clearly an important property, but the membranes also need to be chemically stable and mechanically robust for at least 5000 operating hours. The materials must also be affordable and easy to manufacture in order to compete with internal combustion engines. The following section is a brief survey of some of the more prominent PEM materials explored thus far and techniques to improve the properties of existing materials.

PFSA materials

The current baseline PEM material is Nafion, a PFSA (perfluorosulfonic acid) membrane produced by DuPont. Nafion consists of a polytetrafluoroethylene backbone with sulfonated side chains. The backbone gives the material good mechanical and thermal stability, while the sulfonic acid groups on the side chains allow proton conduction [38]. However, Nafion has insufficient operating lifetime because of its susceptibility to peroxide attack [7], [11], [28], [30], [46], [47], [48], and thinning during fuel cell operating cycles [4], [20], [48]. The cost of a fuel cell with Nafion as the PEM is also much higher than DOE targets, even when considering scaled-up production [49].

DuPont competitors Gore, Asahi Glass, Asahi Kasei, Solvay, and 3M have also produced PFSA-based materials similar to Nafion, but with slight chemical or mechanical variations aimed at addressing some of the drawbacks of the Nafion membrane [43]. For instance, the Gore materials differ from Nafion in that they are a composite membrane with an extruded PTFE reinforcement layer in between two layers of PFSA polymer [50]. The reinforcement improves the mechanical properties of the composite material, so the PEM itself can be thinner, although the through-plane conductivity of these PEMs is lower than pure PFSA materials. Reducing membrane thickness reduces overall cell resistance, so there is a trade-

off in using thinner materials with lower proton conductivity. Unfortunately, the enhanced mechanical properties do not sufficiently improve operating lifetime, so membranes of this type are not yet commercially viable [51].

Another technique used to improve PFSA membranes is the introduction of fillers to enhance the proton conductivity at high temperatures and low relative humidities. Silica [52], [53], [54], [55], [56], [57], titania [52], [58], [59] and zirconia [60], [61], [62] are examples of additives which have been successfully used for this application. These fillers increase the water uptake of PFSA materials at low relative humidities, which in turn improves proton conductivity. Some fillers have also demonstrated the ability to improve mechanical properties, such as dimensional stability during water uptake [63], [57]. Materials for fillers and techniques for incorporating them into PFSA membranes for enhanced properties and performance are topic of ongoing research.

Hydrocarbon Materials

Rather than attempt modifications to PFSA membranes, other researchers are looking to new classes of membrane materials for PEMs. One of the most promising groups is sulfonated hydrocarbons [55]. The materials may be fluorinated, such as the PEMs developed by Ballard Power Systems [64], although most are not [65]. Examples of non-fluorinated materials are sPEEK, sPEK, sPES, sPBI, sPI, sPPQ, and sPPZ [66]. Various forms of poly(arylene ether sulfone) (PAES, also called BPSH) have been researched, both fluorinated and unfluorinated [67-69]. The material under investigation in the present work is also a hydrocarbon, sulfonated perfluorocyclobutane (PFCB), blended with polyvinylidene difluoride (PVDF). Several groups have explored PEMs with PFCB [70], [71], [72], but the variation used in the present study is described in [73].

In general, these materials are much cheaper to produce than the PFSA membranes and exhibit better proton conductivity at higher temperatures and lower relative humidities. Another benefit is the ease with which the electrochemical properties and structure can be modified. Since these are essentially custom-built, various processing techniques and monomer additives can be used to customize the end product. However, none has demonstrated sufficient operating lifetime under fuel cell operating conditions, primarily due to poor oxidative stability [51]. The use of reinforcements and fillers in sulfonated hydrocarbons is being explored to improve durability.

Non-sulfonated Materials

Researchers have also explored non-sulfonated materials as potential PEMs. Examples of these include anhydrous membranes and solid acids. The structure and proton conduction mechanisms in these systems differ significantly from the PEMs already discussed. These materials are also intended for PEMFCs operating at temperatures between 100°C and 200°C. Because of these differences, they will not be discussed further. For information on these and the previously discussed materials, please refer to review papers such as those by Zhang [48], Hickner [51], Hamrock [65], Dupuis [66], Peighambardoust [74], and Devanathan [75].

2.3. Material Characterization Techniques

Development of improved PEM materials requires knowledge about the material properties of current and proposed membranes. The following paragraphs detail some of the techniques used to explore these properties, highlighting those which are relevant to the current work. Because the focus of this research is on mechanical properties, the bulk of the review is on mechanical tests, but additional experimental techniques relevant to fuel cell materials are also covered.

2.3.1. Electrochemical Characteristics

Material properties important for electrochemical performance in a fuel cell include proton conductivity, water uptake (because of its correlation with proton conductivity for PFSA materials), gas permeability and resistance to electrochemical degradation. The effect of environmental conditions such as hydration level and temperature on each of these categories may also be very important.

Proton conductivity

Proton conductivity is measured by a variety of techniques. Electrochemical impedance spectroscopy (EIS) excites the PEMFC system or individual components with a small voltage or current oscillation around a constant value and measures the current or voltage response and phase angle between input and response. When performed over a range of frequencies, this technique provides information about the various transport processes occurring during fuel cell operation. For instance, the system response to a high-frequency input is limited by the ion transport through the membrane; this gives information about the proton conductivity through the PEM. Conversely, the response to a low-frequency input is dominated by mass transport through the system, so that water and fuel transport can be studied. The constant value about which the sinusoidal input occurs also affects the information contained in the response; for oscillations around small constant voltages, charge transport dominates the response, even at low frequency excitations [74], [76].

Another technique used to measure proton conductivity is nuclear magnetic resonance (NMR) spectroscopy. During this type of experiment, an electromagnetic pulse is applied to a material and the effect of that pulse on the magnetic nuclei within the material is measured. Protons are affected by the magnetic field, so information about the location and movement of protons through a material, in addition to how they interact with other magnetic atoms, can be obtained from NMR experiments conducted with various frequencies, similar to the EIS analysis [66].

The proton conductivity of the material under investigation in the present work was measured previously [42]. Conductivity of the PFCB/PVDF material was found to depend on the hygrothermal history of the material sample. This discovery is important in the treatment of fuel cell membranes because allowing the PEM to experience certain hygrothermal conditions for extended periods of time may compromise its conductivity. Experiments in the present work were performed on samples with known hygrothermal histories for consistency between results.

Water Uptake

As mentioned earlier, PFSA materials and some hydrocarbon PEM conduct protons more effectively when moderately hydrated. Hydration level for many PEMs is a function of temperature and reaction

rate, since water is produced by the reaction at the cathode, so experiments correlating water uptake to fuel cell operating conditions can be useful in comparing PEM materials. Perhaps the simplest experiment for determining water uptake is to compare the mass of a dry PEM with that of one which has been allowed to equilibrate under known temperature and moisture conditions [74]. This is known as a gravimetric technique for determining water uptake.

In the present work, water uptake measurements from [42] are used to define the relationship between the water content of the PFCB/PVDF blend and the environment to which the material is exposed. Water content is expressed as λ, which is defined as the number of water molecules, in moles, per the number sulfonic acid sites in the material. This ratio may depend on temperature and relative humidity, as well as the hygrothermal history of the material.

Gas Permeability

The ability of the PEM to separate the reactant gases in an operating fuel cell is critical to cell performance. Membrane resistance to gas permeability can be characterized by pressurizing two sides of an assembled cell to different levels and observing the pressure change over time [74]. Also, if the cell is assembled but not loaded by an external circuit, measurements of the small current produced can be indicative of the electrochemical reaction proceeding due solely to gas leakage through the PEM [7].

In the present work, an experiment is conducted in which the failure mode is also gas permeability. The 'blister test' is described in detail later, but essentially consists of a material specimen pressurized from one side. The deflection of the disk, which forms a blister shape, can be analyzed to obtain the stress and strain state of the sample. The blister samples experience failure through bursting or pinhole development, both of which result in measureable gas permeability. Thus, this experimental setup has the inherent advantage of detecting failures relevant to fuel cell operation.

Durability

Membrane resistance to chemical degradation is also a crucial characteristic to consider when comparing PEM materials. The performance of two materials would best be compared by subjecting both to a drive cycle reflecting actual usage. However, fuel cell target lifetimes of greater than 5000 hours make this comparison impractical. Accelerated lifetime tests are used instead, in which the membranes are subjected to 'worst-case' scenarios which cause them to degrade more rapidly than they would in service. Factors which accelerate the failure of a PEM include high temperature, low relative humidity, open circuit voltage conditions, and rapid cycling of temperature, humidity or voltage [43]. Degradation of PEMs under these conditions can be observed through changes in the EIS response of the cell, increased gas permeability and the concentration of fluorine ions in the water produced on the cathode. For PFSAs and fluorinated hydrocarbons, the fluorine atoms are essential components of the side chains that are responsible for proton conductivity, and thus separation of these side chains reduces proton conductivity. By measuring the concentration of fluorine leaving the cell, the level of membrane degradation can be estimated while the cell is operating. Other techniques, such as Fenton's test, can be performed on a degraded membrane after the cell is disassembled [28], [43], [66], [74].

Application to PFCB/PVDF Blend

The experiments in the present work are performed on samples which were not subjected to protocols intended to accelerate degradation. Rather, the experiments in this analysis were designed to avoid degradation by any of these known degradation mechanisms, thus isolating mechanical effects.

2.3.2. Morphology

Changes in a material on the microscopic level can give rise to macroscopically observable phenomena. It is helpful to understand the morphology of a PEM in order to understand how and why it fails, and potentially how to avoid those failure mechanisms. The techniques discussed below are used to explore the morphology of PEMs and other polymers for this purpose.

X-ray and neutron scattering/diffraction

Scattering and diffraction techniques obtain information about a material by bombarding a sample with an electromagnetic wave and measuring the intensity of what the material scatters at a range of scattering angles. X-ray techniques probe the response of bound atomic electrons within the samples. Neutron techniques look at the interactions of the incoming wave with individual atomic nuclei within the sample. If only the X-rays scattered by individual electrons are measured, the technique is called 'scattering', while a 'diffraction' technique uses both the information from the scattered X-ray waves and interference between them [66]. Neutron scattering and diffraction are defined analogously.

Atoms of various elements have unique scattering profiles, so the location of atoms within a sample can be explored using these techniques. For instance, in Nafion, the sulfonic acid groups have higher electron density than other regions of the material. This results in a large amount of scattering from these groups, so they show up very clearly (have high intensity) in a scattering experiment. If multiple peaks (multiple regions of high intensity) are present in a plot, information about the size of the sulfonic acid groups and the distance between them can be obtained. This type of experiment has been heavily utilized to explore the morphology of Nafion membranes [38]. Depending on the range of reflected angles captured by the instrument, an x-ray experiment may be classified as small angle x-ray scattering (SAXS) or wide angle x-ray scattering (WAXS).

NMR spectroscopy

This experiment was discussed previously as a means to measure proton conductivity, but it may also be used to study morphology of a material which contains magnetically active nuclei besides protons. Because of the interactions between nuclei in chemical bonds or physical proximity, not all nuclei of the same type will exhibit the same response to a particular magnetic impulse. Knowledge of the anticipated and actual response of the NMR spectrum of a material can thus provide information on the bonding, spacing and interaction of molecules in the polymer [66], [77].

Vibrational Spectroscopy

Each type of bond within a material has a characteristic vibrational frequency. Vibrational spectroscopy takes advantage of this property by irradiating a sample with a light source and determining what frequencies are absorbed by the material, indicating the presence of particular bonds [77]. If the light source is polychromatic (contains multiple frequencies), the technique is called infrared spectroscopy since the wavelengths absorbed by bonds are in the infrared spectrum. Fourier Transform Infrared

(FTIR) is an example of this type of experiment. If the light source is monochromatic, the technique is called Raman scattering. This experiment observes the elastic and inelastic scatter of photons and uses the photons that are inelastically scattered (have a change in frequency due to interaction with the sample) to infer knowledge about the material structure [66].

Microscopy

Microscopy techniques allow visualization of a material's physical structure on a scale much smaller than the unaided human eye can resolve. Various types of microscopy are used in exploring the morphology of materials. Scanning electron microscopy, transmission electron microscopy and atomic force microscopy will be briefly discussed here.

A scanning electron microscope (SEM) explores the surface of a sample by illuminating it with a focused electron beam and collecting the reflected electrons. Regions of the material which have higher electron density reflect more of the electron beam and appear brighter in the resulting image. A sample needs to be coated in a conductive layer in order to view it with SEM. PEM materials may be sputter-coated in a thin layer of gold to enhance the surface conductivity. This technique is able to resolve features on the sample surface of approximately 3 nanometers [77].

Transmission electron microscopy (TEM) also illuminates a sample with an electron beam, but rather than capturing what is reflected by the sample, it measures electrons that pass through the sample. Because electrons interact with the material as they pass through it, TEM gives information about the physical arrangement inside the sample rather than just on the surface. Extremely thin samples are required for TEM to provide useful information; electrons passing through a thick sample will interact with many bonds, making it difficult or impossible to decipher the actual structure. The resolution of TEM approaches tenths of nanometers under ideal conditions, but is more often between 1 and 100 nanometers [77].

Atomic Force Microscopy

Atomic force microscopy (AFM) provides information about the surface structure of a sample by moving a cantilevered tip across the surface. A laser is focused on the back of the cantilever, which reflects the laser to a light detecting mechanism. Topography can be measured by dragging the tip, since the deflection of the cantilever will change when the specimen surface height changes. If the tip is tapped on the surface of the sample, regions which are relatively softer or harder can be resolved by interpreting the elastic and inelastic response of the material surface to the sinusoidal tapping input [77].

Thermal Analysis

Material properties can be strongly affected by temperature because of the changes in morphology at various temperatures. A material may be crystalline or semi-crystalline at a low temperature but become amorphous upon heating as the crystallites melt. Additionally, an increase in temperature increases the free volume in a material. If the temperature is high enough to allow long-range segmental motion in a polymer, the magnitude and time dependence of the material properties are significantly

affected. Performing thermal analysis on PEM materials in the range of potential fuel cell operating temperatures can provide valuable information about how morphology varies with temperature.

Digital scanning calorimetry (DSC) provides information about sample morphology by measuring the amount of energy it takes to increase the temperature of a sample. Melting, for example, of crystalline regions, is a constant-temperature process, although this effect may be convoluted in semi-crystalline materials because of the differing response of the crystalline and amorphous regions. Periods of a temperature sweep experiment during which the sample is absorbing energy rather than increasing in temperature may indicate a decrease in order in crystalline regions. DSC can also give information about the glass transition temperature and other thermal transitions which occur within a material [77].

During a thermal gravimetric analysis (TGA) experiment, the mass of a sample is monitored during heating. Mass loss can indicate removal of residual solvent or water, or may imply material loss as bonds within the material break. A mass spectrometer can be used to analyze the contents of the gas coming off the sample during the temperature sweep and identify which components of the sample degrade at various temperatures [77].

Application to PFCB/PVDF Blend

Many of the techniques just discussed were applied to the PFCB/PVDF material to investigate the morphology of the blend and potential links between changes in morphology and mechanical properties that result from hygrothermal treatments. This relationship is of interest because if certain hygrothermal treatments affect the morphology in a way that negatively impacts the mechanical properties, these environments should be avoided not only during fuel cell operation, but also during mechanical characterization experiments, such as those performed in the present work.

For instance, SAX experiments demonstrated phase separation through the material on the order of tens of nanometers which depended on processing procedures [42], [78]. NMR studies indicated the diffusion of water through the blend is comparable to that observed in Nafion [42]. Infrared spectroscopy showed that there is increased phase separation in the blend after extended periods (>8 hours) of immersion in high temperature (> 80°C) liquid water [42]. SEM images of such immersion treated specimens showed development of surface defects, and TEM images indicate growth of ionic aggregates within the material as a function of treatment time [42]. AFM experiments demonstrated phase separation on the surface of samples, much like SAX found within the samples [78]. DSC experiments indicated blend compatibility and also suggested that PVDF crystallinity increased with temperature of liquid water in which the samples were immersed, and TGA was used to confirm water uptake measurements performed in another instrument [42].

The key finding from these morphology studies which relates to the present work is the development of phase separation. As the PFCB and PVDF phases separate, proton conductivity decreases, and therefore fuel cell performance drops. In order to characterize the PFCB/PVDF membrane in the state it would be used in an operating fuel cell, environments known to accelerate phase separation (i.e., immersion in water warmer than 80°C for extended time periods) were avoided during experiments in the present work.

2.3.3. Mechanical

Durability issues with PEM materials make mechanical properties an important factor in developing new membranes. Both thinning and cracking are relevant PEM failure modes, so the properties related to these should be considered. The effect of environmental conditions on material expansion and material properties is also important to quantify. Experimental techniques for measuring these characteristics are discussed below.

Viscoelastic Properties

As mentioned previously, PEM materials have time dependent or viscoelastic mechanical properties. Experiments to measure these properties fall into two categories: those under a constant load are called static tests, and those under a sinusoidal oscillation are called dynamic tests. Both are usually performed with loading in a single direction, such as a simple tension test, although biaxial loads are also useful to consider because a PEM is biaxially constrained during fuel cell operation.

Creep and relaxation are both examples of static experiments. During a uniaxial creep test, a sample is held in grips at the top and bottom and subjected to a constant force (or stress) and the deformation of the sample is measured over time. The creep compliance of a material is defined as the ratio of time-dependent strain to the constant applied stress. A relaxation test records the force (or stress) required to hold a sample at a constant deformation with time. The relaxation modulus determined from this experiment is the ratio of time-dependent stress to the constant applied strain [37].

Dynamic experiments may be force or displacement controlled. During a dynamic uniaxial tension experiment, for example, the applied force oscillates between maximum and minimum values at a constant frequency while distance between the driven grips is recorded. In an elastic material, the force would track with the displacement instantaneously because all of the energy is stored. In a viscoelastic material, however, some of the energy is dissipated, so there is a lag in the displacement response of the sample. This displacement response is characterized by a storage modulus and a loss modulus, with the ratio of loss to storage modulus giving the phase angle between the displacement input and force response. The magnitudes of the loss and storage moduli vary with the oscillation frequency just as the relaxation modulus and creep compliance vary with time [37].

Biaxial experiments are less common than uniaxial experiments on PEMs. Two methods that have been reported in literature are a flat specimen and a blister or bulge specimen. A flat specimen is gripped on each edge and the force (displacement) of each edge is controlled while the displacement (force) is measured. Specimens used for this technique may be circular [79], [80], [81], square [82], rectangular [82], or cruciform-shaped [83]. A blister or bulge specimen is initially flat and constrained at all edges. In some cases, a pressure differential is applied across the specimen and the resulting deformation is measured, often optically. Other blister or bulge experiments apply deformation by contact, for instance, with a hemispherical probe, and measure the force required to produce deformation. Bulge or blister specimens are typically squares, rectangles, or circles.

Strength

Some PEM materials fail during operation as a result of cracks, which initiate at pinholes or other point defects, propagating through the membrane. This increases the area through which hydrogen may permeate the membrane and react directly with the oxygen. Thus, understanding the crack propagation behavior in PEMs is a useful tool for durability comparison.

The double-edge notch test, trouser tear test and knife slit test have been used to measure fracture energy in PEMs [84]. This is a material property which quantifies the amount of energy required for a crack to propagate through a material. Li, et al found that the region of plastic deformation was minimized in the knife slit test, so this experiment gave the best estimate of intrinsic fracture energy and therefore was the most useful. In a knife slit experiment, a strip of membrane is pre-notched and loaded so that a sharp blade is directly in line with the cut. The knife is then driven through the material at a controlled rate and the force applied on the knife by the material during cutting is measured. Fracture energy can be calculated from the force measurement [84], [85], [86].

The blister test mentioned previously has also been used to study the fracture mechanics of PEMs under biaxial loading conditions. It has been observed that the rate of pressure loading influences the failure mechanism in blister experiments on PEMs. Slow ramp rates, constant applied pressures or fatigue tests tend to fail through small pinholes which develop in the membrane over time. However, fast ramp rates often cause failure through the bursting of the membrane, which is a fracture-driven mechanism. Grohs, et al. [80] and Dillard, et al. [87] have reported the bursting behavior of PEMs in blister experiments.

Environmental Response

The environment in which a PEM is operating has significant influence on its properties and behavior. For this reason, experiments which aim to determine mechanical properties of PEMs, such as those discussed above, are often performed over a range of environmental conditions relevant to fuel cell operation. Also, like all materials, PEMs experience thermal expansion with temperature increases; a hygral expansion component is also present and is often more significant than the thermal expansion [31], [88]. The thermal and hygral expansion are typically characterized by loading a uniaxial specimen of known dimensions at a reference environmental condition under minimal tension and varying the environment. After allowing time for equilibration in the new environment, the new length of the specimen at minimal stress is measured. The difference in length is then attributed to the expansion or contraction of the material based on the change in environmental conditions [42], [89]. Other researchers measure the change in thickness of the specimen at different environmental conditions and use this dimensional change to calculate expansion coefficients [90]. Experiments indicate that PEMs often have greater expansion coefficients through-plane than in-plane [31], [88]. Some literature addresses the anisotropy of hygral expansion when conducting simulations of through-plane membrane behavior [91]. However, many studies are only interested in the in-plane membrane behavior, so these often assume isotropic swelling [89], [92].

The thermal and hygral expansion of the PFCB/PVDF membrane were characterized using the first technique, which gives in-plane expansion properties because it relies on a length measurement [42].

For this material, the hygral expansion is far more significant than the thermal expansion in the range of fuel cell operation (30-90°C, 0-80%RH).

2.4. Constitutive Equations

The information gathered through experiments on PEMs is often used to develop a numerical model of material behavior. This model will then be used to simulate the behavior of the PEM under conditions that were not tested experimentally but are of interest to the researcher. The equations which relate factors such as environment and mechanical loads to material response are known as constitutive expressions or constitutive models. The wide variety of behaviors exhibited by PEMs – time dependence, permanent strain, hygral expansion, etc – have led to the development of a large collection of constitutive equations. A few of these are discussed below.

2.4.1. General Categories

Constitutive equations can be classified into many categories. A useful way to categorize them is based on the material behaviors they can express. An elastic constitutive equation will always predict that a material returns to its initial dimensions after the removal of an applied load, while an inelastic equation predicts non-recoverable deformation. Some equations assume a linear relationship between inputs and outputs over the full range of operation, while others are able to capture various forms of non-linearity. Finally, the time dependence of mechanical properties of PEMs and the impact of that dependence on material failure leads some researchers to include time dependent properties in their constitutive equations.

2.4.2. Survey of Constitutive Equations Useful for PEMs

Perhaps the most basic constitutive equation is that for a linear, elastic spring. This equation relates the strain ε of a spring to the stress σ required to maintain that deformation with a constant coefficient E, as shown in Equation 2-1. A linear elastic constitutive model for a PEM takes a similar form, using a constant modulus, E, to relate stress and strain. Although the modulus may be a function of temperature or relative humidity, it does not depend on stress, strain or time for a linear elastic material. Tang, et al. used a linear elastic constitutive equation to describe the response of Nafion in a numerical investigation of fuel cell behavior [33].

$$\sigma = E\varepsilon \qquad \textbf{2-1}$$

Later experimental work by the same research group indicated that significant permanent strain occurred in Nafion samples during testing under fuel cell conditions [93]. They further concluded that the permanent strain could be expressed by a linear elastic/perfectly plastic constitutive equation [88]. This expression assumes all strain is linear elastic up to a specific value of stress, the yield stress. Once the stress state in the material reaches the yield stress, permanent or plastic strain begins to develop in addition to the elastic strain. The plastic strain is a function only of the instantaneous value of stress and not the stress history. Additionally, for a perfectly plastic constitutive expression, the material response does not exhibit any hardening; each stress increment beyond yield has the same relative effect. A later

publication included isotropic hardening in the constitutive equation to more accurately express the mechanical response of Nafion [91].

These analyses are useful in exploring mechanical response of PEM materials, but various research groups have shown significant time dependence in the mechanical properties of PEM materials [3], [41], [42], [89], [94], so constitutive expressions which incorporate time or rate effects are also frequently used. One method for expressing time dependent material properties is the Prony series. This equation expresses the variation of a material property through time by summing a series or parallel arrangement of springs and dashpots. The springs represent elastic deformation, while the dashpots represent deformation during which energy is dissipated (viscous or inelastic). A spring and a dashpot in parallel with each other result in deformation which is time dependent, because of the dashpot, but recoverable, because of the spring. The ratio of the dashpot viscosity, η, to the spring constant, E, is called the characteristic time of the combined element, τ, and governs the time range over which the element relaxes. By placing such combined elements in series and/or parallel, materials with multiple characteristic times can be modeled. For instance, consider the three-element mechanical analog of the Voigt-Kelvin viscoelastic solid in Figure 2-2.

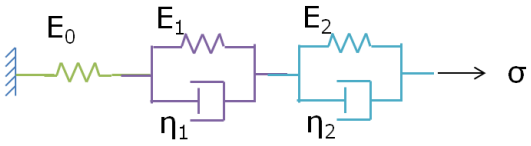

Figure 2-2. Mechanical analog of a Voigt-Kelvin solid under creep load.

The material in Figure 2-2 is a solid because there are no free dashpots, so the analog will return to its original length if the applied stress is removed. Because the elements are in series, all elements experience the same stress and the total strain response is the sum of the strains in the individual elements. For materials with time dependent properties under time varying loads, a convolution integral is used to properly capture the material response. Thus, the constitutive equation for the Voigt-Kelvin solid takes the form of Equation 2-2, in which ρ is a dummy variable for the convolution integral.

$$\varepsilon(t) = \int_{-\infty}^{t} D(t-\rho)\sigma(\rho)\, d\rho \qquad \textbf{2-2}$$

In this equation, D(t) is the total creep compliance, which is the sum of the compliance of all elements. For the Voigt-Kelvin solid, the total compliance takes the form of Equation 2-3, in which E is the modulus associated with each spring and τ is the characteristic time of an element, representing the ratio of η, the dashpot viscosity, to E. This expression is a Prony series and is a convenient and popular way to express material properties associated with viscoelastic materials.

$$D(t) = \frac{1}{E_0} + \frac{1}{E_1}\left(1 - exp^{-\frac{t}{\tau_1}}\right) + \frac{1}{E_2}\left(1 - exp^{-\frac{t}{\tau_2}}\right) \qquad \textbf{2-3}$$

The time-temperature-superposition-principle (TTSP), as discussed earlier, can be used with a Prony series to incorporate temperature effects into the material properties. With a Prony series, this is

implemented by using a variable which is a function of temperature, called the thermal shift factor a_T, to multiplicatively change the relaxation times. If the material is thermorheologically simple, that is, a temperature change has the same effect on all time dependent aspects of a material, then the same shift factor is applied to all elements for a specified temperature. An analysis which employs TTSP might express the total compliance in the form of Equation 2-4. Moisture effects may be included in a similar manner, expressing the shift factor as a function of moisture rather than, or in addition to, temperature.

$$D(t,T) = \frac{1}{E_0} + \frac{1}{E_1}\left(1 - exp^{-\frac{t}{\tau_1 * a_T(T)}}\right) + \frac{1}{E_2}\left(1 - exp^{-\frac{t}{\tau_2 * a_T(T)}}\right) \quad \textbf{2-4}$$

The Prony series and convolution integral technique has been successfully used to model the behavior of PEM materials in both uniaxial [41] and biaxial configurations [79]. One drawback to this technique is that it is only able to capture linear stress-strain behavior; that is, regions of material response where the material properties are independent of stress and strain. For PEMs, it is frequently found that the operating conditions extend into the region of non-linear material response. For instance, Silberstein [89] shows that Nafion becomes non-linear at less than 5% strain in uniaxial tensile tests for a range of humidities, temperatures, and strain rates. The yield stress which corresponds to the onset of non-linearity ranges from less than 1 MPa when immersed and heated to 100˚C to 12 MPa when dry at room temperature. A PEM which is biaxially constrained and subjected to RH cycles similar to fuel cell conditions has been demonstrated to develop strains up to 9% and stress up to 4 MPa for an RH change of 40% [3]. This clearly suggests that including non-linear effects in a constitutive equation for PEM modeling may be essential for reasonable simulation results.

One way to include non-linearity in a time dependent constitutive equation is to modify the elements in the Prony series to be dependent on the stress or strain state. Schapery [95] developed a constitutive equation of this form with non-linear parameters related to instantaneous elastic response (g_0), time dependent elastic response (g_1), the rate of loading (g_2) and the effect of the stress or strain state on the characteristic relaxation times of the material (a_σ). The integral form of this equation is shown in Equation 2-5, and further discussion of the parameters is performed in the Analytical Techniques chapter.

$$\varepsilon^{NLVE}(t) = g_0(\sigma(t))D_0\sigma(t) + g_1(\sigma(t))\int_0^t \Delta D(\varphi(t) - \varphi(\rho))\frac{dg_2(\sigma(\rho))\sigma(\rho)}{d\rho}d\rho \quad \textbf{2-5}$$

$$\varphi(t) = \int_0^t \frac{d\rho}{a_\sigma(\sigma(\rho))}$$

The Schapery non-linear viscoelastic constitutive equation has been used to model the response of many polymeric materials, including polyester fibers [96], polyethylene [97], polyisobutylene [95], polypropylene [98] and PMMA [99]. Values for the non-linear parameters in the Schapery model are typically determined from two-step static load experiments (creep or stress relaxation) in order to simplify the convolution integral, but the model is applicable to continuously varying loads.

Some literature reports extensions to the Schapery model in which the authors add a term to capture time dependent inelastic behavior which cannot be captured by the non-linear parameters in the Schapery model, for instance, by including a linear dashpot term in the Prony series. The additional terms are called various names; in this document, they will be referred to as 'viscoplastic', indicating time dependent behavior resulting in non-recoverable strain for which the non-linearity is not captured by the viscoelastic constitutive expression.

For instance, Lai and Bakker [100] used the Schapery equation to express the non-linear viscoelastic behavior and an equation with both stress and time dependence to express the viscoplastic behavior of high density polyethylene. Zapas and Crissman [101] perform a similar analysis on ultra-high molecular weight polyethylene, although the form of their viscoplastic equation differs from that of Lai and Bakker.

Another example of a non-linear viscoelastic and viscoplastic constitutive equation is found in [94]. This equation models the material behavior with two parallel mechanisms; one governs time independent (elastic-plastic) behavior and the other expresses the observed time dependent (elastic-viscous) behavior. The elastic-plastic behavior is expressed through an elastic spring constant and isotropic strain hardening based on equivalent plastic strain. The elastic viscous behavior has a separate spring constant and time dependent plasticity through the Norton-Hoff rate law.

One thing the Schapery-based equations have in common with that of Khattra [94] is that they both assume deformations are small: in order to sum the strain components, this assumption must hold. For the general case, the multiplicative decomposition theory in continuum mechanics dictates that the strain *rate* tensors, rather than the strain tensors, be summed for the basis of the analysis.

Constitutive equations originally developed to capture the large deformations in elastomers are consistent with continuum mechanics and capable of expressing non-linear viscoelastic behavior. Kusoglu [102] examines the applicability of two such constitutive equations to Nafion immersed in liquid water. They concluded that Ogden's strain energy formulation [103] provided a more accurate approximation of the material behavior than the Mooney-Rivlin theory [104], [105]. While the results for immersed Nafion were encouraging, the authors noted that neither model was able to express the behavior of membranes equilibrated in vapor.

The work of Silberstein is also consistent with continuum mechanics at large strains. The constitutive equation employed by Silberstein is an extension of the Arruda and Boyce model [106] and assumes two mechanisms are responsible for deformation. One mechanism expresses the intermolecular interactions occurring in the polymer and the other captures behavior due to alignment of the molecular network. The response of Nafion has been successfully captured in both uniaxial [89] and biaxial [83] tests with this model, and the model has further been implemented in a finite element program to investigate the behavior of Nafion [83], [107].

Due to the interest in using finite element analysis (FEA) to simulate fuel cell operation, several research groups have selected constitutive equations which are available in standard finite element packages. For instance, Solasi [92] selected a two-layer viscoplastic model available in the commercial software ABAQUS to model the behavior of Nafion over a range of temperatures and hydration levels. With this

model they were able to predict the response of Nafion in stress relaxation and strain ramp experiments.

Additional examples of non-linear viscoelastic viscoplastic constitutive equations include those of Drozdov [108-112], Yoon [113] and Zhang [114]. These equations have not been applied directly to PEM materials, but are similar in form to the equations just discussed and could also be useful in numerical analysis of PEM materials.

2.5. Finite Element Models

Constitutive models can be used independently to calculate material response to uniform loading conditions in the absence of geometric effects. However, if the effects of sample geometry or non-uniform or dynamic loading conditions are of interest, a more advanced technique is needed to address these factors. One popular technique is the use of finite element models. In a finite element model, a geometric representation of a system is developed in one, two or three dimensions. Constitutive properties are assigned to the material comprising the model and boundary conditions, and loads are applied. The model is usually discretized into a number of subdomains and the forces, displacements, etc., at all subdomains are determined through an iterative solution. This type of analysis gives the researcher insight into gradients that occur within a system due to non-uniform sample geometries and load applications.

2.5.1. Survey of FEA Models Used for Fuel Cells

Many researchers have used finite element models to study the response of PEM materials to fuel cell like conditions. For instance, Tang, et al. [33], used a 2D finite element model to explore the effect of gas channel alignment on the stresses in Nafion during temperature and moisture changes. The gas channels constrain the membrane out-of-plane, and they may be assembled so that the grooves and surfaces alternate or align. Analysis showed that hygrothermally driven stresses in the membrane were slightly lower when the gas channels were aligned than when they were alternating. In other words, if the membrane was pinched on both sides (between the lands of the bipolar plates), the stresses were smaller than if the membrane was able to swell into the channel on one side. A later study with a 3D model showed that hygrothermal cycling induces residual tensile stresses in the dried membrane, supporting the theory that residual tensile stresses cause membrane thinning over many fuel cell cycles [115]. The constitutive model for these studies accounted for thermal and hygral effects on strain and material properties, but did not include time dependence of the constitutive properties of the material.

Lai, et al. [31] also accounted for thermal and hygral strain in their model, but in addition considered time-dependence of material properties, as determined by creep experiments. They also used TTMSP to express thermal and hygral effects on the material properties. A linear viscoelastic constitutive model was used to predict the transient response of a Nafion PEM constrained in-plane during hygrothermal cycling. Like Tang, et al. [115], these authors found that increasing moisture in a constrained membrane induces compressive stresses and that subsequent drying leaves residual tensile stresses.

Nafion was also modeled as a two–layer viscoelastic/viscoplastic material by Solasi, et al [92]. With this constitutive definition, they found reasonable agreement with strain ramp and stress relaxation

experiments at several environmental conditions, although the environment was held constant through the duration of each test.

Silberstein and Boyce [89] developed and validated an elastic-viscoplastic constitutive model for Nafion implemented in a finite element program. Although hygral and thermal expansion were included, the material properties were independent of environmental conditions. Validation experiments were performed for membranes under both uniaxial and biaxial tensile loading conditions and the validated finite element model was used to examine several loading conditions. For example, the response of a membrane constrained in a fuel cell stack was examined for hygrothermal cycling [107], and the stress distributions and yield behavior in a biaxially constrained cruciform sample were investigated [83].

A model which is applicable for both uniaxial and multiaxial loads, such as that demonstrated by Silberstein, et al. [107] is highly desirable in the development of PEM materials. In order to develop such a model, the behavior of the PEM should be experimentally investigated. A constitutive expression can then be selected to express key material behaviors observed in the experiments. As demonstrated in the literature review, these behaviors include time, temperature and moisture dependent properties and non-linear mechanical stresses and strains arising from changes in the hygrothermal conditions surrounding a constrained PEM. Previous work by the GM/VT research group characterized some of these behaviors in the linear viscoelastic region [42] and the present work is focused on extending that work to apply to non-linear stresses, such as the PFCB/PVDF blend would experience during fuel cell operation.

Uniaxial experiments were used to characterize the linear viscoelastic response of the PFCB/PVDF blend and are useful for the extension to non-linear analysis because they are simple to conduct and analyze. However, the actual operating conditions of a PEM involve multiaxial constraints and deformations, so a constitutive model should also be validated against multiaxial experiments. The goal of the present work is to develop a constitutive expression for the PFCB/PVDF behavior from uniaxial experiments which is also applicable to biaxial loads. That applicability will be investigated by implementing the constitutive expression in a finite element model and comparing model simulations with experiments at various environmental conditions.

3. Experimental Techniques

3.1. Material Description and Preparation

The material used for this research is a polymer blend consisting of 70 wt% sulfonated perfluorocyclobutane copolymer (PFCB) and 30 wt% polyvinylidene fluoride (PVDF), as described in [73]. The membrane was prepared by General Motors Company using a commercial casting system by depositing a solution of the PFCB/PVDF suspended in DMAC onto Teflon coated Kapton sheets. The nominal thickness of the resulting sheet of material is 18 µm. Residual solvent was removed from the specimen prior to performing mechanical experiments by clamping small sheets of membrane in a Teflon frame and submerging the clamped sheets in 50˚C deionized water for two hours. Upon removal from the water bath, residual water droplets on the specimens were removed by lightly dabbing with Kimwipes and the material, still clamped in the frame, was left to dry at room conditions.

Significant tensile stress developed in the membrane during this drying process. To release these stresses, each individual specimen was subjected to a hygrothermal pretreatment before performing mechanical experiments. In this pretreatment, the specimen was first heated at 1˚C/min to 100˚C, at 0%RH and held at 100˚C, 0%RH for two hours. The temperature was then ramped down to the intended testing temperature at 1˚C/min and the humidity was subsequently raised to the intended testing humidity at approximately 1%RH/min. The testing conditions were maintained for two hours prior to beginning the experiment. Most experiments were performed at 70˚C, 30%RH, so the pretreatment profile for this condition is included in Figure 3-1 as an example.

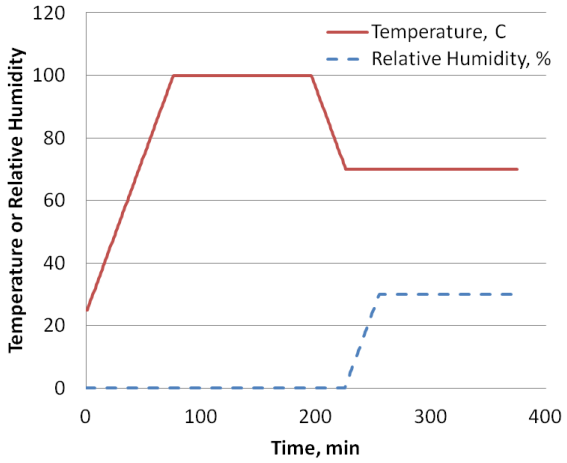

Figure 3-1. Environmental pretreatment process.

3.2. Uniaxial Characterization Experiments

The PFCB/PVDF blend was characterized in uniaxial tension in a TA Instruments DMA Q800 with a humidity accessory. Creep and recovery tests, in which the sample ass subjected to a constant stress (creep) followed by a period of negligible stress (recovery) were performed on tensile specimens at 70˚C, 30%RH; temperature control was ±0.5˚C and relative humidity control was ±3%RH. The

specimens were prepared from sheets of material which had been through the submersion treatment by cutting with a rule die supplied by General Motors. The resulting specimen geometry is illustrated in Figure 3-2. The distance between the grips is approximately 12 mm. When loaded in the DMA, the samples were gripped so that the portion of the sample between the grips consisted of three parallel strips, each 3 mm wide, as indicated in Figure 3-2. This geometry maintains an aspect ratio and gauge length appropriate for DMA tensile testing while increasing the effective sample cross-sectional area (and hence the required force) by a factor of three, thus reducing the significance of the experimental uncertainty in the force measurement.

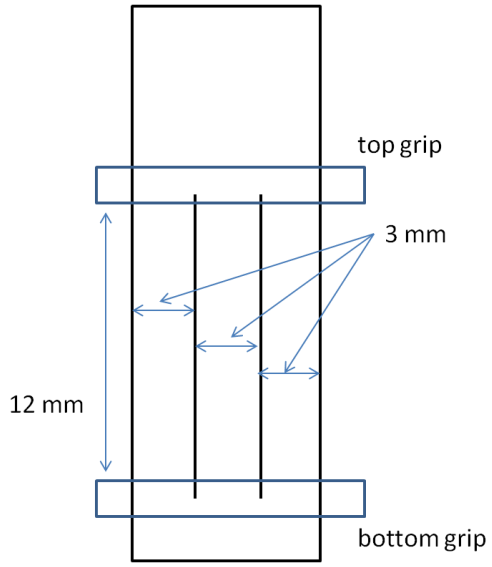

Figure 3-2. Sample geometry for DMA experiments.

Experimental work by Li, et al. [3] demonstrated that Nafion develops strains up to 9% (corresponding to 4 MPa stress) for RH changes of 40% at 80˚C. Similar work performed on the PFCB/PVDF blend [116] demonstrated that tensile stresses due to hygrothermal cycling approach 10 MPa, so characterization experiments on the PFCB/PVDF blend were attempted at creep stresses of up to 10 MPa. Creep times of 20 minutes and 200 minutes were imposed; recovery times were ten times longer than the imposed creep time. The force applied during recovery for all creep stresses was 0.001 N, which corresponds to an engineering stress of 0.006 MPa. This value was sufficiently large to prevent the specimen from buckling but small enough that further creep was negligible.

It was discovered that the tensile specimens elongated quickly during long duration experiments at high stress such that the stroke limit of the DMA was reached prior to the intended completion of the experiment. This limited the range of stresses and loading times under which creep experiments were performed. Table 3-1 shows stresses and times for the creep recovery experiments which were ultimately performed for characterization. Five replicates at each condition were tested to characterize the experimental uncertainty in the data.

Table 3-1. Experimental matrix for uniaxial characterization.

Creep Stress, MPa	Creep Time, min	Recovery Time, min
0.5	20	200
0.5	200	2000
2	20	200
2	200	2000
4	20	200
4	200	2000
6	20	200
6	50	500
8	20	200

3.3. Uniaxial Validation Experiments

Experiments for validating the uniaxial model were performed at 70˚C, 30%RH in the DMA Q800 on tensile specimens with the geometry illustrated in Figure 3-2. All specimens were subjected to the hygrothermal pretreatment illustrated in Figure 3-1 directly before the mechanical experiment. Three types of experiments were performed: stress relaxation, force ramp, and multiple step creep and recovery. Stress relaxation experiments, in which the specimen is stretched to a fixed length and the stress required to maintain that length are measured, were performed at elongations equivalent to 0.5%, 1.0%, and 3.0% strain. Additionally, force ramp experiments at rates of 0.01 N/min, 0.1 N/min, and 1.0 N/min were performed. Multiple step creep experiments with the force profiles illustrated in Figure 3-3 were also conducted. In the profile called 'MultiA', there were five 20 minute force applications corresponding to engineering stresses of 2.0 MPa, 7.0 MPa, 4.0 MPa and 5.0 MPa, followed by a recovery period of 200 minutes under an engineering stress of 0.006 MPa (a negligible load intended to prevent buckling). The second profile, MultiB, consisted of 20 minute applications of 2.0 MPa, 5.0 MPa, 4.0 MPa and 7.0 MPa, followed by the same recovery period. The order of the stress steps was different between these two experiments to verify that the model was able to capture the behavior of the material after a large stress loading period.

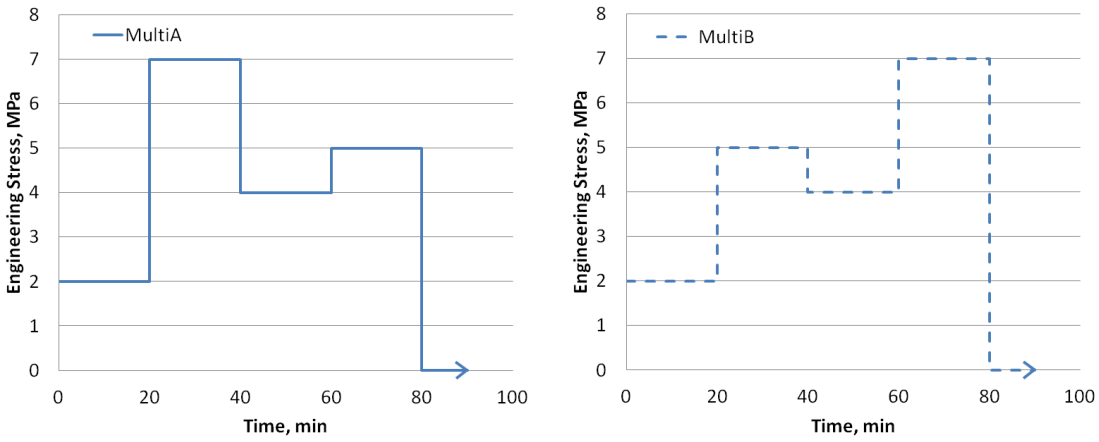

Figure 3-3. Multistep force profile for uniaxial validation experiments.

3.4. Digital Image Correlation

The mechanical experiments discussed above determine strain only in the axial direction of a sample, and the value reported is an average across the whole sample since only the displacement at the grips is known. For some applications, it is desirable to know the distribution of strains across the surface of the sample and/or strains in the transverse direction. In other applications, the experimental setup does not lend itself to the use of a physical (contact) extensometer. For these situations, digital image correlation (DIC) is a useful tool for measuring strain.

The DIC system used for this research was purchased from Trilion Quality Systems. It consists of two cameras, each 2 Megapixels, and the hardware necessary to have them collect images simultaneously. The cameras have 50mm Schneider Kreuznach lenses. The software used to process the images is Aramis v6.0.2.1 [117]. The following paragraphs briefly outline the operating principles of this DIC system.

The physical configuration of the DIC components is illustrated in Figure 3-4. The two cameras are positioned some distance from the sample and angled so that they observe the same location on the sample surface. Both cameras record images simultaneously as the sample deforms. A random pattern applied to the sample prior to testing makes it possible for the software to track deformations on the sample surface, since the pattern moves with the surface during deformation. Out-of-plane deformation within the depth of the measuring volume can be determined with this technique because two cameras are being used.

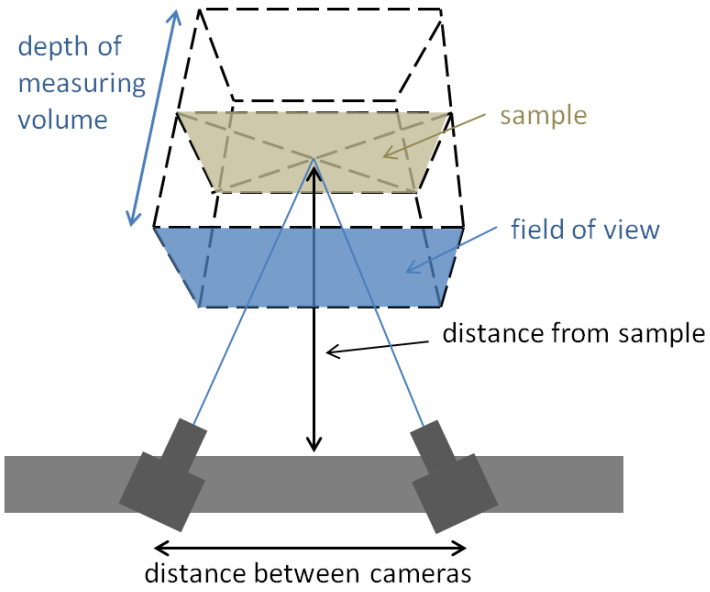

Figure 3-4. General configuration of sample and cameras for the digital image correlation (DIC) system.

The system configuration (distance from sample and between the cameras) can be adjusted to increase or decrease the field of view the system is able to resolve on the sample surface. Custom calibration panels are available to calibrate the system for various configurations. The surface of each panel has an extremely precise spot pattern; the size of and distance between the spots is pre-coded into the software. After the proper panel is selected for the desired system configuration, it is imaged at specific distances and orientations. These images are processed along with the pre-coded information to properly correlate movement of features in the images to the actual displacement occurring on the sample surface.

Rather than having to apply a specific spot pattern to all samples, a random pattern of speckles is applied to the sample surface. The necessary speckle size and density varies with the desired field of view and the resolution of the cameras. Generally, the speckles should cover 5-7 pixels in the images and there should be enough space between them that they are distinct from each other. A speckle pattern of black ink (Higgins Waterproof Black Magic) was airbrushed onto the surface of the samples for the cameras to resolve the motion of the sample. This is a water-based ink with no solvents in the mixture to avoid degrading the samples. DMA experiments showed that the ink did not significantly affect the mechanical properties of the samples.

As the sample deforms, the speckles shift locations from image to image. Deformations on the sample surface are determined by defining groups of pixels, called ‘facets’, which are roughly square on the undeformed sample. The software tracks the movement of the speckles from one image to the next and changes the size and shape of the associated facet accordingly. The location of each facet is reported as the location its center; this location is called the ‘measuring point’. The measuring point for each facet is correlated in both the left and right images to a user-defined tolerance, usually of 0.04 pixels.

The number of pixels in a facet (facet size) and extent of overlap with neighboring facets (facet step) can be adjusted. Larger facets and smaller step sizes improve accuracy but increase the time it takes to track facets through the whole image series because more pixels are included in each calculation, and more calculations are performed since the facets overlap. Smaller facets and larger facet steps have the opposite effect.

Strain is calculated from the changing facet field. A single strain value is calculated from a collection of measuring points, similar to the way a measuring point is calculated from a collection of speckles. The number of measuring points used in the strain calculation is referred to as the 'computation size'. Increasing the computation size increases the number of measuring points used in the strain calculation, effectively averaging the strain over a larger area. A single strain value is reported at the center of each computation domain. Again, this is analogous to the single measuring point reported for each facet.

The theoretical resolution of a displacement measurement using DIC is a function of the camera resolution and field of view. For example, the 2 Megapixels cameras used in this analysis result in images which are 1600x1280 pixels. For a 10x8 mm field of view, this translates to 6.25 μm per pixel. If the coordinates of the center of a facet are determined within 0.04 pixels, this translates to a theoretical displacement resolution of 0.25 μm.

The theoretical resolution of the strains reported by the DIC is a function of the facet step and computation size used for an analysis. The facet step controls the distance between measuring points while the computation size controls how many adjacent points are included in the strain calculation for a particular facet. Thus, increasing the facet step and increasing the computation size both increase the length of the effective strain gauge. Again, consider the 2M cameras and a 10x8 mm field of view. The default facet step of 13 pixels results in 81.25 μm between each measuring point. The default computation size of 3 indicates that one point on each side of the facet is used for calculating the strain in that facet. The locations of the outer measuring points, which define the length of the strain gauge, are known to within 0.04 pixels, or 0.25 μm. From the parameters just stated, the distance between these points is known to be 26 pixels in the undeformed state. For an experiment with strains on the order of 1%, the theoretical uncertainty in the strain calculation is therefore 0.4%.

Unfortunately, experimental conditions are rarely perfect, and therefore it is useful to have a measure of the actual displacement uncertainty, in addition to the theoretical uncertainty. The actual uncertainty may be measured for any experiment by taking two (or more) pairs of images of the test specimen without applying any loads or deformations in between the time the images were taken. Theoretically, the pictures would be exactly identical and the deformation in the second pair of images, as referenced to the first pair, would be zero. When looking at actual images, any 'phantom' displacements observed in the second pair of images gives a measurement of the actual displacement uncertainty. This procedure was performed for the experiments below to obtain such a measurement. The approximate displacement uncertainty obtained by this method was averaged over the surface of the sample and is reported below as the 'experimental noise floor'. The theoretical resolution and system configurations are also reported below in the sections detailing each of the experimental procedures which use DIC.

3.5. Poisson's Ratio Experiments

The tensile experiments described above characterize the uniaxial mechanical property (creep compliance or relaxation modulus) of the membrane in a single dimension. In a fuel cell, the PEM is biaxially constrained. In order to make predictions of the in-situ mechanical behavior of a PEM, a constitutive model should be applicable to multiaxial loading conditions. One way to perform multiaxial simulations is to assume that the material has isotropic mechanical properties and use the material properties measured in uniaxial experiments in all material directions during a simulation. In multiaxial simulations, out-of-plane mechanical effects must be accounted for, so in addition to the uniaxial property already measured, either the bulk property (compliance or modulus) or Poisson's ratio must be specified. For viscoelastic materials, the time dependence of the Poisson's ratio and bulk property must also be addressed.

Previously, the GM/VT research group has assumed a constant bulk modulus and an initial elastic value for Poisson's ratio, then used the Laplace transform of the relation between the elastic constants to assign time dependence to Poisson's ratio consistent with that measured in the uniaxial property (relaxation modulus or creep compliance) [80]. (For further explanation, please see the development of the multiaxial constitutive expressions in Chapter 4.) This approach is common in the literature [118]. However, including the actual magnitude and time dependence of Poisson's ratio would improve the constitutive model, so experiments were performed to measure the Poisson's ratio of the PFCB/PVDF blend. Poisson's ratio is defined at the ratio of axial strain to transverse strain. For time dependent materials the data reduction is greatly simplified if the axial strain is constant throughout the experiment. Thus, stress relaxation experiments were performed. Poisson's ratio is also defined specifically in the region of linear mechanical response, so small strains were applied. (During analysis in the non-linear region it is assumed that all non-linearity is expressed by the shear and bulk properties, so Poisson's ratio remains independent of applied load or strain.)

An Instron (model 5800) with small pneumatic grips was used to apply the axial extension. Temperature and relative humidity were controlled by an environmental chamber developed in-house; temperature control was $\pm 0.5^{\circ}C$ and relative humidity control was $\pm 3\%RH$. Axial and transverse strains were measured by a Trilion digital image correlation (DIC) system through a double-pane glass window in the door of the environmental chamber. This experimental apparatus is shown in Figure 3-5.

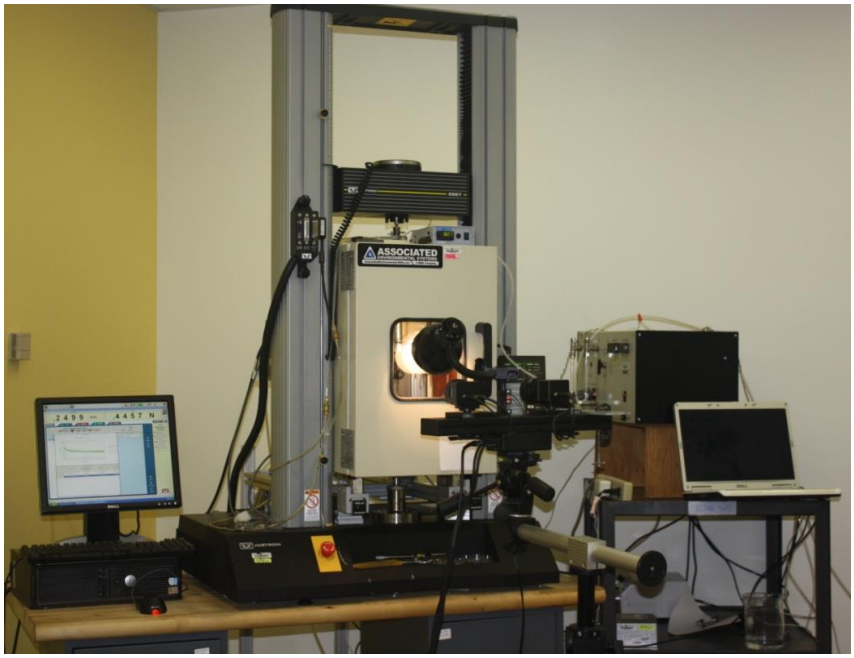

Figure 3-5. Instron, environmental chamber, and DIC system used to perform Poisson's ratio experiments.

Prior to testing, all samples were subjected to the water bath and hygrothermal pretreatment described previously. After being loaded into the environmental chamber in the Instron, samples were allowed to equilibrate with the 70˚C, 30%RH testing conditions for one hour. The specimens had a simple rectangular geometry, 9mm wide and approximately 40mm long. Stress relaxation tests at about 1% strain were conducted for 30 minutes, during which time the DIC system imaged the specimen at discreet intervals. Images were taken at a rate that decreased with the length of test time so that more images were recorded frequently early in the experiment (max frame rate: two images per second) but increasingly farther apart as the experiment progressed (minimum frame rate: one image per minute). The Aramis software within the DIC system was used to compute strains on the surface of the specimen. Table 3-2 details the DIC configuration for the Poisson's ratio experiments.

Table 3-2. DIC configuration for Poisson's ratio experiments.

Feature	Dimension
Distance from sample	560 mm
Distance between cameras	250 mm
Field of view	65 mm x 48 mm
Depth of measuring volume	4.8 mm
Theoretical displacement resolution	1.5 µm
Experimental noise floor	3 µm

In initial experiments, a single sample was mounted in the Instron grips inside the environmental chamber and imaged through the door. However, significant curling was noted in these single layer

samples. The curling resulted from equilibration with the higher moisture content in the environmental chamber. The low extensions required to measure Poisson's ratio were not sufficient to remove curling from the sample. Therefore, the DIC measured artificially small strains in the transverse direction. This led to values of Poisson's ratio which were physically unreasonable (greater than 0.5).

At larger axial extensions, the single layer samples developed puckers due to geometric instabilities associated with very thin specimens [119]. Again, this resulted in artificially low measures of transverse strain and artificially high values of Poisson's ratio.

To counter these effects, two-layer samples were used for experiments. The two layers were assembled in the following manner: A rectangular sheet of membrane was laid on a vacuum plate with the vacuum turned on. Thin strips of Kapton were used to press wrinkles out of the membrane surface. A second rectangular sheet of membrane was then laid on top of the first sheet such that the long axes of the two rectangles were perpendicular to each other. This orientation facilitated removing wrinkles from the second sheet since the vacuum acted directly on the second sheet at the edges where it did not overlap the first sheet. Care was taken to cut the individual sheets such that the machine directions were aligned in the two layers.

The two sheets were then carefully removed from the vacuum plate and placed in a hot press, where they were pressed lightly for 30 seconds between heated platens at 70˚C. This step improved the bond between the two sheets. Samples for the Poisson's ratio experiments were cut from this two-layer assembly using a rule die. Experiments with these samples exhibited significantly less curling and puckering than those conducted on single-layer specimens.

3.6. Biaxial Validation Experiments

Specimens were tested under biaxial loading using the pressure loaded blister fixture shown in Figure 3-6 [120]. In this experiment, a circle of membrane is constrained around the perimeter such that it has a free radius of 9.5mm and is pressurized from behind. This results in a bubble or blister-like shape in the membrane. In the center, away from regions where the edge constraints have an effect, the loading is equal-biaxial.

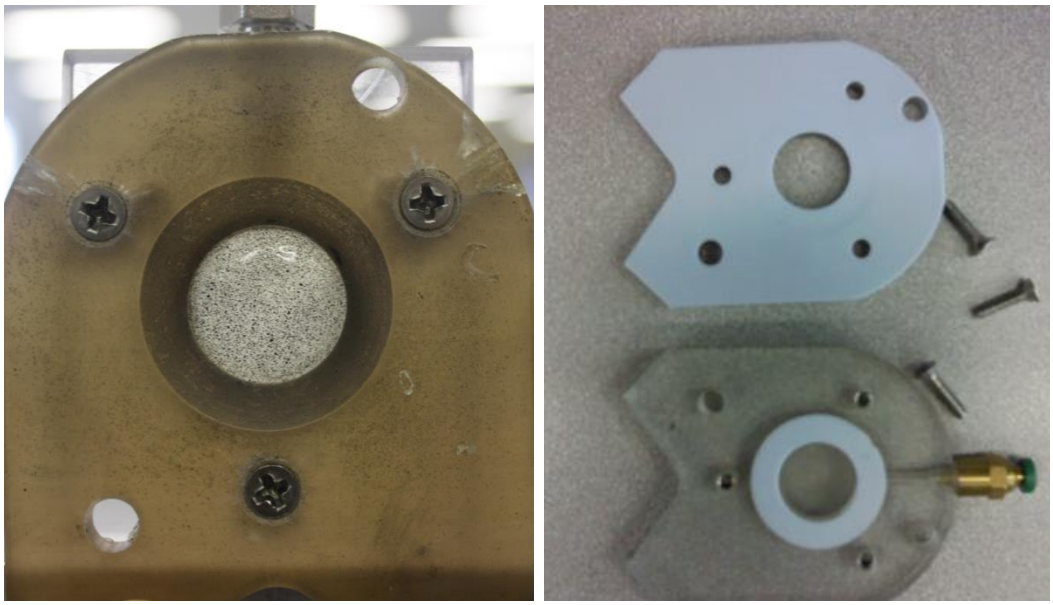

Figure 3-6. Left: Speckled PFCB/PVDF membrane loaded in blister fixture. Right: Blister fixture disassembled.

Blister experiments on the PFCB/PVDF blend were performed at 70˚C, 30%RH in an environmental chamber developed in-house; temperature control was ±1˚C and relative humidity control was ±2%RH. The samples went through the standard water bath and hygrothermal pretreatment. After being loaded in the blister fixture, samples were allowed to equilibrate in the environmental chamber for one hour prior to applying pressure. The environmental chamber used for blister experiments was different than that for Poisson's ratio experiments; it is shown in Figure 3-7.

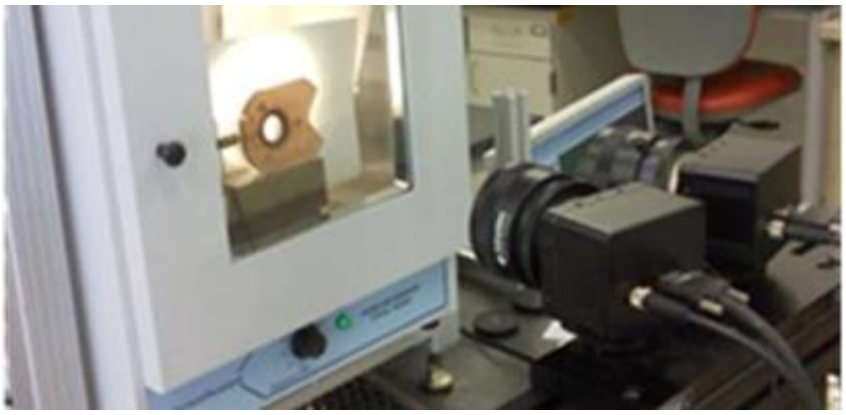

Figure 3-7. Environmental chamber for blister experiments.

A constant pressure of 5kPa, 10kPa, 15kPa, or 20kPa was applied for 40 minutes. Each experiment was performed on a fresh sample. Pressure was controlled with a LabVIEW program also developed in-house, and strains on the surface of the blister were measured through a glass window in the environmental chamber with the DIC system in the configuration detailed in Table 3-3. Like the Poisson's ratio experiments, a speckle pattern with black ink was airbrushed onto the sample.

Table 3-3. DIC configuration for pressure-loaded blister experiments.

Feature	Dimension
Distance from sample	280 mm
Distance between cameras	130 mm
Field of view	25 mm x 18 mm
Depth of measuring volume	1.4 mm
Theoretical displacement resolution	0.625 µm
Experimental noise floor	2 µm

Stresses in the central region of the blister were calculated using thin-walled pressure vessel theory by Equation 3-1. Pressure (p) was measured and recorded by the LabVIEW program mentioned previously. The radius of curvature (R) was obtained from the Aramis software by fitting a sphere to the central region of the deformed blister. This region is well-fit by a sphere for the lower three pressure levels used in this study, and the radius of curvature of the sphere fit was not sensitive to the surface area selected for performing the fit, as long as the region with edge effects was excluded. The thickness (t) of each blister specimen was measured with a Mitutoyo drop-gauge micrometer prior to testing.

$$\sigma = \frac{pR}{2t} \qquad \textbf{3-1}$$

3.7. Uniaxial Experiments at Additional Hygrothermal Conditions

All experiments discussed thus far were conducted at constant environmental conditions of 70˚C, 30%RH. Fuel cells operate at varying temperature and moisture, so a constitutive model should be able to simulate the response of the PEM to time-varying hygrothermal conditions. The influence of temperature and relative humidity on the linear viscoelastic response has previously been characterized by Finlay [42] with TTMSP hygrothermal shift factors and linear hygral and thermal expansion coefficients. However, the shift factor experiments were performed in regions where the viscoplastic response is negligible, so no information about the effect of temperature or relative humidity on viscoplastic strain was obtained. Therefore, the current work incorporates experiments to investigate the environmental dependence of the viscoplastic response. (This analysis assumes that the non-linear viscoelastic parameters are independent of environment. The validity of this assumption will be investigated in the Results chapter.) The MultiB profile discussed above was used in the DMA Q800 for these experiments.

To isolate the effect of environment on the viscoelastic and viscoplastic components of response, two conditions were selected which required no shifting to agree with reference condition (70˚C, 30%RH) in the linear viscoelastic region. Thus, any discrepancy between results would be due entirely to the environmental dependence of the non-linear viscoelastic or viscoplastic parameters. The conditions selected were 50˚C, 55%RH and 80˚C, 10%RH. Additional experiments were performed at 50˚C, 10%RH, 50˚C, 30%RH, and 70˚C, 10%RH, to provide more data for model development.

3.8. Uniaxial Experiments at Varying Hygrothermal Conditions

The constitutive model is ultimately intended to predict material response in an operating fuel cell. The environmental conditions in an operating fuel cell are not constant because the power demands from the cell change with driving conditions – acceleration, deceleration, hills, etc. Therefore, two uniaxial experiments were performed in the DMA Q800 at varying hygrothermal conditions to investigate the applicability of the model to non-constant hygrothermal conditions.

The first was performed under a static force of 0.1 N. During this test, the relative humidity was held constant at 30%RH while the temperature was cycled between 30˚C and 70˚C. The temperature ramped linearly from 30˚C to 70˚C over 50 minutes and then ramped back down to 30˚C over 50 minutes. This cycle was repeated ten times. The second experiment was similar to the first, except that the temperature was held constant at 70˚C and the relative humidity was ramped between 30%RH to 70%RH over 40 minutes and held for 10 minutes at the extremes.

3.9. A Discussion on Experimental Data Reduction

The experiments performed for this study rely on two parameters to characterize mechanical response: force and deformation. In order to compare the results of experiments from different samples, it is convenient to remove sample-specific information by converting force into stress and deformation into strain. For uniaxial configurations, stress is typically defined as applied force divided by initial cross-sectional area; this is known as the engineering stress. Engineering strain is defined as the change in sample length divided by initial length.

These definitions, although useful for many applications, are approximations. Consider the effect of large deformations on the value of engineering stress: as the sample extends, the Poisson effect dictates that the cross-sectional area decrease. The actual stress in the material is now the applied force divided by the reduced cross-sectional area. Similarly, the engineering strain is a linearization of the true definition of strain from continuum mechanics. It is useful for small deformations, but becomes increasingly inaccurate for strains above 5%, as will be demonstrated in the discussion around Figure 3-8. The finite element program used for simulations in this research, Abaqus, uses the accurate definitions for stress and strain. Therefore, it is essential to use the proper definitions of stress and strain with all experimental data. These definitions are briefly described below. For a more thorough treatment, the reader is referred to a continuum mechanics textbook such as that by Batra [121].

Continuum mechanics defines strain from the deformation gradient, which is a tensor description of motion. The initial position at point A is defined by vector coordinates X1, X2, X3 and the new location by x1, x2, x3. The deformation gradient, ***F***, is a tensor 'map' of the motion between the original and current locations. It is defined in Equation 3-2.

$$F_{iA} = \frac{\partial x_i}{\partial X_A} = \begin{bmatrix} \frac{\partial x_1}{\partial X_1} & \frac{\partial x_2}{\partial X_1} & \frac{\partial x_3}{\partial X_1} \\ \frac{\partial x_1}{\partial X_2} & \frac{\partial x_2}{\partial X_2} & \frac{\partial x_3}{\partial X_2} \\ \frac{\partial x_1}{\partial X_3} & \frac{\partial x_2}{\partial X_3} & \frac{\partial x_3}{\partial X_3} \end{bmatrix} \quad \textbf{3-2}$$

Now consider a body made up of many such points. When that body is deformed, the points will move relative to each other. This motion can be divided into two categories: pure stretch and pure rotation. The deformation gradient at each point on the body describes the stretching and rotation that occurs during the deformation.

Strain tensors are derived from the deformation gradient such that they are identically zero if no stretching of the body occurs during motion. For a Lagrangian (or referential or material) description of motion, in which the motion of a single particle is tracked through the deformation, the Green-St. Venant strain tensor is used. This tensor is defined in Equation 3-3, where ***F*** is the deformation gradient and δ is the Kronecker delta, which denotes a matrix whose elements are zero except for those on the diagonal, which have values of one. The Almansi-Hamel strain tensor, shown in Equation 3-4, is used for an Eulerian (or spatial) description of motion, in which material points which move through a fixed point in space are observed. Given the deformation gradient, both strain tensors can be determined.

$$E_{AB} = \frac{(F_{iA}F_{iB} - \delta_{AB})}{2} \quad \textbf{3-3}$$

$$\epsilon_{AB} = \frac{\left(\delta_{ij} - F_{iA}F_{jA}\right)}{2} \quad \textbf{3-4}$$

Stress tensors express the distribution of force, per unit area, on the surfaces of an infinitesimally small volume element within a material. The Cauchy stress tensor, ***T***, is defined over the actual area of the surface, that is, the present rather than reference configuration. Experimentally, usually only the referential configuration is known. The stress tensor defined on the area in the reference conditions is called the nominal, engineering, or first Piola-Kirchhoff stress tensor, $\widetilde{\boldsymbol{T}}$. The engineering stress tensor is related to the Cauchy stress tensor by the deformation gradient through Equation 3-5. The new subscripts *m* and *n* are introduced as free indices

$$\tilde{T}_{iB} = det(\boldsymbol{F})T_{ij}(F^{-1})_{Bj} \quad \textbf{3-5}$$

The impact of this theoretical discussion on the interpretation of experimental data is illustrated in Figure 3-8. The plot illustrates the results for the first 20 minutes of a creep experiment on the PFCB/PVDF blend at 70˚C, 30%RH. The applied force was nearly constant at 1.192 N and the sample was initially 22.6 microns thick and 9mm wide. As seen in the figure, this corresponds to an engineering stress of approximately 5.88 MPa. The engineering strain in this tensile experiment, calculated as change in length divided by initial length, approaches 8%.

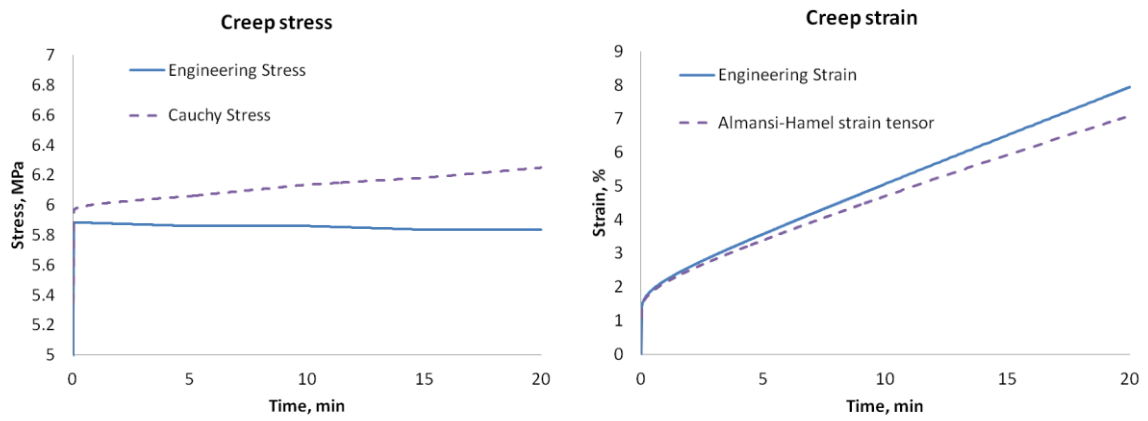

Figure 3-8. Demonstration of engineering stress/strain and Cauchy stress, Almansi-Hamel strain differences during a 20 minute creep experiment at 6.0 MPa.

Recall that a deformation gradient is necessary for converting between the engineering stress/strain tensors and the other tensors. For a uniaxial experiment, the deformation gradient is approximately constant, or homogeneous, through the entire sample, and is given in Equation 3-6. The uniaxial extension, β, is measured experimentally and for this example, Poisson's ratio is denoted by ν and is the assumed to be the same in and out of plane for the duration of the experiment. This assumption dictates the values of F_{11} and F_{33} because of the Poisson effect. Thus, the Almansi-Hamel strain tensor and the Cauchy stress tensor can be calculated by Equations 3-7 and 3-8, respectively.

$$F_{iA} = \frac{\partial x_i}{\partial X_A} = \begin{bmatrix} \alpha & 0 & 0 \\ 0 & \beta & 0 \\ 0 & 0 & \alpha \end{bmatrix} \tag{3-6}$$

$$\epsilon_{ij} = \begin{bmatrix} -\frac{1}{2}\nu\left(1-\frac{1}{\beta^2}\right) & 0 & 0 \\ 0 & \frac{1}{2}\left(1-\frac{1}{\beta^2}\right) & 0 \\ 0 & 0 & -\frac{1}{2}\nu\left(1-\frac{1}{\beta^2}\right) \end{bmatrix} \tag{3-7}$$

$$T_{ij} = \begin{bmatrix} 0 & 0 & 0 \\ 0 & \sigma_{ENGR}\left(1+\nu\frac{1}{2}\left(1-\frac{1}{\beta^2}\right)\right) & 0 \\ 0 & 0 & 0 \end{bmatrix} \tag{3-8}$$

As shown in Figure 3-8, the Cauchy stress increases steadily throughout the experiment as a result of the changing cross-sectional area of the sample. Poisson's ratio is assumed to be 0.4 for this figure. The Almansi-Hamel strain measure is initially identical to the engineering strain, but approaches 7% toward the end of the experiment, significantly smaller than the engineering strain value of 8%. *Because of the significance demonstrated here, all uniaxial experimental data is expressed in Cauchy stress and Almansi-Hamel strain prior to model development or comparison with simulations.*

The results from biaxial experiments are also expressed as Cauchy stress and Almansi-Hamel strain. The deformation gradient for the central region of the blister, where the stresses are analyzed, is shown in Equation 3-9. Using Hooke's Law for equal-biaxial load in an isotropic material, the through-plane extension can be expressed in terms of the in-plane extensions and an assumed value of Poisson's ratio. This relationship is shown in 3-10. With this information, the stresses calculated using thin-walled pressure vessel theory and the strains reported by the DIC software can be properly converted by Equations 3-11 and 3-12 by determining the extension γ from the engineering strains.

$$F_{iA} = \frac{\partial x_i}{\partial X_A} = \begin{bmatrix} \gamma & 0 & 0 \\ 0 & \gamma & 0 \\ 0 & 0 & \varphi \end{bmatrix} \quad \textbf{3-9}$$

$$\gamma = \sqrt{\frac{1}{1 + 4\epsilon_{22}\frac{\nu}{1-\nu}}} \quad \textbf{3-10}$$

$$\epsilon_{ij} = \begin{bmatrix} \frac{1}{2}\left(1 - \frac{1}{\gamma^2}\right) & 0 & 0 \\ 0 & \frac{1}{2}\left(1 - \frac{1}{\gamma^2}\right) & 0 \\ 0 & 0 & \frac{1}{2}\left(1 - \frac{1}{\varphi^2}\right) \end{bmatrix} \quad \textbf{3-11}$$

$$T_{ij} = \begin{bmatrix} \frac{\sigma_{ENGR}}{\gamma\varphi} & 0 & 0 \\ 0 & \frac{\sigma_{ENGR}}{\gamma\varphi} & 0 \\ 0 & 0 & 0 \end{bmatrix} \quad \textbf{3-12}$$

3.10. A Note on Experimental Repeatability

One of the challenges encountered during the present work was obtaining consistent results across several replicates of the same experiment. The pretreatment procedure described in the Experimental Techniques chapter was found to be essential to obtaining repeatable results. Additionally, the creep and recovery experiments at large stresses required monitoring in order to adjust the applied force to maintain constant true stress on the sample. Because each sample had slightly different thickness, the applied force profile was not identical even for experimental replicates at the same creep stress. Thus, measuring the thickness of each sample prior to testing was necessary. Another important factor for obtaining repeatable results was careful loading of the uniaxial tensile specimens, such that the specimen was aligned properly with the instrument grips. Finally, the influence of relative humidity was clearly demonstrated in the Poisson's ratio results. Tight control of the environmental conditions is required due to the sensitivity of the mechanical properties to temperature and relative humidity. These observations should be considered during future work with similar materials.

4. Analytical Techniques

This chapter discusses the selected constitutive equations, the determination of values for the parameters in those equations, and the implementation of the equations in a finite element program.

4.1. Constitutive Equations

The constitutive equations to be implemented in the numerical model must describe non-linear, time dependent, partially recovering behavior. Additionally, a method to include the environmental effects on strain and mechanical properties is needed. The uniaxial equations and techniques for including environmental dependence are outlined below. Multiaxial constitutive equations are developed and reported in the Finite Element Implementation section.

4.1.1. Linear Viscoelastic Behavior

The mechanical properties of the PFCB/PVDF blend show significant time dependence. Previous work by the VT/GM research group has addressed the time dependent mechanical properties of Nafion with a linear viscoelastic Prony series [41], [31], [42], [80]. The same technique is used for the PFCB/PVDF blend. Equation 4-1 shows the expression for calculating strain from a linear viscoelastic Prony series subjected to a time varying stress input. The variable ρ is a 'dummy variable' used for integration and is necessary to properly capture the convoluted effect of time varying properties and stress. The mechanical property used here is the creep compliance D(t), shown as a Prony series in the second expression.

$$\varepsilon(t) = \int_0^t D(t-\rho)\frac{d\sigma(\rho)}{d\rho}d\rho$$

$$D(t) = D_0 + \sum_{i=1}^{N} D_i\left(1 - exp^{-\frac{t}{\tau_i}}\right) \qquad \text{4-1}$$

Because the mechanical response of the PFCB/PVDF blend is non-linear at higher stresses, it is important to ensure that the Prony series, which expresses only the linear portion of the response, is developed from an experiment which is linear viscoelastic. An isochronous plot is used to determine the onset of non-linearity. Results from the creep and recovery experiments, performed to characterize the material, are used to construct an isochronous plot. The strain value at a particular time is obtained from experiments at several stresses. This is done for both long and short times, since the onset of non-linearity may be time, as well as stress, dependent. The onset of non-linearity is defined as the location at which a line through the origin and an experimental point at low stress no longer intercepts the experimental strain values at all stresses.

Figure 4-1 shows the isochronous stress/strain plot for the PFCB/PVDF blend at three times: 6, 60, and 200 seconds after the creep load is applied. Also present are lines for each time which fit the data points via the equations indicated in the figure. The curvature of each line is plotted on the right. The data at 6 seconds is fit well by a linear trendline, indicating that there is no stress-based non-linearity at early times. However, significant curvature in the stress/strain response is evident in the 60 and 200 seconds

fits at larger strains, indicating the onset of non-linearity. Because the curvature is least significant at low strains, the experimental response in the low stress/ low strain region is the most appropriate region from which to extract linear viscoelastic properties. *Therefore, 0.5 MPa is used as the linear viscoelastic region for the present analysis.*

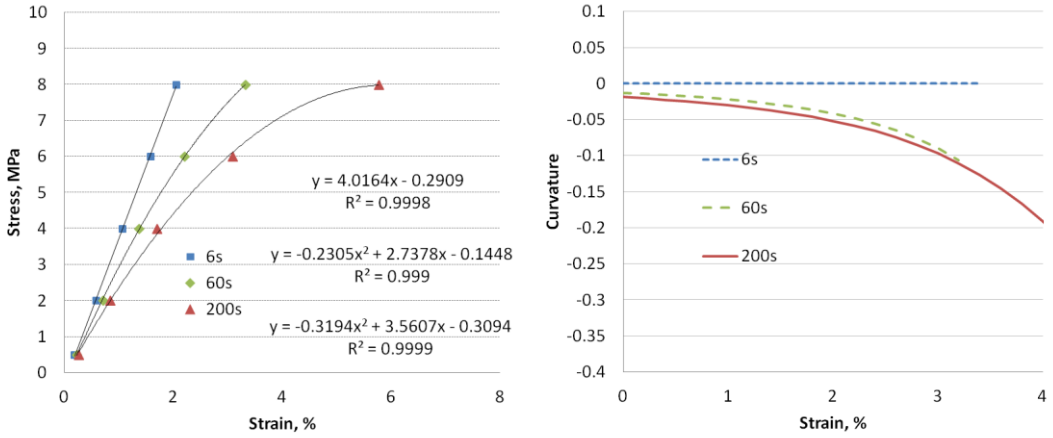

Figure 4-1. (Left) Isochronous plot from 20 min creep data. (Right) Curvature of trendlines from the left figure.

4.1.2. Non-linear Viscoelastic Behavior

The mechanical response of the PFCB/PVDF blend is significantly non-linear in the range of stresses and strains relevant to fuel cell operation. (As mentioned previously, this range was established from RH cycling experiments on a constrained PFCB/PVDF sample. At 80˚C, the peak stresses for RH cycles from 0% to 90% were on the order of 10 MPa [116].) Therefore, a linear viscoelastic Prony series alone is not sufficient to describe the full mechanical response of the blend. The non-linear viscoelastic strains which develop in the membrane are modeled with an equation proposed by Schapery [95]. The integral form of this equation is shown in Equation 4-2 where Equation 4-3 is the definition of the reduced time parameter.

$$\varepsilon^{NLVE}(t) = g_0(\sigma(t))D_0\sigma(t) + g_1(\sigma(t))\int_0^t \Delta D(\varphi(t)-\varphi(\rho))\frac{dg_2(\sigma(\rho))\sigma(\rho)}{d\rho}d\rho \qquad \textbf{4-2}$$

$$\varphi(t) = \int_0^t \frac{d\rho}{a_\sigma(\sigma(\rho))} \qquad \textbf{4-3}$$

In this constitutive equation, the linear viscoelastic creep compliance is modified by non-linear coefficients. In the first term, the elastic compliance D_0 is multiplied by the non-linear coefficient g_0, which expresses non-linearity in the purely elastic response. It is indirectly a function of time because it is a function of the time-varying stress. Similarly, the time dependent compliance ΔD, which is the total compliance D(t) minus the elastic compliance D_0, is expressed as a Prony series and modified by the coefficient g_1. This parameter governs non-linearity in the viscoelastic response. The third parameter, g_2,

expresses non-linearity in the relationship between the thermodynamic generalized force and the local material stress state. This constitutive model was developed using state variables q_i to describe generalized coordinates and generalized forces Q_i which are work conjugate to the generalized coordinates. For any material, the stress and strain are also work conjugate. This is expressed by Equation 4-4.

$$\delta W = Q\delta q = \sigma\delta\varepsilon \quad \textbf{4-4}$$

Rearranging Equation 4-4 gives stress as a function of Q, q, and ε. For sufficiently small strains, q and ε are identical, so Q and σ are also identical. However, at large strains, there may exist a non-linear relationship between q and ε. This results in a non-linear relationship between Q and σ, which is expressed as g_2 in Equation 4-2. Finally, a_σ is the stress shift factor, like the thermal shift factor of TTSP, which accounts for the accelerating effect that large stresses have on the relaxation time of a material. Larger stresses may increase the free volume and therefore allow the material to relax more quickly.

Although the parameters in Equation 4-2 are not tied to specific aspects of a material's microstructure, the equation itself was developed from thermodynamics [122], [123]. Therefore, the parameter values must remain consistent with their thermodynamic origin. For instance, the Prony coefficients and characteristic times must be positive. There are also constraints on the behavior of the non-linear parameters: each must monotonically increase or decrease as a function of applied stress, may not become negative for any value of stress, and must be equal to one at stresses in the linear viscoelastic region. This restricts the functional forms available to fit the stress dependence of the non-linear parameters. For this study, the arccotangent equation, shown in Equation 4-5 and plotted for two examples in Figure 4-2, was selected to capture the stress dependence of g_0, g_1,and g_2 because of its flexibility to model increasing or decreasing tends. Note that in Figure 4-2, the curves are not based on experimental results but demonstrate the flexibility of the arccotangent equation using three sample sets of coefficients.

$$g_i = g_{i1} + g_{i2}acot(\sigma - g_{i3}) \quad \textbf{4-5}$$

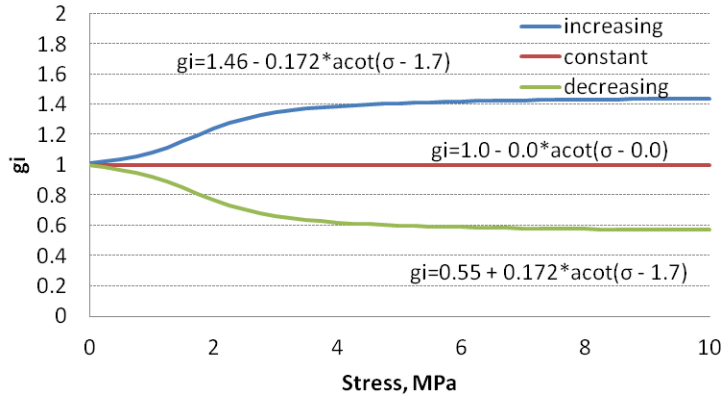

Figure 4-2. Demonstration of behavior of the arccotangent equation for three sample sets of coefficients.

The fourth non-linear parameter, a_σ, performs a function analogous to the thermal and hygral shift factors of TTMSP. These shift factors express the effect that a change in temperature or moisture has on the time dependence of the mechanical properties. For instance, an increase in temperature results in accelerated relaxation behavior. A decrease in temperature has the opposite effect. Thus, hygral and thermal shift factors may be greater than or less than unity, which is located at the reference condition. In the case of the stress shift factor, however, the maximum stress shift factor will occur in the linear viscoelastic region. Any increase in stress will result in an acceleration of material behavior; there is no stress loading which behaves analogous to a decrease in temperature. Therefore, the arccotangent equation was also used to describe the variation in a_σ with applied stress instead of one of the equations commonly used to express hygral or thermal shift factors.

4.1.3. Non-linear Viscoplastic Behavior

It is possible to model non-recoverable, or viscoplastic, strain using the Prony series. By including a free dashpot term in the Prony series, the constitutive expression would produce time-dependent permanent strain that varied linearly with applied stress. Similarly, a free dashpot term could be included in the Prony series inside the non-linear viscoelastic equation; this viscoplastic strain would be governed by the same non-linearity as the viscoelastic strains since it would be modified by the g_1, g_2 and a_σ parameters.

However, not all materials exhibit viscoplastic behavior that can be modeled with those two techniques. Various reasons exist for why viscoplastic behavior may exhibit non-linearity independent of the viscoelastic behavior. Perhaps the most intuitive is that viscoplastic strains arise from different deformation mechanisms than viscoelastic strains. The source of recoverable viscoelastic strain is the stretching of chemical bonds and local reorganization of polymer chains. Viscoplastic strain is not recoverable and often results from damage in the material such as broken polymer chains or large-scale slipping of chains past each other.

In these cases, researchers may include an additional term in the constitutive equation to express non-linear, time dependent, permanent (viscoplastic) strain independent of the non-linear viscoelastic constitutive equation. Several authors in the literature have done so with the Schapery equation for non-linear viscoelastic behavior. Zapas and Crissman [101] demonstrated that the creep behavior of polyethylene could be modeled with the Schapery equation and a viscoplastic term which was a function of stress and time raised to a power. The integral form of their equation is shown in Equation 4-6.

$$\varepsilon^{VP}(t) = \left[C \int_0^t \sigma(\rho)^p d\rho \right]^q \qquad \textbf{4-6}$$

An alternative expression for viscoplastic strain uses an exponential function of stress, rather than the power law in the Zapas-Crissman equation. This form is consistent with the equation proposed by Tobolsky and Eyring [124] to model the permanent strain in polymers which arises from slipping and tearing during chain motion. The Tobolsky-Eyring equation formulated for this research is shown in

Equation 4-7. Other authors have used a similar technique but different expressions for viscoplastic strain. For examples, please refer to Kim [125] or Lai [100].

$$\varepsilon^{VP}(t) = \left[C \int_0^t \exp(\sigma(\rho)) d\rho \right]^{q} \quad \text{4-7}$$

4.1.4. Technique for Combining Multiple Constitutive Equations

The non-linear viscoelastic and viscoplastic constitutive equations are combined in order to express the mechanical response of the PFCB/PVDF blend. However, they cannot simply be added when expressed as *strains*. Instead, they must be considered in terms of *extension*. To explain why, consider the mechanical analog in Figure 4-3. The element on the left, consisting of a spring in parallel with a dashpot, results in time dependent, recoverable strains. This element represents the non-linear viscoelastic component of the constitutive model. The right element, a free dashpot, results in time dependent, permanent strains, and represents the viscoplastic component of deformation. For simplicity, let the general expressions in Equation 4-8 and Equation 4-9 represent the constitutive equations which govern the relationship between stress and strain for the two elements.

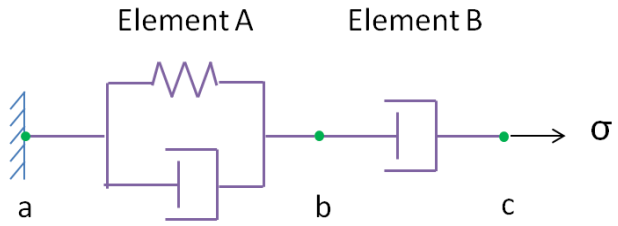

Figure 4-3. Mechanical analog for a two-element linear viscoelastic material.

$$\epsilon_A = NLVE(\sigma) \quad \text{4-8}$$

$$\epsilon_B = VP(\sigma) \quad \text{4-9}$$

Recall that uniaxial creep and recovery experiments were performed to characterize the material. During this type of experiment, a load is applied to one end of a sample while the other end is pinned, as demonstrated in Figure 4-3. This results in the sample lengthening in the direction of applied load and contracting in the directions perpendicular to the applied load, due to the Poisson effect. From the experiment, the total extension of the mechanical analog (a-c) is known as a function of applied stress. Performing a force balance at point b shows that both elements experience the same total applied stress, σ. From the constitutive models, an algebraic relationship between the strain in each element and the total applied stress is known. Additionally, the total extension is known to be the sum of the extensions of the two elements. However, the parameter values in those algebraic relationships are not known. In order to fit parameter values, the total deformation must be properly partitioned into the deformations of the individual elements.

The uniaxial experimental data is analyzed in terms of the total deformation gradient, ***F***, which is expressed below in Equation 4-10. This analysis uses the Almansi-Hamel strain tensor, which can be calculated from the deformation gradient by Equation 4-11. The only extension value obtained from the uniaxial experiment is the extension in the axial direction, λ, which is equal to the ratio of the final length of a-c to the initial length of a-c. The following analysis uses the full deformation gradient matrix to demonstrate that the final result is also valid for multiaxial experiments.

$$\boldsymbol{F} = \begin{bmatrix} \eta & 0 & 0 \\ 0 & \lambda & 0 \\ 0 & 0 & \varphi \end{bmatrix} \tag{4-10}$$

$$\boldsymbol{\epsilon} = \begin{bmatrix} \frac{1}{2}\left(1-\frac{1}{\eta^2}\right) & 0 & 0 \\ 0 & \frac{1}{2}\left(1-\frac{1}{\lambda^2}\right) & 0 \\ 0 & 0 & \frac{1}{2}\left(1-\frac{1}{\varphi^2}\right) \end{bmatrix} \tag{4-11}$$

The total deformation gradient may be separated into the deformation gradients of elements A and B by multiplicative decomposition. The deformation gradients of the individual elements A and B are expressed in Equations 4-12 and 4-14, respectively. Their respective strain tensors are given in Equations 4-13 and 4-15.

$$\boldsymbol{F_A} = \begin{bmatrix} \alpha & 0 & 0 \\ 0 & \beta & 0 \\ 0 & 0 & \gamma \end{bmatrix} \tag{4-12}$$

$$\boldsymbol{\epsilon_A} = \begin{bmatrix} \frac{1}{2}\left(1-\frac{1}{\alpha^2}\right) & 0 & 0 \\ 0 & \frac{1}{2}\left(1-\frac{1}{\beta^2}\right) & 0 \\ 0 & 0 & \frac{1}{2}\left(1-\frac{1}{\gamma^2}\right) \end{bmatrix} \tag{4-13}$$

$$\boldsymbol{F_B} = \begin{bmatrix} \varphi & 0 & 0 \\ 0 & \theta & 0 \\ 0 & 0 & \omega \end{bmatrix} \tag{4-14}$$

$$\boldsymbol{\epsilon_B} = \begin{bmatrix} \frac{1}{2}\left(1-\frac{1}{\varphi^2}\right) & 0 & 0 \\ 0 & \frac{1}{2}\left(1-\frac{1}{\theta^2}\right) & 0 \\ 0 & 0 & \frac{1}{2}\left(1-\frac{1}{\beta^2}\right) \end{bmatrix} \tag{4-15}$$

Multiplicative decomposition of **F** into $\mathbf{F_A}$ and $\mathbf{F_B}$ requires that the relationship in Equation 4-16 holds.

$$\boldsymbol{F} = \begin{bmatrix} \eta & 0 & 0 \\ 0 & \lambda & 0 \\ 0 & 0 & \varphi \end{bmatrix} = \begin{bmatrix} \alpha & 0 & 0 \\ 0 & \beta & 0 \\ 0 & 0 & \gamma \end{bmatrix} \begin{bmatrix} \varphi & 0 & 0 \\ 0 & \theta & 0 \\ 0 & 0 & \omega \end{bmatrix} = \begin{bmatrix} \alpha\varphi & 0 & 0 \\ 0 & \beta\theta & 0 \\ 0 & 0 & \gamma\omega \end{bmatrix} \quad \textbf{4-16}$$

In the uniaxial tension experiment, only the axial component of **F**, $F_{22,}$ is measured. Equations 4-13 and 4-15 can be used to express the final lengths of the individual elements A and B, (which are expressed by the scalar values β and θ, respectively) in the 22 direction in terms of strain rather than extension. For example, Equation 4-17 is the axial strain in element A.

$$\epsilon_{A22} = \frac{1}{2}\left(1 - \frac{1}{\beta^2}\right) \quad \textbf{4-17}$$

Solving Equation 4-17 for β as a function of strain and substituting the constitutive expression for the strain in element A yields Equation 4-18.

$$\beta = \sqrt{\frac{1}{1 - 2 * \epsilon_{A22}}} = \sqrt{\frac{1}{1 - 2 * NLVE(\sigma_{22})}} \quad \textbf{4-18}$$

Similarly, solving for θ yields Equation 4-19.

$$\theta = \sqrt{\frac{1}{1 - 2 * \epsilon_{B22}}} = \sqrt{\frac{1}{1 - 2 * VP(\sigma_{22})}} \quad \textbf{4-19}$$

For the uniaxial tension experiment, this results in the following expressions for the total extension of the sample, in terms of the constitutive equations of the individual elements.

$$F_{22} = \lambda = \beta\theta = \sqrt{\frac{1}{1 - 2 * NLVE(\sigma_{22})}}\sqrt{\frac{1}{1 - 2 * VP(\sigma_{22})}} \quad \textbf{4-20}$$

$$\epsilon_{22} = \frac{1}{2}\left(1 - \frac{1}{\lambda^2}\right) = \frac{1}{2}\left(1 - \frac{1}{\frac{1}{(1 - 2 * NLVE(\sigma_{22}))}\frac{1}{(1 - 2 * VP(\sigma_{22}))}}\right) \quad \textbf{4-21}$$

$$\epsilon_{22} = \frac{1}{2}\left(1 - (1 - 2 * NLVE(\sigma_{22}))(1 - 2 * VP(\sigma_{22}))\right) \quad \textbf{4-22}$$

$$\epsilon_{22} = NLVE(\sigma_{22}) + VP(\sigma_{22}) - 2 * NLVE(\sigma_{22}) * VP(\sigma_{22}) \quad \textbf{4-23}$$

$$\epsilon_{22} = \epsilon_{A22} + \epsilon_{B22} - 2\epsilon_{A22}\epsilon_{B22} \quad \textbf{4-24}$$

Note from the final expression, Equation 4-24, that the total strain, unlike total extension, is not the sum of the individual components. At low strains, this effect is not significant, but it becomes increasingly important as the strains grow larger. Table 4-1 demonstrates the importance of correctly combining strain from the two elements when the strains are large. When the strain in each element is on the order of 1%, the difference in the direct sum and the correct combination is only 0.2% strain. However,

if the strain in element A is 5% and the strain in element B is 10%, there is a 1% difference in the strain calculated by the two techniques. In other words, the summation technique results in a 7% error in the solution, since the error, 1, is 7% of the actual value, 14.

Table 4-1. Effect of correctly and incorrectly combining non-linear viscoelastic and viscoplastic strains.

ε_A (%)	ε_B (%)	$\varepsilon=\varepsilon_A+\varepsilon_B$ (%)	ε actual (%)
1	1	2	1.98
5	5	10	9.5
5	10	15	14

Based on this discussion, it is clear that in order to properly combine the non-linear viscoelastic and viscoplastic constitutive equations for analyzing uniaxial experimental data, Equation 4-25 must be used.

$$\varepsilon(t) = \varepsilon^{NLVE}(t) + \varepsilon^{VP}(t) - 2\varepsilon^{NLVE}(t)\varepsilon^{VP}(t) \quad \textbf{4-25}$$

4.1.5. Environmental Effects in Constitutive Equations

The constitutive equations just discussed are used to model the mechanical response of a material at a single environmental condition. Because the environment changes during fuel cell operation, a method to incorporate the hygral and thermal expansion in the numerical model is needed. For the PFCB/PVDF blend, the mechanical properties also vary significantly with environment, so this effect must be incorporated into the constitutive model as well. In the present analysis, Equation 4-26 is used to convert water activity *a* (%RH divided by 100) to λ [42]. This expression was determined directly from the linear viscoelastic experiments on PFCB/PVDF, rather than the standard equation which is applied to PFSA materials in general.

$$\lambda = 0.000013a^3 - 0.001192a^2 + 0.065369a \quad \textbf{4-26}$$

4.1.5.1. Hygrothermal Expansion

When the environment changes, the dimensions of a material change according to its coefficients of hygral and thermal expansion. This changes the actual strain experienced by the sample according to Equation 4-27, where α is the coefficient of thermal expansion, T(t) is the temperature at time t, and T_0 is the reference temperature. Similarly, β is the coefficient of hygral expansion, λ(t) is the moisture content at time t, and λ_0 is the reference moisture content.

$$\varepsilon^{mechanical}(t) = \varepsilon(t) - \varepsilon^{thermal}(t) - \varepsilon^{hygral}(t) \quad \textbf{4-27}$$

$$= \varepsilon(t) - \alpha(T(t) - T_0) - \beta(\lambda(t) - \lambda_0)$$

The coefficients of hygral and thermal expansion were characterized by Finlay [42] and are summarized in

Table 4-2. Plotting the results in Table 4.2 reveals that the CHE is relatively independent of temperature with an average value of $1.3*10^{-2}\ \lambda^{-1}$ and the CTE may be approximated by a third order polynomial as a function of lambda. The polynomial used in the present analysis for CTE is included in Equation 4-28.

Table 4-2. Coefficients of hygral (left) and thermal (right) expansion for the PFCB/PVDF blend.

	Coefficient of Hygral Expansion (x $10^2\ \lambda^{-1}$)		Coefficient of Thermal Expansion (x 10^5 °C^{-1})
30°C	1.15	0% RH	13.0
40°C	1.18	10% RH	14.2
50°C	1.27	20% RH	15.0
60°C	1.45	30% RH	13.9
70°C	1.13	40% RH	15.1
80°C	1.45	50% RH	14.7
90°C	1.39	60% RH	19.9
100°C	1.38	70% RH	22.6
		80% RH	22.8
		90% RH	39.3

$$CTE = (13.794 - 0.4028\lambda + 0.8116\lambda^2)x\ 10^{-5}\ °C^{-1} \quad \textbf{4-28}$$

4.1.5.2. Environmental Dependence of Mechanical Properties

The theory of time temperature superposition (TTSP) states that an increase in temperature increases the free volume in a material, which accelerates the relaxation processes because more room is available for segmental motion [37]. The amount by which relaxation is increased is quantified by a thermal shift factor a_T, which is only a function of temperature. A similar argument is used for the effect of moisture in time moisture superposition (TMSP) with hygral shift factors a_H. The two theories may be combined by multiplying the hygral and thermal shift factors. The combined value is then called a hygrothermal shift factor and designated a_{TH}. The shift factor is applied to the constitutive model by multiplying all characteristic times in the Prony series governing viscoelastic behavior. In the case of the Schapery equation for non-linear viscoelastic behavior, the hygral and thermal shift factors are also multiplied by the stress shift factor a_σ, resulting in the reduced time defined by Equation 4-29.

$$\varphi(t) = \int_0^t \frac{d\rho}{a_\sigma(\sigma(\rho)) * a_T(\rho) * a_H(\rho)} \quad \textbf{4-29}$$

Finlay [42] has characterized the hygral and thermal shift factors of the PFCB/PVDF blend and reports the resulting hygrothermal shift factor using Equation 4-30.

$$T \leq 70^{\circ}C \qquad \log(a_{TH}) = \frac{0.000063 * (T - 70^{\circ}C) + 0.00304 * (\lambda - 1.24)}{0.00261 + 0.00007 * (T - 70^{\circ}C) + 0.000357 * (\lambda - 1.24)} + 0.0319 * (T - 70^{\circ}C)$$

4-30

$$T > 70^{\circ}C \qquad \log(a_{TH}) = \frac{0.000063 * (T - 70^{\circ}C) + 0.00304 * (\lambda - 1.24)}{0.00261 + 0.00007 * (T - 70^{\circ}C) + 0.000357 * (\lambda - 1.24)} + 0.0993 * (T - 70^{\circ}C)$$

This experimental determination of the hygral and thermal shift factors was performed at very low stresses where non-linear viscoelastic and viscoplastic effects are not significant or distinguishable. It is plausible that both the non-linear viscoelastic and viscoplastic parameters are dependent on the environmental conditions in a manner that is not captured by the linear viscoelastic shift factors. Characterization of the temperature and moisture dependence of both the non-linear viscoelastic parameters and viscoplastic parameters would require a considerable experimental effort and in fact exceeds the amount of PFCB/PVDF material available to the VT/GM research group. Because the non-linear viscoelastic function includes some temperature and moisture dependence through the hygrothermal shift factors, *the present work focuses only on the environmental dependence of the viscoplastic parameters*. Experiments which extended into the non-linear region were conducted to probe the effect of environment on the viscoplastic parameters, as discussed in the previous chapter. An expression for the environmental dependence of the viscoplastic parameters will be developed in the Results chapter based on the results of those experiments.

4.2. Parameter Determination

The uniaxial creep and recovery experiments were used to determine appropriate values for the parameters in the constitutive equations. The following sections describe the effect of each parameter on the final model, the procedure for systematically estimating initial parameter values and the non-linear regression technique for finalizing parameter values.

4.2.1. Effect of Individual Parameters

Before beginning an explanation of parameter estimation, it is useful to consider the effect that changing the value of a particular parameter will have on the model output. The following sections systematically demonstrate the effect of each parameter in the constitutive equation of a creep and recovery experiment. Please note that the figures in the following section are not based on experimental results, but are intended only to demonstrate the effect of the parameters. Parameter values were chosen so that the effect of each is clearly demonstrated.

4.2.1.1. Linear Viscoelastic Prony Series

First, consider the linear viscoelastic Prony series. Let the case study have a Prony series with an elastic element and three viscoelastic elements with characteristic times of 10, 300, and 10,000 seconds. The equation for calculating strains from this Prony series is shown in Equation 4-31, assuming the applied stress is constant, as is the case for the creep experiments.

$$\varepsilon(t) = \sigma\left[D_0 + D_1\left(1 - exp^{-\frac{t}{10}}\right) + D_2\left(1 - exp^{-\frac{t}{300}}\right) + D_3\left(1 - exp^{-\frac{t}{10{,}000}}\right)\right] \quad \textbf{4-31}$$

The magnitude of an element's compliance coefficient, D_i, dictates the magnitude of the response of that element. The characteristic time of an element governs the time period during which it is active, due to the exponential function being calculated from the ratio of current time to the element's characteristic time. For the element with a characteristic time of 10 seconds, the response of the element becomes significant at approximately 0.3 seconds, and the element reaches its full response around 30 seconds. This is demonstrated in Figure 4-4. The elastic compliance results in an instantaneous, constant, vertical offset, most noticeable in the left figure. The magnitude of the first time dependent element is much larger than the other two, so most of the strain which develops is due to this element. Because the first element has a characteristic time of 10 seconds, the strain develops between 0.3 and 30 seconds and the response due to the element stabilizes after that. The slight increase in strain at times beyond 30 seconds is due to the other two elements.

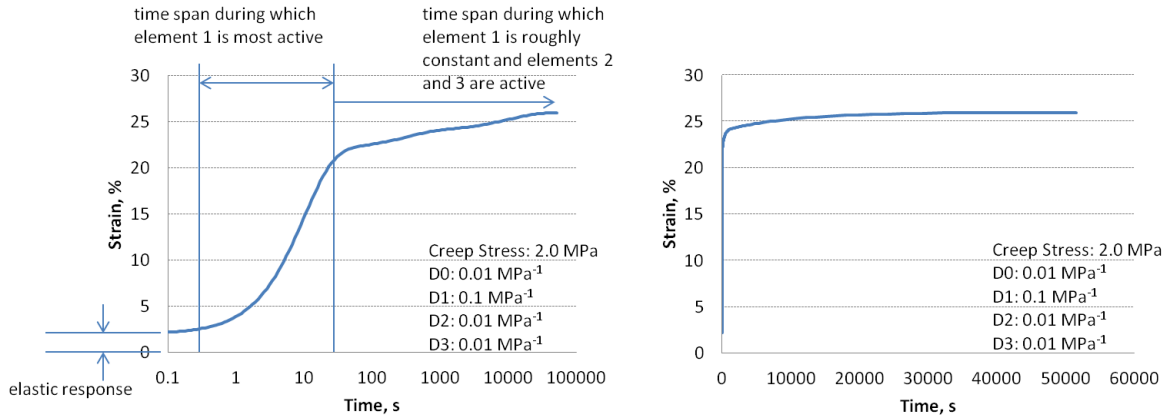

Figure 4-4. Example strain response of the three-element linear viscoelastic material, with a dominant element at 10 seconds, to a creep load. Logarithmic time scale (left) and linear time scale (right).

In contrast to Figure 4-4 (above), consider the strain response in Figure 4-5 (below). The elastic compliance results in the same vertical offset as before, as evidenced by the intercept on the strain axis. However, in this example, the coefficient of the third element (with a characteristic time of 10,000 seconds) has a significantly larger magnitude than the other elements, so most of the strain develops as a result of this element. Because the characteristic time is later in the experimental time frame, most of the strain develops later in the experiment, after 300 seconds.

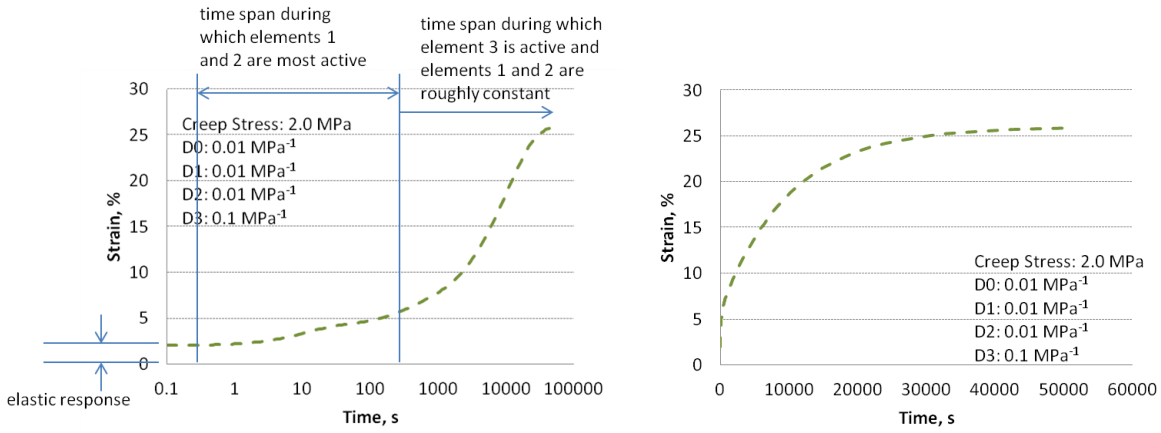

Figure 4-5. Example strain response of the three-element linear viscoelastic material, with a dominant element at 10,000 seconds, to a creep load. Logarithmic time scale (left) and linear time scale (right).

4.2.1.2. Non-linear Viscoelastic Parameters

For convenience, these examples are based on the creep and recovery experimental profile. The integral form of the non-linear viscoelastic constitutive expression, Equation 4-2, can be simplified for this profile by solving the integral for the constant stress during the creep and recovery periods separately. This results in the algebraic expressions in Equations 4-32 and 4-33. In these expressions, σ_a is the stress applied during the first step and σ_b the stress in the second step. The superscripts on the non-linear parameters indicate the stress from which they are calculated. D_0 and ΔD are the linear elastic compliance and transient linear viscoelastic compliance, respectively. The time at which the applied stress switches from σ_a to σ_b is t_{creep}.

$$\varepsilon(t) = {g_0}^a D_0 \sigma_a + {g_1}^a {g_2}^a \Delta D \left(\frac{t}{{a_\sigma}^a}\right)\sigma_a \qquad t < t_{creep} \qquad \textbf{4-32}$$

$$\begin{aligned}\varepsilon(t) = {g_0}^b D_0 \sigma_b \\ + {g_1}^b \left[{g_2}^a \sigma_a \Delta D \left(\frac{t_{creep}}{{a_\sigma}^a} + \frac{t - t_{creep}}{{a_\sigma}^b}\right)\right. \\ \left. + \left({g_2}^b \sigma_b - {g_2}^a \sigma_a\right)\Delta D \left(\frac{t - t_{creep}}{{a_\sigma}^b}\right)\right]\end{aligned} \qquad t > t_{creep} \qquad \textbf{4-33}$$

Because the stress applied during recovery is so much less than the creep stress, it can be safely neglected. This further simplifies the constitutive equations to what is shown in Equations 4-34 and 4-35. Here, all non-linear parameters which appear in the equation are calculated from σ_{creep}, which was called σ_a in Equations 4-32 and 4-33.

$$\varepsilon_{creep}(t) = \left[g_0 D_0 + g_1 g_2 \Delta D \left(\frac{t}{a_\sigma}\right)\right]\sigma_{creep} \qquad t < t_{creep} \qquad \textbf{4-34}$$

$$\varepsilon_{recovery}(t) = \left[\Delta D \left(\frac{t_{creep}}{a_\sigma} + t - t_{creep}\right) - \Delta D\left(t - t_{creep}\right)\right] g_2 \sigma_{creep} \qquad t > t_{creep} \qquad \textbf{4-35}$$

There are four non-linear terms in the viscoelastic constitutive equation. The first, g_0, modifies the elastic compliance. If the value of g_0 increases with stress, the material exhibits stress softening behavior. A g_0 trend which decreases with stress results in stiffening. This is demonstrated in Figure 4-6. In the far left figure, three sample g_0 behaviors are demonstrated: one increases with stress (labeled 'increasing'), one remains constant at a value of 1 ('constant'), and one decreases with stress ('decreasing')[2]. The center figure shows the effect that each g_0 curve has on the elastic strain and the rightmost figure illustrates the effect each trend has on the creep behavior at two stress levels. Note from Figure 4-6(c) that g_0 changes the vertical shift in the creep strain, but has no effect during recovery. This is expected based on Equation 4-35.

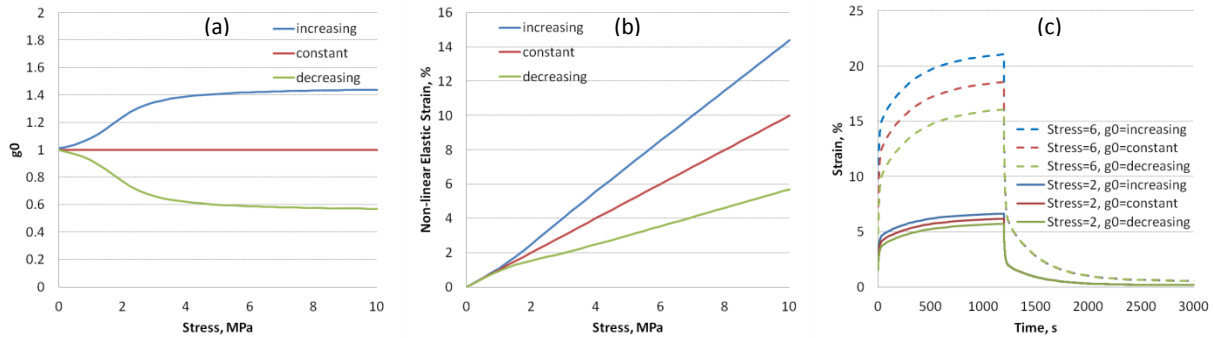

Figure 4-6. (a) Examples of g_0 as a function of stress. (b) Effect of g_0 trends from (a) on elastic strain. (c) Effect of g_0 trends from (a) on creep strain at two stress levels (6MPa – dash; 2MPa – solid).

The second non-linear viscoelastic parameter, g_1, performs a role similar to g_0, but affects the time dependent compliance instead of the elastic compliance. Similar to the example above, Figure 4-7(a) demonstrates increasing (softening), constant (linear viscoelastic) and decreasing (stiffening) relationships for g_1 as a function of stress. Figure 4-7(b) shows the effect of g_1 on creep and recovery strain. Like g_0, g_1 only affects the response during creep, as can be predicted from Equation 4-34. However, rather than resulting in a constant vertical shift between curves at the same stress, as g_0 does, g_1 causes the distance between the curves to increase as time progresses during creep. For example, the 6MPa curves have about twice as much strain difference at the end of creep than at the beginning of creep.

[2] Recall that the non-linear viscoelastic parameters are always 1 at low stresses, because this region corresponds to linear viscoelastic response, and that the parameters must always be greater than zero, and either increase or decrease only; they may not 'turn around' as a function of stress.

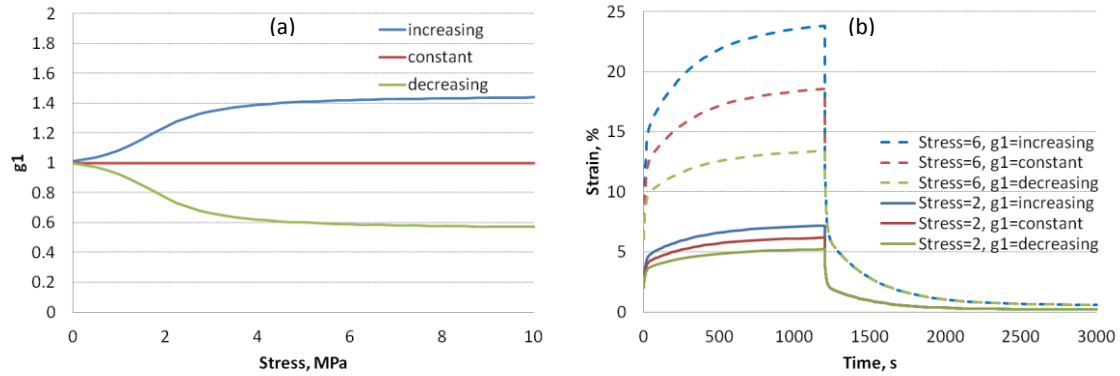

Figure 4-7. (a) Examples of g_1 as a function of stress. (b) Effect of g_1 trends from (a) on creep strain at two stress levels (6MPa – dash; 2MPa – solid).

The third non-linear viscoelastic parameter is g_2. Thermodynamically, this parameter arises from a non-linear relationship between applied force and local material stress. Because of its location in the convolution integral, it modifies the effect of time-varying stresses and therefore captures rate effects. For the creep and recovery experiments, the stress only changes at the very beginning of the test, when the sample is first loaded, and during the theoretically instantaneous transition from creep to recovery. Therefore, the effect of g_2 during the creep step is unchanging throughout that step (since the stress does not continue to change). The effect of g_2 is similarly constant during recovery.

Note that the value of g_2 active during the *recovery* period is calculated from the stress applied during *creep*. This is because of the 'memory' exhibited by viscoelastic materials; even though the creep stress has been removed, the material still 'remembers' during recovery that stress was applied previously, so it continues to affect material response. This behavior is anticipated from the integral form of the non-linear viscoelastic constitutive equation (Equation 4-33) because g_2 appears inside the convolution integral. Note that in Equation 4-35 there is also a g_2 parameter which is a function of the stress during the second step, which describes the material's 'memory' of the stress change between steps. However, when the second step occurs at low stress (i.e., recovery), this parameter has a value of one since the stress during recovery is linear viscoelastic, so it does not appear in Equation 4-35.

Figure 4-8 demonstrates the effect of increasing, constant and decreasing g_2 as for the previous parameters. Because g_2 is the only parameter active for these plots (i.e., all other parameters are equal to 1) and has an identical value to g_1 as a function of stress, its effect on the creep strain is identical to that of g_1. However, g_2 is also active during recovery. While the strains are recovering, g_2 scales the magnitude of the recovered strain as a function of time, causing the curves at a single stress level to fan out from each other as g_2 varies. Contrast this is the Figure 4-7, where the recovery curves for all three g_1 values are identical.

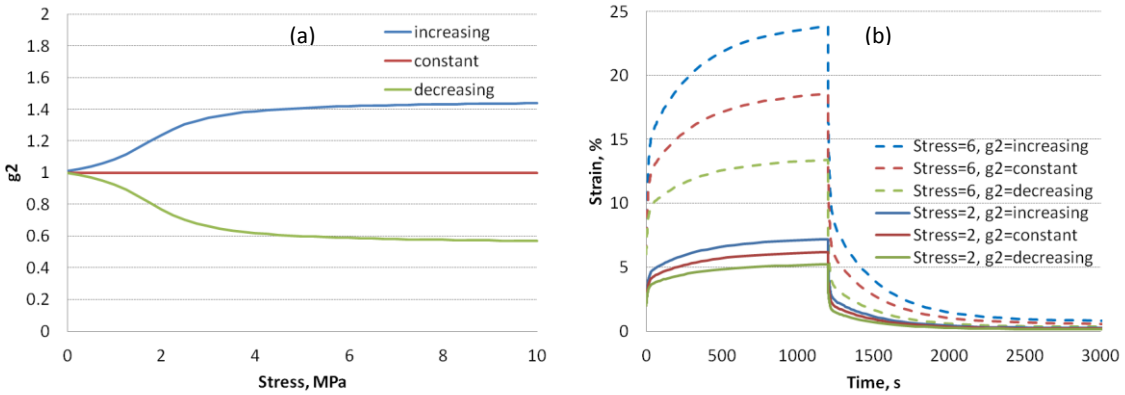

Figure 4-8. (a) Examples of g_2 as a function of stress. (b) Effect of g_2 trends from (a) on creep strain at two stress levels (6MPa – dash; 2MPa – solid).

Finally, consider the effect of the stress shift factor, a_σ. Recall that this parameter is analogous to the thermal shift factor associated with TTSP because it arises from the relationship between increasing stress and the free volume in a material. As the chains are stretched from a stable conformation due to an applied load, additional free space is generated in the material. However, this effect is limited; eventually, the chains will begin to pack more densely as they align and entropic resistance to further deformation will develop. That is, as the chains become more ordered, the entropy of the system decreases. Eventually, additional decreases to the entropy related to chain alignment will require more energy than is available from the stress state. Unlike the other non-linear parameters, a_σ can only decrease with increasing stress. An increase in a_σ with increasing stress would equate to a deceleration of chain motion in the presence of increased free volume, which is not a physically reasonable behavior.

Therefore, rather than considering trends between a_σ and stress that were used for the other non-linear parameters, instead consider those demonstrated in Figure 4-9(a). One is constant at a value of 1, indicating that increased stress has no effect on relaxation time. The second is a weak function of stress and therefore slowly approaches zero asymptotically. The third is a strong function of stress and asymptotically approaches zero rapidly over the stress range demonstrated. The result of each of these trends on the strain response is demonstrated in Figure 4-9(b). Note that the third a_σ curve results in a significantly softer response than the others, since it causes elements to act much earlier than they would without stress shifting. The effect of stress shifting persists during recovery because the shift factor appears within the convolution integral and therefore is 'remembered' by the material even after the creep stress is removed.

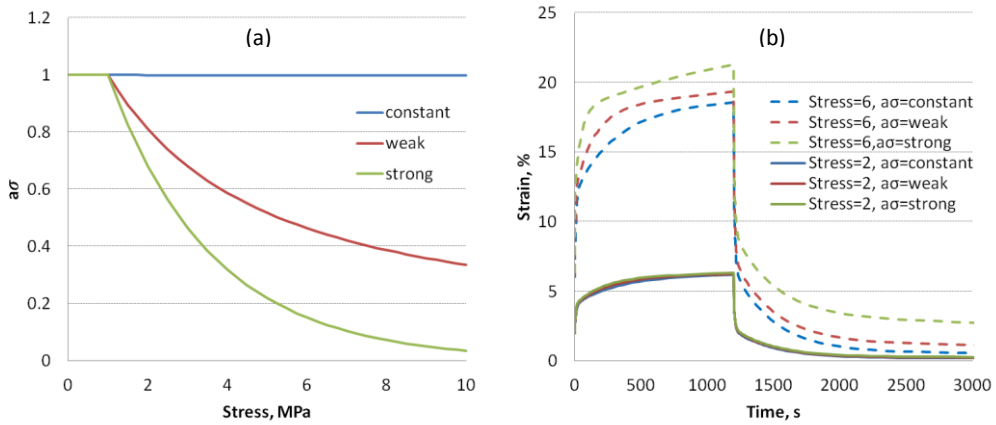

Figure 4-9. (a) Examples of a_σ as a function of stress. (b) Effect of a_σ trends from (a) on creep strain at two stress levels: 6MPa – dash; 2MPa – solid.

4.2.1.3. Non-linear Viscoplastic Parameters

Because the experimentally observed strains never fully recover, a viscoplastic expression will be used to express the permanent strain that develops in the material. Both of the viscoplastic equations mentioned above (Equations 4-6 and 4-7) have three terms. One modifies the time dependence of the response, another the stress dependence, and the final adjusts the magnitude of the whole response. Like the non-linear viscoelastic examples, the effects of the viscoplastic parameters on the strain response are demonstrated for a constant stress (creep) load. The integral forms can be simplified by solving the integral for a constant stress application. This results in Equation 4-36 for the Zapas-Crissman expression and Equation 4-37 for the Tobolsky-Eyring expression.[3]

$$\varepsilon^{VP}(t) = \left[C\int_0^t \sigma(\tau)^p d\tau\right]^q = C^q\sigma^{pq}t^q = A\sigma^b t^c \qquad \textbf{4-36}$$

$$\varepsilon^{VP}(t) = \left[C\int_0^t exp(\sigma(\tau))d\tau\right]^q = C^q[exp(\sigma)]^b t^q = Aexp(b\sigma)t^c \qquad \textbf{4-37}$$

The effect of parameter A is the same for both forms: the constant coefficient multiplies the stress and time dependent components of the response and adjusts the magnitude of the entire response. This can easily be seen in Figure 4-10, where the value of A in the dashed curve is half that of the solid curve. The values of b and c are identical in the two curves.

[3] Note that due to the properties of the exponential, it is not possible to simplify the Tobolsky-Eyring form by moving parameter b outside of the exponential. If parameter b was added to stress inside the exponential, this could be done, but it is multiplied rather than added in this equation.

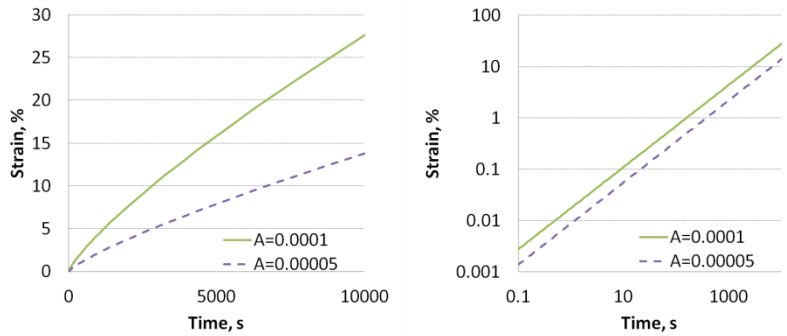

Figure 4-10. Example of the effect large (solid) and small (dash) values of the parameter A have on the viscoplastic strain. Linear time and strain axes (left) and logarithmic time and strain axes (right).

Similarly, both forms express time dependence by raising the time under load to the power of parameter c. Values of c greater than one result in strains which increase with time and accelerate with time. When c is equal to one, the response increases linearly with time. For values of c less than one, the strains still increase with time, but the rate of increase (the slope) decreases as time grows larger. Figure 4-11 demonstrates this behavior.

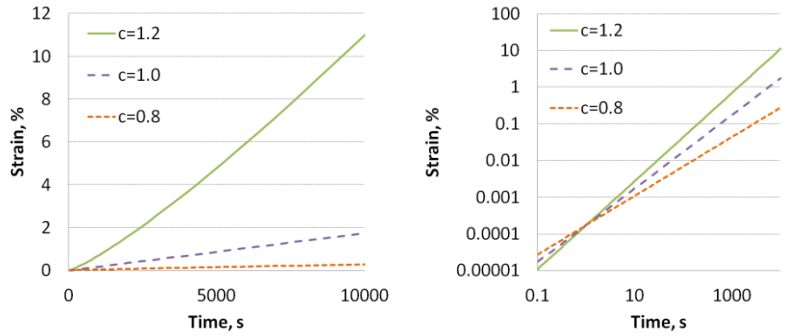

Figure 4-11. Example of the effect large (solid), moderate (long dash) and small (short dash) values of the parameter c have on the viscoplastic strain. Linear time and strain axes (left) and logarithmic time and strain axes (right).

For the Zapas-Crissman equation for viscoplastic strain, stress is raised to the power of parameter b. This results in the behavior shown in Figure 4-12. These figures demonstrate the effect of b less than, equal to, and greater than one on three values of stress.

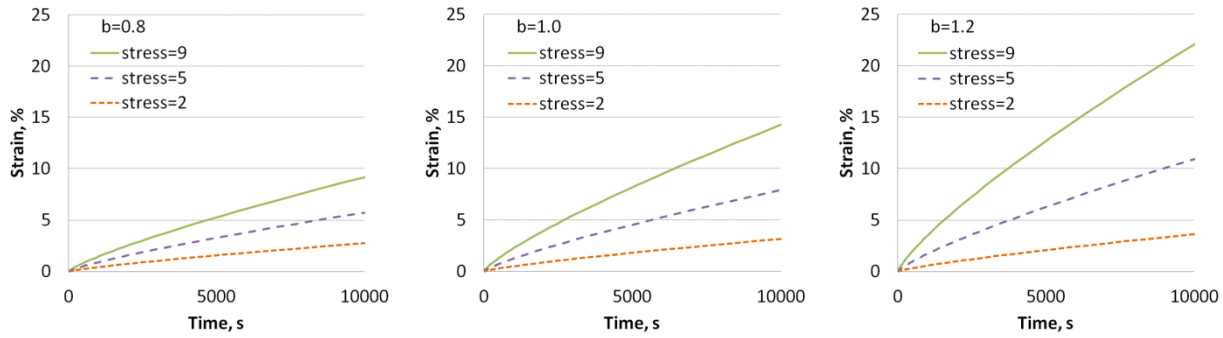

Figure 4-12. Example of the effect large (left), moderate (center) and small (right) values of the parameter b have on the Zapas-Crissman viscoplastic strain for three stress levels: 9MPa – solid, 5MPa – long dash, 2MPa – short dash.

The Tobolsky-Eyring equation gives strain as a function of the exponential of stress times the parameter b. The effects of values of parameter b which are less than, equal to, and greater than one are demonstrated in Figure 4-13. Because of the exponential, the Tobolsky-Eyring expression is much more sensitive to b at large stresses than the Zapas-Crissman expression.

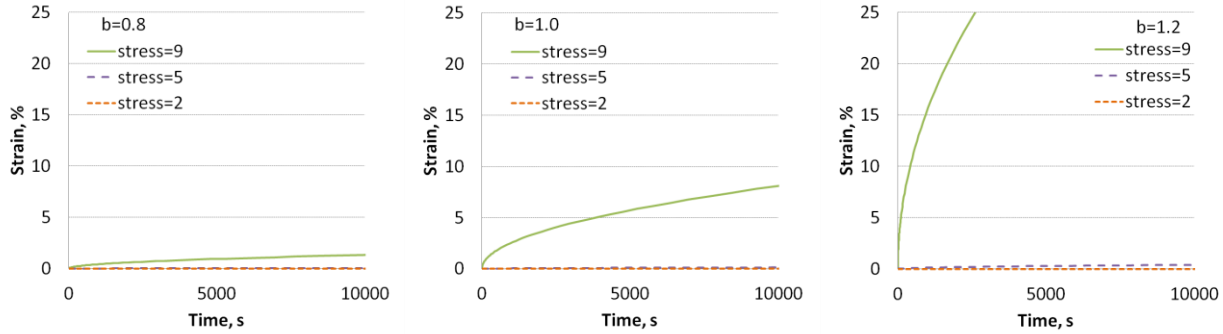

Figure 4-13. Example of the effect large (left), moderate (center) and small (right) values of the parameter b have on the Tobolsky-Eyring viscoplastic strain for three stress levels: 9MPa – solid, 5MPa – long dash, 2MPa – short dash.

The difference in the Zapas-Crissman and Tobolsky-Eyring viscoplastic expressions is more clearly demonstrated in Figure 4-14. For this figure, the parameter b was varied to bring the two equations into the best agreement possible at the 5MPa stress. (Parameters A and c are the same in both expressions.) This example demonstrates that the Tobolsky-Eyring form has significantly greater stress dependence at high stresses than the Zapas-Crissman form does.

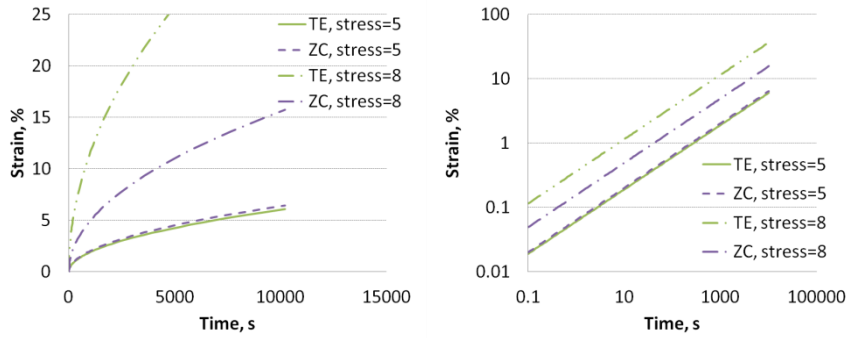

Figure 4-14. Example of the difference between the stress dependence of viscoplastic strain in the Zapas-Crissman and Tobolsky-Eyring equations. The parameters for each were selected so that the viscoplastic strains matched at 5MPa: Tobolsky-Eyring – solid, Zapas-Crissman – dash. The viscoplastic strain predicted by the equations for an 8MPa loading is significantly different: Tobolsky-Eyring – dash-double-dot, Zapas-Crissman – dash-dot.

4.2.2. Initial Parameter Estimation

As noted previously, there is no simple way to separate the recoverable and non-recoverable components of experimental response for parameter estimation. However, simplifying assumptions can be made which allow initial estimates of the parameter values.

For instance, the isochronous plot in Figure 4-1 indicates that the experiments at 0.5MPa are in the linear viscoelastic region. This means all of the non-linear viscoelastic parameters must be equal to one for these experiments. Further, because the stress applied during recovery is small, the growth of viscoplastic strain is small compared to the recovery of linear viscoelastic strain. Therefore, initial values for the parameters for the linear viscoelastic response – the Prony coefficients – can be obtained from the recovery portion of the 0.5MPa experiments by assuming viscoplastic strain is constant during recovery.

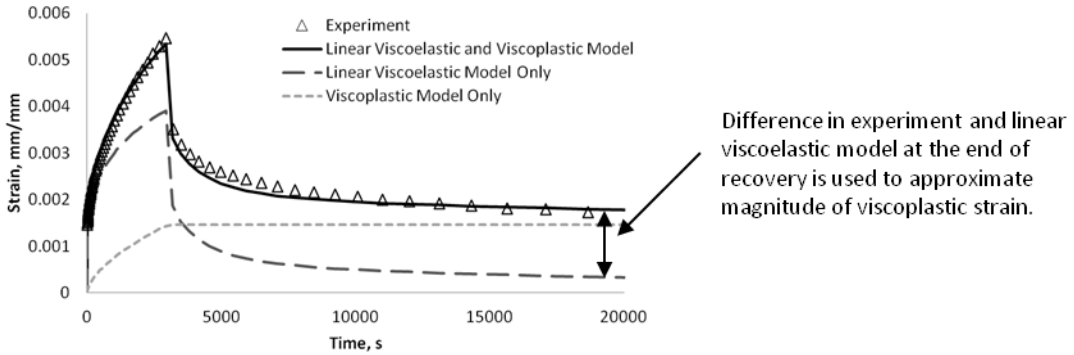

Figure 4-15. Illustration of the technique for estimating viscoplastic strain from the recovery portion of creep experiments/ This example is a 0.5MPa experiment.

After estimating a Prony series from the linear viscoelastic experiments, initial estimates for the viscoplastic parameters can be obtained. To do so, the linear viscoelastic prediction is compared to the actual strain in each experiment. The difference between the predicted strains and experimental strains at the end of recovery is used as an estimate for the magnitude of viscoplastic strain, as demonstrated in

Figure 4-15. This estimate is performed for every experiment, and the resulting viscoplastic strain estimates are used to approximate values for the viscoplastic constitutive parameters. *This approach initially neglects the effect of the non-linear viscoelastic parameters.* The recursive parameter determination technique described in the next section incorporates the effect of non-linear viscoelasticity in the refinement of viscoplastic parameter values.

Three of the non-linear viscoelastic parameters can be estimated from the experimental results as well. The first 6 seconds of all experiments are used to estimate the values of g_0, since the elastic response is dominant in this portion of the experiment.

The recovery portion of experiments in the non-linear stress range (stresses greater than 0.5MPa) can be used to estimate values for g_2 and a_σ. Equations 4-34 and 4-35 show that these are the only non-linear viscoelastic parameters active during recovery, and if the growth of viscoplastic strain is calculated from the previously estimated parameters and the stress applied during recovery, differences in the linear viscoelastic prediction and actual experimental strain may be corrected by varying g_2 and a_σ.

The final non-linear viscoelastic parameter, g_1, is active only during the creep portion of the experiments, as can be seen in Equation 4-35. However, because all of the other parameters are also active during this part of the experiment, it is not possible to obtain an estimate of g_1 independent of the other parameters. Instead, g_1 is used to capture non-linearity in the creep response that the other parameters cannot express during the final parameter determination.

4.2.3. Parameter Refinement Procedure

The final parameter values are determined using non-linear regression in a Mathematica program [126]. The constitutive model in the form of Equations 4-34 through 4-37 is coded and the experimental data is imported into the program. The small effect of viscoplastic strain that develops during recovery, which was neglected during the initial estimate, is now included. Further description of the iterative process used for improving on the initial parameter set may be found in Appendix B.

A weighting scheme is applied to the non-linear regression to normalize the effect of experiment length and strain magnitude during different parts of the experiment. Longer experiments have more data points than short ones, but only short experiments were completed at higher stresses due to experimental limitations. The additional data points in the long experiments are in the recovery region, where the strains are small. This causes the model to be artificially weighted toward agreement with lower strains as a result of the correlation between long times and low strains. To address this issue, a weight was assigned to each data point used in the non-linear regression.

The weights were calculated to give every decade of time in an experiment equal significance. The number of data points in each decade (1 second to 10 seconds, 10 seconds to 100 seconds, etc.) in an experiment was determined. Each data point was weighted by the reciprocal of the number of points in its decade of time. Figure 4-16 demonstrates this technique graphically. There are 29 data points between 10 seconds and 100 second, but 109 between 1,000 seconds and 10,000 seconds. Therefore, the data points between 10 and 100 seconds each have a weight of 1/29, or 0.035, while those between 1,000 and 10,000 have a weight of 1/109, or 0.0092.

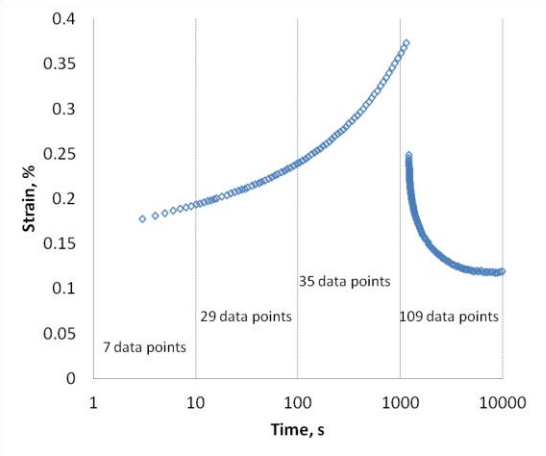

Figure 4-16. Illustration of the technique for calculating regression weight for experimental data.

4.3. Finite Element Implementation

The constitutive equations developed for modeling the response of PFCB/PVDF are not available in standard finite element programs. However, the commercial program used for this analysis, Abaqus [127], allows a user to develop his own constitutive equations and incorporate them into a finite element analysis through a user-defined material (UMAT) subroutine. There are specific instructions on how this subroutine must be constructed in order to properly interface with Abaqus. The section below describes the development of the non-linear viscoelastic viscoplastic UMAT for use with Abaqus.

4.3.1. Recursive Uniaxial Constitutive Equations

Abaqus operates by specifying a strain increment over a discreet time step at each node in the geometric model and then solving for the stress increment required to produce that strain increment. Rather than solving the integral constitutive equation every time the UMAT subroutine is called, the constitutive equation may be converted to an incremental (or recursive) form. This was done by assuming that applied stress is constant over every discreet time step and solving the integral over that time step. This is a reasonable assumption for most experiments, even ones in which stresses vary widely, if the time steps are sufficiently small.

4.3.1.1. Non-linear Viscoelastic

The following equations describe the development of the recursive form for the non-linear viscoelastic constitutive equation. The integral form is divided into two time periods: one which covers all time up to the beginning of the current time increment, and the other which models the behavior during the current time increment. This is demonstrated in Equation 4-38.

$$\varepsilon^{NLVE}(t) = g_0(\sigma)D_0\sigma(t) + g_1(\sigma)\int_0^t \Delta D\big(\varphi(t)-\varphi(\rho)\big)\frac{dg_2(\sigma)\sigma(\rho)}{d\rho}d\rho$$
$$= g_0(\sigma)D_0\sigma(t) + g_1(\sigma)\int_0^{t-\Delta t} \Delta D(\varphi(t)-\varphi(\rho))\frac{dg_2(\sigma)\sigma(\rho)}{d\rho}d\rho \quad \textbf{4-38}$$
$$+ g_1(\sigma)\int_{t-\Delta t}^t \Delta D(\varphi(t)-\varphi(\rho))\frac{dg_2(\sigma)\sigma(\rho)}{d\rho}d\rho$$

In a recursive analysis, the value of the first integral, from t=0 to the end of the previous time step, is equivalent to the sum of the results of all previous increments. The second integral is solved by assuming stress is a constant during the time increment. Collecting the sum of the results from previous increments and constant-stress solution from the most recent increment yields Equation 4-39, which is the strain increment during the current time step, in which hereditary effects from all previous time steps are incorporated through Equation 4-40. The effects of previous loads and time-dependent mechanical properties are naturally included in this formulation through properties of the convolution integral. For a more thorough discussion of this technique, please refer to [37].

$$\Delta\varepsilon^{NLVE}(t) = \left(g_0(\sigma)D_0 + g_1(\sigma)g_2(\sigma)\sum_{n=1}^{N} D_n\left(1-\frac{1-exp\left(-\frac{\Delta t}{a_\sigma(\sigma)\tau_n}\right)}{\frac{\Delta t}{a_\sigma(\sigma)\tau_n}}\right)\right)\sigma(t) \quad \textbf{4-39}$$

$$-\sum_{n=1}^{N} D_n\left(g_1(\sigma)\,exp\left(-\frac{\Delta t}{a_\sigma(\sigma)\tau_n}\right) - g_1(\sigma(t-\Delta t))\right)q_n(\mathrm{t}-\Delta t)$$

$$-\left(g_0(\sigma(t-\Delta t))D_0 + g_1(\sigma(t-\Delta t))g_2(\sigma(t-\Delta t))\sum_{n=1}^{N} D_n\left(1-\frac{1-exp\left(-\frac{t-\Delta t}{a_\sigma(\sigma)\tau_n}\right)}{\frac{t-\Delta t}{a_\sigma(\sigma)\tau_n}}\right)\right)\sigma(t-\Delta t)$$

$$-g_2(\sigma(t-\Delta t))\sum_{n=1}^{N} D_n\left[g_1(\sigma(t-\Delta t))\frac{1-exp\left(-\frac{t-\Delta t}{a_\sigma(\sigma)\tau_n}\right)}{\frac{t-\Delta t}{a_\sigma(\sigma)\tau_n}} - g_1(\sigma)\frac{1-exp\left(-\frac{\Delta t}{a_\sigma(\sigma)\tau_n}\right)}{\frac{\Delta t}{a_\sigma(\sigma)\tau_n}}\right]\sigma(t-\Delta t)$$

$$q_n(\mathrm{t}) = exp\left(-\frac{\Delta t}{a_\sigma(\sigma)\tau_n}\right)q_n(\mathrm{t}-\Delta t) \quad \textbf{4-40}$$
$$+(g_2(\sigma)\sigma(t) - g_2(\sigma(t-\Delta t))\sigma(t-\Delta t))\frac{1-exp\left(-\frac{\Delta t}{a_\sigma(\sigma)\tau_n}\right)}{\frac{\Delta t}{a_\sigma(\sigma)\tau_n}}$$

4.3.1.2. Non-linear Viscoplastic

The viscoplastic constitutive equation is also converted from the integral to recursive form by solving the integral form for a constant applied stress, as described for the non-linear viscoelastic equation. Equations 4-41 through 4-43 demonstrate this procedure with the Zapas-Crissman equation.

$$\varepsilon^{VP}(t) = \left[C \int_0^t \sigma(\tau)^p d\tau\right]^q \quad \textbf{4-41}$$

$$\varepsilon^{VP}(t) = \left[C \int_0^t \bar{\sigma}^p d\tau\right]^q \quad \textbf{4-42}$$

$$\varepsilon^{VP}(t) = [C\bar{\sigma}^p t]^q = A\bar{\sigma}^b t^c \quad \textbf{4-43}$$

The last equation yields the strain profile for a constant stress applied over the time interval 0 to t. In order to calculate the strain profile for time-varying stresses, an incremental form is developed. The incremental viscoplastic strain is the difference in the viscoplastic strain at the end of the current time increment and that at the end of the previous time increment. This is given by Equations 4-44 through 4-46, again for a constant stress loading over the entire experiment.

$$\Delta\varepsilon^{VP}(t) = \varepsilon^{VP}(t) - \varepsilon^{VP}(t - \Delta t) \quad \textbf{4-44}$$

$$\Delta\varepsilon^{VP}(t) = A\bar{\sigma}^b t^c - A\bar{\sigma}^b (t - \Delta t)^c \quad \textbf{4-45}$$

$$\Delta\varepsilon^{VP}(t) = A\bar{\sigma}^b (t^c - (t - \Delta t)^c) \quad \textbf{4-46}$$

Unlike the non-linear viscoelastic constitutive equation, the viscoplastic constitutive equation does not contain time-dependent properties. Equation 4-36 was developed assuming the applied stress is constant during the entire experiment, but the model should be applicable to variable stress simulations, so modifications must be made to extend the applicability of the viscoplastic expression.

The effect of the stress/strain history of the material can be incorporated into the viscoplastic analysis in two ways: time hardening or strain hardening. To illustrate the difference in these two techniques, consider two uniaxial creep experiments on a material whose response to constant stress experiments is depicted in Figure 4-17. The experiments are at stresses A and B, where σ_B is greater than σ_A.

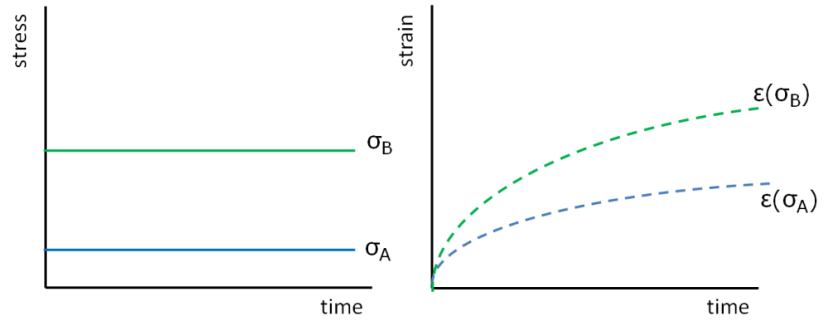

Figure 4-17. Illustration of response of a representative viscoplastic material to constant stress load at two stress levels.

Now consider a multi-step experiment, which starts at σ_A but at some time t_A is increased to σ_B. The first part of the multi-step strain response, up to time t_A, matches the strain response of the creep test at σ_A. After the stress changes to σ_B, the strain response falls somewhere between the creep responses to stresses A and B. Equation 4-47 describes this behavior. Unlike Equation 4-46, the stress in Equation 4-47 is only required to be constant during the time step, rather than during the entire time interval. Thus, Equation 4-47 can be used to calculate the strain profile resulting from a time-varying stress by approximating that profile as a series of sequential constant stress steps.

$$\Delta\varepsilon^{VP}(t_A + \Delta t, \sigma_B) = \varepsilon^{VP}(t_A, \sigma_A) + \Delta\varepsilon^{VP}(\Delta t, \sigma_B) \quad \textbf{4-47}$$

Incorporating history dependence through *time hardening* assumes that the strain increment $\Delta\varepsilon^{VP}$ that occurs in the multi-step experiment after t_A is identical to that in the creep experiment at σ_B over the same time range. Thus, the total strain at the end of the increment Δt after the stress changes is the sum of the strain at t_A and the change in strain that occurs under σ_B for a time step Δt beginning at t_A. This is shown in Equation 4-48 and illustrated in Figure 4-18.

$$\varepsilon^{VP}(t) = \varepsilon^{VP}(t_A) + A{\sigma_B}^b\left((t_A + \Delta t)^c - {t_A}^c\right) \quad \textbf{4-48}$$

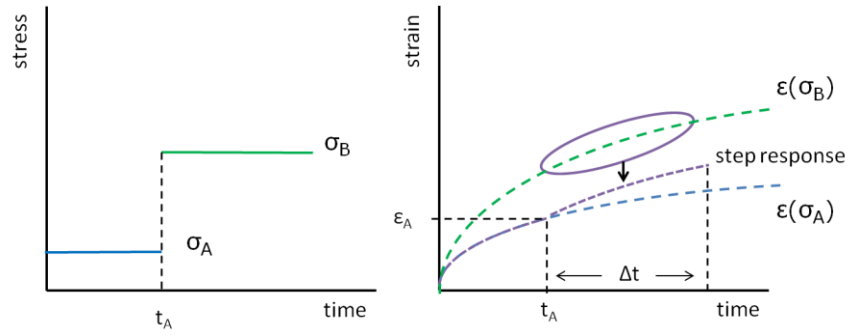

Figure 4-18. Illustration of time hardening response of a representative viscoplastic material to multi-step loading. The response after time t_A is obtained by vertically the shifting the response of the material to σ_B from t_A to $t_A+\Delta t$.

Strain hardening takes into account the strain state of the material at the time of the stress change. Rather than evaluating the strain increment at the actual time the stress changed, strain hardening begins at an effective time, corresponding to the time at which the response to σ_B had a value of strain equivalent to that at t_A. The effective time is calculated using Equation 4-50 and the strain at the end of the increment by Equation 4-49. Strain hardening is demonstrated graphically in Figure 4-19.

$$\varepsilon^{VP}(t) = \varepsilon^{VP}(t_A) + A{\sigma_B}^b\left(\left(t_{eff} + \Delta t\right)^c - {t_{eff}}^c\right) \quad \textbf{4-49}$$

$$t_{eff} = \left[\frac{\varepsilon(t_A)}{A(\sigma_B)^b}\right]^{1/c} \quad \textbf{4-50}$$

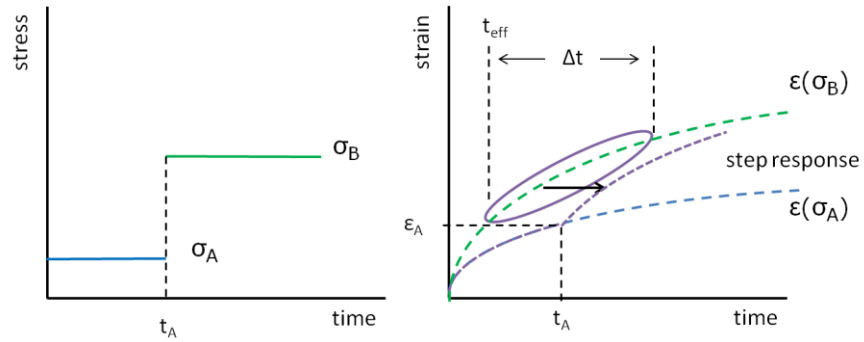

Figure 4-19. Illustration of strain hardening response of a representative viscoplastic material to multi-step loading. The response after time t_A is obtained by horizontally the shifting the response of the material to σ_B from t_{eff} to $t_{eff}+\Delta t$, where t_{eff} is calculated from the magnitude of strain at t_A.

In this manner, the viscoplastic strain resulting from many sequential increments of varying stress can be calculated. Multistep experiments will be used to determine whether time or strain hardening is the more appropriate choice for the PFCB/PVDF blend in the Results chapter.

The previous example used the Zapas-Crissman constitutive equation for viscoplastic strain. The Tobolsky-Eyring equation can also be expressed in the recursive form by time hardening, as in Equation 4-51, or strain hardening, as in Equation 4-52. The effective time for the Tobolsky-Eyring expression is giving in Equation 4-53.

$$\varepsilon^{VP}(t) = \varepsilon^{VP}(t_A) + Aexp(b\sigma_B)\left((t_A + \Delta t)^c - {t_A}^c\right) \quad \textbf{4-51}$$

$$\varepsilon^{VP}(t) = \varepsilon^{VP}(t_A) + Aexp(b\sigma_B)\left(\left(t_{eff} + \Delta t\right)^c - {t_{eff}}^c\right) \quad \textbf{4-52}$$

$$t_{eff} = \left[\frac{\varepsilon(t_A)}{Aexp(b\sigma_B)}\right]^{1/c} \quad \textbf{4-53}$$

4.3.2. Recursive Multiaxial Constitutive Equations

Discussions about the constitutive model thus far have dealt solely with uniaxial experiments and uniaxial equations. However, the loading state in an operating fuel cell is multiaxial. Thus, it is desirable for the constitutive expressions to apply to loading in both directions in the plane of the material. The in-plane multiaxial constitutive expressions are developed from the uniaxial expressions in the paragraphs below.

4.3.2.1. Multiaxial Notation

To move from the uniaxial equations to the multiaxial equations for non-linear viscoelastic response, the stress, strain and material properties must be considered in all material directions. A convenient way to express these multidimensional relationships is through matrices and tensors. For example, the stresses, σ_{kl}, and strains, ε_{ij}, in an elastic material are related by a matrix with constant coefficients which are the elastic compliances, S_{ijkl}, as shown in Equation 4-54.

$$\varepsilon_{ij} = S_{ijkl}\sigma_{kl} \quad \textbf{4-54}$$

The full matrix notation for a strain state is Equation 4-55. The first subscript of each term in the matrix indicates which face of a material element the strain is calculated on, and the second subscript indicates the direction in which the strain is occurring. Similarly, for the stress tensor, the first subscript indicates the face on which the stress acts and the second indicates the direction in which it acts.

$$\varepsilon_{ij} = \begin{bmatrix} \varepsilon_{11} & \varepsilon_{12} & \varepsilon_{13} \\ \varepsilon_{21} & \varepsilon_{22} & \varepsilon_{23} \\ \varepsilon_{31} & \varepsilon_{32} & \varepsilon_{33} \end{bmatrix} \quad \textbf{4-55}$$

For experiments in which the out-of-plane stress is negligible compared to the in-plane stresses, the matrix can be simplified to that in Equation 4-56, which is used for 2D plane stress analysis. (Z-directional strain, ε_{33}, could also be calculated, but neglecting it does not affect the strains in the alternate directions because it exists only from Poisson effects.)

$$\varepsilon_{ij} = \begin{bmatrix} \varepsilon_{11} & \varepsilon_{12} & 0 \\ \varepsilon_{21} & \varepsilon_{22} & 0 \\ 0 & 0 & (\varepsilon_{33}) \end{bmatrix} \quad \textbf{4-56}$$

If the material is isotropic in-plane, the stress and strain matrices are symmetric and can be expressed in Voigt notation. This reduces the 3x3 matrix into a 1x3 vector, as shown for the strain matrix in Equation 4-57 and the stress matrix in Equation 4-58 , which in turn reduces the tensor order of the compliance matrix from four to two. In matrix notation, ε_{11} is the strain in the x-direction, ε_{22} is the strain in the y-direction and ε_{12} = ε_{21} represents the shear strain between the x- and y- directions.

$$\varepsilon_{ij} = \begin{Bmatrix} \varepsilon_{11} \\ \varepsilon_{22} \\ \varepsilon_{12} \end{Bmatrix} \quad \textbf{4-57}$$

$$\sigma_{ij} = \begin{Bmatrix} \sigma_{11} \\ \sigma_{22} \\ \sigma_{12} \end{Bmatrix} \quad \textbf{4-58}$$

Any total stress or strain tensor can be divided into two tensors which contain only deviatoric or dilatational components. Deviatoric stresses (s_{ij}) are those which cause shear strain (e_{ij}), or shape changes without any volume change. Dilatational stresses (σ_{kk}) result in volume changes but no shape change. The deviatoric strains are a function only of deviatoric stress, and the dilatational strains (ε_{kk}) are a function only of dilatational stress. The dilatational stress is the sum of the diagonal components of the total stress tensor, and likewise for the strain tensor. In tensor notation, these relationships are expressed by Equations 4-59 through 4-62.

$$\sigma_{ij} = s_{ij} + \frac{1}{3}\sigma_{kk}\delta_{ij} \quad \textbf{4-59}$$

$$\sigma_{kk} = \sum_{k=1}^{3} \sigma_{ij} = \sigma_{11} + \sigma_{22} + \sigma_{33} \quad \textbf{4-60}$$

$$\varepsilon_{ij} = e_{ij} + \frac{1}{3}\varepsilon_{kk}\delta_{ij} \quad \textbf{4-61}$$

$$\varepsilon_{kk} = \sum_{k=1}^{3} \varepsilon_{ij} = \varepsilon_{11} + \varepsilon_{22} + \varepsilon_{33} \quad \textbf{4-62}$$

In an analysis decomposed into deviatoric and dilatational components, the uniaxial compliance alone is not sufficient to characterize the material properties. Instead, the shear compliance, *J*, is used to relate deviatoric stresses and strains and the bulk compliance, *B*, is used to relate the dilatational stresses and strains. If the material is isotropic, the shear and bulk compliance are the same in all directions (i.e., $J_{11} = J_{22} = J_{33} = J$) and can be calculated from the creep compliance and in-plane Poisson's ratio by the conversions in Equations 4-63 and 4-64. In this analysis, only the in-plane properties are used because the geometries in consideration are two-dimensional, and because of isotropy, the subscripts are neglected on these properties. It is assumed that the in-plane Poisson's ratios are identical. For an anisotropic material, similar relationships hold but the directional Poisson's ratio must be used to calculate the directional shear and bulk compliances.

$$J = 2(1 + \nu)D \quad \textbf{4-63}$$

$$B = 3(1 - 2\nu)D \quad \textbf{4-64}$$

4.3.2.2. Non-linear Viscoelastic

The form of the non-linear viscoelastic constitutive equation from uniaxial calculations is applied twice during a multiaxial analysis; once for deviatoric strain as a function of shear compliance and deviatoric stress, and again for dilatational strain as a function of bulk compliance and dilatational stress. The resulting strain vectors are combined into total strain using Equation 4-61.

If the mechanical properties of the PFCB/PVDF blend were purely elastic, Equations 4-63 and 4-64 could be used to convert from the creep compliance to the shear and bulk compliances. However, this is not the case. In order to properly convert between time dependent mechanical properties, the Laplace transform of the elastic equations must be used. These equations are demonstrated in Equations 4-66 and 4-68, where s is the Laplace domain variable.

$$\pounds[J(t)] = \pounds[2(1 + \nu(t))D(t)] \quad \textbf{4-65}$$

$$\mathrm{J(s)} = 2(1 + s\nu(s))D(s) \quad \textbf{4-66}$$

$$\pounds[B(t)] = \pounds[3(1 - 2\nu(t))D(t)] \quad \textbf{4-67}$$

$$\mathrm{B}(s) = 3(1 - 2s\nu(s))D(s) \quad \textbf{4-68}$$

Without prior knowledge of a property besides the creep compliance, the solutions to the equations above are indeterminate; there is no way of knowing how much time dependence from the creep compliance should be attributed to Poisson's ratio and how much to the other properties. A simplifying assumption that is frequently made as this point is to acknowledge that for most materials, the bulk compliance is significantly less time dependent than the shear compliance [37], [118]. Thus, if the bulk compliance is assumed to be relatively constant, all time dependence in the creep compliance in Equation 4-68 can be attributed to Poisson's ratio, and then the time dependent Poisson's ratio can be used in Equation 4-66 to solve for the time dependent shear compliance. This assumption is made at this point in the research. Later comparison between experimental Poisson's ratio measurements and the Poisson's ratio calculated from assuming a constant bulk compliance will demonstrate the validity of this assumption.

Another important consideration for a multidimensional analysis is how the multiaxial stress state at a point in the material affects the degree of non-linearity in the response at that point. In the uniaxial experiments conducted to characterize non-linearity, the only information available is the axial stress and resulting axial strain. How would this knowledge be extended to an equal biaxial stress state? Would the degree of non-linearity (the value of the non-linear parameters) be the same in both in-plane directions? In other words, would the value of g_i in the 11 direction be the same as that in the 22 direction? It is reasonable to assume so. But what about a general biaxial stress state, in which the stresses in the 11 and 22 directions are not equal? Would there be different values for the non-linear parameters in each material direction? Or should the stress state be collapsed to a single equivalent stress and the non-linear parameters be calculated from that equivalent stress value rather than the directional stresses? Schapery considered these questions in [95] and demonstrated that the non-linearity of polyvinylchloride (PVC) under constant combined tension and torsion stress could be expressed as a function of the octahedral shear stress. Haj-Ali also successfully used octahedral shear stress to calculate the non-linear parameters for a model of a polymethylmethacrylate (PMMA) rectangular plate with a hole in the center [99], [128]. In the present work, the same technique is used. The octahedral stress for a 2D plane stress analysis is shown in Equation 4-69.

$$\bar{\sigma} = \sqrt{\frac{1}{2}((\sigma_{11} - \sigma_{22})^2 + {\sigma_{11}}^2 + {\sigma_{22}}^2 + 6{\sigma_{12}}^2)} \qquad \textbf{4-69}$$

Once the octahedral shear stress is determined, the various non-linear parameters are calculated in the same way as for the uniaxial case (using Equation 4-5) with octahedral shear stress replacing the uniaxial stress. It is interesting to note that for both uniaxial tensile loading and equal biaxial loading, the octahedral shear stress reduces to Equation 4-70.

$$\bar{\sigma} = \sigma_{22} \qquad \textbf{4-70}$$

4.3.2.3. Non-linear Viscoplastic

The effect of the multiaxial stress state on the strain response in a particular direction must also be considered for the viscoplastic constitutive equation. Again, it is reasonable to conclude that the strain response in a particular direction is a function not only of the stress in that direction, but also the stresses in other directions.

One way to address this is through equivalent plastic strain theory, as described by Argon [129]. In this theory, an equivalent stress, σ_{equiv}, is calculated from the total stress state and compared to the yield stress of the material. If the equivalent stress exceeds the yield stress, an 'equivalent plastic strain' increment, $\Delta\bar{\varepsilon}^P$, is computed from that equivalent stress according to the selected constitutive equation. The direction of the equivalent plastic strain increment depends on the stress state which caused the strain to develop through an expression called a 'flow rule'. Directions which have more stress experience more plastic strain.

For the PFCB/PVDF material, permanent strains begin to develop at very small stresses. Thus, it does not exhibit yield behavior as is typically observed in metals, which equivalent plastic strain theory was developed to model. Therefore, in this analysis, the viscoplastic portion of strain is treated as a non-linear dashpot rather than an element with a distinct yield criterion. However, the logic of equivalent plastic strain theory still applies in that the total stress state drives the development and magnitude of viscoplastic strain increments in various directions. In this analysis, an approach similar to equivalent plastic strain theory is used. This is expressed in Equation 4-71, in which the directional deviatoric stress, scaled by the magnitude of the stress deviator, modifies the total plastic strain increment. Deviatoric rather than total stress is used because only deviatoric stresses cause plastic strain [129]. The factor 1.118 is necessary for this equation to reduce to the constitutive expression developed from a uniaxial tensile experiment.

$$\Delta\varepsilon_{ij}^{VP} = 1.118\Delta\bar{\varepsilon}^P \frac{s_{ij}}{\|s_{ij}\|} \qquad \textbf{4-71}$$

In Equation 4-71, the choice of the constitutive relationship between $\Delta\bar{\varepsilon}^P$ and the equivalent stress increment is left to the researcher. Both the Zapas-Crissman and Tobolsky-Eyring constitutive equations may be used. The equivalent stress measure used is octahedral shear stress, as given in Equation 4-69. It should also be noted that time and strain hardening are both applicable to this multidimensional analysis.

4.3.3. User Defined Material Subroutine (UMAT)

A finite element program relies on two models to carry out an analysis. One is a physical model defining geometry and boundary conditions. The other is a constitutive model, which determines how the material responds to an imposed force or deformation at a point. Abaqus has many pre-coded forms for constitutive models, such as elastic, hyperelastic, and plastic with various hardening equations. There is also a material model which uses linear viscoelasticity through a Prony series and TTSP shift factors. However, the present analysis uses a constitutive model not included in the standard Abaqus library because the available models do not adequately describe the behavior of the PFCB/PVDF material. A

UMAT (user-defined material) adds flexibility to the finite element program by allowing a user to define his own constitutive relationships. Abaqus uses those constitutive relationships in conjunction with a physical model to perform the stress/strain analysis.

4.3.3.1. General Operation

The purpose of the UMAT is to calculate the stress that results at a particular node for an applied displacement during a time increment. The physical finite element model consists of numerous elements, each of which responds to its neighbors' deformation and stress state. When Abaqus calculates the stress response at a node, it sends the UMAT information about that node's current stress/strain state and the displacement being applied. Logically, mechanical loads are included, but stress and strain arising from thermal gradients may also be sent to the UMAT in a coupled thermal-mechanical analysis. These effects are incorporated through the coefficients of hygral and thermal expansion and the hygrothermal shift factor influence on the time scale of material behavior. The UMAT is called for every node in every time step since the stress/strain state at the nodes vary depending on geometry, boundary conditions, etc.

In addition to the current stress/strain state, the UMAT also needs information about the material properties so it can calculate the appropriate response. An Input file is used to define the model geometry, boundary conditions, loading condition and material parameters. An additional input method is available for the UMAT. At the end of a particular nodal calculation, the operator may define a vector of variables (called STATEV) to be passed back to Abaqus and used when that node is called again in the next time step. This vector may contain anything the user desires. For the Schapery stress model it is used to pass converged hereditary terms, like the parameter q_n, to the next time step.

When the UMAT is called by Abaqus, it first reads in the stress/strain state and other information about the load. It then obtains material properties from the input file and reads the STATEV if one is defined. Ultimately, the UMAT must return the equilibrium stress state at the node and the Jacobian matrix (partial derivative of the change in stress with respect to the change in strain) that result from the applied deformation. The path between the required inputs and outputs is defined entirely by the user.

4.3.3.2. Specific Implementation

The UMAT employed in this analysis operates on the principles described above. Abaqus passes the UMAT a strain increment and the UMAT determines the stress increment that will produce the strain increment. The constitutive equations express strain as a function of stress, so an iterative minimization algorithm is used within the UMAT to converge on the proper stress increment for a given strain increment.

The iterative minimization algorithm uses the magnitude of the error in the strains (Abaqus defined strain increment vs. strain increment from current trial stress increment) and the Jacobian matrix (derived in Appendices A and B) to determine whether to increase or decrease the trial stress increment and by how much. Additionally, for multidimensional analyses, the algorithm accounts for which direction of strain needs the most correction and which stress consequently needs the most change. The method used for this multidimensional optimization is the conjugate gradient method as developed

by Press, et. al [130]. Further details may be found in Appendix C. Figure 4-20 represents the order of operations in the UMAT created for this analysis.

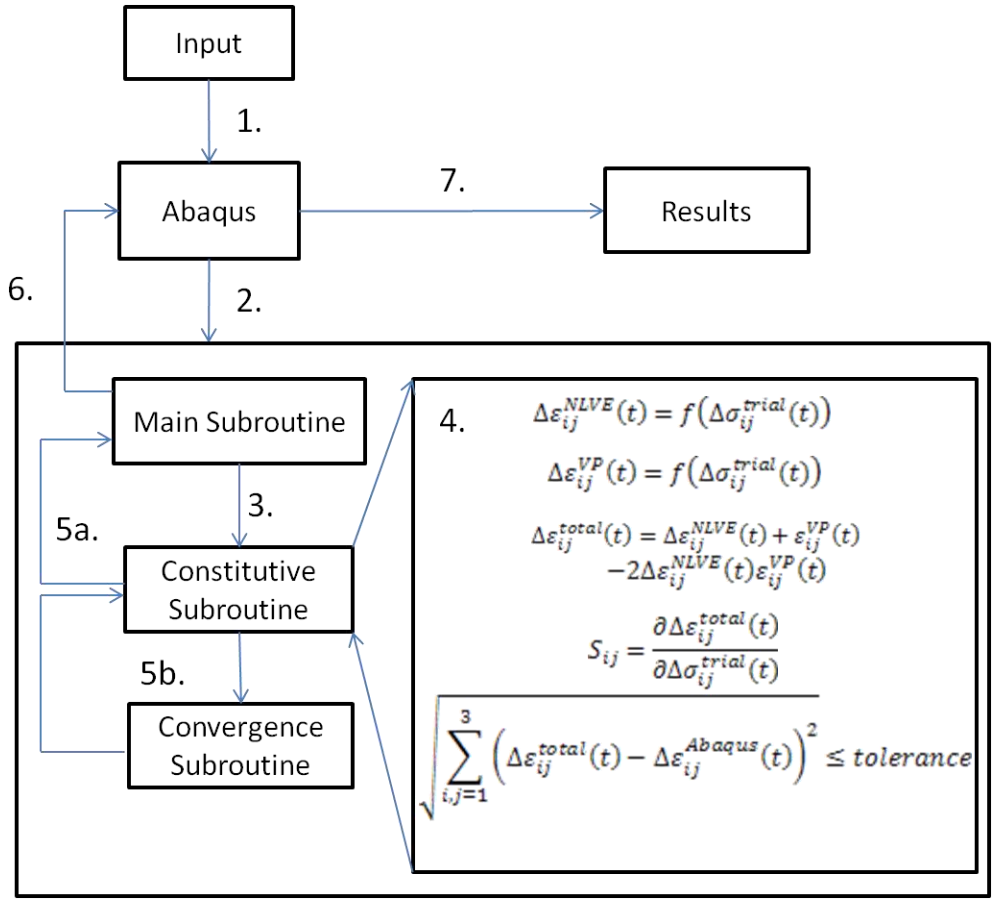

Figure 4-20. Order of operations for constitutive model when coded in a UMAT for Abaqus simulations.

1. Abaqus loads material properties, geometric model, boundary conditions, applied load from Input file.

2. Abaqus calls the UMAT subroutine for a particular node. It passes the following information: previous stress, strain, and time increments, new strain and time increments, STATEV

3. The Main Subroutine formats all variables into a single array and calls the Constitutive Subroutine. The first trial stress increment is equal to the stress increment at that node in the previous time step.

4. The Constitutive Subroutine calculates the strain increment from the trial stress increment and compares it to the strain increment prescribed by Abaqus.

5a. If the strain increment from the trial stress increment and that prescribed by Abaqus agree to within a preset tolerance, the algorithm passes the stress increment back to the Main Subroutine.

5b. If the strain increment from the trial stress increment and that prescribed by Abaqus do not agree to within a preset tolerance, the algorithm sends the current trial stress increment, along with the Jacobian matrix, to a Convergence Subroutine. The algorithm within this subroutine uses the Jacobian matrix to modify the trial stress increment. This new trial stress increment is passed back to the Constitutive subroutine and step 4 is repeated.

6. If the trial stress increment results in the correct strain increment, it along with various hereditary constitutive variables are returned to the UMAT Main Subroutine, which revises STATEV to include the updated variables and returns the stress increment, Jacobian matrix, and STATEV to Abaqus.

7. Abaqus repeats this procedure for every node, for every time step, until the forces and displacements in the geometric model are converged. It then proceeds to the next time step, and so on, until the simulation is complete.

4.3.4. User Defined Expansion Subroutine (UEXPAN)

The UMAT, as discussed above, is used to model the mechanical behavior of the material, including how the temperature and relative humidity affect the mechanical properties. Hygral and thermal expansion are accounted for in a separated subroutine called UEXPAN, for user defined expansion. Similar to the UMAT, Abaqus passed certain information to the UEXPAN and requires certain information from it. Specifically, the UEXPAN in the present analysis receives the temperature and lambda values and increments of the material at the point being evaluated from Abaqus. The coefficient of hygral expansion and the expression for the coefficient of thermal expansion as a function of lambda of the PFCB/PVDF material are hard-coded into the UEXPAN, and from them this subroutine computes the total expansion which occurs over the time increment and the rate at which expansion is occurring. These two values are returned to Abaqus and used to modify the mechanical strain at the point in the material under evaluation.

The process Abaqus uses to define the geometry has the inherent ability to account for temperature at any material point. However, moisture is not included in the standard set of properties in Abaqus. Instead, Abaqus allows the use of 'field variables' which the user must define and update appropriately. In the present analysis, lambda is included in the computation through a field variable.

4.3.5. Finite Element Geometries

Two finite element geometries are used in this analysis: one for uniaxial simulations and one for biaxial simulations. For the uniaxial tensile specimens, the thickness of the sample is significantly less than either of the in-plane dimensions (length or width). Similarly, for the blister specimens, the thickness of the sample is significantly smaller than the in-plane dimensions (radius). Because of these dimension ratios and because no stresses are applied through the thickness, plane stress is assumed in both models, so both are 2D rather than 3D geometries. The geometric models are discussed below.

4.3.5.1. Uniaxial Geometry

The geometry of the uniaxial finite element model used in this research mimics the experiments. A strip of material is assumed to be fixed vertically and horizontally along the top edge. The bottom surface is fixed in width but is loaded vertically, either with a uniformly distributed force or an imposed deformation. Although loading is only applied in the y-direction, deformations in the x-direction occur through the Poisson effect, as demonstrated in Figure 4-21. The geometry is meshed with 2D plane stress elements (Abaqus element type CPS4 [127]). There are ten elements along the width (x-direction) of the model and forty along the length. Mesh independence will be demonstrated in the Results chapter.

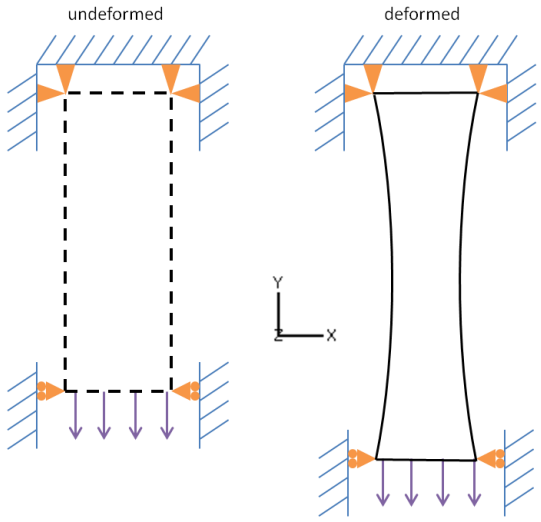

Figure 4-21. Geometry and boundary conditions for uniaxial finite element model.

4.3.5.2. Biaxial Geometry

For biaxial simulations, a second finite element model is used which mimics the geometry of the blister experiments. Again, plane stress is assumed for this geometry. As illustrated in Figure 4-22, the axisymmetric properties of a circular blister about its center are used to simplify the geometric model. Rather than performing calculations for a full blister, the geometry is a model of a single 'slice' of the

blister beginning at the center and proceeding along the surface to the edge where the blister is clamped. In the finite element model, the center of the blister slice is constrained to deform only vertically and the edge of the blister slice may rotate but not translate. The model is meshed with 50 evenly spaced Abaqus SAX1 elements [127].

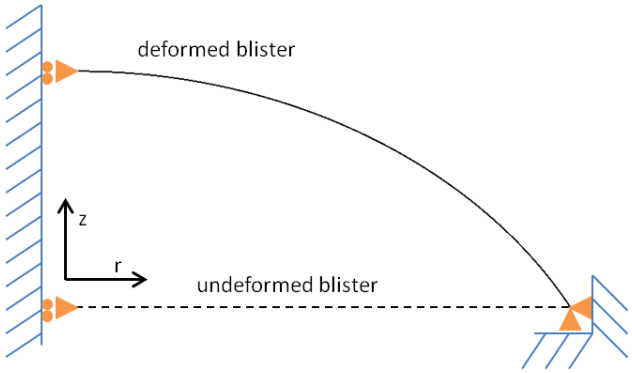

Figure 4-22. Geometry and boundary conditions for biaxial finite element model.

5. Results and Discussion

The following chapter presents the uniaxial and biaxial experimental results and model simulations. Qualitative and quantitative analysis of the agreement between experiments and model results is discussed. Where appropriate, details are given about techniques used to perform the analysis and /or potential ways to improve on the current techniques.

5.1. Uniaxial Characterization

As stated previously, the PFCB/PVDF copolymer blend was characterized in uniaxial tension with creep and recovery experiments at 70°C, 30%RH. The experimental results are presented in Figure 5-1 through Figure 5-5 with the figure titles indicating applied stress and time under load. The solid line represents the average of five replicate experiments and the dashed lines demonstrate the 95% confidence interval calculated from the replicates. Only the first half of the recovery period is included in these figures in order to allow better visualization of the creep step.

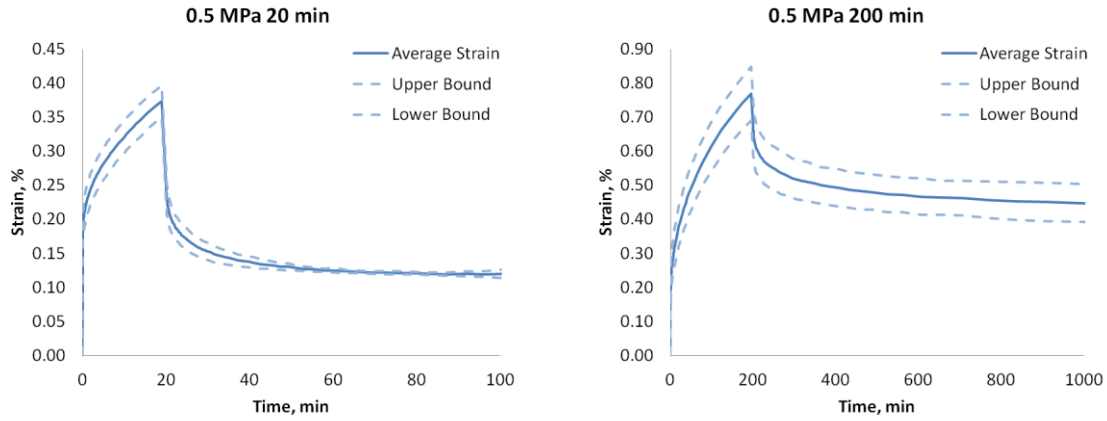

Figure 5-1. Experimental results from creep and recovery experiments at 0.5 MPa. The dashed lines represent the 95% confidence interval calculated from five replicates. (Left) 20 minute creep results and (right) 200 minute creep results.

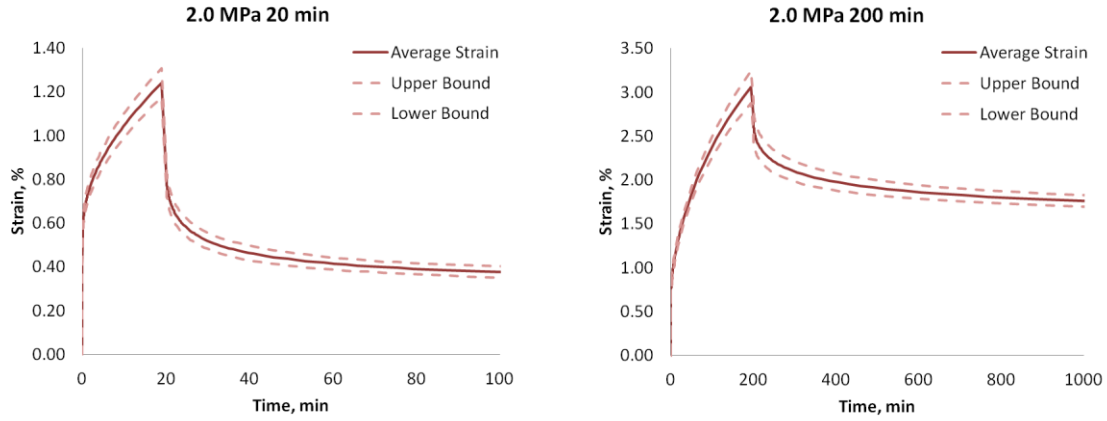

Figure 5-2. Experimental results from creep and recovery experiments at 2.0 MPa. The dashed lines represent the 95% confidence interval calculated from five replicates. (Left) 20 minute creep results and (right) 200 minute creep results.

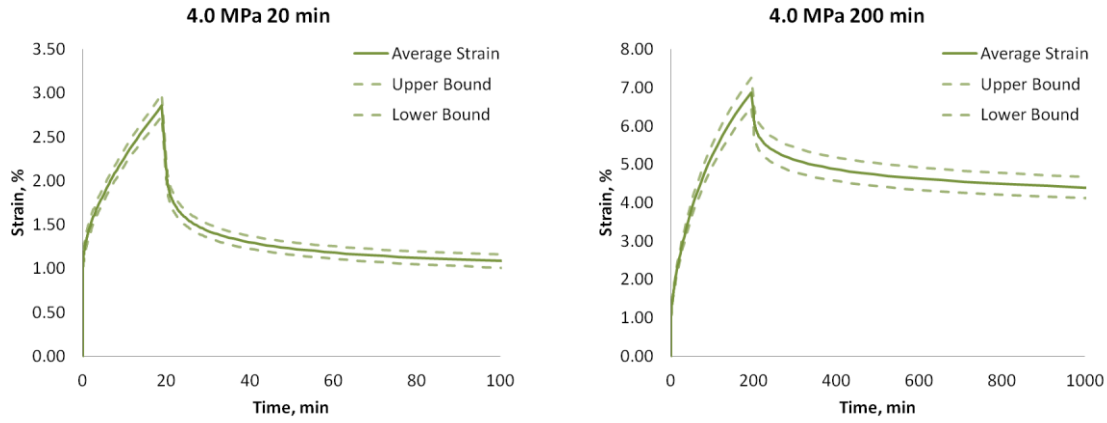

Figure 5-3. Experimental results from creep and recovery experiments at 4.0 MPa. The dashed lines represent the 95% confidence interval calculated from five replicates. (Left) 20 minute creep results and (right) 200 minute creep results.

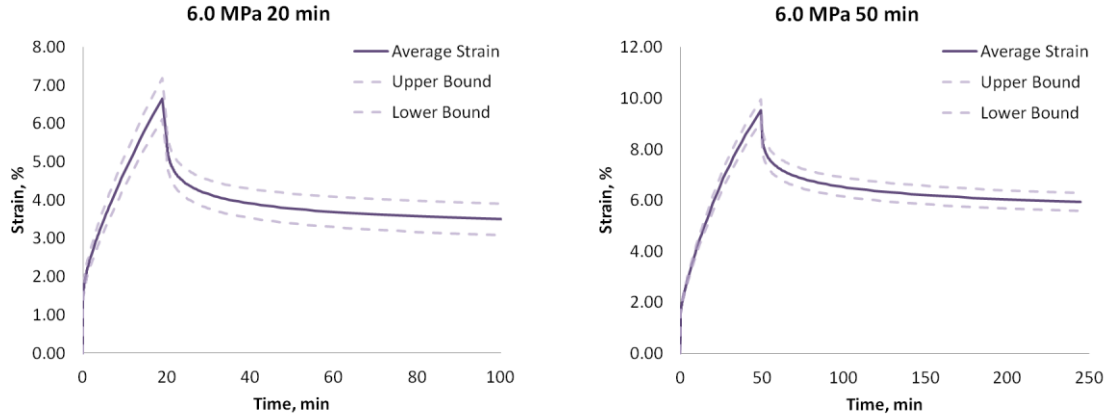

Figure 5-4. Experimental results from creep and recovery experiments at 6.0 MPa. The dashed lines represent the 95% confidence interval calculated from five replicates. (Left) 20 minute creep results and (right) 200 minute creep results.

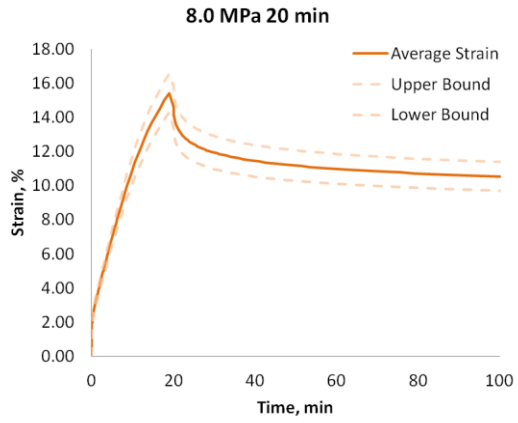

Figure 5-5. Experimental results from 20 minute creep and recovery experiments at 8.0 MPa. The dashed lines represent the 95% confidence interval calculated from five replicates.

For the 0.5 MPa and 2 MPa experiments, a constant force applied during the creep step resulted in a constant true (Cauchy) stress. (For these experiments, Cauchy stress is computed from engineering stress using the equations outlined in the Analytical Techniques chapter with a constant Poisson's ratio of 0.4.) However, for the experiments at larger stresses, it was necessary to decrease the applied force during creep in order to maintain the appropriate true stress. This was done manually while the experiments were running. Because the thickness of the samples varied, and other potential factors such as microscopic defects, etc, the same force profile did not always result in the desired stress level for replicates. For example, Figure 5-6 shows the actual true stresses applied during the 20 minute creep step in the 2 and 8 MPa creep experiments. Variations in the applied true stress account for some of the uncertainty in the experimental strains, especially at high stresses, but even for low stresses cases where the applied stress is nearly identical in all replicates there is noticeable variation in the experimental response.

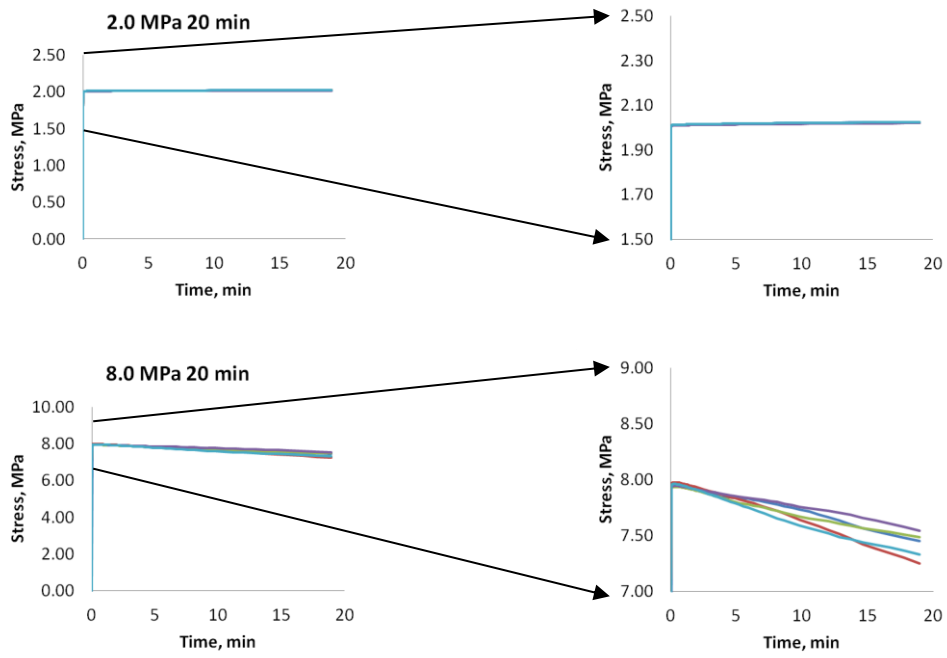

Figure 5-6. Stability of true (Cauchy) stress during creep experiments.

With the exception of the experiments at 8 MPa, experiments in which the true stress differed from the desired value by more than 2% were not included in the analysis. The range of acceptable error for the 8 MPa experiments was extended to 10%. The PFCB/PVDF blend was extremely compliant under this load and adjusting the applied force while the experiment was running in an attempt to maintain a constant true stress proved very challenging. In all, 21 experiments were attempted for the 8 MPa stress level. The five whose stress profiles were closest to 8 MPa were selected for model development; these are shown in Figure 5-6.

5.2. Model Development

The average values for each of the above experiments were used to develop the uniaxial model.

5.2.1. Viscoplastic Parameters

The viscoplastic parameters were estimated first from the creep and recovery experiments. It is assumed here that the material is fully recovered at the end of the recovery period, which is ten times longer than the creep period. Therefore, estimates of viscoplastic strain were obtained from the final recorded strain value from each uniaxial experiment. This is illustrated in Figure 5-7. It should be noted that this technique over-predicts the actual amount of viscoplastic strain in each experiment since the material is not fully recovered at the last data point of each experiment, although the rate of recovery at each point indicated in the figure is less than 0.00001 %/s. The parameter refinement procedure discussed later addresses this issue by decreasing the magnitude of viscoplastic strain in order to balance it with viscoelastic strain.

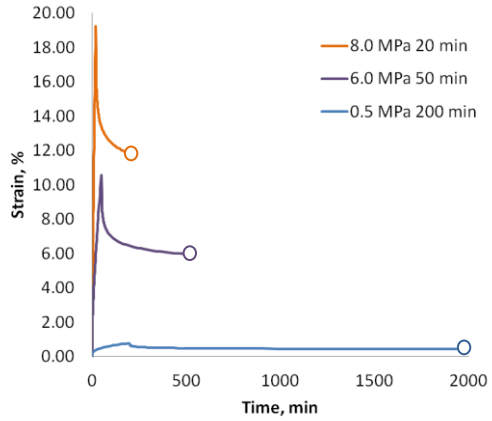

Figure 5-7. Illustration of experimental data used for initial estimate of viscoplastic strain. The last strain value recorded in each experiment, highlighted with a circle in the figure, is assumed to be the total viscoplastic strain which developed during the creep portion of the experiment. This value is refined later.

Both the Zapas-Crissman and Tobolsky-Eyring forms were considered for this fit. The Zapas-Crissman form modeled the low strain data (and consequently the low stress data) well, and the Tobolsky-Eyring form appears to express behavior at all stresses very well. The phenomenon is expected based on the stress dependence of each equation. The exponential function of stress in the Tobolsky-Eyring expression results in a small sensitivity to stress when the stress is small. The Zapas-Crissman term, on the other hand, is quite sensitive in the low-stress region. These behaviors were demonstrated in the Analytical Techniques chapter. Figure 5-8 shows the best-fit scenarios for each form over the entire range of stresses.

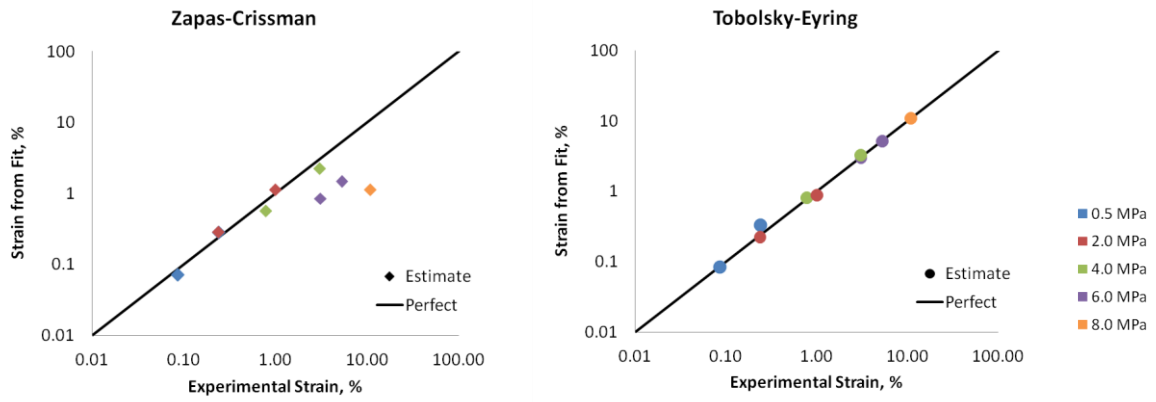

Figure 5-8. Best-fit results for Zapas-Crissman (left) and Tobolsky-Eyring (right) viscoplastic equations to estimated viscoplastic strain. Data points are color-coded by stress according to the legend on the right.

What cannot be seen in Figure 5-8 is the behavior of the two viscoplastic expressions at very low stresses, such as that used during recovery. In this region, it was found that the Tobolsky-Eyring form predicted strains significantly larger than those observed experimentally. Because both forms have reasonable agreement for stresses below 6 MPa, the two forms were combined such that the Zapas-Crissman equation describes viscoplastic behavior for stresses up to and including 4 MPa and the Tobolsky-Eyring equation is used for stress greater than 4 MPa. Because the two forms are nearly identical at 4 MPa, no discontinuity results during numerical simulations.

5.2.2. Linear Viscoelastic Parameters

After estimating the viscoplastic strain, the 0.5 MPa, 20 minute and 200 minute experiments were used to determine coefficients for the linear viscoelastic solid Prony series. The resulting Prony series is compared to the experimental data in Figure 5-9. Some discrepancy is observed during the recovery period, most likely due to the overprediction of viscoplastic strains as mentioned above. The discrepancy seems significant in the figure, but when compared to the full range of strains for which the non-linear viscoelastic viscoplastic model is applicable (out to 15%), a difference of 0.1% strain is not troubling.

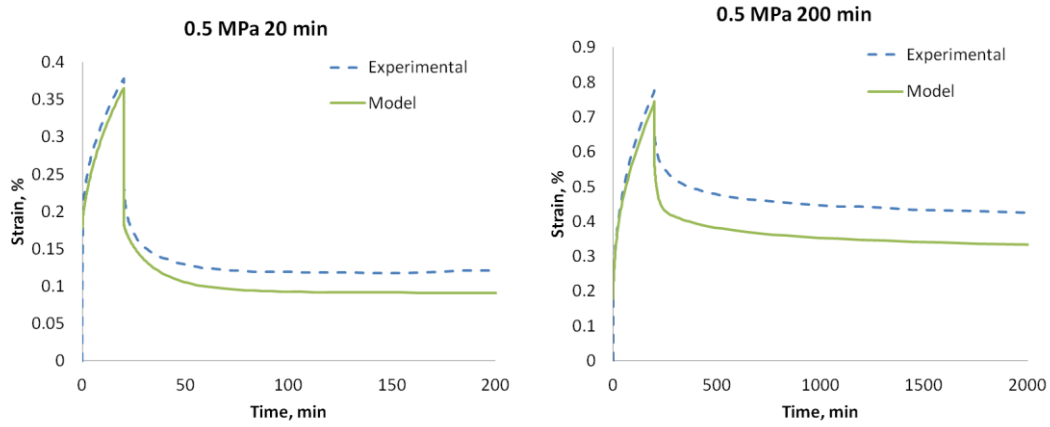

Figure 5-9. Linear viscoelastic viscoplastic model results for determining Prony series coefficients from 20 minute (left) and 200 minute (right) creep experiments at 0.5 MPa.

5.2.3. Non-linear Viscoelastic Parameters

As mentioned previously, the relationship of g_0 with stress is evident during the first few seconds of the creep experiments from the difference in the apparent elastic compliance and the elastic compliance measured in the linear viscoelastic region. The expression for g_0 was determined directly from experimental data, independently of the other parameters.

In the left image of Figure 5-10, the strain at several creep stresses is plotted for the first 10 seconds of the experiment. The right image shows the data at three seconds, which is circled, plotted as strain vs. stress. The slope of the strain vs. stress curve is the elastic compliance. Note that the experimental data exhibits a non-linear elastic compliance which is stiffer than the linear elastic value determined from the 0.5 MPa experiment. The parameter g_0 is the multiplicative factor used to express the difference of the observed elastic compliance from the linear elastic compliance. These values and the arccotangent fit are demonstrated in Figure 5-11. Although a physical mechanism for stiffening behavior is not apparent, parameter development without a g_0 term yielded results inferior to those presented here.

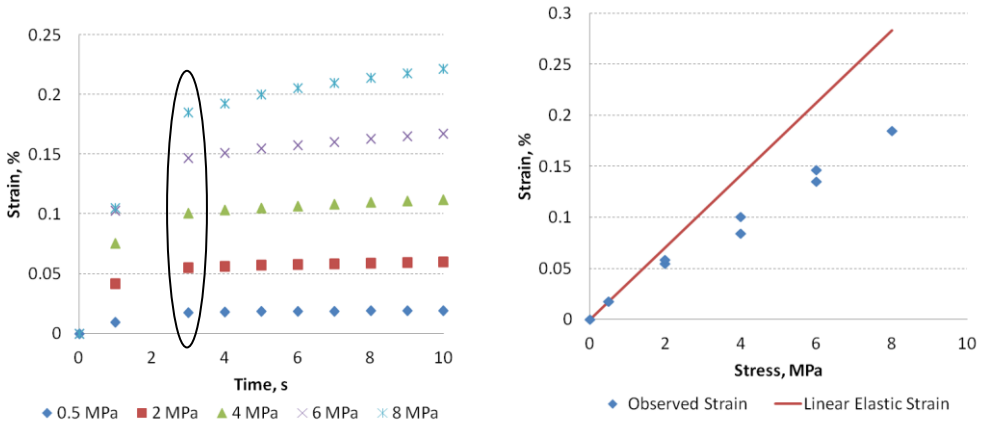

Figure 5-10. Illustration of technique for determining g_0 as a function of stress. Left: Strain as a function of time for the first ten seconds of creep. Right: Theoretical linear elastic strain vs. actual strain after three seconds of creep.

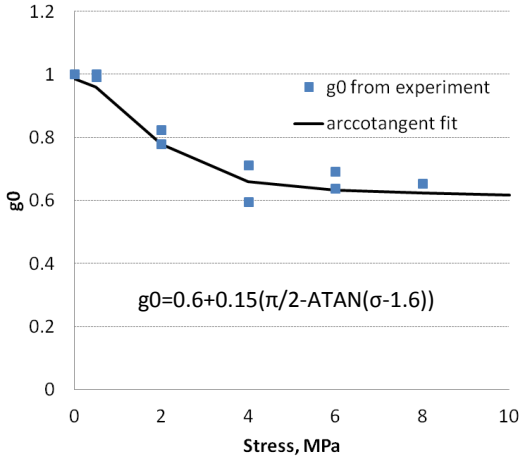

Figure 5-11. Determination of g_0 from experimental results: values and arccotangent fit.

5.2.4. Parameter Refinement

The viscoplastic parameters, g_0, and the linear viscoelastic Prony series were coded into a Mathematica program [126] which allowed the user to control each parameter in the full non-linear viscoelastic viscoplastic model, as discussed in Appendix B. Non-linear regression was used to find functions of g_2 and a_σ which improved agreement between the experiments and the initial model from the estimation procedures just described. During this process, the $g_{0,}$ linear viscoelastic and viscoplastic parameters were left unchanged. It was determined that including g_1 did not significantly improve the quality of the model over the range of interest.

The constitutive expression has a large number of parameters and many are active simultaneously with other parameters. For instance, both g_2 and the viscoplastic parameters affect the magnitude of the strain response during the creep step. It can be difficult to separate the influence of complementary or competing mechanisms, so multiple parameter sets exist which approximate the experimental results. In other words, a single optimum parameter set is difficult or impossible to find. Rather, one must select a group of parameters from the large number of combinations which closely but imperfectly describe the material behavior in most regions.

The model results from the parameter set ultimately selected are shown in Figure 5-12. The left figure compares the model to selected experiments which encompass the full range of stresses and strains to be predicted. The model exhibits similar agreement with the other experiments, but these are omitted here for clarity. Strains are plotted on a logarithmic axis, so that both large and small strains can be seen. The right figure demonstrates the correlation between the experimental and model strains in a different way. Good agreement is observed for the full range of strains.

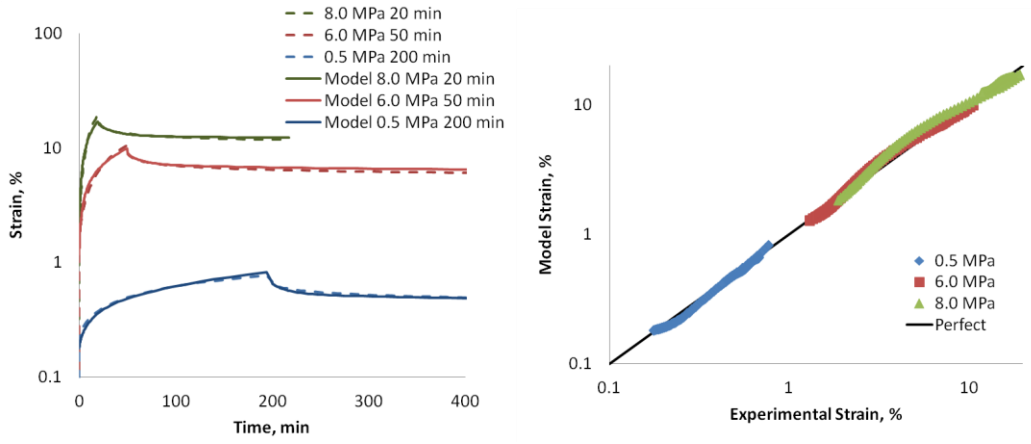

Figure 5-12. Uniaxial constitutive model compared to several of the experiments on which it is based.

The non-linear viscoelastic parameters which give the results in Figure 5-12 are plotted in Figure 5-13 as a function of stress. The elastic parameter, g_0, is unchanged from the previous plot. This parameter set does not include any non-linearity from g_1, which affects the time-dependent viscoelastic response during the creep step. However, stress softening is observed from both g_2 and a_σ. Both of these parameters are modeled with an arccotangent equation. The values for various parameters in the constitutive model are summarized in Table 5-1.

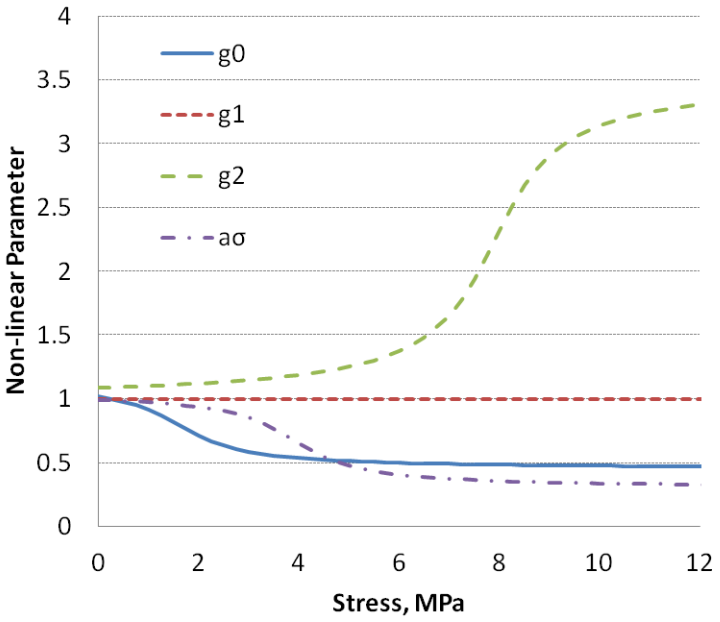

g0=0.6+0.15(π/2-ATAN(σ-1.6))

g1=1.0+0.0(π/2-ATAN(σ-0.0))=1.0

g2=3.5-0.8(π/2-ATAN(σ-7.9))

aσ =0.3+0.24(π/2-ATAN(σ-3.9))

Figure 5-13. Non-linear viscoelastic parameters as a function of stress.

Table 5-1. Parameter values for uniaxial constitutive model.

D_0 [1/MPa]	0.003544
v_0 [ND]	0.35

D_i [1/MPa]	**τ_i [s]**
8.65E-05	5
8.32E-05	10
9.91E-05	100
1.92E-04	300
2.16E-03	1000
1.30E-03	10000
1.98E-03	30000
1.29E-02	100000
1.22E-02	1000000

	x_1	**x_2**	**x_3**
g_0 [ND]	0.450	0.220	1.600
g_1 [ND]	1.000	0.000	0.000
g_2 [ND]	3.500	-0.800	7.900
a_σ [ND]	0.300	0.240	3.900

	A	**b**	**c**
ZC [m/m]	2.00E-05	1.000	0.600
TE [m/m]	2.61E-06	0.681	0.737

5.3. Uniaxial Validation

The uniaxial model developed from creep and recovery experiments was validated against multistep force, stress relaxation, and force ramp experiments. Simulations were performed in Abaqus using a 2D plane stress implementation of the constitutive expressions in a UMAT in conjunction with the 2D uniaxial geometry. Mesh independence of this geometry is demonstrated in Figure 5-14. This figure shows the 6 MPa 50 minute simulation with geometries meshed at 5x20 elements, 10x40 elements and 20x80 elements. Because the results are identical for the 10x40 and 20x80 cases, the simulation is

independent of mesh size when there are 10 elements across the width of the geometric model and 40 elements along the length. This mesh was therefore used for all remaining uniaxial simulations.

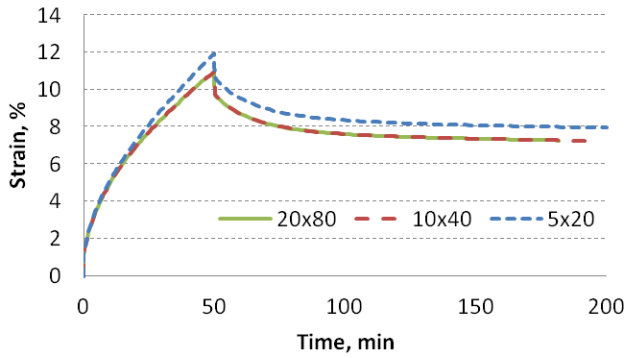

Figure 5-14. Finite element model results for 6MPa loading for 50 minutes with three meshing schemes. For each scheme, the first number indicates the number of elements across the width of the model and the second is the number of elements along the length. Because the 10x40 and 20x80 cases yield the same results, the results are independent of the mesh for the 10x40 case. Therefore, this meshing scheme is used for the uniaxial model validation simulations.

Uniaxial experiments with multiple steps were used to compare the time and strain hardening assumptions for incremental viscoplasticity. The profile called 'MultiA' is shown in Figure 5-15; it consists of four 20 minute force steps which correspond to engineering stresses of 2, 7, 4, and 5 MPa each, followed by a recovery period under a 0.006 MPa load. The strain profile is shown on the left and the true stress profile is shown on the right. During the 7 MPa step, the strains increase rapidly. This causes the stress to rise during this step, even though the force is held constant. The strain hardening response predicts strains much larger than the experiments, to the extent that the simulation failed after about 50 minutes. The time hardening response predicts slightly lower strains than observed experimentally. From this set of simulations, it appears that time hardening is a more accurate technique for capturing viscoplastic response.

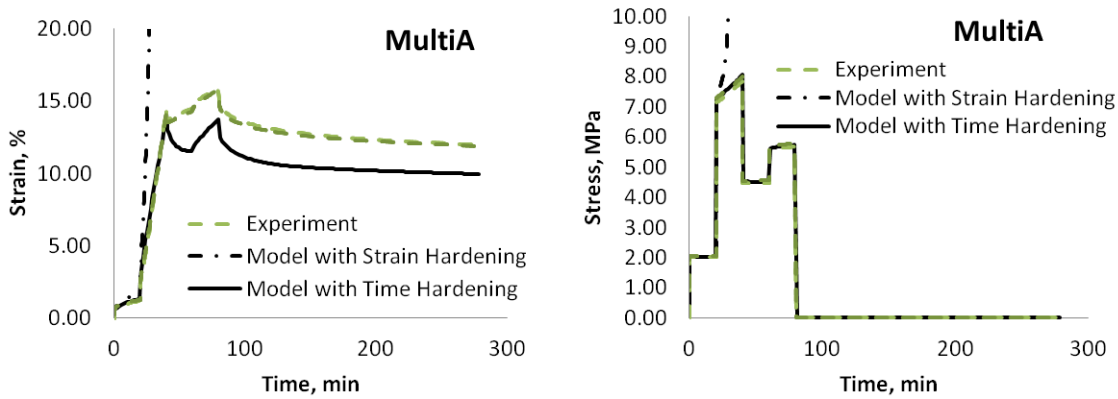

Figure 5-15. 'MultiA' multiple step creep experiments (dashed) and model prediction (solid). The strains are shown in the left figure and the true stress profile is in the right figure.

The second multistep profile, called 'MultiB', consists of four 20 minute force steps which correspond to engineering stresses of 2, 5, 4, and 7 MPa each, also followed by a recovery period under a 0.006 MPa load. The simulation for this profile tracks with the experiment very well, as demonstrated in Figure 5-16. For this profile, the strain hardening simulation again predicts significantly larger strains than are experimentally observed. However, the time hardening response agrees well with the experiments. Therefore, it appears that time hardening is the more appropriate assumption for incremental viscoplastic calculations. Time hardening will be used in the remaining simulations.

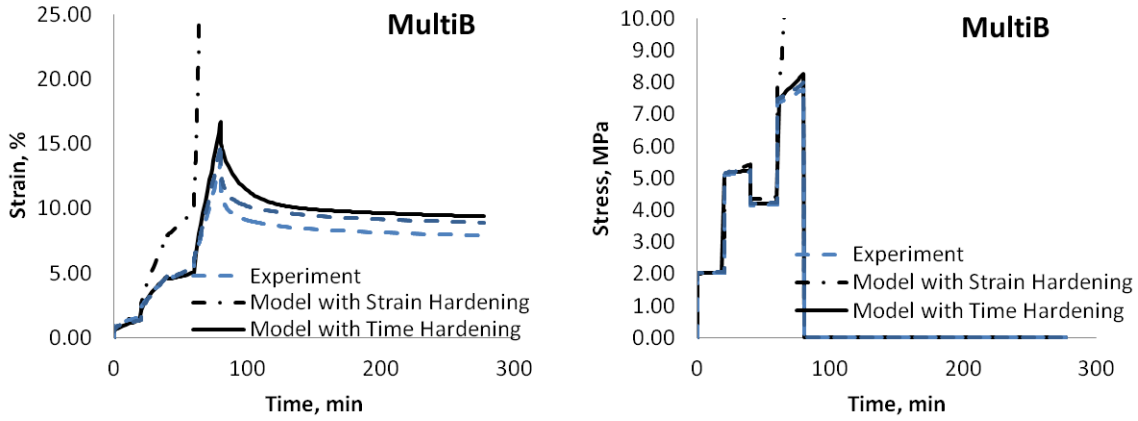

Figure 5-16. 'MultiB' multiple step creep experiments (dashed) and model prediction (solid). The strains are shown in the left figure and the true stress profile is in the right figure.

The stress relaxation experiments and simulations are compared in Figure 5-17. Two experiments were performed at strains of 0.5%, 1.0% and 3.0% strain; a new sample was used for each experiment. Good agreement is observed between these experiments and the simulations. It is especially encouraging to note that the initial stress in the 3.0% stress relaxation experiment is out of the range of stresses used for calibration but the model still captures the material behavior well.

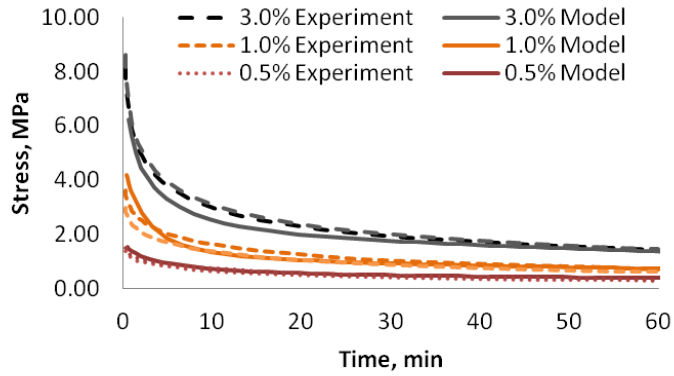

Figure 5-17. Stress relaxation experiments (dashed) and model prediction (solid).

The model also successfully simulates force ramp experiments at 0.01 N/min, 0.1 N/min and 1.0 N/min, as demonstrated in Figure 5-18. Again, although the creep and recovery experiments used for model

development only included stresses up to 8 MPa, the model does a reasonable job predicting the response of the PFCB/PVDF blend at much higher stresses.

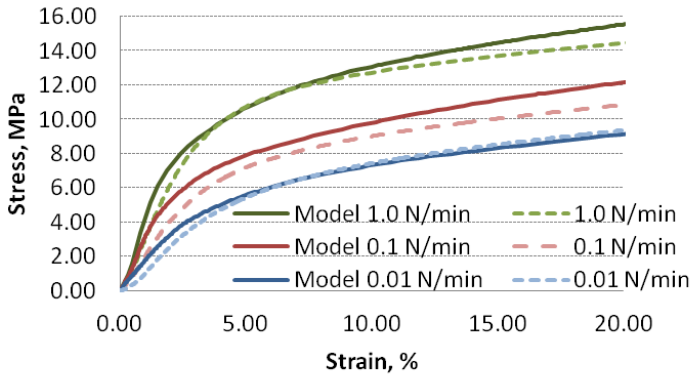

Figure 5-18. Force ramp experiments (dashed) and model prediction (solid).

The figures above demonstrate that the uniaxial constitutive model is capable of predicting the response of the PFCB/PVDF blend under a variety of uniaxial tensile configurations.

5.4. Poisson's Ratio

Information about the time dependence of Poisson's Ratio is needed in order to extend the uniaxial constitutive model to biaxial configurations. The Poisson's Ratio of the PFCB/PVDF blend was calculated from stress relaxation experiments in uniaxial tension at 70°C, 30%RH. A sample of the initial results for Poisson's Ratio is given in Figure 5-19. Both the axial (y-direction) and transverse (x-direction) strains are reported from the DIC results.

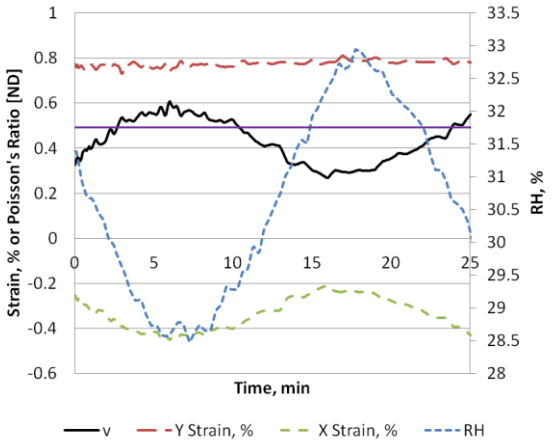

Figure 5-19. Example Poisson's Ratio experiment. Solid purple line indicates 0.5, the theoretical maximum value for Poisson's ratio.

This figure, and replicate experiments, show significant oscillation in the value of the x-strain and therefore the Poisson's Ratio. The magnitude of the oscillation results in values of Poisson's ratio which

are greater than 0.5, indicated by the solid purple line for clarity. This is not a physically permissible value for Poisson's Ratio and indicates an error in the experiment.

After investigation, it was determined the oscillation tracked very closely with the relative humidity fluctuations in the sample chamber, which were on the order of 2%RH over the course of the experiment. Coefficients of hygral expansion reported by Finlay [42] were used to correct the sample dimensions in both the axial and transverse directions. The data in Figure 5-19, after correcting for hygral expansion, is provided in Figure 5-20. Not all of the oscillation in Poisson's Ratio is removed, but the value is significantly more stable than before the correction was made.

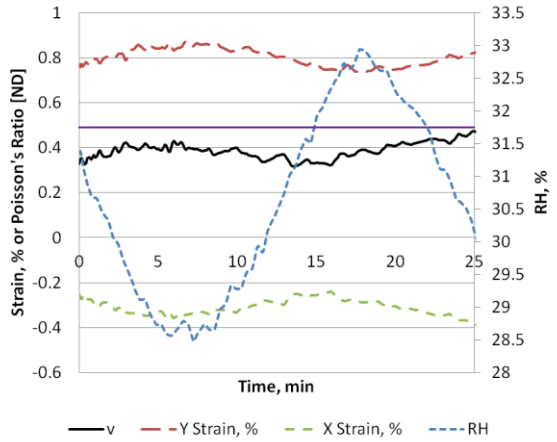

Figure 5-20. Example Poisson's Ratio experiment, after correcting strains for hygral expansion. Solid purple line indicates 0.5, the theoretical maximum value for Poisson's ratio.

Three replicates were completed for the Poisson's Ratio measurement. Figure 5-21 shows the average and 95% confidence interval of experiments after correcting for relative humidity variations. Also included in this figure is the Poisson's Ratio that results from the Laplace conversion with an initial Poisson's ratio of 0.35, as demonstrated by the experiments, and time dependence consistent with a constant bulk compliance and the experimentally measured time dependence of the creep compliance. Because the Poisson's ratio approximation was much smoother than the experimental measurements, but generally fell within the uncertainty limits, the approximation was used for biaxial simulations.

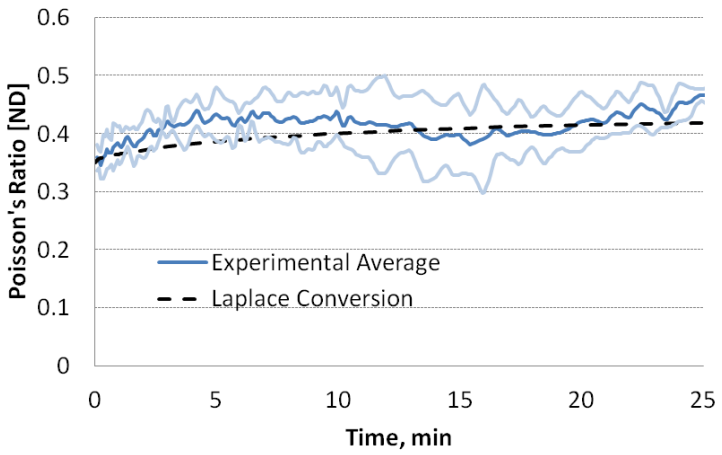

Figure 5-21. Poisson's Ratio experiments (solid) and approximation from constant bulk modulus assumption (dashed).

While conducting experiments, it was found that high-quality Poisson's ratio data was difficult to obtain with the available resources. Several factors influenced the quality of the experimental data, including environmental control, as shown previously. Other obstacles included samples puckering along the loading axis and samples curling due to environmental changes. Samples which exhibited significant puckering (more than 0.07mm local out-of-plane deformation) were not used in the analysis. To avoid issues arising from sample curling, double-layer samples were assembled by hot pressing two layers of material together. Curling in these thicker samples was much less significant. The results reported above are all from double-layer samples.

5.5. Biaxial Validation

Blister experiments were conducted at 70°C, 30%RH at constant applied pressures of 5, 10, 15, and 20kPa. (The experiments which were intended to be loaded with 10kPa actually experienced 9kPa loading. Therefore, they are reported below as 9kPa experiments.) A new sample was used for each experiment, and at least three experiments were conducted at each pressure level. Figure 5-22 reports the average stress near the center of the blister for each pressure level and error bars which represent the 95% confidence interval calculated from the replicates.

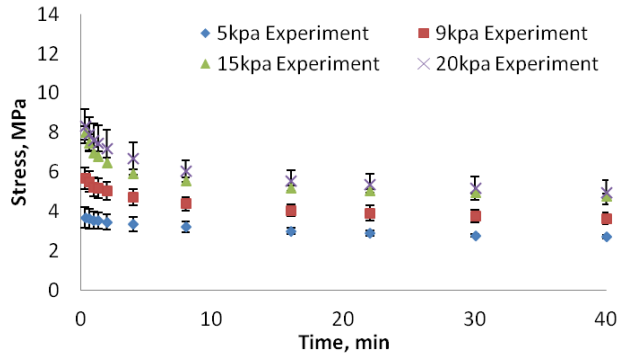

Figure 5-22. Experimental blister results: stresses calculated near the center of the blister. Error bars show 95% confidence interval from at least three replicates.

The experimental results demonstrate the expected trend with stress increasing with applied pressure. The spacing of the individual pressure levels is not consistent, but this is likely due to differences in average sample thickness at each pressure level. For instance, the average thickness of the 9kPa samples was a micron less than any of the other pressure levels. This influences the stress results in two ways: directly in the stress calculation since stress scales with the inverse of sample thickness, and indirectly through the radius of curvature which develops during the experiment. For a given pressure level, one would expect a thicker sample to exhibit less strain than a thin one, which means the radius of curvature is larger for the thicker sample. Because the relationship between radius of curvature and sample thickness is non-linear, the effects do not cancel each other in the stress calculation and do affect the final results. Additional uncertainty may result from slight temperature and relative humidity variations in the different experiments.

Biaxial simulations were performed with the axisymmetric shell geometric model and the 2D plane stress UMAT containing the constitutive model. Figure 5-23 demonstrates two features of the 15kPa simulations. First, the simulation results are independent of the meshing scheme when there are at least 50 elements. The simulations in the remainder of this document were performed with the 50 element model since it provides the same results as models with finer mesh but runs more quickly. Additionally the influence of the boundary condition imposed on the edge of the blister geometry is apparent. The blister specimen is clamped under the fixture at this location, but it was not clear whether a pinned (rotation but no translation) or an encastre (no rotation or translation) boundary condition was a more appropriate way to model that constraint. Figure 5-23 demonstrates that an encastre boundary condition at the location where the blister meets the fixture results in much higher stresses than a pinned boundary condition. Because the blister specimens are very thin, the bending stiffness should be negligible, so the pinned boundary condition is more representative of the experimental setup.

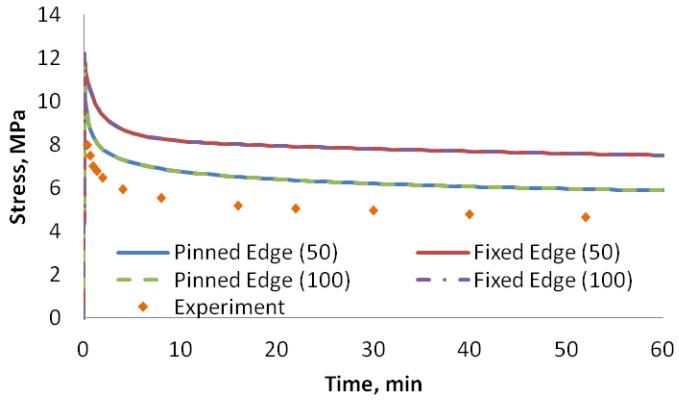

Figure 5-23. Finite element model results for 15kPa loading on the biaxial geometry. The results from twp meshing schemes are shown, one with 50 evenly spaced elements, and one with 100. (The number in parentheses in the figure legend indicates the number of elements used in the simulation.) Also illustrated is the effect of the boundary condition where the blister specimen contacts the fixture.

Although the pressure application during the experiments was nearly instantaneous, the simulations applied the pressure over a five second ramp to avoid initial high stresses far outside of the stress range

used for developing the constitutive model. Figure 5-24 shows the strains and Figure 5-25 the stresses calculated by the finite element model in comparison with experimentally determined stresses and strains.

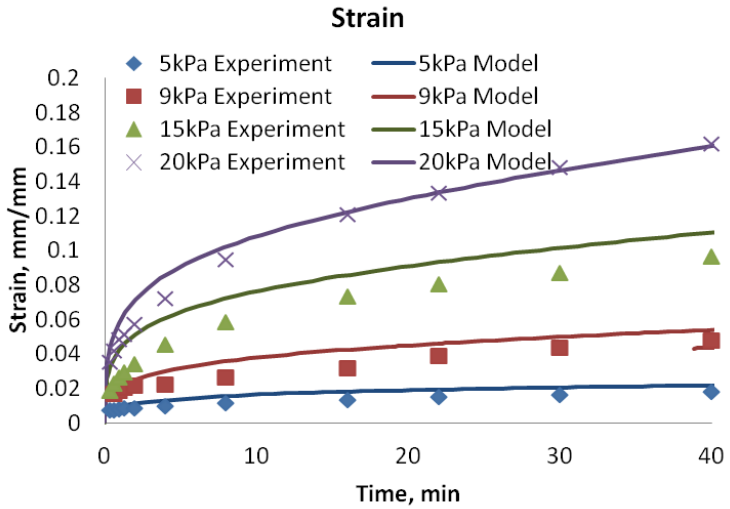

Figure 5-24. Surface strains near the center of the blister from experiments (points) and simulation (lines).

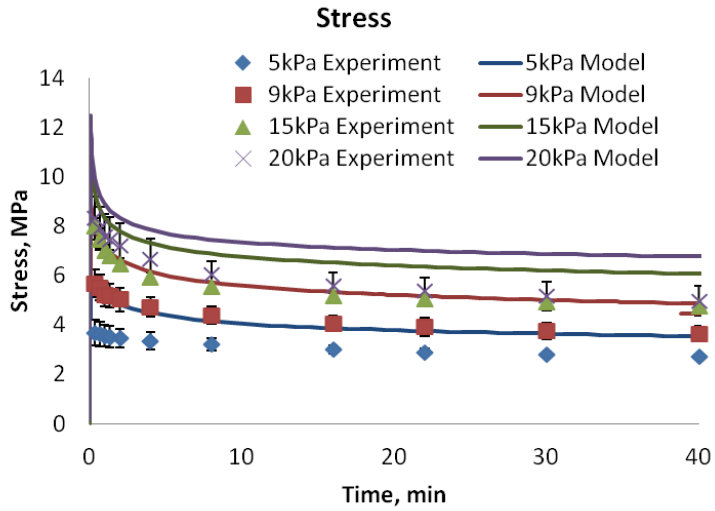

Figure 5-25. Stress near the center of the blister from experiments (points) and simulation (lines). Error bars on stress data demonstrate 95% confidence interval from at least three replicates.

The stress simulations in Figure 5-25 consistently overpredict the experiments[4] with long-term values at all stresses exhibiting greater than 20% error relative to the experiments. However, the strain

[4] The 20kPa experiments deform beyond a hemisphere, which violates the spherical cap assumption. Thus, it is not surprising that these results are not predicted by the model.

simulations demonstrate reasonable agreement. The largest error in the strain simulation is around two minutes, but after this the response settles and predicts the experimental strains to within 10% error. The exception to this observation is the 15kPa strain simulation, which has a consistent error of about 15%. This is a curious discrepancy because the model essentially correctly predicts the experimental strains based on the applied boundary conditions but does not agree with experimental stresses computed from curvature measurements.

Investigation into the source of this issue, as documented in Appendix G, systematically ruled out errors in experimental pressure measurement, the effect of the ink used to speckle the samples, and the region on the blister surface used to determine the radius of curvature from out-of-plane displacement measured by the DIC. Similarly, the value of through-plane Poisson's ratio used in the blister model and the effect of potential initial 'slack' in a blister specimen were ruled out as sources of error from the simulations. The thickness of the sample for each simulation is equivalent to the average thickness of the samples at the corresponding pressure level. To remove any thickness effects, the membrane force resultant was computed by integrating the stress through the thickness of the sample. These results are shown in Figure 5-26, and exhibit some improvement over the stress results from Figure 5-24. In Figure 5-26 there is 15% error between the experimental and simulated force resultants at 5 kpa, but less than 10% error at all other pressure levels.

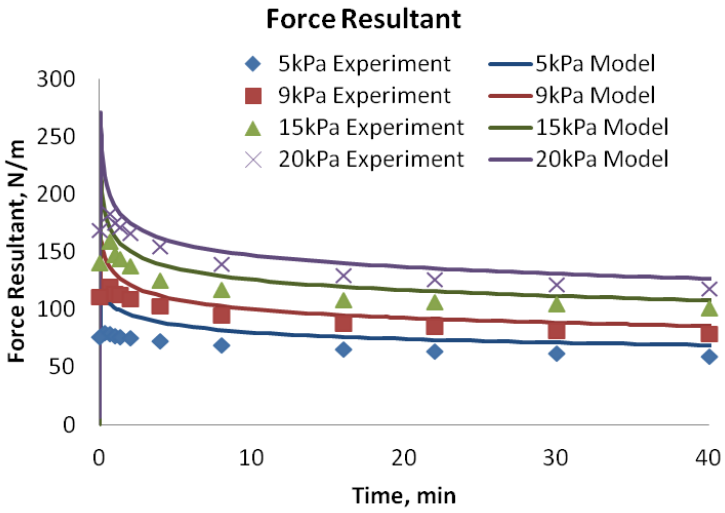

Figure 5-26. Membrane force resultant from blister experiments (points) and simulation (lines). The membrane force resultant is a quantity related to stress but which removes the effect of specimen thickness.

The most probable source of this error is the expressions used for computing viscoplastic strain. Recall that these expressions were developed from uniaxial experiments and equivalent plastic strain theory was used to apply these expressions to the biaxial load state present in the blister. Potential sources of discrepancy include the expression used for equivalent stress and the flow rule definition. Additional experiments under multiaxial loads are needed to confidently express the viscoplastic strain which develops during multiaxial loading.

5.6. Applicability of Model to Other Hygrothermal Conditions

All of the experiments conducted for model development and validation were performed at 70°C, 30%RH. To be useful for simulating fuel cell conditions, the model should be able to predict the material response over a range of conditions. The linear viscoelastic thermal and hygral dependence of the PFCB/PVDF blend was characterized by Finlay [42] and expressed as thermal and hygral shift factors.

The simplest approach for extending the linear viscoelastic model to the non-linear viscoelastic region would be to scale time using the hygral and thermal shift factors without altering any of the non-linear viscoelastic parameters (g_0, g_1, g_2, a_σ) or the viscoplastic parameters (A, b, c). However, it is possible that the non-linear viscoelastic and/or viscoplastic parameters are dependent on temperature and moisture.

In an attempt to ascertain the thermal and hygral dependence of the non-linear viscoelastic viscoplastic response, two multistep creep experiments were conducted at conditions other than 70°C, 30%RH. The alternate conditions, 50°C, 55%RH and 80°C, 10%RH, were selected because the empirical hygrothermal shift factors in the linear viscoelastic region were unity. That is, no shifting was required in the linear viscoelastic data to form a master curve of these conditions when referenced to 70°C, 30%RH. This is shown in Figure 5-27, in which the linear viscoelastic stress relaxation modulus, as determined from stress relaxation experiments at 0.5% strain, is plotted on log-log axes. There is a slight difference in the three curves, but when that difference is compared to the 'width' of the master curve, it is negligible.

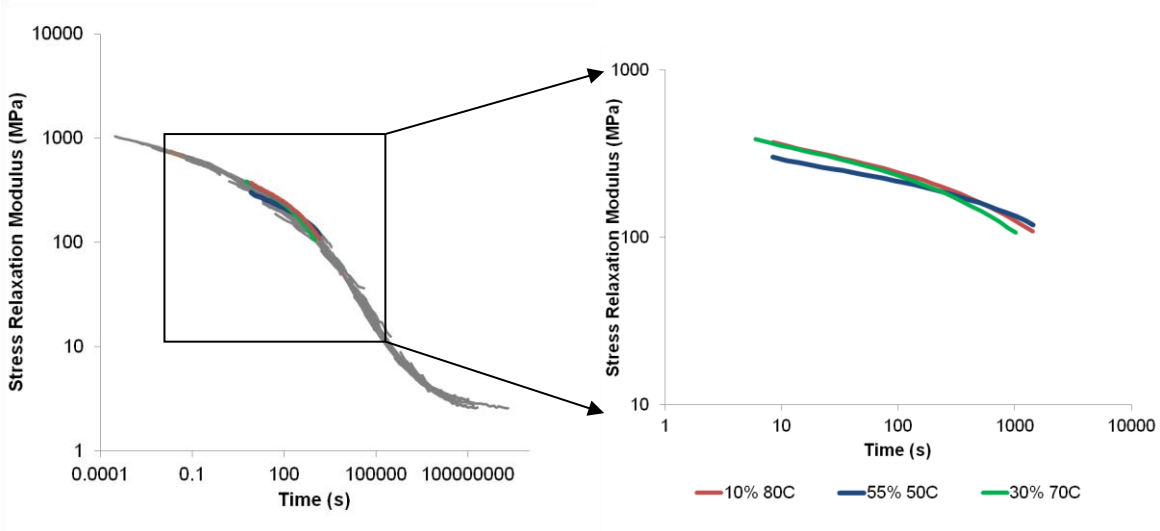

Figure 5-27. (Left) Linear viscoelastic master curve of PFCB/PVDF blend referenced to 70°C, 30%RH (green). (Right) Closer view of selected conditions 80°C, 10%RH (red) and 50°C, 55%RH (blue), which do not require shifting for the master curve.

The experimental results for MultiB experiments at these conditions are shown in Figure 5-28 along with the same multistep experiment conducted at 70°C, 30%RH.

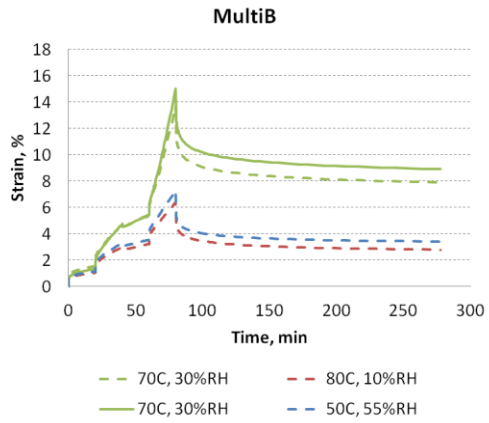

Figure 5-28. Multistep experiments at alternate conditions in the non-linear region. Even though these conditions are hygrothermally equivalent (i.e., do not require hygrothermal shift factors to agree) in the linear viscoelastic region, significant difference are observed here.

There is a clear difference in the response of the PFCB/PVDF blend at these three conditions. This demonstrates that the linear viscoelastic hygrothermal shift factors alone do not express the full temperature and humidity dependence of the PFCB/PVDF behavior. It is worth noting that the differences observed in the multistep experiments are not consistent with the minor differences in the linear viscoelastic experiment. As can be seen in Figure 5-27, the 50°C, 55%RH experiment was slightly different from the other two in the linear viscoelastic example. But, as shown in Figure 5-28, in the non-linear region the 70°C, 30%RH response is significantly different from the other two conditions, which agree quite well with each other.

Further, the order of experiments is not consistent with the moisture content, expressed as moles of water per sulfonic acid site (lambda). Table 5-2 shows the lambda value for each of the three conditions calculated from the standard equation for PFSA materials and from characterization of the PFCB/PVDF blend [42].

Table 5-2. Moisture content expressed as lambda for each of the three conditions. Lambda values calculated directly from PFCB/PVDF experiments and the lambda equation for PFSA materials are provided.

	PFCB/PVDF lambda (moles H_2O/mole SO_3^- sites)	PFSA lambda (moles H_2O/mole SO_3^- sites)	Observed Non-linear Behavior
80°C, 10%RH	0.55	1.17	Less Complaint
70°C, 30%RH	1.24	2.76	Reference
50°C, 55%RH	2.15	4.15	Less Compliant

5.6.1. Technique for incorporating environmental dependence

Since it is clear that the hygrothermal shift factors alone cannot express the environmental dependence observed in non-linear experiments, the next step in the process of developing a model valid for multiple environments is to characterize that dependence. First, we will assume that the environmental dependence of the viscoelastic (recoverable) response is adequately described by the hygrothermal shift

factors (i.e., that the non-linear viscoelastic terms are independent of environment). In this case, it would only be necessary to determine the environmental dependence of the viscoplastic terms. If this approach is not successful, it will be clear that the non-linear viscoelastic terms are dependent on the environment. In this case, significant additional experimental work will be necessary to characterize that dependence.

If the non-linear viscoelastic parameters are independent of environment then the recoverable component of strain should be very similar in the multistep experiments at the three conditions. Therefore, an initial estimate of the environmentally dependent viscoplastic strain can be obtained by determining what viscoplastic strain would bring agreement with the experiments. In essence, the total experimental strain response is partitioned into the viscoelastic and viscoplastic responses, as demonstrated in Figure 5-29 for the reference environmental condition, 70°C, 30%RH.

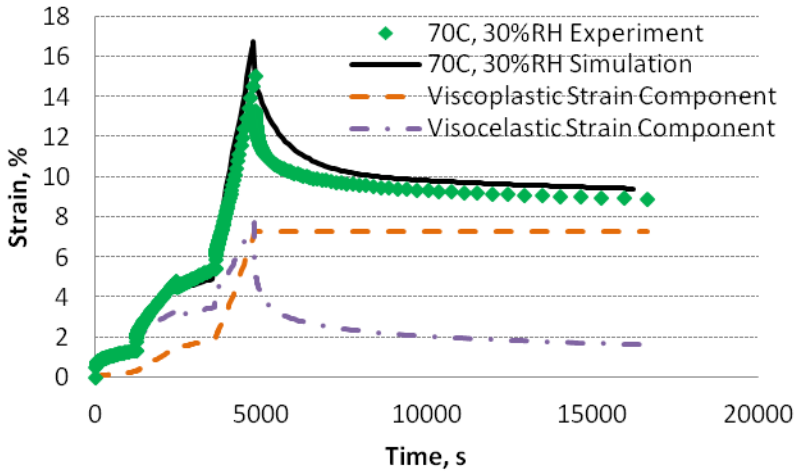

Figure 5-29. Demonstration of the partitioning of total experimental strain from the70/30 experiment (green diamond) into viscoelastic (purple dash-dot) and viscoplastic (orange dash) components.

The original parameter set results in the same strain prediction for 50°C, 55%RH and 80°C, 10%RH if the empirical shift factors are used. However, Finlay's shift factor fit, given by Equation 5-1, results in slightly different shift factors than the empirical shifts, as demonstrated in Figure 5-30, which plots the logarithm of the shift factor as a function of temperature and lambda. Because the equation rather than the individual shift factor values will be used in modeling predictions, this analysis is performed with shift factor values from the equation.

$$T \leq 70^{\circ}C \qquad \log(a_{TH}) = \frac{0.000063 * (T - 70^{\circ}C) + 0.00304 * (\lambda - 1.24)}{0.00261 + 0.00007 * (T - 70^{\circ}C) + 0.000357 * (\lambda - 1.24)} + 0.0319 * (T - 70^{\circ}C)$$

5-1

$$T > 70^{\circ}C \qquad \log(a_{TH}) = \frac{0.000063 * (T - 70^{\circ}C) + 0.00304 * (\lambda - 1.24)}{0.00261 + 0.00007 * (T - 70^{\circ}C) + 0.000357 * (\lambda - 1.24)} + 0.0993 * (T - 70^{\circ}C)$$

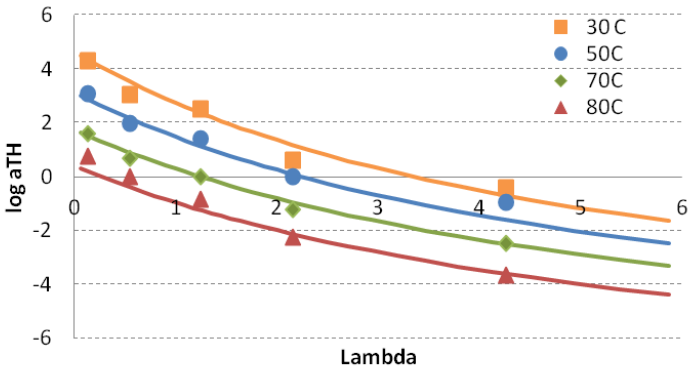

Figure 5-30. Base ten logarithm of the empirical shift factors (data points) and shift factor fit from Equation 5-1.

As shown in Figure 5-30, the equation results in a shift factor of 1.24 = 10^0.53 at 50°C, 55%RH, in contrast to the empirical shift factor value of one. The difference is even greater at 80°C, 10%RH, where the empirical value is again one but the equation yields a shift factor of 0.411 = 10^0.39.

Performing simulations with the parameter set determined at 70°C, 30%RH and the shift factors determined from Equation 5-1 yield the following strain profiles at 50°C, 55%RH and 80°C, 10%RH.

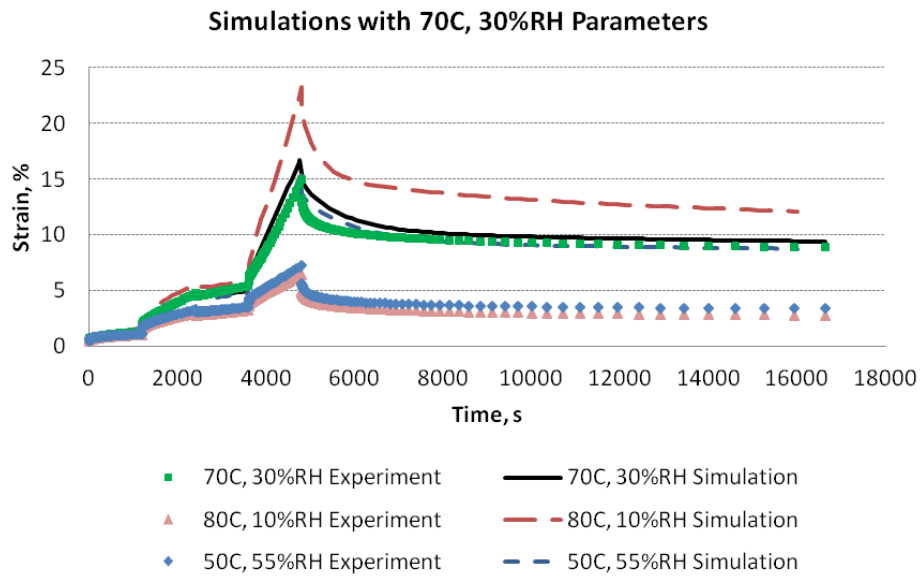

Figure 5-31. Experiments and model simulations at all three conditions. All simulations are conducted with the 70°C, 30%RH viscoplastic parameters and the appropriate hygrothermal shift factor as computed from Equation 5-1.

As anticipated, the simulations significantly overpredict the 50°C, 55%RH and 80°C, 10%RH experiments. In fact, the viscoplastic strain computed from the 70°C, 30%RH parameters alone exceeds the 50°C, 55%RH and 80°C, 10%RH experiments, as demonstrated in Figure 5-32.

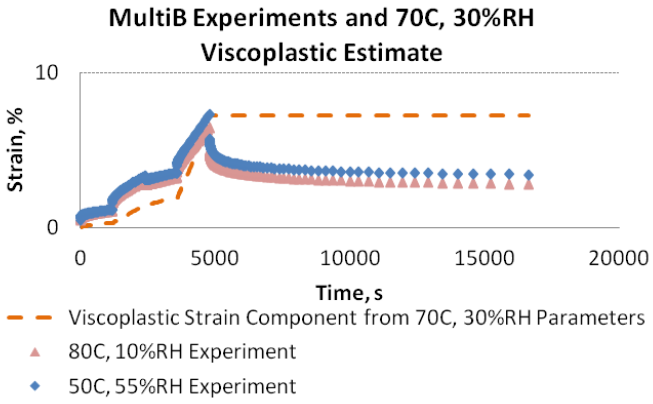

Figure 5-32. Demonstration of how the viscoplastic parameters from the 70°C, 30%RH conditions (orange dash) severely overpredicts total experimental strain observed for the same applied load profile at the hygrothermally equivalent conditions 80°C, 10%RH (pink triangle) and 50°C, 55%RH (blue diamond).

In Figure 5-29, it can be seen that the viscoplastic component of strain is a little greater than ¾ of the total calculated strain at the end of the recovery period for the 70°C, 30%RH parameter set and experiment. By introducing a functional dependence for the viscoplastic parameters A, b, and c on environmental conditions, it may be possible to bring the model into agreement with the experiments at those conditions. Each of the viscoplastic parameters is examined separately below.

5.6.2. Effect of varying A

The parameter A scales the magnitude of the entire response. Recall that this model uses a combined viscoplastic expression with the Tobolsky-Eyring form for stresses greater than 4 MPa and the Zapas-Crissman form for stresses less than or equal to 4 MPa. This means there are two parameters to consider: one which is active during the first and third steps (2 MPa and 4 MPa) and the other during the second and fourth steps (5 MPa and 7 MPa). For convenience, the constitutive equations for viscoplastic strain are repeated below along with the values for each parameter determined from the 70°C, 30%RH experiments.

$$\varepsilon^{VP}(t) = A_1 \sigma^{b_1} t^{c_1} \qquad \sigma \leq 4\ MPa \qquad 5\text{-}2$$

$$\varepsilon^{VP}(t) = A_2 exp(b_2 \sigma) t^{c_2} \qquad \sigma > 4\ MPa \qquad 5\text{-}3$$

Table 5-3. Values of the viscoplastic parameters determined at 70°C, 30%RH.

	Parameter Value		
Zapas-Crissman	A_1=2E-5	b_1=1.0	c_1=0.6
Tobolsky-Eyring	A_2=2.61E-6	b_2=0.68	c_2=0.74

The illustration in Figure 5-33 shows the effect of halving the value of A for both expressions. In this figure, the data points represent the total experimental strain measured at 50°C, 55%RH, the long dash line is the viscoplastic component calculated directly from the indicated values of A, the small dash line is the simulation resulting from running the model with the updated values of A, and the solid line is the simulation resulting from the 70°C, 30%RH parameters. It appears that these values of A are still too large to allow agreement between the simulation and the experiments. Further, it seems that most of the error builds during the second and fourth steps, indicating that the Tobolsky-Eyring parameter is the one which needs to be adjusted.

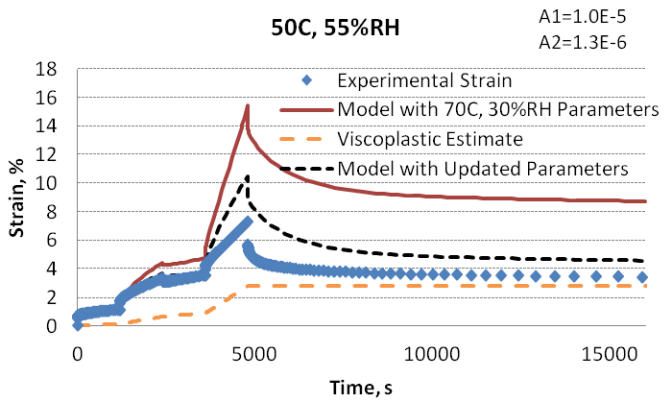

Figure 5-33. Demonstration of total strain predicted from the value of parameter A being half of the value determined from the 70°C, 30%RH experiments (black dash). Also shown are model results from the original values of parameter A (red solid), the experimental strain at 50°C, 55%RH (blue diamond) and the viscoplastic component of the strain calculated from the updated parameter (orange dash).

Changing the parameter A_1 in the Zapas-Crissman equation back to its original value and further decreasing parameter A_2 in the Tobolsky-Eyring equation yields the results in Figure 5-34.

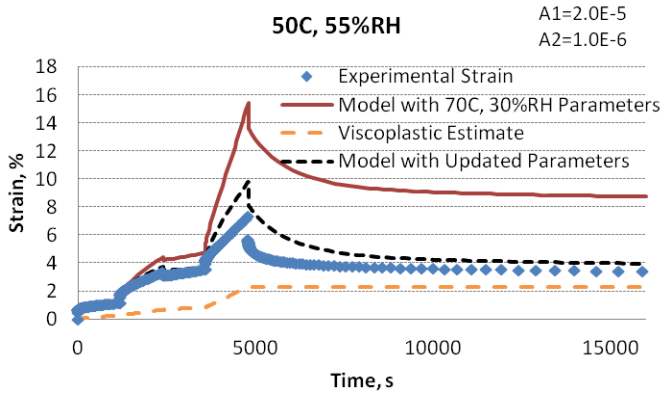

Figure 5-34. Demonstration of total strain predicted from adjusting the value of parameter A_2 (black dash). Also shown are model results from the original values of parameter A (red solid), the experimental strain at 50°C, 55%RH (blue diamond) and the viscoplastic component of the strain calculated from the updated parameter (orange dash).

Figure 5-34 shows further improvement over Figure 5-33, indicating that adjusting the Tobolsky-Eyring parameter alone is effective. After decreasing A_2 further, the curve shown in Figure 5-35 are obtained. This set of parameters provides much better agreement than the original set. Because this analysis is working with the viscoplastic strain, the most important region of the response is when most of the recovery is complete. Therefore, the values in Figure 5-35 are selected because the simulation and experiments converge at the end of the test.

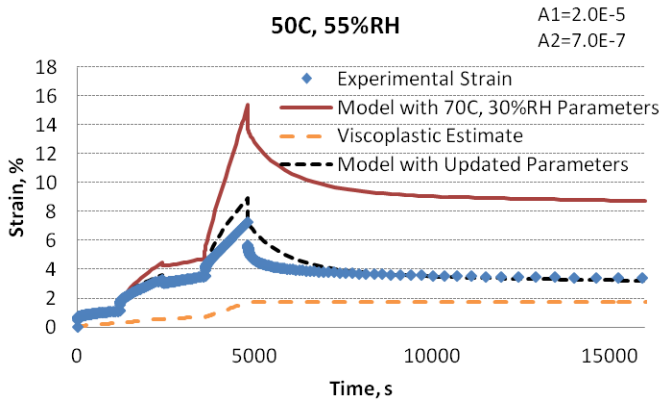

Figure 5-35. Demonstration of total strain predicted from adjusting the value of parameter A (black dash). Also shown are model results from the original values of parameter A (red solid), the experimental strain at 50°C, 55%RH (blue diamond) and the viscoplastic component of the strain calculated from the updated parameter (orange dash).

5.6.3. Effect of varying b

This procedure from the previous section is repeated, but varying the value of 'b' instead of 'A'. The simulation based on the 70°C, 30%RH parameters and that with the updated parameters which seem to best match the experiments are shown in Figure 5-36.

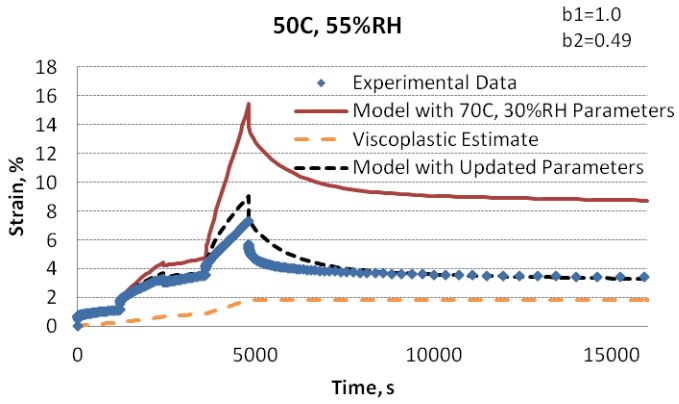

Figure 5-36. Demonstration of total strain predicted from adjusting the value of parameter b (black dash). Also shown are model results from the original values of parameter A (red solid), the experimental strain at 50°C, 55%RH (blue diamond) and the viscoplastic component of the strain calculated from the updated parameter (orange dash).

5.6.4. Effect of varying c

Again, the procedure is used to explore the effect of 'c' on the model results. This is shown in Figure 5-37.

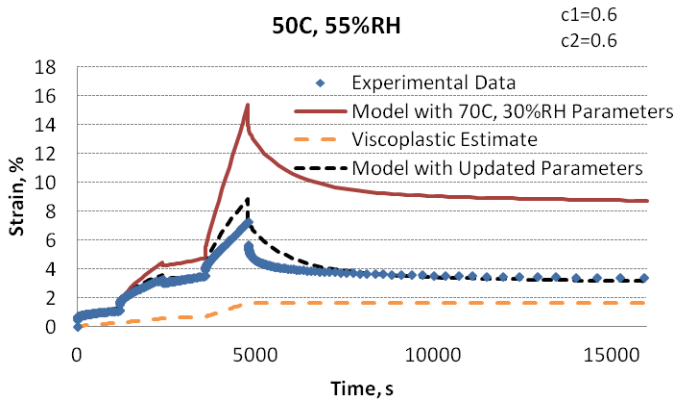

Figure 5-37. Demonstration of total strain predicted from adjusting the value of parameter c (black dash). Also shown are model results from the original values of parameter A (red solid), the experimental strain at 50°C, 55%RH (blue diamond) and the viscoplastic component of the strain calculated from the updated parameter (orange dash).

5.6.5. Comparison of parameter effectiveness

The last three figures demonstrate that none of the viscoplastic parameters by itself can bring the model into perfect agreement with experiments. In fact, if the viscoplastic component of strain is completely neglected, the strain profile in Figure 5-38 results.

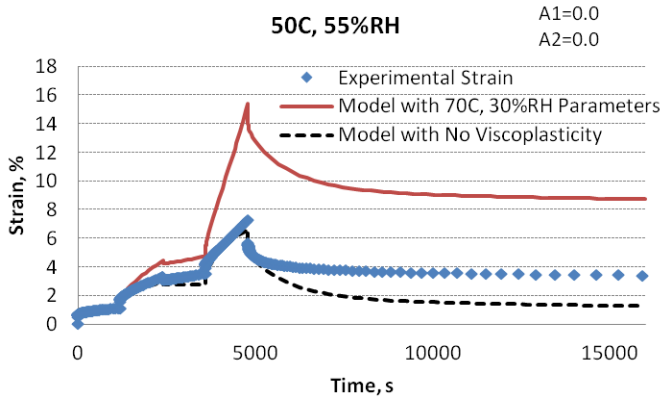

Figure 5-38. Demonstration of total strain predicted from the original non-linear viscoelastic parameters (black dash). Also shown are the experimental strain at 50°C, 55%RH (blue diamond) and the model results with the original viscoplastic parameter values (red solid).

Without any viscoplastic strain, the model does not agree with the experiments at longer times. Specifically, the non-linear viscoelastic response (from the original parameters at 70°C, 30%RH) alone correctly predicts the 50°C, 55%RH experimental results during loading; during recovery, it significantly underpredicts strain. This indicates that at least some of the difference in the 70°C, 30%RH response and the 50°C, 55%RH response lies in the recoverable strain. In other words, the non-linear viscoelastic parameters appear to have environmental dependence in addition to that exhibited by the viscoplastic parameters.

In the absence of sufficient experimental work to characterize the environmental dependence of the non-linear viscoelastic parameters, this analysis will proceed by attempting to use only the viscoplastic parameters to improve the model agreement with experiments at other environmental conditions. Future work to improve the model applicability should involve determining the temperature and moisture dependence of the non-linear viscoelastic parameters as well.

Now a decision must be made as to which viscoplastic parameter(s) should be used in the attempt to extend the model to other environmental conditions. At each condition, there are 6 possible parameters to vary: A, b, and c from both the Zapas-Crissman and Tobolsky-Eyring equations. At least seven experiments at each condition would be needed if all of the parameters were changed in the attempt to improve the model. From the analysis at 50°C, 55%RH (i.e. Figure 5-34 through Figure 5-37), where each parameter was varied independently, it is difficult to make a strong argument for one over another.

Since all of the parameters seem to perform equally well, it may be reasonable to select the one with the strongest physical explanation. Parameter A is a coefficient which simply scales the magnitude of the stress- and time-dependent response, much like the coefficient of a thermally dependent chemical reaction rate, as described by an Arrhenius equation. In the Arrhenius equation, an exponential term is used to describe temperature dependence through an activation energy, just as the Tobolsky-Eyring expression describes stress dependence. Up to this point, the Tobolsky-Eyring parameters have been determined from experiments at a single environmental condition. In this case, the environmental dependence is a constant and is included in the parameter A. Many materials exhibit thermally activated inelastic deformations which can be expressed through an Arrhenius form [129]. Therefore, there is precedent for using parameter A to ascribe environmental dependence to equations of this form.

Parameter b modifies the sensitivity of the strain response to the applied stress. It is certainly conceivable that such a parameter may be sensitive to temperature and moisture. In the MultiB experiments being used in this discussion, there are four stress steps: 2, 5, 4, and 7 MPa. The value of b was determined from the end of the recovery period of the 70°C, 30%RH creep and recovery experiments. In the MultiB experiments, recovery only occurs at the end of all four steps. Thus, it would be difficult to deconvolute the effect of the stress steps from each other without additional experiments at each stress level. Parameter b is therefore probably not the best parameter to select for this initial study.

Parameter c modifies the time dependence of the viscoplastic strain response. The hygrothermal shift factors from the linear viscoelastic region have already been applied in these experiments (essentially; since the value of the shift factor is unity for both experiments, applying the shift factor does not change the model results since the experiments are performed at the same hygrothermally shifted time.) It would not be surprising to find that the viscoplastic response is governed by a different set of hygral and thermal shift factors than the linear viscoelastic response, since the deformation mechanism is different. However, there is insufficient experimental data to characterize a new set of hygrothermal shift factors.

Independent of the shift factors, the parameter c itself may be temperature and moisture dependent. Adjusting the parameter c for each condition does not affect the full experiment in the same way. That

is, as the amount of viscoplastic strain becomes more significant (at longer times), the sensitivity of the full model response to c increases. In a sense, parameter c 'stretches' or 'shrinks' the time period over which the model is sensitive to the viscoplastic response. Considering the figures above, where the error between the model with approximated viscoplastic response and the actual experimental response does not increase significantly with time, it seems that parameter c is not likely to work well for all conditions.

This indicates that parameter A should be used in the initial attempt to extend the model to other environmental conditions. Because of the basis in the Arrhenius equation [129], Equation 5-4 is proposed for the relationship between A and temperature:

$$A(T) = A_T exp\left({}^{-\mathrm{E}_T}/_{T}\right) \quad \textbf{5-4}$$

Similarly, let Equation 5-5 be used for moisture dependence:

$$A(\lambda) = A_\lambda exp\left({}^{-\mathrm{E}_\lambda}/_{\lambda}\right) \quad \textbf{5-5}$$

Finally, the two equations are combined as in Equation 5-6.

$$A(T,\lambda) = A_T A_\lambda exp\left({}^{-\mathrm{E}_\mathrm{T}}/_{\mathrm{T}}\right) exp\left({}^{-\mathrm{E}_\lambda}/_{\lambda}\right) = A' exp\left({}^{-\mathrm{E}_\mathrm{T}}/_{\mathrm{T}}\right) exp\left({}^{-\mathrm{E}_\lambda}/_{\lambda}\right) \quad \textbf{5-6}$$

In the previous equations, temperature is in Kelvin, so it is an absolute scale. As temperature decreases, the component of A associated with temperature also decreases. This is a physically reasonable form. A singularity exists if temperature ever reaches absolute zero, but the operating range of this model is intended to be between 30°C and 90°C. Similarly, a singularity exists if lambda becomes zero. Although it is improbable that the material would ever be completely dehydrated, this might still cause problems during modeling. Therefore, the value of lambda used in this model should be no less than 0.5, which corresponds to 9%RH[5].

5.6.6. Experiments at other environmental conditions

The final form of the equation for the parameter A has three independent parameters. Therefore, at least three experiments are needed to fit the parameters. Additional MultiB experiments were performed conditions other than the original 70°C 30%RH condition. The results of these experiments are presented in Figure 5-39 below, grouped by temperature. The line style indicates the humidity level at which the experiment was performed.

[5] The expression which relates relative humidity to lambda determined directly from the PFCB/PVDF material is independent of temperature between30°C and 90°C.

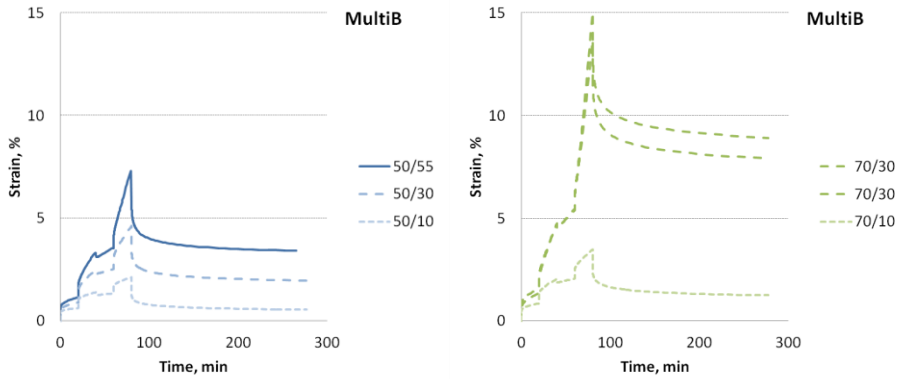

Figure 5-39. Results of MultiB experiments at various conditions.

5.6.7. Parameter determination at other environmental conditions

The same process used to estimate a value for A for the 50°C, 55%RH experiment above was used for determining the three parameters within A at the other conditions. The hygrothermal shift factor was only applied to the recoverable (viscoelastic) portion of strain because the model agreement was not improved when the viscoplastic times were hygrothermally shifted. The model results from the best-fit values, determined by observed agreement at the end of recovery, are shown in Figure 5-40. Table 5-4 contains these values of A for each condition.

Table 5-4. The values of parameter A which yield the model results in Figure 5-40. For all conditions, the Zapas-Crissman value of A, which is active when the applied stress is less than or equal to 4 MPa, is the same as for the original 70°C, 30%RH parameters. Only the Tobolsky-Eyring value of A changes with environment.

		Temperature, C		
		50	70	80
10%RH	ZC	2.00E-05	2.00E-05	2.00E-05
	TE	*8.00E-08*	*1.00E-07*	*0.00*
30%RH	ZC	2.00E-05	2.00E-05	
	TE	*5.00E-07*	*2.61E-06*	
55%RH	ZC	2.00E-05		
	TE	*7.00E-07*		

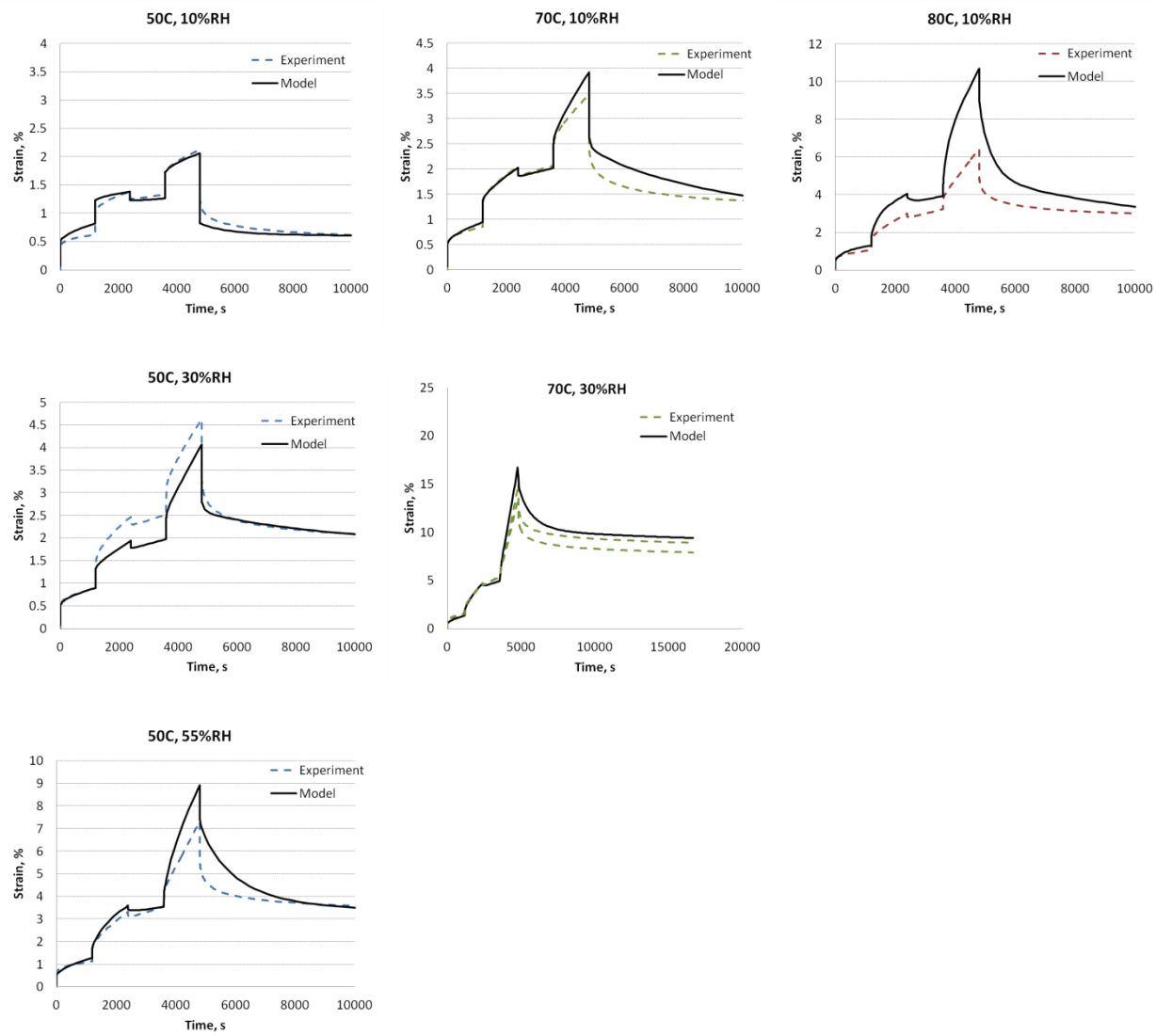

Figure 5-40. Results of MultiB experiments at various conditions and the best-fit calculations based on varying parameter A at each condition.

It is interesting to note that the Zapas-Crissman values for A are unchanged; for all conditions, the value of parameter A when the stress is less than or equal to 4MPa is 2.0E-5. Because the Zapas-Crissman form is active at low stresses and the low stresses occur early in the stress profile, the strain at the end of recovery, which is used to obtain these parameter values, is not as sensitive to the Zapas-Crissman parameters as it is to the Tobolsky-Eyring parameters. There is probably some variation in the Zapas-Crissman parameter with environment, but it cannot be determined with the current experiments.

Another note that should be made pertains to the 80°C, 10%RH condition. At this condition, the linear viscoelastic hygrothermal shift factor results in softening behavior as compared to the 70°C, 30%RH reference. All of the other conditions tested had linear viscoelastic hygrothermal shift factors which provided a stiffening effect. A value for parameter A_2 could not be found which brought the simulation into agreement with the experiment at 80°C, 10%RH. Thus, this condition was not used to fit Equation

5-7, and it is unlikely that Equation 5-7 will apply to other conditions which are hygrothermally softer than 70°C, 30%RH.

Fitting the values of A_2 from Table 5-4 to Equation 5-6 yields Equation 5-7 for A_2 as a function temperature, in Kelvin, and lambda, where lambda is converted from relative humidity using an equation based only on PFCB/PVDF data, rather than data from PFSAs in general. The correlation plot between Equation 5-7 and the values in Table 5-4 is shown in Figure 5-41.

$$A_2(T,\lambda) = 6.38E9 exp\left(-11460/_{T(K)}\right) exp\left(-2.5/_{\lambda}\right) \quad \text{5-7}$$

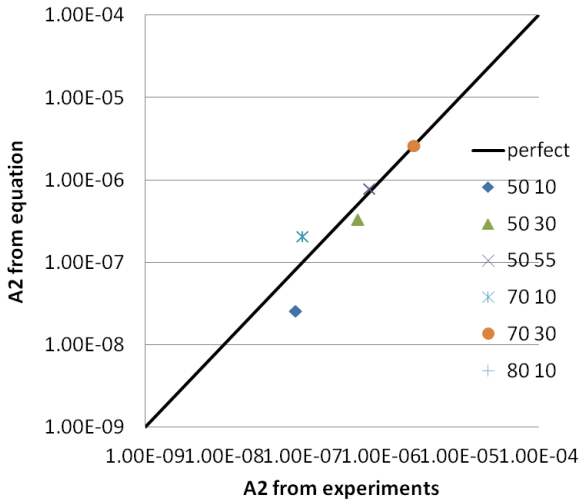

Figure 5-41. Correlation plot of parameter A as a function of temperature and lambda; values from individual experiments (color-coded data points) and best-fit line.

5.6.8. Experimental Validation of Viscoplastic Environmental Dependence

Two additional experiments were performed at 60°C, 30%RH and 60°C, 40%RH. The experimental results are shown in Figure 5-42, along with the simulated strains from the constitutive model with environmental dependence of the viscoplastic parameter. This figure demonstrates that for environments which result in stiffer mechanical behavior than 70°C, 30%RH, such as the 60°C, 30%RH experiment, the environmental dependence of the viscoplastic parameter improves the predictive capability of the model. For this case, the greatest error in the three hour long simulation was about 30% relative to the experiment. However, for conditions which soften the material relative to its response at 70°C, 30%RH, the model significantly under-predicts strain, as observed in the 60°C, 40%RH case. In this case, the maximum error during the three hour simulation approaches 80%. This is likely because all the environmental conditions used to fit the equation governing environmental dependence of viscoplastic behavior were stiffer than the 70°C, 30%RH reference condition. Although experiments at softer conditions were attempted, the strains which developed at those conditions exceeded the stroke limit of the DMA, so the experiments did not run to completion and were therefore not included in the procedure for estimating the environmental dependence of the viscoplastic response.

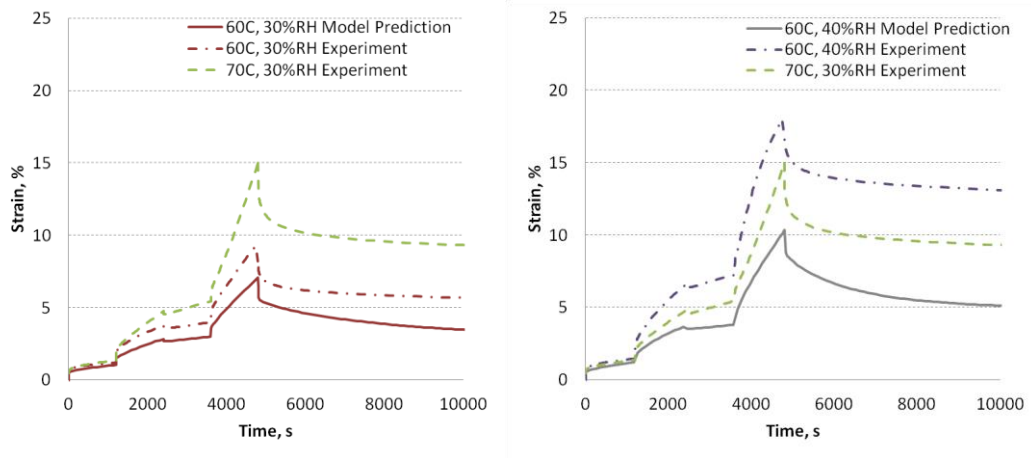

Figure 5-42. MultiB experiments at additional environmental conditions, which were not used to fit environmental dependence of the viscoplastic strain. Also shown are the predicted strain profiles at the environmental condition and the experimental results of the 70°C, 30%RH condition for comparison.

The purpose of this study was to determine whether the environmental dependence of the mechanical response in the non-linear range of stresses of the PFCB material could be characterized and attributed to only the viscoplastic component of strain. This analysis has shown that this is not possible. Although it appears that there is some environmental dependence of the viscoplastic response, there is also clear environmental dependence of the non-linear viscoelastic response which is not captured in the hygrothermal shift factor. *In order to extend the constitutive model to various thermal and hygral conditions, the environmental dependence of both the non-linear viscoelastic and viscoplastic parameters should be determined from experiments.*

5.6.9. Investigation of Model under Varying Hygrothermal Conditions

Although the results of the previous section demonstrate that the current model parameters are not able to predict the response of PFCB/PVDF at conditions other than 70°C, 30%RH, it is still of interest to examine the model response at varying hygrothermal conditions. This will demonstrate that the model is capable of simulating the effect of changing temperature and relative humidity even though the simulations do not accurately reflect the material response.

For this study, two uniaxial tension experiments were conducted at stresses between 0.5 and 0.6 MPa. The first experiment held relative humidity constant at 30%RH and cycled temperature between 30 and 70°C. The second experiment held temperature constant at 70°C and cycled the relative humidity between 30 and 70%RH. Simulations were performed with the non-linear viscoelastic viscoplastic UMAT (i.e. the constitutive model with parameters from Table 5-1 except that A_2 was computed from Equation 5-7), the UEXPAN (for hygral and thermal expansion effects) and the uniaxial finite element geometry. The results of both the experiments and simulations are shown in Figure 5-43 and Figure 5-44.

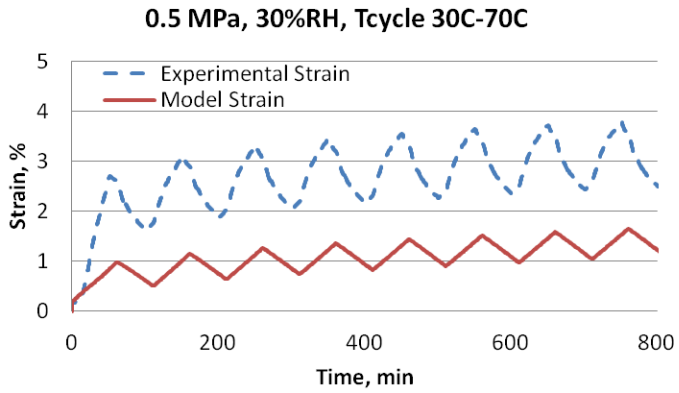

Figure 5-43. Experimental and model strains for a uniaxial tension experiment. Stress was held constant at 0.5 MPa, relative humidity was 30%RH and temperature was cycled between 30°C and 70°C.

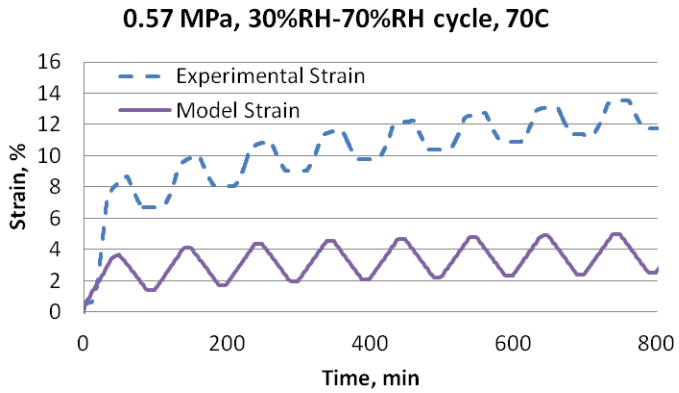

Figure 5-44. Experimental and model strains for a uniaxial tension experiment. Stress was held constant at 0.57 MPa, relative humidity was cycled between 30%RH and 70%RH and temperature was constant at 70°C.

Although the model agrees with the experiments qualitatively, in that strain increases with each cycle and larger strains develop during relative humidity cycling than temperature cycles, the quantitative agreement is poor. In both cases the model predicts significantly less strain than is observed experimentally. However, since the previous section demonstrated that the non-linear viscoelastic parameters are not independent of the environment, and that effect is not included in these simulations, it is not surprising that the model does not agree with the experiments. It is interesting to note that this effect is clear even at stresses as low as 0.5 MPa. This indicates that the onset of non-linearity moves to lower stresses at softer hygrothermal conditions, an observation which should be quantified through future work.

5.7. Summary of Results

In summary, a non-linear viscoelastic viscoplastic model was developed and validated based on uniaxial experiments at 70°C 30%RH. The parameter set is presented in Table 5-1. The model describes uniaxial stress relaxation, force ramp and multistep creep experiments with good accuracy (+/-15% error).

The uniaxial non-linear viscoelastic viscoplastic model was then extended to equal biaxial loading using experiments to justify an in-plane Poisson's ratio with an elastic value of 0.35 and time-dependence consistent with the experimentally measured creep compliance and a constant bulk compliance. Results from biaxial validation experiments demonstrated good agreement with experimental strains (less than 10% error for most cases) and yielded membrane force resultants between 10% and 15% larger than experimental values computed with thin wall pressure vessel theory.

The model was further extended to describe mechanical behavior at other environmental conditions by using linear viscoelastic hygrothermal shift factors developed by Finlay [42] and modifying *one* of the viscoplastic parameters to reflect hygrothermal dependence (Equation 5-7). The resulting simulations provided rough agreement (30% error) with validation experiments at environmental conditions which led to stiffer mechanical behavior. The simulations did not provide adequate agreement at environmental conditions which led to softer mechanical behavior.

Finally, the model was extended by introducing constitutive expressions for hygral and thermal expansion developed by Finlay [42]. The results indicated qualitative agreement but were substantially different from the experiment in magnitude.

6. Conclusions and Future Work

6.1. Summary of Work

The objectives of the present work have been threefold: 1) to characterize the mechanical response of a PFCB/PVDF blend membrane through experiments at fuel-cell like conditions, 2) to develop a constitutive expression which captures that mechanical behavior, and 3) to implement that constitutive expression in a finite element model and validate that model against additional experiments. This finite element model will then assist researchers who are investigating the PFCB/PVDF material and other alternative PEMs by allowing rapid evaluation of material response to the load conditions which occur in an operating fuel cell. Simulations with such a model require less time and resources than experimentally evaluating all cases of interest, thus aiding in the development of new PEM materials and contributing to the commercialization of PEMFCs for energy source for transportation and other applications.

Uniaxial creep and recovery experiments were performed on the PFCB/PVDF blend at 70°C, 30%RH to characterize the mechanical response of the material at a temperature and humidity likely to be encountered in an operating fuel cell. The material was found to exhibit significant non-linear mechanical behavior at conditions which would be encountered in a fuel cell. Additionally, at the end of the recovery portion of the experiment, not all strain developed during creep had recovered. Later experimental work demonstrated that these non-linear and non-recoverable effects were dependent on temperature and relative humidity in ways not captured by hygrothermal shift factors developed from linear viscoelastic experiments. Future work with this and similar materials should probe the full range of time, stress, strain and environments over which a constitutive model would be applied.

A constitutive expression consisting of non-linear viscoelastic and viscoplastic terms was selected. The non-linear viscoelastic expression was based on that proposed by Schapery [95] and the viscoplastic expression was based on a form by Zapas and Crissman [101] at stresses less than 4 MPa and a form by Tobolsky and Eyring [124] at higher stresses. Parameters for the constitutive expression were determined from the creep and recovery experiments. This constitutive expression was implemented in a finite element model through a user-defined material subroutine, or UMAT. This UMAT was then used with a uniaxial finite element geometry and simulations were validated against uniaxial stress relaxation, force ramp, and multistep creep experiments at 70°C, 30%RH. The constitutive model successfully simulated these experiments out to stresses of 8 MPa and strains approaching 15%, which is the maximum hygrothermal strain expected in an operating fuel cell.

Because the membrane experiences a biaxial in-plane stress state during fuel cell operation, the constitutive expression would be more useful if applicable to this scenario. Poisson's ratio is needed to extend the uniaxial model to biaxial cases, so stress relaxation experiments at small strains were performed on the PFCB/PVDF blend at 70°C, 30%RH. A Digital Image Correlation (DIC) system was used to measure the axial and transverse strains in the samples during stress relaxation. Analysis of the experimental results revealed that the time dependence of the in-plane Poisson's ratio of the PFCB/PVDF blend at 70°C, 30%RH was consistent with a constant bulk modulus assumption.

To validate the biaxial simulations, constant pressure blister experiments were also performed on the PFCB/PVDF material at 70°C, 30%RH. Again, DIC was used to measure deflection on the sample surface during these experiments. From the deflection, in-plane strains and the radius of curvature of the deformed blister were computed. Thin wall pressure vessel theory was used to estimate in-plane stress from convert the radius of curvature. An axisymmetric finite element geometry was used to represent the blister geometry, and biaxial simulations were performed with the UMAT developed from uniaxial results. Biaxial strains were accurately predicted by the model (+/- <10% error). Simulation membrane force resultants, which are related to stresses, also matched those estimated from the experimental radius of curvature to within 10%-15%. Although the simulations qualitatively predicted the material behavior for these experiments, the magnitude of predicted stresses was larger than the experimental stresses, presumably due to inadequate definition of equivalent plastic strain under multiaxial loading.

In an operating fuel cell, the environmental conditions are not constant. In order to be useful for fuel cell research, the constitutive model should be applicable at conditions other than 70°C, 30%RH. Hygrothermal shift factors and hygral and thermal expansion coefficients determined by Finlay [42] in the linear viscoelastic region were incorporated into the finite element model and simulations of multistep creep profiles were compared to experiments at other temperatures and relative humidities. Incorporation of the hygrothermal time shifting suggested by the LVE model was found to be inadequate for describing the hygrothermal behavior at higher stresses and strains. Specifically, it was found that both the non-linear viscoelastic and viscoplastic parameters are dependent on environment. The present work suggests that the model can be improved by modifying the Tobolsky-Eyring expression for viscoplastic strain to be a function of temperature and moisture through an Arrhenius relationship. However, an accurate description will require future experiments to better characterize the effects of environment on both the viscoplastic and non-linear viscoelastic behavior. Comparison of experiments and simulations of tensile experiments subjected to small uniaxial stress and hygral or thermal cycles confirmed the previous observation and indicated that the onset of non-linearity also depends on the hygrothermal environment.

In the future, experiments should be performed across the range of environments expected during fuel cell operation to characterize the environmental dependence of the non-linear viscoelastic and viscoplastic behavior. Once this is done, the UMAT developed in the present work can be modified and used to perform simulations of time-varying temperature, moisture, stress, and/or strain profiles. This will aid in the evaluation of PEMs and advance PEMFC technology development.

6.2. Comparison to Models in Literature

In comparison with other constitutive models published in the literature for modeling PEM materials [89], [92], [94], the present work offers several benefits. For instance, the model developed in the present work exhibits a clear transition from linear viscoelastic behavior to non-linear viscoelastic behavior, and the linear viscoelastic equations are much simpler than their non-linear counterparts. This causes the simulations to run more quickly in the linear viscoelastic region. Similarly, the use of creep and recovery experiments to develop the constitutive equation clearly demonstrates the need for a non-linear time dependent permanent strain expression, which in the present work has been referred to as ‘viscoplastic’. Were a similar analysis to be performed on another material, a few simple creep and

recovery experiments would indicate the significance of both non-linear viscoelasticity and viscoplasticity.

Another benefit of the current work is the applicability of TTSP and TMSP. These techniques have been very useful for describing the response of PEM materials in the linear viscoelastic region, so it is desirable to employ them for non-linear analyses as well. However, it should be noted that the full environmental dependence of the PFCB/PVDF blend was not captured by TTMSP alone, and that the alternative techniques found in literature [89] , [92], [94] were able to express environmental dependence of the PEM response more adequately. For this reason, further testing should be performed on the PFCB/PVDF material to extend its range of application to various environmental conditions.

Finally, the current work clearly captures the material response during recovery and subsequent reloading, for instance, from the multistep creep validation experiments. Some of the literature validates the recovery and reloading response of the PEM materials [89], but others do not [92], [94]. Because the stresses in an operating fuel cell are constantly changing, both increasing and decreasing, this is an important effect to capture.

6.3. Recommendations for Future Work

The present work used uniaxial creep and recovery experiments to develop the constitutive model parameters. However, stress relaxation experiments are more representative of the loading conditions in an operating fuel cell. Thus, it might be more appropriate to develop the model from stress relaxation experiments. For the non-linear viscoelastic constitutive expression, this is easily done. Two-step stress relaxation experiments may be used to determine the linear viscoelastic relaxation modulus and strain-dependent non-linear parameters. However, the viscoplastic response would be more challenging to characterize. In a stress relaxation experiment, viscoelastic and viscoplastic components of stress act simultaneously throughout the experiment. This would make it difficult to determine an appropriate expression for viscoplastic strain, if such an expression was necessary. It would be best to perform several creep and recovery experiments to provide insight into the stress and time dependence of viscoplastic behavior, develop an expression based on those results, and then determine the parameter values for the constitutive model from both the stress relaxation and creep and recovery experiments.

For someone interested in repeating the present work with a different material, the characterization and validation experiments would need to be performed with that material and appropriate parameter values determined for the constitutive equation. The uniaxial creep and recovery experiments performed in this work to characterize the PFCB/PVDF material took 62,800 machine hours to complete, not counting experiments which were unusable. (For instance, the 8MPa experiments during which the true stress was not constant.) The uniaxial validation experiments took another 12,000 hours of machine operating time. The Poisson's ratio experiments took 3,000 hours and the blister experiments 13200 hours. (These times would decrease considerably if the six-hour pretreatment on each specimen was not necessary.)

After the completion of the creep and recovery development experiments, the linear viscoelastic region of response should be identified, for instance, from an isochronous plot. Experiments in the linear viscoelastic region should be used to determine the linear viscoelastic creep compliance. During this stage, care should be taken to estimate how much viscoplastic strain remains in the material at the end of recovery, if any. An expression should then be selected to capture that behavior. Then, the Mathematica program may be used to determine parameter values for both the non-linear viscoelastic parameters and viscoplastic parameters. This stage of the analysis may take several days, as it will take some time for the analyst to develop an understanding of the balance between various parameters and investigate various parameter sets which describe the development data equally well. The Poisson's ratio experiments can then be used to determine the time dependence of Poisson's ratio and compute the shear and bulk compliances of the new material.

Once a parameter set is selected, it should take no more than a day or two to format it appropriately for use with the UMAT in Abaqus. If a different constitutive expression is developed for viscoplastic behavior, the UMAT should be modified to include the recursive form of that expression. An input file for the finite element geometry should then be generated with material properties (parameter values) in the appropriate format. Multistep simulations with time hardening and strain hardening versions of the recursive viscoplastic expression should be compared with multistep creep and recovery experiments to determine which technique is more appropriate. At this point, the analyst will have completed the procedures outlined in this document, with a total time investment of 1500 hours of experimental time and approximately 100 additional hours of analytical time. Some of the experiments could be performed simultaneously since they use different instruments, and most of the analysis may be performed while validation experiments are being performed. In total, this process would take a little over three months.

Additional multidimensional experiments to improve the equivalent plastic strain expression would likely take several weeks, as would the experimental characterization of the environmental dependence of the non-linear viscoelastic and viscoplastic parameters. Analysis of these experiments would take several weeks as well, adding two or three months to the time necessary to develop this constitutive expression for a different material. However, this additional work would expand the applicability of the model, making it useful in the evaluation of PEMs and advancement PEMFC technology development through the ability to simulate the mechanical response of PEMS under biaxial constraint and time varying environmental conditions, as exist in an operating fuel cell.

7. References

[1] Papageorgopoulos, D., 2012, "2012 Annual Progress Report," U. S. D. o. Energy, ed.
[2] DOE, 2011, "Progress and Accomplishments in Hydrogen and Fuel Cells " Energy Efficiency and Renewable Energy Information Center, D. o. Energy, ed.
[3] Li, Y., Dillard, D., Lai, Y.-H., Case, S., Ellis, M., Budinski, M., and Gittleman, C., 2011, "Experimental Measurement of Stress and Strain in Nafion Membrane during Hydration Cycles," Journal of the Electrochemical Society, 159(2), p. 12.
[4] Rama, P., Chen, R., and Andrews, J., 2008, "A review of performance degradation and failure modes for hydrogen-fuelled polymer electrolyte fuel cells," Proceedings of the Institution of Mechanical Engineers, Part A: Journal of Power and Energy, 222(5), pp. 4214-4441.
[5] Scholta, J., Rohland, B., Trapp, V., and Focken, U., 1999, "Investigations on novel low-cost graphite composite bipolar plates," Journal of Power Sources, 84(2), pp. 231-234.
[6] Davies, D. P., Adcock, P. L., Turpin, M., and Rowen, S. J., 2000, "Bipolar plate materials for solid polymer fuel cells," Journal of Applied Electrochemistry, 30(1), pp. 101-105.
[7] de Bruijn, F. A., Dam, V. A. T., and Janssen, G. J. M., 2008, "Review: Durability and Degradation Issues of PEM Fuel Cell Components," Fuel Cells, 8(1), pp. 3-22.
[8] Makkus, R. C., Janssen, A. H. H., de Bruijn, F. A., and Mallant, R. K. A. M., 2000, "Use of stainless steel for cost competitive bipolar plates in the SPFC," Journal of Power Sources, 86(1-2), pp. 274-282.
[9] Davies, D. P., Adcock, P. L., Turpin, M., and Rowen, S. J., 2000, "Stainless steel as a bipolar plate material for solid polymer fuel cells," Journal of Power Sources, 86(1-2), pp. 237-242.
[10] Silva, R. F., Franchi, D., Leone, A., Pilloni, L., Masci, A., and Pozio, A., 2006, "Surface conductivity and stability of metallic bipolar plate materials for polymer electrolyte fuel cells," Electrochimica Acta, 51(17), pp. 3592-3598.
[11] Schmittinger, W., and Vahidi, A., 2008, "A review of the main parameters influencing long-term performance and durability of PEM fuel cells," Journal of Power Sources, 180(1), pp. 1-14.
[12] von Ganski, A., Muller, A., Kauranen, P., and Hell, B., 2006, "Injection moulding of graphite composite bipolar plates," Journal of Power Sources, 154(2), pp. 467-471.
[13] Zhang, S., Yuan, X., Wang, H., Mérida, W., Zhu, H., Shen, J., Wu, S., and Zhang, J., 2009, "A review of accelerated stress tests of MEA durability in PEM fuel cells," International Journal of Hydrogen Energy, 34(1), pp. 388-404.
[14] Gurau, V., Bluemle, M. J., De Castro, E. S., Yu-Min, T., Mann, J. A., Jr., and Zawodzinski, T. A., Jr., 2006, "Characterization of transport properties in gas diffusion layers for proton exchange membrane fuel cells," Journal of Power Sources, 160(2), pp. 1156-1162.
[15] Lin, G., and Van Nguyen, T., 2005, "Effect of thickness and hydrophobic polymer content of the gas diffusion layer on electrode flooding level in a PEMFC," Journal of the Electrochemical Society, 152(10), pp. A1942-A1948.
[16] Bevers, D., Rogers, R., and von Bradke, M., 1996, "Examination of the influence of PTFE coating on the properties of carbon paper in polymer electrolyte fuel cells," Journal of Power Sources, 63(2), pp. 193-201.
[17] St-Pierre, J., Wilkinson, D. P., Knights, S., and Bos, M. L., 2000, "Relationships between water management, contamination and lifetime degradation in PEFC," Journal of New Materials for Electrochemical Systems, 3(2), pp. 99-106.
[18] Schulze, M., Wagner, N., Kaz, T., and Friedrich, K. A., 2007, "Combined electrochemical and surface analysis investigation of degradation processes in polymer electrolyte membrane fuel cells," Electrochimica Acta, 52(6), pp. 2328-2336.

[19] Ferreira, P. J., la O, G. J., Shao-Horn, Y., Morgan, D., Makharia, R., Kocha, S., and Gasteiger, H. A., 2005, "Instability of Pt/C electrocatalysts in proton exchange membrane fuel cells," Journal of the Electrochemical Society, 152(11), pp. 2256-2271.
[20] Xie, J., Wood Iii, D. L., Wayne, D. M., Zawodzinski, T. A., Atanassov, P., and Borup, R. L., 2005, "Durability of PEFCs at high humidity conditions," Journal of the Electrochemical Society, 152(1), pp. A104-A113.
[21] Xie, J., Wood, D. L., More, K. L., Atanassov, P., and Borup, R. L., 2005, "Microstructural changes of membrane electrode assemblies during PEFC durability testing at high humidity conditions," Journal of the Electrochemical Society, 152(5), pp. 1011-1020.
[22] Guilminot, E., Corcella, A., Chatenet, M., Maillard, F., Charlot, F., Berthome, G., Iojoiu, C., Sanchez, J. Y., Rossinot, E., and Claude, E., 2007, "Membrane and active layer degradation upon PEMFC steady-state operation," Journal of the Electrochemical Society, 154(11), pp. B1106-B1114.
[23] Borup, R. L., Davey, J. R., Garzon, F. H., Wood, D. L., and Inbody, M. A., 2006, "PEM fuel cell electrocatalyst durability measurements," Journal of Power Sources, 163(1 SPEC. ISS.), pp. 76-81.
[24] Darling, R. M., and Meyers, J. P., 2005, "Mathematical model of platinum movement in PEM fuel cells," Journal of the Electrochemical Society, 152(1), pp. A242-A247.
[25] Kienitz, B., Baskaran, H., Zawodzinski Jr, T., and Pivovar, B., 2007, "A half cell model of steady state PEM fuel cell performance degradation under contamination by foreign cationic species," ECS Transactions, 11, pp. 777-788.
[26] Meyers, J. P., and Darling, R. M., 2006, "Model of carbon corrosion in PEM fuel cells," Journal of the Electrochemical Society, 153(8), pp. A1432-A1442.
[27] Zhang, J., Wang, H., Wilkinson, D. P., Song, D., Shen, J., and Liu, Z.-S., 2005, "Model for the contamination of fuel cell anode catalyst in the presence of fuel stream impurities," Journal of Power Sources, 147(1-2), pp. 58-71.
[28] La Conti, A. B., Hamadam, M., and McDonald, R. C., 2003, "Mechanisms of Membrane Degradation," Handbook of Fuel Cells: Fundamentals, Technology and Applications, W. Vielstich, A. Lamm, and H. Gasteiger, eds., Wiley, Chichester, pp. 647-662.
[29] Okada, T., 2003, "Effect of Ionic Contaminants," Handbook of Fuel Cells - Fundamentals, Technology and Applications, W. Vielstich, H. Gasteiger, and A. Lamm, eds., John Wiley and Sons, Ltd., pp. 627 - 646.
[30] Curtin, D. E., Lousenberg, R. D., Henry, T. J., Tangeman, P. C., and Tisack, M. E., 2004, "Advanced materials for improved PEMFC performance and life," Journal of Power Sources, 131(1-2), pp. 41-48.
[31] Lai, Y.-H., Mittelsteadt, C. K., Gittleman, C. S., and Dillard, D. A., 2009, "Viscoelastic Stress Analysis of Constrained Proton Exchange Membranes Under Humidity Cycling," Journal of Fuel Cell Science and Technology, 6(2), p. 021002.
[32] Lai, Y.-H., and Dillard, D., 2009, "Mechanical Durability Characterization and Modeling of Ionomeric Membranes," Handbook of Fuel Cells: Advances in Electrocatalysis, Materials, Diagnostics and Durability, W. Vielstich, A. Lamm, H. A. Gasteiger, and H. Yokokawa, eds., John Wiley & Sons, Chichester, England; Hoboken, N.J., pp. 403-419.
[33] Tang, Y., Santare, M., Karlsson, A., Cleghorn, S., and Johnson, W., 2006, "Stresses in proton exchange membranes due to hygro-thermal loading," Journal of Fuel Cell Science and Technology, 3, p. 6.
[34] Huang, X., Solasi, R., Zou, Y., Feshler, M., Reifsnider, K., Condit, D., Burlatsky, S., and Madden, T., 2006, "Mechanical endurance of polymer electrolyte membrane and PEM fuel cell durability," Journal of Polymer Science Part B: Polymer Physics, 44(16), pp. 2346-2357.
[35] DOE, 2007, "Fuel Cell Technologies Program Multi-Year Research, Development and Demonstration Plan," D. o. Energy, ed., pp. 3.4-1. 3.4-42.
[36] Garland, N. L., Benjamin, T. G., and Kopasz, J. P., 2007, "DOE fuel cell program: Durability technical targets and testing protocols," ECS Transactions, 11, pp. 923-931.

[37] Brinson, H. F., and Brinson, L. C., 2008, Polymer Engineering Science and Viscoelasticity: An Introduction, Springer, New York.
[38] Mauritz, K. A., and Moore, R. B., 2004, "State of Understanding of Nafion," Chemical Reviews, 104(10), pp. 4535-4586.
[39] Karnaukhov, V. G., 1978, "Nonlinear Theory of Thermoviscoelasticity for a Generalized Thermorheologically Simple Material," Prikladnaya Mekhanika, 14(1), pp. 16-24.
[40] Markovitz, H., 1975, "Superposition in Rheology," Polymer Science, 50(1), pp. 431-456.
[41] Patankar, K. A., Dillard, D. A., Case, S. W., Ellis, M. W., Lai, Y.-H., Budinski, M. K., and Gittleman, C. S., 2008, "Hygrothermal characterization of the viscoelastic properties of Gore-Select 57 proton exchange membrane," Mechanics of Time-Dependent Materials, 12(3), pp. 221-236.
[42] Finlay, K., A., 2012, "Characterization of Sulfonated Perfluorocyclobutane/Poly(Vinylidene Difluoride) (PFCB/PVDF) Blends for Use as Proton Exchange Membranes," PhD, Virginia Polytechnic Institutive and State University, Blacksburg.
[43] Borup, R., Meyers, J., Pivovar, B., Kim, Y. S., Mukundan, R., Garland, N., Myers, D., Wilson, M., Garzon, F., Wood, D., Zelenay, P., More, K., Stroh, K., Zawodzinski, T., Boncella, J., McGrath, J. E., Inaba, M., Miyatake, K., Hori, M., Ota, K., Ogumi, Z., Miyata, S., Nishikata, A., Siroma, Z., Uchimoto, Y., Yasuda, K., Kimijima, K.-i., and Iwashita, N., 2007, "Scientific Aspects of Polymer Electrolyte Fuel Cell Durability and Degradation," Chemical Reviews, 107(10), pp. 3904-3951.
[44] Alberti, G., Narducci, R., and Sganappa, M., 2008, "Effects of hydrothermal/thermal treatments on the water-uptake of Nafion membranes and relations with changes of conformation, counter-elastic force and tensile modulus of the matrix," Journal of Power Sources, 178(2), pp. 575-583.
[45] Kreuer, K.-D., Dippel, T., Meyer, W., and Maier, J., "Nafion membranes: Molecular diffusion, proton conductivity and proton conduction mechanism," MRS Proceedings, pp. 273-282.
[46] Wilkinson, D. P., and St-Pierre, J., 2003, "Durability," Handbook of Fuel Cells - Fundamentals, Technology and Applications, W. Vielstich, H. Gasteiger, and A. Lamm, eds., John Wiley & Sons, Ltd., pp. 611-626.
[47] Healy, J., Hayden, C., Xie, T., Olson, K., Waldo, R., Brundage, M., Gasteiger, H., and Abbott, J., 2005, "Aspects of the chemical degradation of PFSA ionomers used in PEM fuel cells," Fuel Cells, 5(2), pp. 302-308.
[48] Zhang, H., and Shen, P. K., 2012, "Recent Development of Polymer Electrolyte Membranes for Fuel Cells," Chemical Reviews, 112(5), pp. 2780-2832.
[49] Mathias, M. F., Makharia, R., Gasteiger, H. A., Conley, J. J., Fuller, T. J., Gittleman, C. J., Kocha, S. S., Miller, D. P., Mittelsteadt, C. K., Tao, X., Yan, S. G., and Yu, P. T., 2005, "Two fuel cell cars in every garage?," Electrochemical Society Interface, 14(3), pp. 24-35.
[50] Bahar, B., Cavalca, C., Cleghorn, S., Kolde, J., Lane, D., Murthy, M., and Rusch, G., 1999, "Effective selection and use of advanced membrane electrode power assemblies," Journal of New Materials for Electrochemical Systems, 2(3), pp. 179-182.
[51] Hickner, M. A., Ghassemi, H., Kim, Y. S., Einsla, B. R., and McGrath, J. E., 2004, "Alternative Polymer Systems for Proton Exchange Membranes (PEMs)," Chemical Reviews, 104(10), pp. 4587-4612.
[52] Watanabe, M., Uchida, H., Seki, Y., Emori, M., and Stonehart, P., 1996, "Self-humidifying polymer electrolyte membranes for fuel cells," Journal of the Electrochemical Society, 143(12), pp. 3847-3852.
[53] Antonucci, P. L., Arica, A. S., Cretae, P., Ramunni, E., and Antonucci, V., 1999, "Investigation of a direct methanol fuel cell based on a composite Nafion®-silica electrolyte for high temperature operation," Solid State Ionics, 125(1-4), pp. 431-437.
[54] Park, K. T., Jung, U. H., Choi, D. W., Chun, K., Lee, H. M., and Kim, S. H., 2008, "ZrO2-SiO2/Nafion composite membrane for polymer electrolyte membrane fuel cells operation at high temperature and low humidity," Journal of Power Sources, 177(2), pp. 247-253.

[55] Park, C. H., Lee, C. H., Guiver, M. D., and Lee, Y. M., 2011, "Sulfonated hydrocarbon membranes for medium-temperature and low-humidity proton exchange membrane fuel cells (PEMFCs)," Progress in Polymer Science, 36(11), pp. 1443-1498.
[56] Tang, H., Wan, Z., Pan, M., and Jiang, S. P., 2007, "Self-assembled Nafion-silica nanoparticles for elevated-high temperature polymer electrolyte membrane fuel cells," Electrochemistry Communications, 9(8), pp. 2003-2008.
[57] Pereira, F., Valle, K., Belleville, P., Morin, A., Lambert, S., and Sanchez, C., 2008, "Advanced mesostructured hybrid silica-nafion membranes for high-performance PEM fuel cell," Chemistry of Materials, 20(5), pp. 1710-1718.
[58] Chen, S. Y., Han, C. C., Tsai, C. H., Huang, J., and Chen-Yang, Y. W., 2007, "Effect of morphological properties of ionic liquid-templated mesoporous anatase TiO2 on performance of PEMFC with Nafion/TiO2 composite membrane at elevated temperature and low relative humidity," Journal of Power Sources, 171(2), pp. 363-372.
[59] Uchida, H., Ueno, Y., Hagihara, H., and Watanabe, M., 2003, "Self-humidifying electrolyte membranes for fuel cells," Journal of the Electrochemical Society, 150(1), pp. 57-62.
[60] Carbone, A., Casciola, M., Cavalaglio, S., Costantino, U., Ornelas, R., Fodale, I., Sacca, A., and Passalacqua, E., 2004, "Composite Nafion membranes based on PWA-zirconia for PEFCs operating at medium temperature," Journal of New Materials for Electrochemical Systems, 7(1), pp. 1-5.
[61] Alberti, G., and Casciola, M., 2003, "Composite membranes for medium-temperature PEM fuel cells," Annual Review of Materials Research, 33, pp. 129-154.
[62] Choi, P., Jalani, N. H., and Datta, R., 2005, "Thermodynamics and proton transport in Nafion," Journal of the Electrochemical Society, 152(8), pp. 1548-1554.
[63] Tang, H. L., Pan, M., and Wang, F., 2008, "A mechanical durability comparison of various perfluocarbon proton exchange membranes," Journal of applied polymer science, 109(4), pp. 2671-2678.
[64] Steck, A. E., and Stone, C., "Development of the BAM membrane for fuel cell applications," Proc. First International Symposium on New Materials for Fuel Cells and Modern Battery Systems, Ecole Polytech. Montreal, pp. 792-807.
[65] Hamrock, S. J., and Yandrasits, M. A., 2006, "Proton Exchange Membranes for Fuel Cell Applications," Polymer Reviews, Taylor & Francis Ltd, pp. 219-244.
[66] Dupuis, A.-C., 2011, "Proton exchange membranes for fuel cells operated at medium temperatures: Materials and experimental techniques," Progress in Materials Science, 56(3), pp. 289-327.
[67] Hae-Seung, L., Roy, A., Lane, O., Dunn, S., and McGrath, J. E., 2008, "Hydrophilic-hydrophobic multiblock copolymers based on poly(arylene ether sulfone) via low-temperature coupling reactions for proton exchange membrane fuel cells," Polymer, 49(3), pp. 715-723.
[68] McGrath, J. E., and Baird, D. G., 2010, "High Temperature, Low Relative Humidity, Polymer-type Membranes Based on Disulfonated Poly(arylene ether) Block and Random Copolymers Optionally Incorporating Protonic Conducting Layered Water Insoluble Zirconium Fillers," Technical Report of DOE Contract #DE-FG36-06G016038, p. 73.
[69] Roy, A., Hae-Seung, L., and McGrath, J. E., 2008, "Hydrocarbon based BPSH-BPS multiblock copolymers as novel proton exchange membranes," ECS Transactions, 6(26), pp. 1-7.
[70] Kim, D.-J., Chang, B.-J., Kim, J.-H., Lee, S.-B., and Joo, H.-J., 2008, "Sulfonated poly(fluorenyl ether) membranes containing perfluorocyclobutane groups for fuel cell applications," Journal of Membrane Science, 325(1), pp. 217-222.
[71] Kalaw, G. J. D., Wahome, J. A. N., Yuanqin, Z., Balkus, K. J., Jr., Musselman, I. H., Duck-Joo, Y., and Ferraris, J. P., 2013, "Perfluorocyclobutyl (PFCB)-based polymer blends for proton exchange membrane fuel cells (PEMFCs)," Journal of Membrane Science, 431, pp. 86-95.

[72] Guoqing, Q., Smith, D. W., Jr., and Benicewicz, B. C., 2009, "Synthesis and characterization of high molecular weight perfluorocyclobutyl-containing polybenzimidazoles (PFCB-PBI) for high temperature polymer electrolyte membrane fuel cells," Polymer, 50(16), pp. 3911-3916.
[73] Jiang, R., Fuller, T., Brawn, S., and Gittleman, C., 2013, "Perfluorocyclobutane and poly(vinylidene fluoride) blend membranes for fuel cells," Electrochimica Acta, 110(0), pp. 306-315.
[74] Peighambardoust, S. J., Rowshanzamir, S., and Amjadi, M., 2010, "Review of the proton exchange membranes for fuel cell applications," International Journal of Hydrogen Energy, 35(17), pp. 9349-9384.
[75] Devanathan, R., 2008, "Recent developments in proton exchange membranes for fuel cells," Energy & Environmental Science, 1(1), pp. 101-119.
[76] Gomadam, P. M., and Weidner, J. W., 2005, "Analysis of electrochemical impedance spectroscopy in proton exchange membrane fuel cells," International Journal of Energy Research, 29(12), pp. 1133-1151.
[77] Campbell, D., Pethrick, R. A., and White, J. R., 2000, Polymer Characterization: Physical Techniques, Stanley Thornes (Publishers) Ltd., Cheltenham.
[78] May, N. H., 2011, "A Morphological Study of PFCB-Ionomer/Poly(Vinylidene Fluoride) Copolymer Blends for Fuel Cell Applications," Master of Science, Virginia Polytechnic Institute and State University, Blacksburg.
[79] Grohs, J. R., Yongqiang, L., Dillard, D. A., Case, S. W., Ellis, M. W., Yeh-Hung, L., and Gittleman, C. S., 2010, "Evaluating the time and temperature dependent biaxial strength of Gore-Select series 57 proton exchange membrane using a pressure loaded blister test," Journal of Power Sources, 195(2), pp. 527-531.
[80] Grohs, J., 2009, "Analysis and Modeling of the Mechanical Durability of Proton Exchange Membranes Using Pressure-Loaded Blister Tests," Master of Science, Virginia Tech, Blacksburg.
[81] Li, Y., Dillard, D. A., Case, S. W., Ellis, M. W., Lai, Y.-H., Gittleman, C. S., and Miller, D. P., 2009, "Fatigue and creep to leak tests of proton exchange membranes using pressure-loaded blisters," Journal of Power Sources, 194(2), pp. 873-879.
[82] Vlassak, J. J., and Nix, W. D., 1992, "A new bulge test technique for the determination of Young's modulus and Poisson's ratio of thin films," Journal of Materials Research, 7(12), pp. 3242-3249.
[83] Silberstein, M. N., Pillai, P. V., and Boyce, M. C., 2011, "Biaxial elastic-viscoplastic behavior of Nafion membranes," Polymer, 52(2), pp. 529-539.
[84] Li, Y., Quincy, J. K., Case, S. W., Ellis, M. W., Dillard, D. A., Lai, Y.-H., Budinski, M. K., and Gittleman, C. S., 2008, "Characterizing the fracture resistance of proton exchange membranes," Journal of Power Sources, 185(1), pp. 374-380.
[85] Patankar, K., Dillard, D. A., Case, S. W., Ellis, M. W., Li, Y., Lai, Y.-H., Budinski, M. K., and Gittleman, C. S., 2009, "Characterizing fracture energy of proton exchange membranes using a knife slit test," Journal of Polymer Science Part B: Polymer Physics, 48(3), pp. 333-343.
[86] Gordon, A. R., Ellis, M. W., Dillard, D. A., Case, S., Moore, R., B., Li, Y., Lai, Y.-H., and Gittleman, C. S., "Characterization of the Fracture Energy of a PFCB/PVDF Polymer Electrolyte Fuel Cell Membrane Using a Knife Slit Test," Proc. ASME 2012 6th International Conference on Energy Sustainability and 10th Fuel Cell Science, Engineering and Technology Conference, ASME.
[87] Dillard, D., Li, Y., Grohs, J., Case, S., Ellis, M., Lai, Y.-H., Budinski, M., and Gittleman, C., 2009, "On the Use of Pressure-Loaded Blister Tests to Characterize the Strength and Durability of Proton Exchange Membranes," Journal of Fuel Cell Science and Technology, 6, p. 8.
[88] Kusoglu, A., Karlsson, A. M., Santare, M. H., Cleghorn, S., and Johnson, W. B., 2006, "Mechanical response of fuel cell membranes subjected to a hygro-thermal cycle," Journal of Power Sources, 161(2), pp. 987-996.
[89] Silberstein, M. N., and Boyce, M. C., 2010, "Constitutive modeling of the rate, temperature, and hydration dependent deformation response of Nafion to monotonic and cyclic loading," Journal of Power Sources, 195(17), pp. 5692-5706.

[90] Morris, D. R., and Sun, X., 1993, "Water-sorption and transport properties of Nafion 117 H," Journal of Applied Polymer Science, 50(8), pp. 1445-1452.
[91] Kusoglu, A., Karlsson, A. M., Santare, M. H., Cleghorn, S., and Johnson, W. B., 2007, "Mechanical behavior of fuel cell membranes under humidity cycles and effect of swelling anisotropy on the fatigue stresses," Journal of Power Sources, 170(2), pp. 345-358.
[92] Solasi, R., Zou, Y., Huang, X., and Reifsnider, K., 2008, "A time and hydration dependent viscoplastic model for polyelectrolyte membranes in fuel cells," Mechanics of Time-Dependent Materials, 12(1), pp. 15-30.
[93] Tang, Y., Karlsson, A. M., Santare, M. H., Gilbert, M., Cleghorn, S., and Johnson, W. B., 2006, "An experimental investigation of humidity and temperature effects on the mechanical properties of perfluorosulfonic acid membrane," Materials Science and Engineering A, 425(1-2), pp. 297-304.
[94] Khattra, N. S., Karlsson, A. M., Santare, M. H., Walsh, P., and Busby, F. C., 2012, "Effect of time-dependent material properties on the mechanical behavior of PFSA membranes subjected to humidity cycling," Journal of Power Sources, 214(0), pp. 365-376.
[95] Schapery, R. A., 1969, "On the characterization of nonlinear viscoelastic materials," Polymer Engineering and Science, 9(4), p. 16.
[96] Chailleux, E., and Davies, P., 2005, "A Non-Linear Viscoelastic Viscoplastic Model for the Behaviour of Polyester Fibres," Mechanics of Time-Dependent Materials, 9(2-3), pp. 147-160.
[97] Gerngross, T., Xu, Y., and Pellegrino, S., 2008, "Viscoelastic behaviour of pumpkin balloons," Advances in space research, 42(10), pp. 1683-1690.
[98] Levesque, M., Derrien, K., Baptiste, D., and Gilchrist, M., 2008, "On the development and parameter identification of Schapery-type constitutive theories," Mechanics of Time-Dependent Materials, 12(2), pp. 95-127.
[99] Haj-Ali, R. M., and Muliana, A. H., 2004, "Numerical finite element formulation of the Schapery non-linear viscoelastic material model," International Journal for Numerical Methods in Engineering, 59(1), pp. 25-45.
[100] Lai, J., and Bakker, A., 1995, "An integral constitutive equation for nonlinear plasto-viscoelastic behavior of high-density polyethylene," Polymer Engineering & Science, 35(17), pp. 1339-1347.
[101] Zapas, L. J., and Crissman, J. M., 1984, "Creep and recovery behaviour of ultra-high molecular weight polyethylene in the region of small uniaxial deformations," Polymer, 25(1), pp. 57-62.
[102] Kusoglu, A., Tang, Y., Lugo, M., Karlsson, A. M., Santare, M. H., Cleghorn, S., and Johnson, W. B., 2010, "Constitutive response and mechanical properties of PFSA membranes in liquid water," Journal of Power Sources, 195(2), pp. 483-492.
[103] Ogden, R. W., 1972, "Large deformation isotropic elasticity - on the correlation of theory and experiment for incompressible rubberlike solids," Proceedings of the Royal Society of London, Series A (Mathematical and Physical Sciences), 326(1567), pp. 565-584.
[104] Mooney, M., 1940, "Theory of large elastic deformation," Journal of Applied Physics, 11, pp. 582-592.
[105] Rivlin, R. S., 1948, "Large elastic deformations of isotropic materials. IV. Further developments of the general theory," Philosophical Transactions of the Royal Society of London. Series A (Mathematical and Physical Sciences), 241, pp. 379-397.
[106] Arruda, E. M., and Boyce, M. C., 1993, "Three-dimensional constitutive model for the large stretch behavior of rubber elastic materials," Journal of the Mechanics and Physics of Solids, 41(2), pp. 389-389.
[107] Silberstein, M. N., and Boyce, M. C., 2011, "Hygro-thermal mechanical behavior of Nafion during constrained swelling," Journal of Power Sources, 196(7), pp. 3452-3460.
[108] Drozdov, A. D., and Gupta, R. K., 2003, "Non-linear viscoelasticity and viscoplasticity of isotactic polypropylene," International Journal of Engineering Science, 41(20), pp. 2335-2361.

[109] Drozdov, A. D., 1999, "A constitutive model in linear thermoviscoelasticity of polymers based on the concept of cooperative relaxation," Continuum Mechanics and Thermodynamics, 11(3), pp. 193-216.
[110] Drozdov, A. D., and Christiansen, J. d., 2003, "Model for the viscoelastic and viscoplastic responses of semicrystalline polymers," Journal of Applied Polymer Science, 88(6), pp. 1438-1450.
[111] Drozdov, A. D., 2001, "A model for the viscoelastic and viscoplastic responses of glassy polymers," International Journal of Solids and Structures, 38(46-47), pp. 8285-8304.
[112] Drozdov, A. D., 1999, "Modelling volume recovery in glassy polymers," Mechanics Research Communications, 26(5), pp. 535-540.
[113] Yoon, W., and Huang, X., 2011, "A nonlinear viscoelastic/viscoplastic constitutive model for ionomer membranes in polymer electrolyte membrane fuel cells," Journal of Power Sources, 196(8), pp. 3933-3941.
[114] Zhang, C., and Moore, I. D., 1997, "Finite element modelling of inelastic deformation of ductile polymers," Geosynthetics international, 4(2), pp. 137-163.
[115] Tang, Y., Kusoglu, A., Karlsson, A. M., Santare, M. H., Cleghorn, S., and Johnson, W. B., 2008, "Mechanical properties of a reinforced composite polymer electrolyte membrane and its simulated performance in PEM fuel cells," Journal of Power Sources, 175(2), pp. 817-825.
[116] Li, Y., 2012, "Residual Stress Hygral Expansion Processed Results," J. May, ed., Personal Communication.
[117] 2007, "ARAMIS User Manual," GOM Optical Measuring Techniques.
[118] Tschoegl, N. W., Knauss, W. G., and Emri, I., 2002, "Poisson's Ratio in Linear Viscoelasticity – A Critical Review," Mechanics of Time-Dependent Materials, 6(1), pp. 3-51.
[119] Cerda, E., and Mahadevan, L., 2003, "Geometry and physics of wrinkling," Physical Review Letters, 90(7), pp. 074302-074301.
[120] Siuta, C. M., 2011, "Measuring Material Properties of Proton Exchange Membranes using Pressure Loaded Blister Testing and Digital Image Correlation," Master of Science, Virginia Polytechnic Institute and State University, Blacksburg.
[121] Batra, R. C., 2006, Elements of continuum mechanics, American Institute of Aeronautics and Astronautics, Reston, VA.
[122] Schapery, R. A., "Theory of nonlinear thermoviscoelasticity based on irreversible thermodynamics," Proc. 5th U.S. Nat. Cong. Appl. Mech, ASME, pp. 511-530.
[123] Schapery, R. A., 1964, "Application of thermodynamics to thermo-mechanical, fracture and birefringent phenomena in viscoelastic media," Journal of Applied Physics, 35(5), pp. 1451-1465.
[124] Tobolsky, A., and Eyring, H., 1943, "Mechanical properties of polymeric materials," Journal of Chemical Physics, 11, pp. 125-134.
[125] Kim, J.-S., and Muliana, A. H., 2010, "A combined viscoelastic viscoplastic behavior of particle reinforced composites," International Journal of Solids and Structures, 47(5), pp. 580-594.
[126] 2013, "Mathematica 9 Documentation," Wolfram Research, Inc.
[127] 2010, "Abaqus 6.10 Documentation," Dassault Systèmes.
[128] Lai, J., and Bakker, A., 1996, "3-D schapery representation for non-linear viscoelasticity and finite element implementation," Computational Mechanics, 18(3), pp. 182-191.
[129] Argon, A., 2013, "The Physics of Deformation and Fracture of Polymers," Cambridge University Press.
[130] Press, W. H., Teukolsky, S. A., Vetterling, W. T., and Flannery, B. P., 1992, Numerical Recipes in Fortran, Press Syndicate of the University of Cambridge, New York, NY.

Appendix A. Mathematica code used for parameter determination

The following excerpt demonstrates the definition of the creep and recovery simplification for the constitutive model and the formatting for fitting the parameter g_2.

```
σLVE=0.5;
σrec=0.006;
Paramsα={0.6,0.15,1.8}; (*acot eqtn*)
Paramsβ={1.0,0,0};(*1 always for acot eqtn*)
Paramsγ={1.0,0,0};(*1 always for acot eqtn*)
Paramsδ={1.0,0,0};(*1 always for acot eqtn*)
Paramsvp1={2.80*10^-5,1.15,0.6};(*ZC params*)
Paramsvp2={1.03*10^-5,0.6494,0.5792};(*TE params*)
D0i=0.003544;
Results={};

Prony={1*10^-10 ,0.000295432 ,0.000395899, 0.001971031
,0.001146411 ,0.004678574 ,8.04241*10^-06, 0.037973762
,3.55047*10^-09};
tau={5, 10, 100 ,1000 ,10000 ,30000, 100000, 300000, 1000000};


ΔD[t_,D1_,D2_,D3_,D4_,D5_,D6_,D7_,D8_,D9_]:=D1*(1-Exp[-
t/tau[[1]]])+D2*(1-Exp[-t/tau[[2]]])+D3*(1-Exp[-
t/tau[[3]]])+D4*(1-Exp[-t/tau[[4]]])+D5*(1-Exp[-
t/tau[[5]]])+D6*(1-Exp[-t/tau[[6]]])+D7*(1-Exp[-
t/tau[[7]]])+D8*(1-Exp[-t/tau[[8]]])+D9*(1-Exp[-t/tau[[9]]]);

g0[σcreep_,α1_,α2_,α3_]:=α1+α2*(1.570796-ArcTan[σcreep-α3]);
g0Range[α1_,α2_,α3_]:=Table[g0[σ,α1,α2,α3],{σ,0,15}];
startg0[α1_,α2_,α3_]:=α1+α2*(1.570796-ArcTan[0.51-α3]);

g1[σcreep_,β1_,β2_,β3_]:=β1+β2*(1.570796-ArcTan[σcreep-β3]);
g1Range[β1_,β2_,β3_]:=Table[g1[σ,β1,β2,β3],{σ,0,15}];
startg1[β1_,β2_,β3_]:=β1+β2*(1.570796-ArcTan[0.51-β3]);

g2[σcreep_,γ1_,γ2_,γ3_]:=γ1+γ2*(1.570796-ArcTan[σcreep-γ3]);
g2Range[γ1_,γ2_,γ3_]:=Table[g2[σ,γ1,γ2,γ3],{σ,0,15}];
startg2[γ1_,γ2_,γ3_]:=γ1+γ2*(1.570796-ArcTan[0.51-γ3]);

aσ[σcreep_,δ1_,δ2_,δ3_]:=δ1+δ2*(1.570796-ArcTan[σcreep-δ3]);
aσRange[δ1_,δ2_,δ3_]:=Table[aσ[σ,δ1,δ2,δ3],{σ,0,15}];
startaσ[δ1_,δ2_,δ3_]:=δ1+δ2*(1.570796-ArcTan[0.51-δ3]);

ϵve[t_,σcreep_,tswitch_,D0_,ΔD_,D1_,D2_,D3_,D4_,D5_,D6_,D7_,D8_,
D9_,g0_,g1_,g2_,aσ_,α1_,α2_,α3_,β1_,β2_,β3_,γ1_,γ2_,γ3_,δ1_,δ2_,
δ3_]:=If[t<=tswitch,
```

```
σcreep*g0[σcreep,α1,α2,α3]*D0+σcreep*g1[σcreep,β1,β2,β3]*g2[σcre
ep,γ1,γ2,γ3]*ΔD[(t/aσ[σcreep,δ1,δ2,δ3]),D1,D2,D3,D4,D5,D6,D7,D8,
D9],σrec*D0+σcreep*g2[σcreep,γ1,γ2,γ3]*ΔD[t-
tswitch+(tswitch/aσ[σcreep,δ1,δ2,δ3]),D1,D2,D3,D4,D5,D6,D7,D8,D9
]+(σrec-σcreep*g2[σcreep,γ1,γ2,γ3])*ΔD[t-
tswitch,D1,D2,D3,D4,D5,D6,D7,D8,D9]];

ϵvp[t_,σcreep_,tswitch_,A1_,b1_,c1_,A2_,b2_,c2_]:=If[σcreep<=4,I
f[t<=tswitch,
    (A1*(σcreep)^b1*(t)^c1),
    (A1*(σcreep)^b1*(tswitch)^c1)+(A1*(σrec)^b1*((t)^c1-
(tswitch)^c1))],If[t<=tswitch,
    (A2*Exp[(σcreep)*b2]*(t)^c2),
    (A2*Exp[(σcreep)*b2]*(tswitch)^c2)+(A1*(σrec)^b1*((t)^c1-
(tswitch)^c1))]];

ϵ[t_,σcreep_,tswitch_,D0_,ΔD_,D1_,D2_,D3_,D4_,D5_,D6_,D7_,D8_,D9
_,g0_,g1_,g2_,aσ_,α1_,α2_,α3_,β1_,β2_,β3_,γ1_,γ2_,γ3_,δ1_,δ2_,δ3
_,A1_,b1_,c1_,A2_,b2_,c2_]:=ϵve[t,σcreep,tswitch,D0,ΔD,D1,D2,D3,
D4,D5,D6,D7,D8,D9,g0,g1,g2,aσ,α1,α2,α3,β1,β2,β3,γ1,γ2,γ3,δ1,δ2,δ
3]+ϵvp[t,σcreep,tswitch,A1,b1,c1,A2,b2,c2]-
2*ϵvp[t,σcreep,tswitch,A1,b1,c1,A2,b2,c2]*ϵve[t,σcreep,tswitch,D
0,ΔD,D1,D2,D3,D4,D5,D6,D7,D8,D9,g0,g1,g2,aσ,α1,α2,α3,β1,β2,β3,γ1
,γ2,γ3,δ1,δ2,δ3];

ϵrecover[t_,σcreep_,tswitch_,D0_,ΔD_,D1_,D2_,D3_,D4_,D5_,D6_,D7_,D8_,D
9_,g0_,g1_,g2_,aσ_,α1_,α2_,α3_,β1_,β2_,β3_,γ1_,γ2_,γ3_,δ1_,δ2_,δ3_,A1_
,b1_,c1_,A2_,b2_,c2_]:=If[t<=tswitch+1000,1*10^-
7,ϵ[t,σcreep,tswitch,D0,ΔD,D1,D2,D3,D4,D5,D6,D7,D8,D9,g0,g1,g2,aσ,α1,α
2,α3,β1,β2,β3,γ1,γ2,γ3,δ1,δ2,δ3,A1,b1,c1,A2,b2,c2]]

(*import data*)
Clear[timelistall,strainlistall,stresslistall,tswitchlistall,fit
dataall,straindataall];
Clear[fitdataallplots,straindataallplots];

timelistall=Flatten[Import["311time.txt","List"]];
strainlistall=Flatten[Import["311strainall.txt","List"]];
strainrecoverall=Flatten[Import["311strainrecover.txt","List"]];
stresslistall=Flatten[Import["311stress.txt","List"]];
tswitchlistall=Flatten[Import["311tswitch.txt","List"]];
weightlistall=Flatten[Import["311weight.txt","List"]];
fitdataall=Transpose[{timelistall,stresslistall,tswitchlistall,s
trainlistall}];
straindataall=Transpose[{timelistall,strainlistall}];
```

```
fitdatarecoverall=Transpose[{timelistall,stresslistall,tswitchli
stall,strainrecoverall}];
straindatarecoverall=Transpose[{timelistall,strainrecoverall}];

timelistplots=Flatten[Import["311timeplots.txt","List"]];
strainalllistplots=Flatten[Import["311strainallplots.txt","List"
]];
strainrecoverlistplots=Flatten[Import["311strainrecoverplots.txt
","List"]];
stresslistplots=Flatten[Import["311stressplots.txt","List"]];
tswitchlistplots=Flatten[Import["311tswitchplots.txt","List"]];
fitdataallplots=Transpose[{timelistplots,stresslistplots,tswitch
listplots,strainalllistplots}];
straindataallplots=Transpose[{timelistplots,strainalllistplots}]
;
fitdatarecoverplots=Transpose[{timelistplots,stresslistplots,tsw
itchlistplots,strainrecoverlistplots}];
straindatarecoverplots=Transpose[{timelistplots,strainrecoverlistplots
}];

(*parameter estimation for g2*)

inc=1000;

Paramsα={NonProny[[1]],NonProny[[2]],NonProny[[3]]};
Paramsβ={NonProny[[4]],NonProny[[5]],NonProny[[6]]};
Paramsγ={NonProny[[7]],NonProny[[8]],NonProny[[9]]};
Paramsδ={NonProny[[10]],NonProny[[11]], NonProny[[12]]};
Paramsvp1={NonProny[[13]],NonProny[[14]], NonProny[[15]]};
Paramsvp2={NonProny[[16]],NonProny[[17]], NonProny[[18]]};

TotalFit=NonlinearModelFit[fitdataall,{ϵrecover[t,σcreep,tswitch
,D0i,ΔD,Prony[[1]],Prony[[2]],Prony[[3]],Prony[[4]],Prony[[5]],P
rony[[6]],Prony[[7]],Prony[[8]],Prony[[9]],g0,g1,g2,aσ,Paramsα[[
1]],Paramsα[[2]],Paramsα[[3]],Paramsβ[[1]],Paramsβ[[2]],Paramsβ[
[3]],γ1,γ2,γ3,Paramsδ[[1]],Paramsδ[[2]],Paramsδ[[3]],Paramsvp1[[
1]],Paramsvp1[[2]],Paramsvp1[[3]],Paramsvp2[[1]],Paramsvp2[[2]],
Paramsvp2[[3]]],
    (*nlve constraints*)
    Min[g2Range[γ1,γ2,γ3]]≥
0.001,startg2[γ1,γ2,γ3]≥0.98,startg2[γ1,γ2,γ3]≤1.02,
       (*nlve initial values*)
{{γ1,Paramsγ[[1]]},{γ2,Paramsγ[[2]]},{γ3,Paramsγ[[3]]}},{t,σcree
p,tswitch},Weights→weightlistall,MaxIterations→inc,StepMonitor:→E
xport["Results.xls",AppendTo[Results,Flatten[{j++,"g2,asigma",Su
m[(strainlistall[[i]]-
ϵ[timelistall[[i]],stresslistall[[i]],tswitchlistall[[i]],D0i,ΔD
,Prony[[1]],Prony[[2]],Prony[[3]],Prony[[4]],Prony[[5]],Prony[[6
```

```
]],Prony[[7]],Prony[[8]],Prony[[9]],g0,g1,g2,aσ,Paramsα[[1]],Par
amsα[[2]],Paramsα[[3]],Paramsβ[[1]],Paramsβ[[2]],Paramsβ[[3]],γ1
,γ2,γ3,δ1,δ2,δ3,Paramsvp1[[1]],Paramsvp1[[2]],Paramsvp1[[3]],Par
amsvp2[[1]],Paramsvp2[[2]],Paramsvp2[[3]]])^2,{i,1,Length[timeli
stplots]}],D0i,Prony,Paramsα[[1]],Paramsα[[2]],Paramsα[[3]],Para
msβ[[1]],Paramsβ[[2]],Paramsβ[[3]],γ1,γ2,γ3,Paramsδ[[1]],Paramsδ
[[2]],Paramsδ[[3]],Paramsvp1[[1]],Paramsvp1[[2]],Paramsvp1[[3]],
Paramsvp2[[1]],Paramsvp2[[2]],Paramsvp2[[3]]}]]]];

(*reset initial values to bestfit values*)
Paramsγ={Params[[1,2]],Params[[2,2]],Params[[3,2]]};
Paramsδ={Params[[4,2]],Params[[5,2]],Params[[6,2]]};
NonProny={Paramsα[[1]],Paramsα[[2]],Paramsα[[3]],Paramsβ[[1]],Pa
ramsβ[[2]],Paramsβ[[3]],Paramsγ[[1]],Paramsγ[[2]],Paramsγ[[3]],P
aramsδ[[1]],Paramsδ[[2]],Paramsδ[[3]],Paramsvp1[[1]],Paramsvp1[[
2]],Paramsvp1[[3]],Paramsvp2[[1]],Paramsvp2[[2]],Paramsvp2[[3]]}
;

(*Fit Results*)
Params=TotalFit["BestFitParameters"]
RSquared=TotalFit["AdjustedRSquared"]
TSS=Sum[(strainlistall[[i]]-
ϵ[timelistall[[i]],stresslistall[[i]],tswitchlistall[[i]],D0i,ΔD
,Prony[[1]],Prony[[2]],Prony[[3]],Prony[[4]],Prony[[5]],Prony[[6
]],Prony[[7]],Prony[[8]],Prony[[9]],g0,g1,g2,aσ,Paramsα[[1]],Par
amsα[[2]],Paramsα[[3]],Paramsβ[[1]],Paramsβ[[2]],Paramsβ[[3]],Pa
ramsγ[[1]],Paramsγ[[2]],Paramsγ[[3]],Paramsδ[[1]],Paramsδ[[2]],P
aramsδ[[3]],Paramsvp1[[1]],Paramsvp1[[2]],Paramsvp1[[3]],Paramsv
p2[[1]],Paramsvp2[[2]],Paramsvp2[[3]]])^2,{i,1,Length[timelistpl
ots]}]

Results=AppendTo[Results,Flatten[{inc,"g2,asigma",TSS,D0i,Prony,
NonProny}]];
Export["Results.xls",Results];
EmitSound[Sound[SoundNote[]]]
```

Appendix B. Iterative process for parameter determination

This appendix demonstrates the process used for parameter determination after initial parameter estimates were made.

Begin by considering the model which results from the initial parameter estimates. That is, the instantaneous compliance, elastic non-linear parameter g_0, linear viscoelastic Prony series coefficients, and viscoplastic parameter values determined by the process described in Chapter 4, which are recorded in Table B 1 below. A simulation of creep and recovery for each stress is compared to the appropriate experiment in Figure B 1, in which the lines represent the model from the initial parameter set and the points the experimental data.

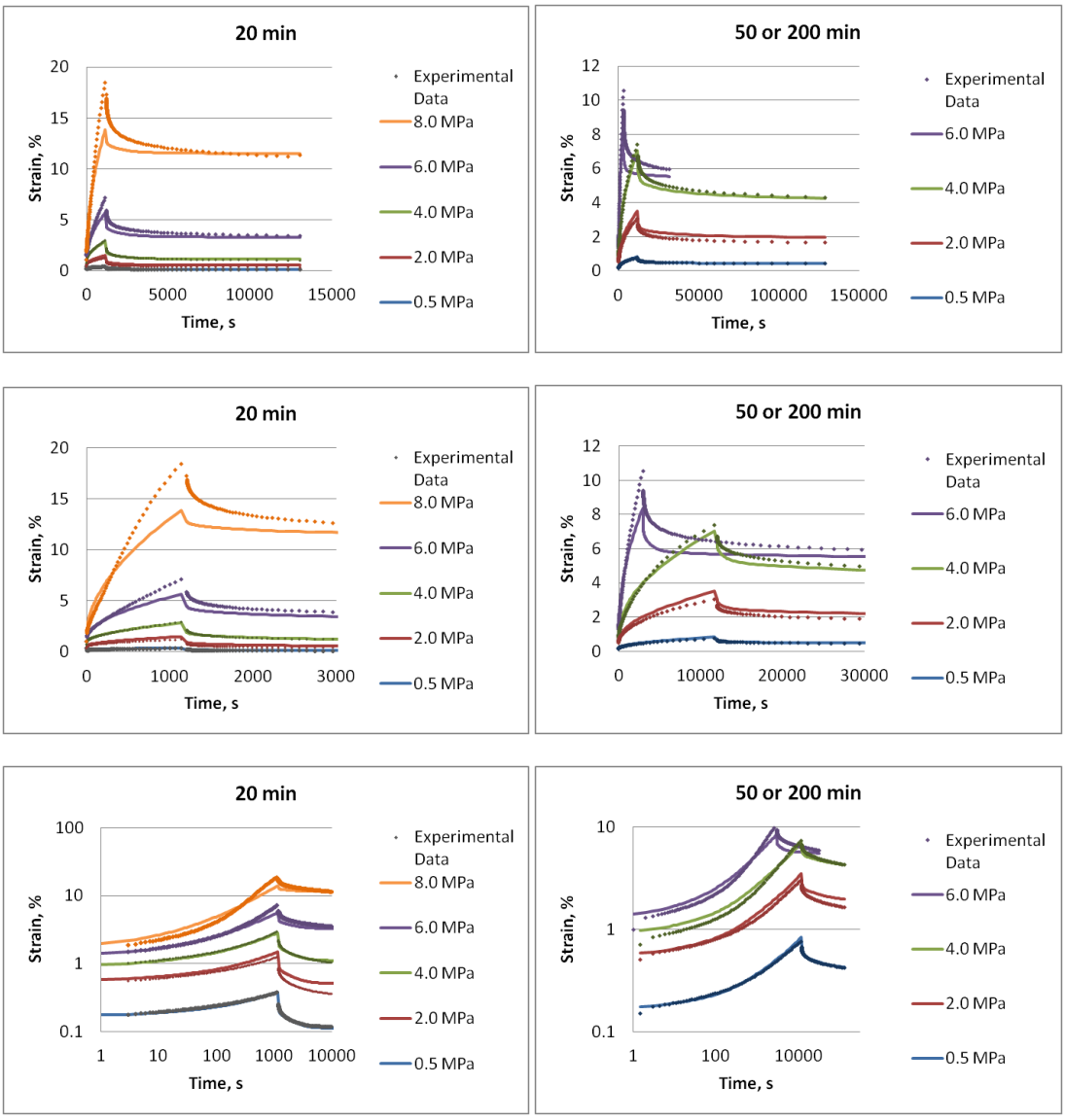

Figure B 1. Initial model, 20 min (left), longer (right); a) linear-linear axes, full time range, b) linear-linear axes, zoomed in on creep region, c) log-log axes, full time range.

Table B 1. The parameter values referred to as 'initial parameter set' in the present document. These values are obtained from independent estimates of linear viscoelastic behavior, non-linear elasticity and long-term viscoplastic behavior.

D0 [1/MPa]	0.003544
v0 [ND]	0.35

Di [1/MPa]	τi [s]
8.65E-05	5
8.32E-05	10
9.91E-05	100
1.92E-04	300
2.16E-03	1000
1.30E-03	10000
1.98E-03	30000
1.29E-02	100000
1.22E-02	1000000

	x1	x2	x3
g0 [ND]	0.450	0.220	1.600
g1 [ND]	1.000	0.000	0.000
g2 [ND]	1.000	0.000	0.000
asigma [ND]	1.000	0.000	0.000

	A	b	c
ZC [m/m]	2.00E-05	1.000	0.600
TE [m/m]	2.61E-06	0.681	0.737

Figure B 2 shows the same information as Figure B 1 but in a different format. Here, the list of experimental strains is plotted with the list of strains computed from the initial parameters. The first 5 sets are the 20 minute experiments in increasing stress order. The 6th set is the 6 MPa, 50 minute experiment and the final three are the 200 minute experiments in increasing stress order.

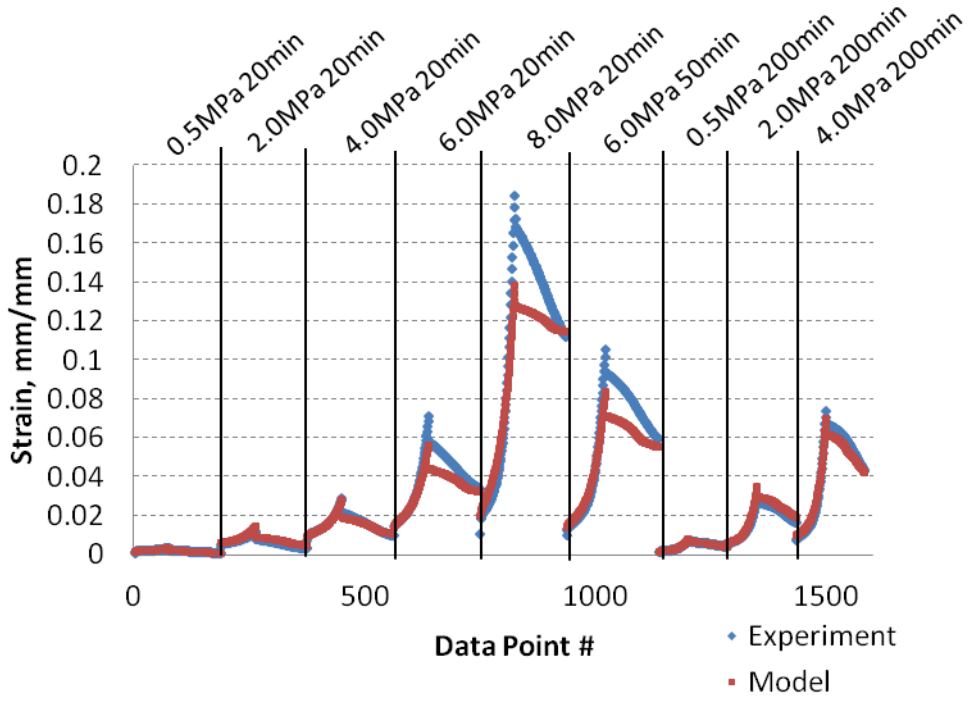

Figure B 2. Plots comparing experimental strains for all creep and recovery tests (blue) to the strains predicted by the initial parameter estimates (red).

As expected, the model closely matches the experimental results in the low stress (0.5 MPa) region. However, as stress increases, the model becomes increasingly inaccurate. The purpose of the parameter determination process is to modify the initial parameter values to improve the quality of the fitted model. Due to the large number of parameters available, only a few are varied simultaneously, and engineering judgment is used to select which parameters to vary.

For instance, in Figure B 1 it can be seen that the long-term recovery response reasonably fits experiments at all stress levels; that is, the strains at the end of recovery are comparable between model and experiments. This region of behavior is primarily governed by the viscoplastic parameters, assuming strain recovery has nearly stopped by the end of the experiment, so significantly modifying the viscoplastic parameters would decrease rather than increase the quality of the fitted model in this region. The agreement at very short times has analogous implications for the values of the elastic compliance and g_0.

Similarly, changing the linear viscoelastic Prony series coefficients would decrease the quality of the model at low stresses, even though it might improve the model at high stresses. The only exceptions to this are the Prony coefficients which correspond to very large characteristic times. The experiments used to determine the Prony coefficients did not extend the full time range, so it is possible that changing the last few Prony coefficients may improve the model. This is because the effect that a_σ has on the time scale of the material. High stress applications essentially accelerate the material response, an effect which is captured by a_σ. Therefore, Prony coefficients which did not affect the model response for low stresses may be very influential at high stresses as the coefficients now act much sooner in the experimental time scale.

These observations suggest that improving the model will most likely involve changing the initial values for the long-time Prony series coefficients and the remaining non-linear viscoelastic parameters, g_1, g_2, and a_σ. All three non-linear parameters are active during creep, but g_2 and a_σ are active during recovery. This means that recovery is the simplest region of the experimental response left to fit, so g_2 and a_σ are now considered.

First consider how g_2 and a_σ alter the model response independently. In Chapter 4, increasing and decreasing functions of g_2 were demonstrated to soften and stiffen the model response, respectively. Because the model in Figure B 2 underpredicts strain during large stresses, a softening g_2 effect is desired. Similarly, it was shown that an a_σ function had to have a negative slope and that values of a_σ closer to zero resulted in softer material behavior. Therefore, constraints are applied to the parameter determination algorithm which force g_2 to increase and a_σ to decrease with increasing stress.

The parameter determination algorithm in Mathematica may be formulated to vary g_2 and a_σ simultaneously or separately. Figure B 3 demonstrates the effect of varying these parameters simultaneously and independently. In each figure below, the fitting algorithm was allowed 500 iterations per parameter, and in each case the original parameter values were those from Figure B 1, in which both g_2 and a_σ were unity for all values of applied stress. For comparison purposes, the total sum of squared

residuals (TSS) is computed for each trial parameter set. The TSS of the model from the initial parameter set is 0.1225, so any value smaller than that indicates an improvement over the initial parameter set.

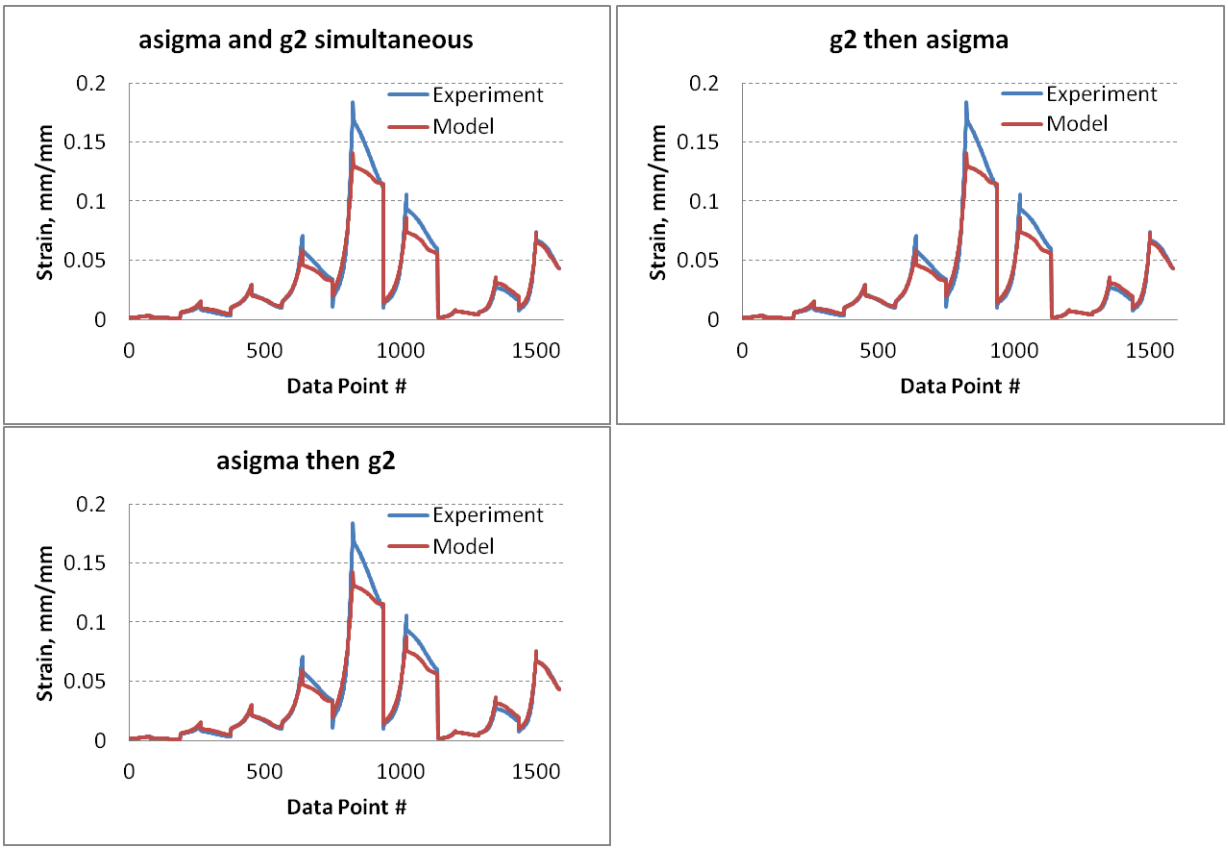

Figure B 3. 500 iterations of a) g_2 and a_σ (TSS=0.1038), b) g_2 then a_σ (TSS=0.1034), c) a_σ then g_2 (TSS=0.0937).

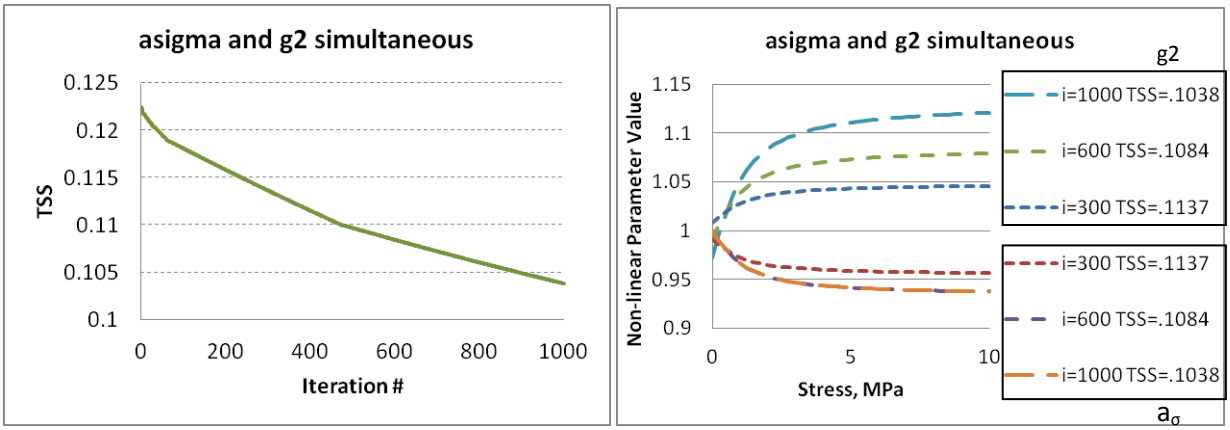

Figure B 4. Demonstration of TSS converging while algorithm is running (left). Intermediate results during algorithm progress, legend indicates parameter, number of iterations completed and current TSS (right).

Although it is clear from Figure B 4 that the algorithm consistently moves toward improved functions for the non-linear parameters, the progress of the algorithm is extremely slow. Rather than continue to use the algorithm to improve upon the initial parameter set, in which g_1, g_2 and a_σ were unity for all values

of stress, it is more useful to select a starting point which already contains some non-linearity. For instance, consider the effect of the g_2 function in Figure B 5. By forcing g_2 to increase with stress, the discrepancy noted at peak strain values is decreased. This demonstrates that the effect of g_2 on creep and recovery tests is to shift the peak strains to larger values while leaving the strains which occur early during creep or near the end of recovery unchanged. Clearly, these parameter sets are superior to any obtained by the parameter estimation algorithm, even after 1000 iterations, from the initial parameter set. The first function has a TSS of 0.0531 and the second function has a TSS of 0.0506. This indicates that function 2 is more appropriate than function 1. Note that modifying the g_2 function involves changing the three parameters $g_2(1)$, $g_2(2)$, $g_2(3)$ in the arccotangent equation which is used to define g_2 as a function of stress. Likewise, changing the a_σ function involves changing the parameters $a_\sigma(1)$, $a_\sigma(2)$ and $a_\sigma(3)$. For simplicity, changes to the parameters in the arccotangent equation associated with g_2 will be denoted as "changing the g_2 function".

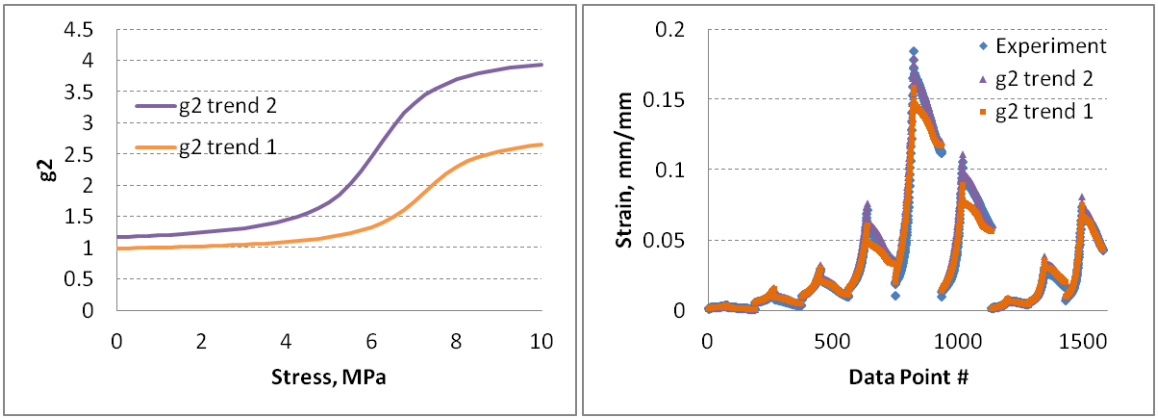

Figure B 5. Example of the impact of g_2 functions on model results.

Similarly, Figure B 6 demonstrates two a_σ functions. Unlike g_2, which alters the slope of the model near the peak stress values, a_σ changes both the slope and the overall magnitude. This shifts the entire strain curve upward at higher stresses. Although this results in improvement over the initial parameter set, (Function 1 results in a TSS of 0.0406 and function 2 has a TSS of 0.0626), it can be seen that a_σ alone will not be sufficient to obtain a reasonable model because the improvements at the peak strain are offset by increased error at short times. Note that these functions are applied with all other non-linear parameters equal to their initial values. That is, neither of the g_2 functions in the previous figure is applied here. Recall that Figure B 4 demonstrated the effect of using the parameter estimation algorithm to search for g_2 and a_σ functions simultaneously, and that the results of running the algorithm for 1000 iterations indicated that both non-linear parameters would likely be useful in improving the model fit. Therefore, a_σ and g_2 will both be applied, but it is useful to understand the effect of each terms separately.

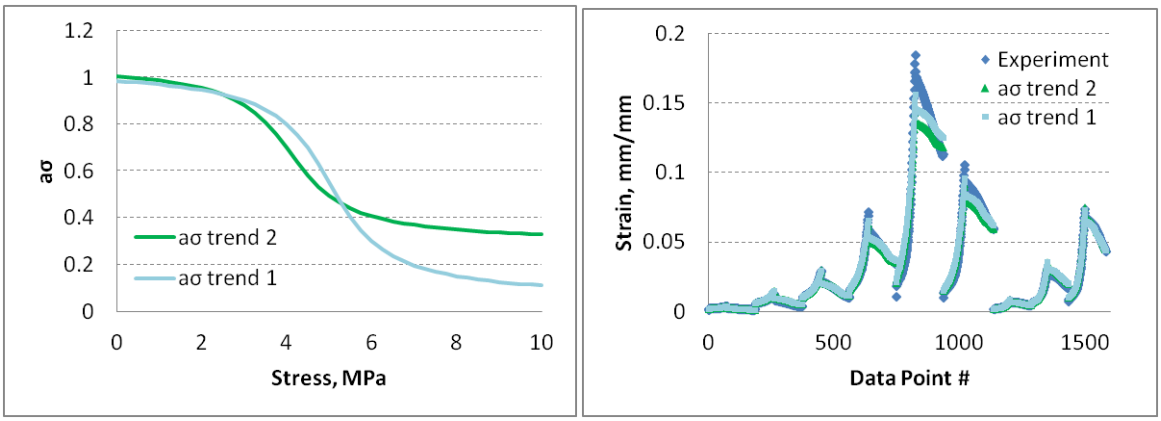

Figure B 6. Example of the impact of a_σ functions on model results.

As mentioned previously, the Prony series coefficients which correspond to long characteristic times may also be manipulated to improve the model. The effect of the a_σ function is convoluted with the value of the Prony terms, so they should be considered together. Figure B 7 demonstrates two parameter sets with the a_σ function 1 from the previous figure but different values of the seventh through ninth Prony coefficients. The original Prony series, in conjunction with a_σ function 1, had a TSS of 0.0406. Prony Series 1 in Figure B 7 has a TSS of 0.1905 and Prony Series 2 has a TSS of 0.0384. Thus, Prony Series 2, in conjunction with a_σ function 1, is an improvement over the initial parameter set. Because the effect of the Prony terms is related to the a_σ effect, they also result in vertical shifts in the model, but the shifts are not significant at short times. Again, adjusting the long-time Prony terms resolves some of the discrepancy, but will not be sufficient on its own.

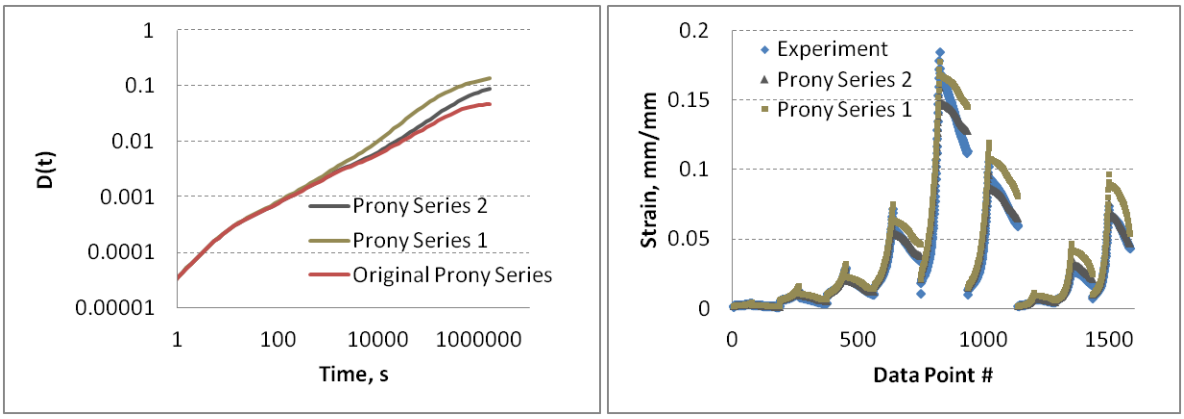

Figure B 7. Example of the impact of long-time Prony coefficients on model results.

By iteratively adjusting the long-term Prony coefficients, g_2 and a_σ functions, an improved parameter set may be obtained. Iteration between the parameters is necessary to avoid wasting time finding the 'perfect' g_2 function which correlates to an inappropriate a_σ function, for example. Recall that a_σ resulted in a vertical shift over the entire time frame, while the vertical shifting due to the Prony series terms was most noticeable during long creep and early recovery times. The effect of g_2 was to increase the height of the peak strain that occurred during the creep/recovery transition without affecting the early creep

or late recovery values. Although not demonstrated in this document, it was found that g1 had very little impact on improving the model fit and is therefore assumed to be unity for all values of applied stress.

This knowledge was used to find an improved parameter set, which was then used as the starting point for the non-linear parameter determination algorithm. Final results from the algorithm are reported in Chapter 5 of this document.

Appendix C. Fortran code

The following code is used for the finite element model. It includes the UMAT and UEXPAN subroutines, in addition to the various subroutines and function necessary for the convergence algorithm that works with the UMAT.

```
      SUBROUTINE UEXPAN(EXPAN,DEXPANDT,TEMP,TIME,DTIME,PREDEF,
     1 DPRED,STATEV,CMNAME,NSTATV,NOEL)
C
      INCLUDE 'ABA_PARAM.INC'
      CHARACTER*80 CMNAME
      DIMENSION EXPAN(*),DEXPANDT(*),TEMP(2),TIME(2),PREDEF(*),
     1 DPRED(*),STATEV(NSTATV)
      REAL*8 alpha,beta,TEMPER,DTEMPER,LAMBDA,DLAMBDA,TEMPER0
      REAL*8 LAMBDA0
C
      TEMPER=TEMP(1)
      LAMBDA=PREDEF(1)
      DTEMPER=TEMP(2)
      DLAMBDA=DPRED(1)
C
C     //define material properties//
      alpha=(13.794-0.4028*LAMBDA+0.8116*LAMBDA**2.)*10.**(-5.)
      beta=1.3E-2
C
C     //calculate expansion//
      EXPAN(1)=alpha*(DTEMPER)+beta*(DLAMBDA)
      DEXPANDT(1)=alpha+beta
C
   RETURN
   END
```

Appendix C

```
SUBROUTINE UMAT(STRESS,STATEV,DDSDDE,SSE,SPD,SCD,
    1 RPL,DDSDDT,DRPLDE,DRPLDT,
    2 STRAN,DSTRAN,TIME,DTIME,TEMP,DTEMP,PREDEF,DPRED,CMNAME,
    3 NDI,NSHR,NTENS,NSTATV,PROPS,NPROPS,COORDS,DROT,PNEWDT,
    4 CELENT,DFGRD0,DFGRD1,NOEL,NPT,LAYER,KSPT,KSTEP,KINC)
C
     INCLUDE 'ABA_PARAM.INC'
     INTEGER M,K,I,J,iter,NMAX,NIMAX,NpS,numg
     PARAMETER(M=9,NMAX=216,NIMAX=3,NpS=150,numg=3,pstens=3)
     REAL*8 Shear0,Shear(M),B0,Bulk(M),TAU(M)
     REAL*8 DSTRESS(NTENS),A1,b1,c1,A2,b2,c2
     REAL*8 g0i(numg),g1i(numg),g2i(numg),asigmai(numg)
     REAL*8 C11,C12,C22,C21,C33,S11,S12,S33,S22,S21
     REAL*8 ftol,fret,fp,xi(pstens),p(NMAX),pSConv(NpS)
     REAL*8 alpha,beta,TEMPER,DTEMPER,aTH,Lambda,dLambda,debug
C
     CHARACTER*80 CMNAME
     DIMENSION STRESS(NTENS),STATEV(NSTATV),
    1 DDSDDE(NTENS,NTENS),DDSDDT(NTENS),DRPLDE(NTENS),
    2 STRAN(NTENS),DSTRAN(NTENS),TIME(2),PREDEF(2),DPRED(2),
    3 PROPS(NPROPS),COORDS(3),DROT(3,3),DFGRD0(3,3),DFGRD1(3,3)
C
C         //import material properties and Temp, Lambda//
          Shear0=PROPS(1)
          B0=PROPS(2)
          DO K=1,M
           Shear(K)=PROPS(2+0*M+K)
           Bulk(K)=PROPS(2+1*M+K)
           TAU(K)=PROPS(2+2*M+K)
          END DO
          DO K=1,numg
           g0i(K)=PROPS(2+3*M+0*numg+K)
           g1i(K)=PROPS(2+3*M+1*numg+K)
           g2i(K)=PROPS(2+3*M+2*numg+K)
           asigmai(K)=PROPS(2+3*M+3*numg+K)
          END DO
          A1=PROPS(2+3*M+4*numg+1)
          b1=PROPS(2+3*M+4*numg+2)
          c1=PROPS(2+3*M+4*numg+3)
          A2=PROPS(2+3*M+4*numg+4)
          b2=PROPS(2+3*M+4*numg+5)
          c2=PROPS(2+3*M+4*numg+6)
          alpha=PROPS(2+3*M+4*numg+7)
          beta=PROPS(2+3*M+4*numg+8)
          TEMPER=TEMP
          DTEMPER=DTEMP
          Lambda=PREDEF(1)
          DLambda=DPRED(1)
```

```
C
C       //calculate environmental effects//
C       //aTH equation from Katherine's dissertation
        IF(TEMPER.le.70.)THEN
          aTH=1./(10**((0.000063*(TEMPER-70.0)+0.00304*(Lambda-1.24))/
     &    (0.002601+0.000007*(TEMPER-70.0)+
     &    0.000357*(Lambda-1.24))+0.0319*(TEMPER-70.0)))
        ELSE
          aTH=1./(10**((0.000063*(TEMPER-70.0)+0.00304*(Lambda-1.24))/
     &    (0.002601+0.000007*(TEMPER-70.0)+
     &    0.000357*(Lambda-1.24))+0.0993*(TEMPER-70.0)))
        ENDIF
C
C       //A2 as a function of temperature and lambda//
          A2=(6.38E+9)*EXP(-11461./(TEMPER+273.)-2.5/Lambda)
C
C       //Define STATEV and p//
        IF(KSTEP.EQ.1.AND.KINC.EQ.1)THEN
         DO K=1,NSTATV
           p(K)=0
           STATEV(K)=0
         END DO
        ELSE
         DO K=1,NSTATV
           p(K)=STATEV(K)
         END DO
        END IF
C
C       //initialize stress increment variables//
        DO K=1,pstens
          p(K+0*pstens)=STRESS(K)
C         p(K+1*pstens)=0
C         p(K+2*pstens)=0
          p(K+3*pstens)=STRAN(K)
          p(K+4*pstens)=DSTRAN(K)
        END DO
        p(5*pstens+1)=0
        p(5*pstens+2)=TIME(2)
        p(5*pstens+3)=DTIME
        p(5*pstens+4)=Shear0
        p(5*pstens+5)=B0
        DO K=1,M
      p(5*pstens+5+0*M+K)=Shear(K)
         p(5*pstens+5+1*M+K)=Bulk(K)
      p(5*pstens+5+2*M+K)=TAU(K)
        END DO
        DO K=1,numg
         p(5*pstens+5+3*M+0*numg+K)=g0i(K)
```

```
          p(5*pstens+5+3*M+1*numg+K)=g1i(K)
          p(5*pstens+5+3*M+2*numg+K)=g2i(K)
          p(5*pstens+5+3*M+3*numg+K)=asigmai(K)
        END DO
        p(5*pstens+17+3*M+1)=A1
        p(5*pstens+17+3*M+2)=b1
        p(5*pstens+17+3*M+3)=c1
        p(5*pstens+17+3*M+4)=A2
        p(5*pstens+17+3*M+5)=b2
        p(5*pstens+17+3*M+6)=c2
        p(5*pstens+17+3*M+7)=1234.567
        p(67)=aTH
        p(68)=0.0
        p(69)=0.0
C
        ftol=1.E-9
        iter=0
        fret=0
        CALL frprmn(p,ftol,iter,fret)
        CALL Schapery(p,fp,xi,pSconv)
C
C       //updatestress, strain vector//
        DO K=1,pstens
          STRESS(K)=p(K)+p(K+1*pstens)
          DSTRESS(K)=p(K+1*pstens)
          STRAN(K)=p(K+3*pstens)+p(K+4*pstens)
        END DO
C
        DO K=1,NpS
         p(70+K)=pSconv(K)
        END DO
C
        S11=pSconv(10)
        S12=pSconv(11)
        S22=pSconv(12)
        S21=pSconv(13)
        S33=pSconv(14)
         DET=(S11*S22*S33-S12*S21*S33)
C
    IF (abs(DET).le.1E-15) THEN
    C11=0
    C12=0
    C22=0
    C21=0
    C33=0
    ELSE
    C11=S33*S22/DET
    C22=S33*S11/DET
```

```
      C12=-S33*S12/DET
      C21=-S33*S21/DET
      C33=(S11*S22-S12*S21)/DET
      ENDIF
C
            DO I=1,NTENS
            DO J=1,NTENS
             DDSDDE(I,J)=0
            END DO
            END DO
            DDSDDE(1,1)=C11
            DDSDDE(2,2)=C22
            DDSDDE(3,3)=C33
            DDSDDE(1,2)=C12
            DDSDDE(2,1)=C21
C
C           //Repack STATEV//
            DO K=1,NSTATV
              STATEV(K)=p(K)
            END DO
C
            SSE=SSE
            SPD=SPD
            SCD=SCD
C
            RETURN
            END
C
C           ////////////////////////////////////
C            /   Subroutine to calculate strain      /
C           /                                        /
C           ////////////////////////////////////
            SUBROUTINE Schapery(p,fpLocal,xiLocal,pSconv)
C
      INTEGER K,NMAX,NIMAX,NpS,NTENS,M,numg,debug
      PARAMETER (NMAX=216,NIMAX=3,NpS=150,NTENS=3,M=9,numg=3,pstens=3)
      REAL*8 p(NMAX),fpLocal,xiLocal(NIMAX),pSprev(NpS)
      REAL*8 pSconv(NpS),STRESS(pstens),DSTRESS(pstens)
      REAL*8 DSTRESSOld(pstens),DSTRAN(pstens),STRAN(pstens)
      REAL*8 g0,g1,g2,asigma,g1old,g2old,ROld
      REAL*8 g0i(numg),g1i(numg),g2i(numg),asigmai(numg)
      REAL*8 A1,b1,c1,A2,b2,c2,HStress,pHStress
      REAL*8 deltat,dzeta,dzetaold,time
      REAL*8 J0,J(M),Jbar,JPronySum,Jbarold,TAU(M)
      REAL*8 B0,Bulk(M),Bbar,BPronySum,Bbarold
C           //X variables
      REAL*8 XStress,XStressDev,XStressDevold,iXStrainVE
      REAL*8 XStrain,iXStrainDev,iXStrainDil,iXStrain,XError
```

```
      REAL*8 XJHSum1,XJHSum2,XJqold(M),XGOAL,iXStrainVP,XStrainVP
      REAL*8 dXJHSum1,dXJHSum2,coefX,dvpxdx,dvpxdy,dvexdx,dvexdy
C         //Y variables
      REAL*8 YStress,YStressDev,YStressDevold,iYStrainVE
      REAL*8 YStrain,iYStrainDev,iYStrainDil,iYStrain,YError
      REAL*8 YJHSum1,YJHSum2,YJqold(M),YGOAL,iYStrainVP,YStrainVP
      REAL*8 dYJHSum1,dYJHSum2,coefY,dvpydx,dvpydy,dveydy,dveydx
C         //S variables
      REAL*8 SStress,SStressDev,SStressDevold,iSStrainVE
      REAL*8 SStrain,iSStrainDev,iSStrainDil,iSStrain,SError
      REAL*8 SJHSum1,SJHSum2,SJqold(M),SGOAL,iSStrainVP,SStrainVP
      REAL*8 dSJHSum1,dSJHSum2,coefS,dvps,dves
C         //other
      REAL*8 StressDil,StressDilold,BHSum1,BHSum2,Bqold(M)
      REAL*8 dg0,dg1,dg2,dasigma,dJbar,dBbar,dJbarSum,dBbarSum
      REAL*8 S11,S12,S33,S22,S21
      REAL*8 ratio(M),Eratio(M),dratio(M),dEratio(M),invratio(M)
      REAL*8 oldratio(M),oldEratio(M),dinvratio(M),timelimit
      REAL*8 iStrainVP,YieldStress,iHStrain,aTH,MagStressDev,L
C
C         //1. Receive information from the main program
          DO K=1,NpS
            pSprev(K)=0
            pSconv(K)=0
          END DO
          DO K=1,pstens
            STRESS(K)=p(K)
            DSTRESS(K)=p(K+pstens)
            DSTRESSOld(K)=p(K+2*pstens)
            STRAN(K)=p(K+3*pstens)
            DSTRAN(K)=p(K+4*pstens)
          END DO
           ROld=p(5*pstens+1)
           time=p(5*pstens+2)
           deltat=p(5*pstens+3)
           J0=p(5*pstens+4)
           B0=p(5*pstens+5)
          DO K=1,M
            J(K)=p(5*pstens+5+0*M+K)
            Bulk(K)=p(5*pstens+5+1*M+K)
            TAU(K)=p(5*pstens+5+2*M+K)
          END DO
          DO K=1,numg
           g0i(K)=p(5*pstens+5+3*M+0*numg+K)
           g1i(K)=p(5*pstens+5+3*M+1*numg+K)
           g2i(K)=p(5*pstens+5+3*M+2*numg+K)
           asigmai(K)=p(5*pstens+5+3*M+3*numg+K)
          END DO
```

```
      A1=p(5*pstens+17+3*M+1)
      b1=p(5*pstens+17+3*M+2)
      c1=p(5*pstens+17+3*M+3)
      A2=p(5*pstens+17+3*M+4)
      b2=p(5*pstens+17+3*M+5)
      c2=p(5*pstens+17+3*M+6)
      aTH=p(67)
C
      DO K=1,NpS
        pSprev(K)=p(K+70)
      END DO
       XStressDevOld=pSprev(1)
       YStressDevOld=pSprev(2)
       SStressDevOld=pSprev(3)
       StressDilOld=pSprev(4)
       g1old=pSprev(5)
       g2old=pSprev(6)
       dzetaold=pSprev(7)
       Jbarold=pSprev(8)
       Bbarold=pSprev(9)
       S11=pSprev(10)
       S12=pSprev(11)
       S22=pSprev(12)
       S21=pSprev(13)
       S33=pSprev(14)
      DO K=1,M
       XJqold(K)=0
       YJqold(K)=0
       SJqold(K)=0
       Bqold(K)=0
      END DO
      DO K=1,M
       XJqold(K)=pSprev(14+0*M+K)
       YJqold(K)=pSprev(14+1*M+K)
       SJqold(K)=pSprev(14+2*M+K)
       Bqold(K)=pSprev(14+3*M+K)
      END DO
C
C     //re-intialize things to zero
       g0=0
       g1=0
       g2=0
       asigma=0
       JPronySum=0
       BPronySum=0
       XJHSum1=0
       XJHSum2=0
       YJHSum1=0
```

```
          YJHSum2=0
          SJHSum1=0
          SJHSum2=0
          BHSum1=0
          BHSum2=0
          coefX=0.
          coefY=0.
          coefS=0.
         DO K=1,M
          ratio(K)=0
          Eratio(K)=0
          Oldratio(K)=0
          OldEratio(K)=0
         END DO
C
C         //2. Calculate deviatoric and dilatational stress
         XStress=STRESS(1)+DSTRESS(1)
         YStress=STRESS(2)+DSTRESS(2)
         SStress=STRESS(3)+DSTRESS(3)
C
         XStressDev=XSTRESS-(XSTRESS+YSTRESS)/3.
         YStressDev=YSTRESS-(XSTRESS+YSTRESS)/3.
         SStressDev=SSTRESS
         StressDil=(XSTRESS+YSTRESS)
         MagStressDev=(XStressDev**2.+YStressDev**2.+
   &   SStressDev**2.)**0.5
C
C         //3. Calculate octahedral shear stress
         Stress0=0.5
         pHStress=(XSTRESS-YSTRESS)**2.+(XSTRESS**2.)
   &        +(YSTRESS**2.)+6.*(SSTRESS**2.)
         HStress=((pHStress/2.)**0.5)
C
C         //4. Calculate non-linear parameters
         g0=g0i(1)+g0i(2)*(1.570796-ATAN(HSTRESS-g0i(3)))
         g1=g1i(1)+g1i(2)*(1.570796-ATAN(HSTRESS-g1i(3)))
         g2=g2i(1)+g2i(2)*(1.570796-ATAN(HSTRESS-g2i(3)))
         asigma=asigmai(1)+asigmai(2)*
   &    (1.570796-ATAN(HSTRESS-asigmai(3)))

C         //5. Calculate material properties
C         //***for convenience, define the following variables***
         IF (deltat.GT.0) THEN
          dzeta=deltat/(aTH*asigma)
         ELSE
          dzeta=1.0
         END IF
         IF (dzetaold.EQ.0) THEN
```

```
          dzetaold=1E-6
          ENDIF
C
          DO K=1,M
           ratio(K)=dzeta/TAU(K)
           invratio(K)=TAU(K)/dzeta
           Eratio(K)=EXP(-dzeta/TAU(K))
           Oldratio(K)=dzetaold/TAU(K)
           OldEratio(K)=EXP(-dzetaold/TAU(K))
          END DO
C
          DO K=1,M
           JPronySum=JPronySum+J(K)*(1.0-(1.0-Eratio(K))/ratio(K))
           BPronySum=BPronySum+Bulk(K)*(1.0-(1.0-Eratio(K))/ratio(K))
          END DO
           Jbar=(g0*J0+g1*g2*JPronySum)/2.0
           Bbar=(g0*B0)/3.0
C
          DO K=1,M
          XJHSum1=XJHSum1+0.5*J(K)*XJqold(K)*(g1*Eratio(K)-g1old)
          XJHSum2=XJHSum2+0.5*J(K)*g2old*XStressDevold*
     &     (g1old*(1.0-OldEratio(K))/Oldratio(K)
     &    -g1*(1.0-Eratio(K))/ratio(K))

          YJHSum1=YJHSum1+0.5*J(K)*YJqold(K)*(g1*Eratio(K)-g1old)
          YJHSum2=YJHSum2+0.5*J(K)*g2old*YStressDevold*
     &     (g1old*(1.0-OldEratio(K))/Oldratio(K)
     &    -g1*(1.0-Eratio(K))/ratio(K))

          SJHSum1=SJHSum1+0.5*J(K)*SJqold(K)*(g1*Eratio(K)-g1old)
          SJHSum2=SJHSum2+0.5*J(K)*g2old*SStressDevold*
     &     (g1old*(1.0-OldEratio(K))/Oldratio(K)
     &    -g1*(1.0-Eratio(K))/ratio(K))

C         BHSum1=BHSum1+(1.0/3.0)*Bulk(K)*Bqold(K)*(g1*Eratio(K)-g1old)
C         BHSum2=BHSum2+(1.0/3.0)*Bulk(K)*g2old*StressDilold*
C    &     (g1old*(1.0-OldEratio(K))/Oldratio(K)
C    &     -g1*(1.0-Eratio(K))/ratio(K))

          END DO
C
C         //6. Calculate partial derivative of HStress WRT total stress
          IF(abs(HStress).GT.1.E-6)THEN
           coefX=(2.0*XStress-YStress)/(2.0*HStress)
           coefY=(2.0*YStress-XStress)/(2.0*HStress)
           coefS=3.0*SStress/HStress
          ENDIF
C
```

```
C       //7. Calculate partial derivative of non-linear params WRT HStress
        dg0=-g0i(2)*(1./(1.+(HSTRESS-g0i(3))**2.))
        dg1=-g1i(2)*(1./(1.+(HSTRESS-g1i(3))**2.))
        dg2=-g2i(2)*(1./(1.+(HSTRESS-g2i(3))**2.))
        dasigma=-asigmai(2)*(1./(1.+(HSTRESS-asigmai(3))**2.))

C       //8. Calculate partial derivative of VEmaterial properties WRT HStress
        dXJHSum1=0.
        dXJHSum2=0.
        dYJHSum1=0.
        dYJHSum2=0.
        dSJHSum1=0.
        dSJHSum2=0.
        dBHSum1=0.
        dBHSum2=0.
        dJbarSum=0.
        dBbarSum=0.
C
        DO K=1,M
         dratio(K)=-dasigma*ratio(K)/asigma
         dinvratio(K)=invratio(K)*dasigma/asigma
         dEratio(K)=-dratio(K)*Eratio(K)
        END DO
C
        DO K=1,M
         dJbarSum=dJbarSum+J(K)*
     &  (dg1*g2+g1*dg2-dg1*g2*invratio(K)
     &   -g1*dg2*invratio(K)-g1*g2*dinvratio(K)
     &   +dg1*g2*invratio(K)*Eratio(K)
     &   +g1*dg2*invratio(K)*Eratio(K)
     &      +g1*g2*dinvratio(K)*Eratio(K)
     &      +g1*g2*invratio(K)*dEratio(K))
C
         dXJHSum1=dXJHSum1+0.5*J(K)*XJqold(K)*
     &  (dg1*Eratio(K)+g1*dEratio(K))
         dXJHSum2=dXJHSum2+0.5*g2old*XStressDevold*J(K)*
     &  (-dg1*invratio(K)-g1*dinvratio(K)
     &   +dg1*invratio(K)*Eratio(K)
     &   +g1*dinvratio(K)*Eratio(K)
     &   +g1*invratio(K)*dEratio(K))
C
         dYJHSum1=dYJHSum1+0.5*J(K)*YJqold(K)*
     &  (dg1*Eratio(K)+g1*dEratio(K))
         dYJHSum2=dYJHSum2+0.5*g2old*YStressDevold*J(K)*
     &  (-dg1*invratio(K)-g1*dinvratio(K)
     &   +dg1*invratio(K)*Eratio(K)
     &   +g1*dinvratio(K)*Eratio(K)
     &   +g1*invratio(K)*dEratio(K))
```

```
C
          dSJHSum1=dSJHSum1+0.5*J(K)*SJqold(K)*
     &    (dg1*Eratio(K)+g1*dEratio(K))
          dSJHSum2=dSJHSum2+0.5*g2old*SStressDevold*J(K)*
     &    (-dg1*invratio(K)-g1*dinvratio(K)
     &     +dg1*invratio(K)*Eratio(K)
     &     +g1*dinvratio(K)*Eratio(K)
     &     +g1*invratio(K)*dEratio(K))
C
          dBbarSum=dBbarSum+Bulk(K)*
     &   (dg1*g2+g1*dg2-dg1*g2*invratio(K)
     &    -g1*dg2*invratio(K)-g1*g2*dinvratio(K)
     &    +dg1*g2*invratio(K)*Eratio(K)
     &    +g1*dg2*invratio(K)*Eratio(K)
     &       +g1*g2*dinvratio(K)*Eratio(K)
     &       +g1*g2*invratio(K)*dEratio(K))
C
          dBHSum1=dBHSum1+(1./3.)*Bulk(K)*Bqold(K)*
     &    (dg1*Eratio(K)+g1*dEratio(K))
          dBHSum2=dBHSum2+(1./3.)*g2old*StressDilold*Bulk(K)*
     &    (-dg1*invratio(K)-g1*dinvratio(K)
     &     +dg1*invratio(K)*Eratio(K)
     &     +g1*dinvratio(K)*Eratio(K)
     &     +g1*invratio(K)*dEratio(K))
C
          END DO
C
          dJbar=0.5*(dg0*J0+dJbarSum)
          dBbar=(1./3.)*(dg0*B0+dBbarSum)
C
C         //9. Calculate VE Compliance Matrix terms
          IF(abs(pHStress).GT.1.E-6)THEN
           dvexdx=(2.*Jbar+Bbar)/3.+coefX*(dJbar*XStressDev-dXJHSum1-dXJHSum2+
     &      (dBbar*StressDil-dBHSum1-dBHSum2)/3.)
           dvexdy=(Bbar-Jbar)/3.+coefY*(dJbar*XStressDev-dXJSum1-dXJSum2+
     &      (dBbar*StressDil-dBHSum1-dBHSum2)/3.)
           dveydy=(2.*Jbar+Bbar)/3.+coefY*(dJbar*YStressDev-dYJHSum1-dYJHSum2+
     &      (dBbar*StressDil-dBHSum1-dBHSum2)/3.)
           dveydx=(Bbar-Jbar)/3.+coefX*(dJbar*YStressDev-dYJSum1-dYJSum2+
     &      (dBbar*StressDil-dBHSum1-dBHSum2)/3.)
           dves=Jbar+coefS*(dJbar*SStressDev-dSJHSum1-dSJHSum2)
          ELSE
           dvexdx=(Bbar+2.*Jbar)/3.
           dvexdy=(Bbar-Jbar)/3.
           dveydy=(Bbar+2.*Jbar)/3.
           dveydx=(Bbar-Jbar)/3.
           dves=Jbar
          ENDIF
```

```
C
C       //10. Calculate vp strains, vp Compliance matrix terms
C       //time hardening//
C       **** dvps are WRT directional stress ****
        YieldStress=4.0
        L=1.118
        IF(time.GT.0.0)THEN
         IF(HStress.LT.YieldStress)THEN
          iStrainVP=A1*(HStress**b1)*((time+deltat)**c1-(time)**c1)
           iYStrainVP=L*iStrainVP*YStressDev/MagStressDev
           iXStrainVP=L*iStrainVP*XStressDev/MagStressDev
           iSStrainVP=L*iStrainVP*SStressDev/MagStressDev
           dvpydy=L*A1*((time+deltat)**c1-(time)**c1)*(
     &     b1*HStress**(b1-1.)*coefY*YStressDev/MagStressDev+
     &        (HStress**b1)*(2./3.)/MagStressDev+
     &     (HStress**b1)*YStressDev*(-1./18.)*
     &     (10.*YStress-8.*XStress)/(MagStressDev**3.))

           dvpydx=L*A1*((time+deltat)**c1-(time)**c1)*(
     &     b1*HStress**(b1-1.)*coefX*YStressDev/MagStressDev+
     &        (HStress**b1)*(-1./3.)/MagStressDev+
     &     (HStress**b1)*YStressDev*(-1./18.)*
     &     (10.*XStress-8.*YStress)/(MagStressDev**3.))

           dvpxdx=L*A1*((time+deltat)**c1-(time)**c1)*(
     &     b1*HStress**(b1-1.)*coefX*XStressDev/MagStressDev+
     &        (HStress**b1)*(2./3.)/MagStressDev+
     &     (HStress**b1)*XStressDev*(-1./18.)*
     &     (10.*XStress-8.*YStress)/(MagStressDev**3.))

           dvpxdy=L*A1*((time+deltat)**c1-(time)**c1)*(
     &     b1*HStress**(b1-1.)*coefY*XStressDev/MagStressDev+
     &        (HStress**b1)*(-1./3.)/MagStressDev+
     &     (HStress**b1)*XStressDev*(-1./18.)*
     &     (10.*YStress-8.*XStress)/(MagStressDev**3.))

           dvps=L*A1*((time+deltat)**c1-(time)**c1)*(
     &     b1*HStress**(b1-1.)*coefS*SStress/MagStressDev+
     &        (HStress**b1)*(1.)/MagStressDev+
     &     (HStress**b1)*SStress*(-1./18.)*
     &     (18.*SStress)/(MagStressDev**3.))
          ELSE
           iStrainVP=A2*EXP(b2*HStress)*((time+deltat)**c2-(time)**c2)
           iYStrainVP=L*iStrainVP*YStressDev/MagStressDev
           iXStrainVP=L*iStrainVP*XStressDev/MagStressDev
           iSStrainVP=L*iStrainVP*SStressDev/MagStressDev
           dvpydy=L*A2*((time+deltat)**c2-(time)**c2)*(
     &     b2*EXP(b2*HStress)*coefY*YStressDev/MagStressDev+
```

```
     &          EXP(b2*HStress)*(2./3.)/MagStressDev+
     &       EXP(b2*HStress)*YStressDev*(-1./18.)*
     &       (10.*YStress-8.*XStress)/(MagStressDev**3.))
              dvpydx=L*A2*((time+deltat)**c2-(time)**c2)*(
     &       b2*EXP(b2*HStress)*coefX*YStressDev/MagStressDev+
     &          EXP(b2*HStress)*(-1./3.)/MagStressDev+
     &       EXP(b2*HStress)*YStressDev*(-1./18.)*
     &       (10.*XStress-8.*YStress)/(MagStressDev**3.))
              dvpxdx=L*A2*((time+deltat)**c2-(time)**c2)*(
     &       b2*EXP(b2*HStress)*coefX*XStressDev/MagStressDev+
     &          EXP(b2*HStress)*(2./3.)/MagStressDev+
     &       EXP(b2*HStress)*XStressDev*(-1./18.)*
     &       (10.*XStress-8.*YStress)/(MagStressDev**3.))
              dvpxdy=L*A2*((time+deltat)**c2-(time)**c2)*(
     &       b2*EXP(b2*HStress)*coefY*XStressDev/MagStressDev+
     &          EXP(b2*HStress)*(-1./3.)/MagStressDev+
     &       EXP(b2*HStress)*XStressDev*(-1./18.)*
     &       (10.*YStress-8.*XStress)/(MagStressDev**3.))
              dvps=L*A2*((time+deltat)**c2-(time)**c2)*(
     &       b2*EXP(b2*HStress)*coefS*SStress/MagStressDev+
     &          EXP(b2*HStress)*(1.)/MagStressDev+
     &       EXP(b2*HStress)*SStress*(-1./18.)*
     &       (18.*SStress)/(MagStressDev**3.))
             ENDIF
            ELSE
             iYStrainVP=0.0
             dvpydy=0.0
             dvypdx=0.0
             ixStrainVP=0.0
             dvpxdx=0.0
             dvpxdy=0.0
             iSStrainVP=0.0
             dvps=0.0
            ENDIF
C
C           //11.Calculate total strain increments
             iXStrainDev=Jbar*XStressDev-Jbarold*XStressDevold-XJHSum1-XJHSum2
             iXStrainDil=Bbar*StressDil-Bbarold*StressDilold-BHSum1-BHSum2
             iXStrainVE=iXStrainDev+iXStrainDil/3.
             iXStrain=iXStrainVE+iXStrainVP-2.*iXStrainVE*iXStrainVP
C
             iYStrainDev=Jbar*YStressDev-Jbarold*YStressDevold-YJHSum1-YJHSum2
             iYStrainDil=Bbar*StressDil-Bbarold*StressDilold-BHSum1-BHSum2
             iYStrainVE=iYStrainDev+iYStrainDil/3.
             iYStrain=iYStrainVE+iYStrainVP-2.*iYStrainVE*iYStrainVP
C
             iSStrainVE=Jbar*SStressDev-Jbarold*SStressDevOld-SJHSum1-SJHSum2
             iSStrain=iSStrainVE+iSStrainVP-2.*iSStrainVE*iSStrainVP
```

```
C
C         //12. Assemble Compliance Matrix
            S11=dvexdx+dvpxdx-2.*iXStrainVE*dvpxdx-2.*dvexdx*iXStrainVP
            S12=dvexdy+dvpxdy-2.*iXStrainVE*dvpxdy-2.*dvexdy*iXStrainVP
            S22=dveydy+dvpydy-2.*iYStrainVE*dvpydy-2.*dveydy*iYStrainVP
            S21=dveydx+dvpydx-2.*iYStrainVE*dvpydx-2.*dveydx*iYStrainVP
            S33=dves+dvps-2.*iSStrainVE*dvps-2.*dves*iSStrainVP
C
C         //Update the XJOld,XBold, etc
            DO K=1,M
        XJqold(K)=Eratio(K)*XJqold(K)+
     &    (g2*XStressDev-g2old*XStressDevold)*(1.-Eratio(K))/ratio(K)
        YJqold(K)=Eratio(K)*YJqold(K)+
     &    (g2*YStressDev-g2old*YStressDevold)*(1.-Eratio(K))/ratio(K)
        SJqold(K)=Eratio(K)*SJqold(K)+
     &    (g2*SStressDev-g2old*SStressDevold)*(1.-Eratio(K))/ratio(K)
        Bqold(K)=Eratio(K)*Bqold(K)+
     &    (g2*StressDil-g2old*StressDilold)*(1.-Eratio(K))/ratio(K)
            END DO
C
C         //Compute error in strains calculated, specified
       XError=(iXStrain-p(13))
       YError=(iYStrain-p(14))
       SError=(iSStrain-p(15))
C
            fpLocal=((XError)**2.+(YError)**2.+(SError)**2.)**0.5
            IF(fpLocal.gt.1E-20)THEN
            xiLocal(1)=(XError*S11+YError*S21)/fpLocal
            xiLocal(2)=(YError*S22+XError*S12)/fpLocal
            xiLocal(3)=(SError*S33)/fpLocal
            ELSE
            xiLocal(1)=(XError*S11+YError*S21)
            xiLocal(2)=(YError*S22+XError*S12)
            xiLocal(3)=(SError*S33)
            ENDIF

             pSconv(1)=XStressDev
             pSconv(2)=YStressDev
             pSconv(3)=SStressDev
             pSconv(4)=StressDil
             pSconv(5)=g1
             pSconv(6)=g2
             pSconv(7)=dzeta
             pSconv(8)=Jbar
             pSconv(9)=Bbar
             pSconv(10)=S11
             pSconv(11)=S12
             pSconv(12)=S22
```

```
      pSconv(13)=S21
      pSconv(14)=S33
      DO K=1,M
      pSconv(14+0*M+K)=XJqold(K)
      pSconv(14+1*M+K)=YJqold(K)
      pSconv(14+2*M+K)=SJqold(K)
      pSconv(14+3*M+K)=Bqold(K)
      END DO

      pSconv(51)=time
      pSconv(52)=deltat
      pSconv(53)=XStress
      pSconv(54)=YStress
      pSconv(55)=SStress
      pSconv(56)=dstress(1)
      pSconv(57)=dstress(2)
      pSconv(58)=dstress(3)
      pSconv(59)=stran(1)
      pSconv(60)=stran(2)
      pSconv(61)=stran(3)
      pSconv(62)=dstran(1)
      pSconv(63)=dstran(2)
      pSconv(64)=dstran(3)
      pSconv(65)=XStressDev
      pSconv(66)=YStressDev
      pSconv(67)=SStressDev
      pSconv(68)=StressDil
      pSconv(69)=pHStress
      pSconv(70)=HStress
      pSconv(71)=g0
      pSconv(72)=g1
      pSconv(73)=g2
      pSconv(74)=asigma
      pSconv(75)=dzeta
      pSconv(76)=dzetaold
      pSconv(77)=ratio(1)
      pSconv(78)=invratio(1)
      pSconv(79)=Eratio(1)
      pSconv(80)=JPronySum
      pSconv(81)=Jbar
      pSconv(82)=dJbar
      pSconv(83)=BPronySum
      pSconv(84)=Bbar
      pSconv(85)=dBbar
C
      pSconv(86)=XJHSum1
      pSconv(87)=XJHSum2
      pSconv(88)=XJqold(1)
```

```
      pSconv(89)=YJHSum1
      pSconv(90)=YJHSum2
      pSconv(91)=YJqold(1)
      pSconv(92)=SJHSum1
      pSconv(93)=SJHSum2
      pSconv(94)=SJqold(1)
      pSconv(95)=BHSum1
      pSconv(96)=BHSum2
      pSconv(97)=Bqold(1)
C
      pSconv(98)=ixstraindev
      pSconv(99)=ixstraindil
      pSconv(100)=ixstrain
      pSconv(101)=iystraindev
      pSconv(102)=iystraindil
      pSconv(103)=iystrain
      pSconv(104)=isstrain
C
      pSconv(105)=coefX
      pSconv(106)=coefY
      pSconv(107)=coefS
      pSconv(108)=dg0
      pSconv(109)=dg1
      pSconv(110)=dg2
      pSconv(111)=dasigma
      pSconv(112)=dratio(1)
      pSconv(113)=dinvratio(1)
      pSconv(114)=dEratio(1)
C
      pSconv(115)=dXJHSum1
      pSconv(116)=dXJHSum2
      pSconv(117)=dYJHSum1
      pSconv(118)=dYJHSum2
      pSconv(119)=dSJHSum1
      pSconv(120)=dSJHSum2
      pSconv(121)=dBHSum1
      pSconv(122)=dBHSum2
C
      pSconv(123)=dJbarsum
      pSconv(124)=dBbarSum
      pSconv(125)=dJbar
      pSconv(126)=dBbar
      pSconv(127)=S11
      pSconv(128)=S12
      pSconv(129)=S22
      pSconv(130)=S21
      pSconv(131)=S33
      pSconv(132)=iXStrain
```

```
          pSconv(133)=iYStrain
          pSconv(134)=iSStrain
C
          pSconv(136)=Xerror
          pSconv(137)=Yerror
          pSconv(138)=Serror
          pSconv(139)=fplocal
          pSconv(140)=iXStrainVP
          pSconv(141)=iYStrainVP
          pSconv(142)=pSprev(142)+iXStrainVP
          pSconv(143)=pSprev(143)+iYStrainVP
          pSconv(144)=iHStrain
          pSconv(145)=YieldStress
C
          RETURN
          END
C
C         ////////////////////////////////////
          SUBROUTINE frprmn(p,ftol,iter,fret)

      INTEGER NMAX,NIMAX,NpS,pstens
      PARAMETER (NMAX=216,NIMAX=3,NpS=150,pstens=3)
      REAL*8 p(NMAX),fp,xi(NIMAX),pSconv(NpS),trial1,trial2
          INTEGER iter,ITMAX
          REAL*8 fret,ftol,EPS,func
          EXTERNAL func
          PARAMETER (ITMAX=600,EPS=1.e-10)
C         uses Schapery,linmin
          INTEGER its,j
          REAL*8 dgg,gam,gg,g(NIMAX),h(NIMAX)

          fp=func(p)
          CALL dfunc(p,xi)
          do 11 j=1,NIMAX
            g(j)=-xi(j)
            h(j)=g(j)
            xi(j)=h(j)
 11       enddo

  2       IF(its.lt.ITMAX)THEN
             its=its+1
            iter=its
            call linmin(p,xi,fret)
            trial1=2.*abs(fret-fp)
            trial2=ftol*(abs(fret)+abs(fp)+EPS)
            if(2.*abs(fret-fp).le.ftol*(abs(fret)+abs(fp)+EPS))RETURN
            fp=func(p)
            CALL dfunc(p,xi)
```

```
            gg=0.
            dgg=0.
            do 12 j=1,NIMAX
              gg=gg+g(j)**2.
C             dgg=dgg+xi(j)**2.
              dgg=dgg+(xi(j)+g(j))*xi(j)
 12         enddo
            if(gg.eq.0.)RETURN
            gam=dgg/gg
            do 13 j=1,NIMAX
              g(j)=-xi(j)
              h(j)=g(j)+gam*h(j)
              xi(j)=h(j)
 13     enddo

    IF(its.eq.ITMAX)THEN
          WRITE(*,*) 'frprmn maximum iterations exceeded'
          ENDIF
          goto 2
    ENDIF
          WRITE(*,*) 'fp',fp,ftol
          RETURN
          END


C         ////////////////////////////////////
          SUBROUTINE linmin(p,xi,fret)

    INTEGER NMAX,NIMAX,NpS,pstens
    PARAMETER (NMAX=216,NIMAX=3,NpS=150,pstens=3)
    REAL*8 p(NMAX),xi(NIMAX)
          INTEGER j
          REAL*8 pcom(NMAX),xicom(NIMAX)
          REAL*8 ax,bx,fa,fb,fx,xmin,xx,brent
          COMMON /f1com/ pcom,xicom
          EXTERNAL f1dim
          REAL*8 fret,TOL,f1dim
          PARAMETER (TOL=1.e-9)
C         USES brent,f1dim,mnbrak
    do 11 j=1,NMAX
          pcom(j)=p(j)
  11 enddo
    do 22 j=1,NIMAX
      xicom(j)=xi(j)
  22 enddo
          ax=0.
          xx=1.
          call mnbrak(ax,xx,bx,fa,fx,fb,f1dim)
```

```
          fret=brent(ax,xx,bx,f1dim,TOL,xmin)
C     !changes dstressold to dstress
      DO K=1,pstens
            p(K+2*pstens)=p(K+pstens)
          END DO
           p(16)=fret
C     !changes dstress to dstress+increment from xi
          do 12 j=1,NIMAX
            xi(j)=xmin*xi(j)
            p(j+NIMAX*2)=p(j+NIMAX)
            p(j+NIMAX)=p(j+NIMAX)+xi(j)
  12      enddo
C         WRITE(*,*) 'return linmin'
          RETURN
          END


C         ////////////////////////////////////
          SUBROUTINE mnbrak(ax,bx,cx,fa,fb,fc,func)

      INTEGER NMAX,NIMAX,NpS,pstens
      PARAMETER (NMAX=216,NIMAX=3,NpS=150,pstens=3)
      REAL*8 ax,bx,cx,fa,fb,fc,func,GOLD,GLIMIT,TINY,num
      EXTERNAL func
          PARAMETER (GOLD=1.618034,GLIMIT=10.,TINY=1.e-20)
          REAL*8 dum,fu,q,r,u,ulim
           num=1
          fa=func(ax)
          fb=func(bx)
          if(fb.gt.fa)then
            dum=ax
            ax=bx
            bx=dum
            dum=fb
            fb=fa
            fa=dum
          endif
          cx=bx+GOLD*(bx-ax)
          fc=func(cx)
  1       if(fb.ge.fc)then
            r=(bx-ax)*(fb-fc)
            q=(bx-cx)*(fb-fa)
            u=bx-((bx-cx)*q-(bx-ax)*r)/(2.*sign(max(abs(q-r),TINY),q-r))
            ulim=bx+GLIMIT*(cx-bx)
            if((bx-u)*(u-cx).gt.0.)then
              fu=func(u)
                    if(fu.lt.fc)then
                      ax=bx
```

```
                fa=fb
                bx=u
                fb=fu
                return
              else if(fu.gt.fb)then
                cx=u
                fc=fu
                return
              endif
             u=cx+GOLD*(cx-bx)
    fu=func(u)
    else if((cx-u)*(u-ulim).gt.0)then
     fu=func(u)
              if(fu.lt.fc)then
                bx=cx
                cx=u
                u=cx+GOLD*(cx-bx)
                fb=fc
                fc=fu
       fu=func(u)
              endif
    else if((u-ulim)*(ulim-cx).ge.0.)then
               u=ulim
               fu=func(u)
    else
               u=cx+GOLD*(cx-bx)
      fu=func(u)
    endif
    ax=bx
    bx=cx
    cx=u
    fa=fb
    fb=fc
    fc=fu
    if(fa==0.and.fb==0.and.fc==0.)then
     num=num+1
     if(num.gt.100)then
      ax=0
      bx=0
      cx=0
      fa=0
      fb=0
      fc=1.E-10
     endif
    endif
    goto 1
  endif
  RETURN
```

```
      END


C     ////////////////////////////////////
      FUNCTION f1dim(x)

    INTEGER NMAX,NIMAX,NpS,pstens,j
    PARAMETER (NMAX=216,NIMAX=3,NpS=150,pstens=3)
      REAL*8 f1dim,x,func
C     USES func
      REAL*8 xt(NMAX),pcom(NMAX),xicom(NIMAX)
      COMMON /f1com/ pcom,xicom
      do 11 j=1,NMAX
        if ((j.gt.NIMAX).and.(j.le.2*NIMAX))then
        xt(j)=pcom(j)+x*xicom(j-NIMAX)
        else
        xt(j)=pcom(j)
        endif
 11   enddo
      f1dim=func(xt)
      RETURN
      END


C     ////////////////////////////////////
      FUNCTION brent(ax,bx,cx,f,tol,xmin)

      INTEGER ITMAX,iter
      REAL*8 brent,ax,bx,cx,tol,xmin,f,CGOLD,ZEPS
      PARAMETER(ITMAX=100,CGOLD=0.3819660,ZEPS=1.0e-10)
      REAL*8 a,b,d,e,etemp,fu,fv,fw,fx,p,q,r,tol1,tol2,u,v,w,x,xm
      a=min(ax,cx)
      b=max(ax,cx)
      v=bx
      w=v
      x=v
      e=0.
      fx=f(x)
      fw=fx
      do 11 iter=1,ITMAX
        xm=0.5*(a+b)
        tol1=tol*abs(x)+ZEPS
        tol2=2.*tol1
        if(abs(x-xm).le.(tol2-.5*(b-a))) goto 3
        if(abs(e).gt.tol1) then
          r=(x-w)*(fx-fv)
          q=(x-v)*(fx-fw)
          p=(x-v)*q-(x-w)*r
```

```
          if(q.gt.0.) p=-p
          q=abs(q)
          etemp=e
          e=d
          if(abs(p).ge.abs(.5*q*etemp).or.p.le.q*(a-x).or.
     &       p.ge.q*(b-x)) goto 1
          d=p/q
          u=x+d
          if(u-a.lt.tol2 .or. b-u.lt.tol2) d=sign(tol1,xm-x)
          goto 2
        endif
1       if(x.ge.xm) then
          e=a-x
        else
          e=b-x
        endif
        d=CGOLD*e
2       if(abs(d).ge.tol1) then
          u=x+d
        else
          u=x+sign(tol1,d)
        endif
        fu=f(u)
        if(fu.le.fx) then
          if(u.ge.x) then
            a=x
          else
            b=x
          endif
          v=w
          fv=fw
          w=x
          fw=fx
          x=u
          fx=fu
        else
          if(u.lt.x) then
            a=u
          else
            b=u
          endif
          if(fu.le.fw .or. w.eq.x) then
            v=w
            fv=fw
            w=u
            fw=fu
          else if(fu.le.fv .or. v.eq.x .or. v.eq.w) then
            v=u
```

```
            fv=fu
          endif
        endif
 11     enddo
        pause 'brent exceed maximum iterations'
 3      xmin=x
        brent=fx
        RETURN
        END


C       ////////////////////////
        FUNCTION func(p)

    INTEGER NMAX,NIMAX,NpS,pstens
    PARAMETER (NMAX=216,NIMAX=3,NpS=150,pstens=3)
    REAL*8 p(NMAX),fpfunc,xifunc(NIMAX),pSconv(NpS)
        REAL*8 func
        CALL Schapery(p,fpfunc,xifunc,pSconv)
        func=fpfunc
        return
        END


C       ////////////////////////
        SUBROUTINE dfunc(p,dp)
    INTEGER NMAX,NIMAX,NpS,pstens
    PARAMETER (NMAX=216,NIMAX=3,NpS=150,pstens=3)
    REAL*8 p(NMAX),fpL,xiL(NIMAX),pSconv(NpS),pSend(NMAX)
        REAL*8 dp(NIMAX)
        pSend=p
        CALL Schapery(pSend,fpL,xiL,pSconv)
        dp(1)=xiL(1)
        dp(2)=xiL(2)
        dp(3)=xiL(3)
        return
        END
```

Appendix D. Description of Minimization Algorithm Employed in UMAT

The minimization algorithm employed in the UMAT for converging to the proper stress increment for a specified strain increment is described below. This method is based on that outlined by Press, et. al, [130] and the description follows closely with their text.

When the main UMAT subroutine is called by Abaqus, it is passed a strain increment and must return the corresponding stress increment and the Jacobian matrix (partial derivative of incremental stress with respect to incremental strain). If the analysis has just begun a trial stress increment zero in all directions is passed to the constitutive subroutine. Otherwise, the stress increment which resulted in convergence at that node during the previous time step is used as the first trial stress increment. The constitutive subroutine computes the strains which result from the trial stress increment, $\Delta\varepsilon_{ij}^{total}(t)$, the compliance matrix (which is the inverse of the Jacobian matrix), S_{ij}, the error between the current trial strain and the Abaqus-specified strain, *error*, and the gradient of that error with respect to the trial stress increment, *gradient*. The gradient is calculated analytically .That is, the following four values are generated:

$$\Delta\varepsilon_{ij}^{total}(t) = \Delta\varepsilon_{ij}^{NLVE}(t) + \Delta\varepsilon_{ij}^{VP}(t) - 2\Delta\varepsilon_{ij}^{NLVE}(t)\Delta\varepsilon_{ij}^{VP}(t)$$

$$S_{ij} = \frac{\partial\Delta\varepsilon_{ij}^{total}(t)}{\partial\Delta\sigma_{ij}^{trial}}$$

$$error = \sqrt{\sum_{i,j=1}^{3}\left(\Delta\varepsilon_{ij}^{total}(t) - \Delta\varepsilon_{ij}^{Abaqus}(t)\right)^2}$$

$$gradient = \frac{\partial error}{\partial\Delta\varepsilon_{ij}^{total}(t)} = \frac{\partial}{\partial\Delta\varepsilon_{ij}^{total}(t)}\sqrt{\sum_{i,j=1}^{3}\left(\Delta\varepsilon_{ij}^{total}(t) - \Delta\varepsilon_{ij}^{Abaqus}(t)\right)^2}$$

The value of the error is compared to a pre-defined tolerance, which for the present analysis is set to $1E-9$. If the error is less than the specified tolerance, the algorithm is considered to have converged and the trial stress increment is returned to Abaqus along with the inverse of the compliance matrix.

If the error is not less than the tolerance, the minimization algorithm is initiated. This algorithm employs the Polok-Ribiere variant of the conjugate gradient method to find the trial stresses which minimize the computed error in the strains. This technique assumes that the error of strain increments as a function of stress increments defined by the constitutive equation may be approximated locally as a quadratic form, such that:

$$f(\boldsymbol{x}) \sim c - \boldsymbol{b}\cdot\boldsymbol{x} + \frac{1}{2}\boldsymbol{x}\cdot\boldsymbol{A}\cdot\boldsymbol{x}$$

where bold characters indicate vectors or matrices and plain characters indicate scalar values. In this equation, f(x) is error and x is the vector of trial stress increments. If two vectors are constructed such that the following definitions hold, these vectors are the solution to the quadratic where **g** = **x** and **h** = **b**.

$$\boldsymbol{g}_{i+1} = \boldsymbol{g}_i - \boldsymbol{\lambda}_i \boldsymbol{A} \cdot \boldsymbol{h}_j \qquad \boldsymbol{h}_{i+1} = \boldsymbol{g}_{i+1} + \gamma_i \boldsymbol{h}_i \qquad i = 0,1,2,\ldots$$

These two vectors satisfy the orthogonality[6] and conjugacy[7] conditions.

$$\boldsymbol{g}_i \cdot \boldsymbol{g}_j = 0 \qquad \boldsymbol{h}_i \cdot \boldsymbol{A} \cdot \boldsymbol{h}_j = 0 \qquad \boldsymbol{g}_i \cdot \boldsymbol{h}_j = 0 \qquad i \neq j$$

The scalars are defined by

$$\boldsymbol{\lambda}_i = \frac{\boldsymbol{g}_i \cdot \boldsymbol{g}_i}{\boldsymbol{h}_i \cdot \boldsymbol{A} \cdot \boldsymbol{h}_i} = \frac{\boldsymbol{g}_i \cdot \boldsymbol{h}_i}{\boldsymbol{h}_i \cdot \boldsymbol{A} \cdot \boldsymbol{h}_i} \qquad \gamma_i = \frac{\boldsymbol{g}_{i+1} \cdot \boldsymbol{g}_{i+1}}{\boldsymbol{g}_i \cdot \boldsymbol{g}_i}$$

At this point, the system is still unsolvable unless the matrix **A** is known. However, if the vector **h** is defined as the gradient of the vector **g**, the system can be solved without knowledge of the matrix **A**. Therefore, the trial stresses are placed in the vector **g** and the gradient which was calculated above in the second vector **h**, as defined below.

$$\boldsymbol{g} = \left\{\Delta\sigma_x^{trial}, \Delta\sigma_y^{trial}, \Delta\sigma_s^{trial}\right\}$$

$$\boldsymbol{h} = \left\{\frac{\partial error}{\partial \Delta\varepsilon_x^{total}(t)}, \frac{\partial error}{\partial \Delta\varepsilon_y^{total}(t)}, \frac{\partial error}{\partial \Delta\varepsilon_s^{total}(t)}\right\}$$

The Polok-Ribiere variant of the conjugate gradient method introduces a slight change to the method outlined above by modifying the definition of the scalar γ to the following.

$$\gamma_i = \frac{(\boldsymbol{g}_{i+1} - \boldsymbol{g}_i) \cdot \boldsymbol{g}_{i+1}}{\boldsymbol{g}_i \cdot \boldsymbol{g}_i}$$

This modification is made because it is unlikely that the error function actually has a quadratic form. Therefore, even though the minimum of the quadratic estimate is found by the procedure above, this may not be the true minimum of the error function. The alternate definition of γ is thought to perform

[6] The vectors **u** and **v** are orthogonal if **u**·**v**=0

[7] The vectors **u** and **v** are conjugate with respect to a matrix **A** if $\mathbf{u}^T$·**A**·**v**=0

the transition from the quadratic estimate to the actual functional shape more smoothly than the original definition.

The current vectors $\mathbf{g}_i$ and $\mathbf{h}_i$ are obtained from the current trial stresses and the current strain error, as described above. The updated vectors $\mathbf{g}_{i+1}$ and $\mathbf{h}_{i+1}$ are determined by performing line minimization. That is, for the strain error defined previously as a function of the trial stress increments in $\mathbf{g}_i$, a subroutine determines the minimum of that error function along the direction defined by the gradient $\mathbf{h}_i$. Once the location of that minimum is determined, the original gradient $\mathbf{h}_i$ is updated to express the actual distance moved from $\mathbf{g}_i$ to the new minimum, $\mathbf{h}_{i+1}$, and the new minimum is returned to the conjugate gradient subroutine as the vector $\mathbf{g}_{i+1}$.

The location of new minimum is determined to within a pre-defined tolerance. That is, once the magnitude of change in the error function is smaller that some set value, the line minimization is said to have converged along a particular direction. This particular line minimization routine relies on Brent's method to perform minimize the function along the line. Brent's method uses parabolic interpolation between points on the error function to estimate potential locations of minima within a bracketed range. That is, if the value of the error function at three distinct points is known, a parabolic fit to those points is made and the location of the minimum of the parabola within that range is determined. The value of the error function at that minimum location is calculated and if it is less than the value at any of the bracketing points, the location of the minimum is used to update the bracketing range. In this manner, the location of the actual minimum is bracketed to within successively smaller ranges until the minimum of the error function is located to within a pre-defined tolerance or the minimization routine reaches a limiting number of iterations.

Appendix E. Derivation of Non-linear Viscoelastic Jacobian Matrix

The Jacobian matrix is defined as the partial derivate of the incremental stress vector with respect to the incremental strain vector. Because the constitutive equations are formulated with strain in terms of stress, the Jacobian matrix can be determined from taking the inverse of the compliance matrix, which is the partial derivative of the incremental strains with respect to the incremental stresses. The derivation of this matrix for the non-linear viscoelastic constitutive equation is outlined below.

1. Recursive Equations

Begin with the recursive form of the multiaxial constitutive equation, where λ_n is the inverse of each element's characteristic time τ_n.

$$\varepsilon_{ij}^t = \left(g_0^t D_0 + g_1^t g_2^t \sum_{n=1}^{N} D_n \left(1 - \frac{1 - \exp(-\Delta\varphi\lambda_n)}{\Delta\varphi\lambda_n} \right) \right) \sigma_{ij}^t - g_1^t \sum_{n=1}^{N} D_n \left(q_{nij}^{t-\Delta t} \exp(-\Delta\varphi\lambda_n) - g_2^{t-\Delta t} \sigma_{ij}^{t-\Delta t} \frac{1 - \exp(-\Delta\varphi\lambda_n)}{\Delta\varphi\lambda_n} \right)$$

For this application, the total stress and strain are divided into deviatoric and dilatational components:

$$\sigma_{ij}^t = s_{ij}^t + \frac{1}{3}\sigma_{kk}^t \delta_{ij}$$

$$\varepsilon_{ij}^t = e_{ij}^t + \frac{1}{3}\varepsilon_{kk}^t \delta_{ij}$$

There are now two integral constitutive relationships, one for deviatoric and one for dilatational:

$$e_{ij}^t = \frac{1}{2}\left(g_0^t J_0 + g_1^t g_2^t \sum_{n=1}^{N} J_n \left(1 - \frac{1 - \exp(-\Delta\varphi\lambda_n)}{\Delta\varphi\lambda_n} \right) \right) s_{ij}^t - \frac{1}{2} g_1^t \sum_{n=1}^{N} J_n \left(q_{nij}^{t-\Delta t} \exp(-\Delta\varphi\lambda_n) - g_2^{t-\Delta t} s_{ij}^{t-\Delta t} \frac{1 - \exp(-\Delta\varphi\lambda_n)}{\Delta\varphi\lambda_n} \right)$$

$$q_{nij}^t = \exp(-\Delta\varphi\lambda_n) q_{nij}^{t-\Delta t} + \left(g_2^t s_{ij}^t - g_2^{t-\Delta t} s_{ij}^{t-\Delta t} \right) \frac{1 - \exp(-\Delta\varphi\lambda_n)}{\Delta\varphi\lambda_n}$$

$$\varepsilon_{kk}^t = \left(g_0^t B_0 + g_1^t g_2^t \sum_{n=1}^{N} B_n \left(1 - \frac{1 - \exp(-\Delta\varphi\lambda_n)}{\Delta\varphi\lambda_n} \right) \right) \sigma_{kk}^t - g_1^t \sum_{n=1}^{N} D_n \left(q_{nkk}^{t-\Delta t} \exp(-\Delta\varphi\lambda_n) - g_2^{t-\Delta t} \sigma_{kk}^{t-\Delta t} \frac{1 - \exp(-\Delta\varphi\lambda_n)}{\Delta\varphi\lambda_n} \right)$$

$$q_{nkk}^t = \exp(-\Delta\varphi\lambda_n) q_{nkk}^{t-\Delta t} + \left(g_2^t \sigma_{kk}^t - g_2^{t-\Delta t} \sigma_{kk}^{t-\Delta t} \right) \frac{1 - \exp(-\Delta\varphi\lambda_n)}{\Delta\varphi\lambda_n}$$

In these equations, the nonlinear parameters and octahedral shear stress, respectively, are given by:

$$g_0^t = g0(t) = g0i(1) + g0i(2)\ acot\left(\bar{\sigma} - g0i(3)\right)$$

$$\bar{\sigma} = \sqrt{\frac{\left(\sigma_x - \sigma_y\right)^2 + (\sigma_x)^2 + \left(\sigma_y\right)^2 + 6\left(\tau_{xy}\right)^2}{2}}$$

2. Incremental Form of Recursive Equations

First, consider the deviatoric strains. The incremental deviatoric strain is given by:

$$\begin{aligned}
\Delta e_{ij}^t &= e_{ij}^t - e_{ij}^{t-\Delta t} \\
&= \frac{1}{2}\left(g_0^t J_0 + g_1^t g_2^t \sum_{n=1}^{N} J_n \left(1 - \frac{1-\exp(-\Delta\varphi\lambda_n)}{\Delta\varphi\lambda_n}\right)\right) s_{ij}^t \\
&- \frac{1}{2}\left(g_0^{t-\Delta t} J_0 + g_1^{t-\Delta t} g_2^{t-\Delta t} \sum_{n=1}^{N} J_n \left(1 - \frac{1-\exp\left(-\Delta\varphi^{t-\Delta t}\lambda_n\right)}{\Delta\varphi^{t-\Delta t}\lambda_n}\right)\right) s_{ij}^{t-\Delta t} \\
&- \frac{1}{2} g_1^t \sum_{n=1}^{N} J_n \left(q_{nij}^{t-\Delta t} \exp(-\Delta\varphi\lambda_n) - g_2^{t-\Delta t} s_{ij}^{t-\Delta t} \frac{1-\exp(-\Delta\varphi\lambda_n)}{\Delta\varphi\lambda_n}\right) \\
&- \frac{1}{2} g_1^{t-\Delta t} \sum_{n=1}^{N} J_n \left(q_{nij}^{t-\Delta t-\Delta t} \exp\left(-\Delta\varphi^{t-\Delta t}\lambda_n\right)\right. \\
&\left. - g_2^{t-\Delta t-\Delta t} s_{ij}^{t-\Delta t-\Delta t} \frac{1-\exp\left(-\Delta\varphi^{t-\Delta t}\lambda_n\right)}{\Delta\varphi^{t-\Delta t}\lambda_n}\right)
\end{aligned}$$

Simplifying the last two terms with the definition of q_{nij}^t gives:

$$\begin{aligned}
\Delta e_{ij}^t &= e_{ij}^t - e_{ij}^{t-\Delta t} \\
&= \frac{1}{2}\left(g_0^t J_0 + g_1^t g_2^t \sum_{n=1}^{N} J_n \left(1 - \frac{1-\exp(-\Delta\varphi\lambda_n)}{\Delta\varphi\lambda_n}\right)\right) s_{ij}^t \\
&- \frac{1}{2}\left(g_0^{t-\Delta t} J_0 + g_1^{t-\Delta t} g_2^{t-\Delta t} \sum_{n=1}^{N} J_n \left(1 - \frac{1-\exp\left(-\Delta\varphi^{t-\Delta t}\lambda_n\right)}{\Delta\varphi^{t-\Delta t}\lambda_n}\right)\right) s_{ij}^{t-\Delta t} \\
&- \frac{1}{2} \sum_{n=1}^{N} J_n \left(g_1^t \exp(-\Delta\varphi\lambda_n) - g_1^{t-\Delta t}\right) q_{nij}^{t-\Delta t} \\
&- \frac{1}{2} g_2^{t-\Delta t} \sum_{n=1}^{N} J_n \left[g_1^{t-\Delta t} \frac{1-\exp\left(-\Delta\varphi^{t-\Delta t}\lambda_n\right)}{\Delta\varphi^{t-\Delta t}\lambda_n} - g_1^t \frac{1-\exp(-\Delta\varphi\lambda_n)}{\Delta\varphi\lambda_n}\right] s_{ij}^{t-\Delta t}
\end{aligned}$$

Now introduce some simplified notation:

$$Jbar = \frac{1}{2}\left(g_0^t J_0 + g_1^t g_2^t \sum_{n=1}^{N} J_n \left(1 - \frac{1-\exp(-\Delta\varphi\lambda_n)}{\Delta\varphi\lambda_n}\right)\right)$$

$$Jbar^{old} = \frac{1}{2}\left(g_0^{t-\Delta t}J_0 + g_1^{t-\Delta t}g_2^{t-\Delta t}\sum_{n=1}^{N} J_n\left(1 - \frac{1-\exp\left(-\Delta\varphi^{t-\Delta t}\lambda_n\right)}{\Delta\varphi^{t-\Delta t}\lambda_n}\right)\right)$$

$$JHSum1 = \frac{1}{2}\sum_{n=1}^{N} J_n\left(g_1^t\exp(-\Delta\varphi\lambda_n) - g_1^{t-\Delta t}\right)q_{nij}^{t-\Delta t}$$

$$JHSum2 = \frac{1}{2}g_2^{t-\Delta t}s_{ij}^{t-\Delta t}\sum_{n=1}^{N} J_n\left[g_1^{t-\Delta t}\frac{1-\exp\left(-\Delta\varphi^{t-\Delta t}\lambda_n\right)}{\Delta\varphi^{t-\Delta t}\lambda_n} - g_1^t\frac{1-\exp(-\Delta\varphi\lambda_n)}{\Delta\varphi\lambda_n}\right]$$

The incremental deviatoric strain can now be written:

$$\Delta e_{ij}^t = e_{ij}^t - e_{ij}^{t-\Delta t} = Jbars_{ij}^t - Jbar^{old}s_{ij}^{t-\Delta t} - JHSum1 - JHSum2$$

Similarly, the incremental dilatational strain can be written:

$$\Delta\varepsilon_{kk}^t = \varepsilon_{kk}^t - \varepsilon_{kk}^{t-\Delta t} = Bbar\sigma_{kk}^t - Bbar^{old}\sigma_{kk}^{t-\Delta t} - BHSum1 - BHSum2$$

Where

$$Bbar = \frac{1}{3}\left(g_0^tB_0 + g_1^tg_2^t\sum_{n=1}^{N} B_n\left(1 - \frac{1-\exp(-\Delta\varphi\lambda_n)}{\Delta\varphi\lambda_n}\right)\right)$$

$$Bbar^{old} = \frac{1}{3}\left(g_0^{t-\Delta t}B_0 + g_1^{t-\Delta t}g_2^{t-\Delta t}\sum_{n=1}^{N} B_n\left(1 - \frac{1-\exp\left(-\Delta\varphi^{t-\Delta t}\lambda_n\right)}{\Delta\varphi^{t-\Delta t}\lambda_n}\right)\right)$$

$$BHSum1 = \frac{1}{3}\sum_{n=1}^{N} B_n\left(g_1^t\exp(-\Delta\varphi\lambda_n) - g_1^{t-\Delta t}\right)q_{nkk}^{t-\Delta t}$$

$$BHSum2 = \frac{1}{3}g_2^{t-\Delta t}\sum_{n=1}^{N} B_n\left[g_1^{t-\Delta t}\frac{1-\exp\left(-\Delta\varphi^{t-\Delta t}\lambda_n\right)}{\Delta\varphi^{t-\Delta t}\lambda_n} - g_1^t\frac{1-\exp(-\Delta\varphi\lambda_n)}{\Delta\varphi\lambda_n}\right]\sigma_{kk}^{t-\Delta t}$$

3. Jacobian derivation

If stresses were known, the strain increments could be calculated using these equations. However, in this application the strains are known and the stresses must be determined. A nonlinear regression algorithm is used to converge on the proper stress increments. To guide the algorithm, a Jacobian is defined. This application assumes plane stress, so the only non-zero stress components are $\Delta\sigma_x^t, \Delta\sigma_y^t, and\ \Delta\tau_{xy}^t$. This results in a matrix with the following components:

$$\bar{\bar{J}} = \begin{bmatrix} \frac{\partial \Delta \varepsilon_x^t}{\partial \Delta \sigma_x^t} & \frac{\partial \Delta \varepsilon_x^t}{\partial \Delta \sigma_y^t} & 0 \\ \frac{\partial \Delta \varepsilon_y^t}{\partial \Delta \sigma_x^t} & \frac{\partial \Delta \varepsilon_y^t}{\partial \Delta \sigma_y^t} & 0 \\ 0 & 0 & \frac{\partial \Delta \gamma_{xy}^t}{\partial \Delta \tau_{xy}^t} \end{bmatrix} = \begin{bmatrix} S_{11} & S_{12} & 0 \\ S_{21} & S_{22} & 0 \\ 0 & 0 & S_{33} \end{bmatrix}$$

3.1 Derive S11

To evaluate this matrix, begin with the S_{11} term:

$$S_{11} = \frac{\partial \Delta \varepsilon_x^t}{\partial \Delta \sigma_x^t} = \frac{\partial \Delta e_x^t}{\partial \Delta \sigma_x^t} + \frac{1}{3}\frac{\partial \Delta \varepsilon_{kk}^t}{\partial \Delta \sigma_x^t}$$

3.1.1 Deviatoric component of S11

The partial derivative of the deviatoric component is evaluated in the manner below:

$$\frac{\partial \Delta e_x^t}{\partial \Delta \sigma_x^t} = \frac{\partial}{\partial \Delta \sigma_x^t}\left(Jbars_x^t - Jbar^{old} s_x^{t-\Delta t} - JHSum1 - JHSum2 \right)$$

$$\frac{\partial \Delta e_x^t}{\partial \Delta \sigma_x^t} = \frac{\partial Jbars_x^t}{\partial \Delta \sigma_x^t} - \frac{\partial Jbar^{old} s_x^{t-\Delta t}}{\partial \Delta \sigma_x^t} - \frac{\partial JHSum1}{\partial \Delta \sigma_x^t} - \frac{\partial JHSum2}{\partial \Delta \sigma_x^t}$$

product rule:

$$\frac{\partial \Delta e_x^t}{\partial \Delta \sigma_x^t} = s_x^t \frac{\partial Jbar}{\partial \Delta \sigma_x^t} + Jbar \frac{\partial s_x^t}{\partial \Delta \sigma_x^t} - s_x^{t-\Delta t} \frac{\partial Jbar^{old}}{\partial \Delta \sigma_x^t} - Jbar^{old} \frac{\partial s_x^{t-\Delta t}}{\partial \Delta \sigma_x^t} - \frac{\partial JHSum1}{\partial \Delta \sigma_x^t} - \frac{\partial JHSum2}{\partial \Delta \sigma_x^t}$$

recognizing that the new stress increment has no effect on the results of previous increments:

$$\frac{\partial \Delta e_x^t}{\partial \Delta \sigma_x^t} = Jbar \frac{\partial s_x^t}{\partial \Delta \sigma_x^t} + s_x^t \frac{\partial Jbar}{\partial \Delta \sigma_x^t} - \frac{\partial JHSum1}{\partial \Delta \sigma_x^t} - \frac{\partial JHSum2}{\partial \Delta \sigma_x^t}$$

3.1.1.a $\frac{\partial s_x^t}{\partial \Delta \sigma_x^t}$

Using the definition of the current stress as a function of the stress increment :

$$\sigma_x^t = \sigma_x^{t-\Delta t} + \Delta \sigma_x^t$$

And the definition of deviatoric stress:

$$s_x^t = \sigma_x^t - \frac{1}{3}\sigma_{kk}^t = \sigma_x^t - \frac{1}{3}\left(\sigma_x^t + \sigma_y^t\right)$$

$$s_x^t = \frac{2}{3}\sigma_x^t - \frac{1}{3}\sigma_y^t$$

$$s_x^t = \frac{2}{3}\sigma_x^{t-\Delta t} + \frac{2}{3}\Delta\sigma_x^t - \frac{1}{3}\sigma_y^t$$

$$\frac{\partial s_x^t}{\partial \Delta\sigma_x^t} = \frac{\partial}{\partial \Delta\sigma_x^t}\left(\frac{2}{3}\sigma_x^{t-\Delta t} + \frac{2}{3}\Delta\sigma_x^t - \frac{1}{3}\sigma_y^t\right)$$

$$\frac{\partial s_x^t}{\partial \Delta\sigma_x^t} = \frac{2}{3}$$

and recognizing that the partial derivative of this equation is simply 1 gives:

$$\frac{\partial \Delta e_x^t}{\partial \Delta\sigma_x^t} = \frac{2}{3}Jbar + \frac{\partial}{\partial \Delta\sigma_x^t}(s_x^t Jbar - JHSum1 - JHSum2)$$

$$\frac{\partial \Delta e_x^t}{\partial \Delta\sigma_x^t} = \frac{2}{3}Jbar + \frac{\partial \bar{\sigma}}{\partial \Delta\sigma_x^t}\frac{\partial}{\partial \sigma}(s_x^t Jbar - JHSum1 - JHSum2)$$

$$\frac{\partial \Delta e_x^t}{\partial \Delta\sigma_x^t} = \frac{2}{3}Jbar + \frac{\partial \bar{\sigma}}{\partial \Delta\sigma_x^t}\left(s_x^t\frac{\partial Jbar}{\partial \bar{\sigma}} - \frac{\partial JHSum1}{\partial \bar{\sigma}} - \frac{\partial JHSum2}{\partial \bar{\sigma}}\right)$$

The first partial derivative can be evaluated as below:

$$\frac{\partial \bar{\sigma}}{\partial \Delta\sigma_x^t} = \frac{\partial}{\partial \Delta\sigma_x^t}\sqrt{\frac{\left(\sigma_x - \sigma_y\right)^2 + (\sigma_x)^2 + \left(\sigma_y\right)^2 + 6\left(\tau_{xy}\right)^2}{2}}$$

$$\frac{\partial \bar{\sigma}}{\partial \Delta\sigma_x^t} = \frac{\partial}{\partial \Delta\sigma_x^t}\left(\frac{\left(\sigma_x - \sigma_y\right)^2 + (\sigma_x)^2 + \left(\sigma_y\right)^2 + 6\left(\tau_{xy}\right)^2}{2}\right)^{1/2}$$

$$\frac{\partial \bar{\sigma}}{\partial \Delta\sigma_x^t}$$

$$= \frac{1}{2}\left(\frac{\left(\sigma_x - \sigma_y\right)^2 + (\sigma_x)^2 + \left(\sigma_y\right)^2 + 6\left(\tau_{xy}\right)^2}{2}\right)^{-1/2}\frac{\partial}{\partial \Delta\sigma_x^t}\left(\frac{\left(\sigma_x - \sigma_y\right)^2 + (\sigma_x)^2 + \left(\sigma_y\right)^2 + 6\left(\tau_{xy}\right)^2}{2}\right)$$

$$\frac{\partial \bar{\sigma}}{\partial \Delta\sigma_x^t} = \frac{1}{2\bar{\sigma}}\frac{\partial}{\partial \Delta\sigma_x^t}\left(\frac{\left(\sigma_x - \sigma_y\right)^2 + (\sigma_x)^2 + \left(\sigma_y\right)^2 + 6\left(\tau_{xy}\right)^2}{2}\right)$$

$$\frac{\partial \bar{\sigma}}{\partial \Delta\sigma_x^t} = \frac{1}{4\bar{\sigma}}\frac{\partial}{\partial \Delta\sigma_x^t}\left(\left(\sigma_x - \sigma_y\right)^2 + (\sigma_x)^2 + \left(\sigma_y\right)^2 + 6\left(\tau_{xy}\right)^2\right)$$

$$\frac{\partial \bar{\sigma}}{\partial \Delta\sigma_x^t} = \frac{1}{4\bar{\sigma}}\frac{\partial}{\partial \Delta\sigma_x^t}\left({\sigma_x}^2 - 2\sigma_x\sigma_y + {\sigma_y}^2 + {\sigma_x}^2 + {\sigma_y}^2 + 6\left(\tau_{xy}\right)^2\right)$$

$$\frac{\partial \bar{\sigma}}{\partial \Delta\sigma_x^t} = \frac{1}{4\bar{\sigma}} \frac{\partial}{\partial \Delta\sigma_x^t} \left(2{\sigma_x}^2 - 2\sigma_x\sigma_y + 2{\sigma_y}^2 + 6\left(\tau_{xy}\right)^2 \right)$$

$$\frac{\partial \bar{\sigma}}{\partial \Delta\sigma_x^t} = \frac{1}{4\bar{\sigma}} \frac{\partial}{\partial \Delta\sigma_x^t} \left(2\left({\sigma_x}^{old} + \Delta\sigma_x^t\right)^2 - 2\left({\sigma_x}^{old} + \Delta\sigma_x^t\right)\sigma_y + 2{\sigma_y}^2 + 6\left(\tau_{xy}\right)^2 \right)$$

$$\frac{\partial \bar{\sigma}}{\partial \Delta\sigma_x^t} = \frac{1}{4\bar{\sigma}} \frac{\partial}{\partial \Delta\sigma_x^t} \left(2\left({\sigma_x}^{old}\right)^2 + 2\left(2{\sigma_x}^{old}\Delta\sigma_x^t\right) + 2(\Delta\sigma_x^t)^2 - 2\left({\sigma_x}^{old} + \Delta\sigma_x^t\right)\sigma_y + 2{\sigma_y}^2 + 6\left(\tau_{xy}\right)^2 \right)$$

$$\frac{\partial \bar{\sigma}}{\partial \Delta\sigma_x^t} = \frac{1}{4\bar{\sigma}} \left(4{\sigma_x}^{old} + 4\Delta\sigma_x^t - 2\sigma_y \right)$$

$$\frac{\partial \bar{\sigma}}{\partial \Delta\sigma_x^t} = \frac{1}{2\bar{\sigma}} \left(2\sigma_x - \sigma_y \right)$$

Now consider the remaining terms individually.

3.1.1.b $\partial Jbar$:

First, evaluate $\partial Jbar$:

$$\frac{\partial Jbar}{\partial \bar{\sigma}} = \frac{1}{2} \frac{\partial}{\partial \bar{\sigma}} \left(g_0^t J_0 + g_1^t g_2^t \sum_{n=1}^{N} J_n \left(1 - \frac{1 - \exp(-\Delta\varphi\lambda_n)}{\Delta\varphi\lambda_n} \right) \right)$$

For clarity, write each nonlinear parameter explicitly in terms of the octahedral shear stress:

$$\frac{\partial Jbar}{\partial \bar{\sigma}} = \frac{1}{2} \frac{\partial}{\partial \bar{\sigma}} \left(g_0^t(\bar{\sigma}) J_0 + g_1^t(\bar{\sigma}) g_2^t(\bar{\sigma}) \sum_{n=1}^{N} J_n \left(1 - \frac{1 - \exp\left(-{\Delta t}/{\tau_n a_\sigma(\bar{\sigma})}\right)}{{\Delta t}/{\tau_n a_\sigma(\bar{\sigma})}} \right) \right)$$

Expand:

$$\frac{\partial Jbar}{\partial \bar{\sigma}} = \frac{1}{2} \frac{\partial}{\partial \bar{\sigma}} \left(g_0^t(\bar{\sigma}) J_0 + g_1^t(\bar{\sigma}) g_2^t(\bar{\sigma}) \sum_{n=1}^{N} J_n - g_1^t(\bar{\sigma}) g_2^t(\bar{\sigma}) \sum_{n=1}^{N} J_n \frac{1}{{\Delta t}/{\tau_n a_\sigma(\bar{\sigma})}} + g_1^t(\bar{\sigma}) g_2^t(\bar{\sigma}) \sum_{n=1}^{N} J_n \frac{\exp\left(-{\Delta t}/{\tau_n a_\sigma(\bar{\sigma})}\right)}{{\Delta t}/{\tau_n a_\sigma(\bar{\sigma})}} \right)$$

$$\frac{\partial Jbar}{\partial \bar{\sigma}} = \frac{1}{2} \frac{\partial}{\partial \bar{\sigma}} \left(g_0^t(\bar{\sigma}) J_0 + g_1^t(\bar{\sigma}) g_2^t(\bar{\sigma}) \sum_{n=1}^{N} J_n - g_1^t(\bar{\sigma}) g_2^t(\bar{\sigma}) \sum_{n=1}^{N} J_n \frac{\tau_n a_\sigma(\bar{\sigma})}{\Delta t} + g_1^t(\bar{\sigma}) g_2^t(\bar{\sigma}) \sum_{n=1}^{N} J_n \frac{\tau_n a_\sigma(\bar{\sigma})}{\Delta t} \exp\left(-{\Delta t}/{\tau_n a_\sigma(\bar{\sigma})}\right) \right)$$

Distribute:

Appendix E

$$\frac{\partial Jbar}{\partial \bar{\sigma}} = \frac{1}{2}\left[\frac{\partial}{\partial \bar{\sigma}} g_0^t(\bar{\sigma}) J_0 + \frac{\partial}{\partial \bar{\sigma}} g_1^t(\bar{\sigma}) g_2^t(\bar{\sigma}) \sum_{n=1}^{N} J_n - \frac{\partial}{\partial \bar{\sigma}} g_1^t(\bar{\sigma}) g_2^t(\bar{\sigma}) \sum_{n=1}^{N} J_n \frac{\tau_n a_\sigma(\bar{\sigma})}{\Delta t} + \frac{\partial}{\partial \bar{\sigma}} g_1^t(\bar{\sigma}) g_2^t(\bar{\sigma}) \sum_{n=1}^{N} J_n \frac{\tau_n a_\sigma(\bar{\sigma})}{\Delta t} \exp\left(-{}^{\Delta t}/_{\tau_n a_\sigma(\bar{\sigma})}\right)\right]$$

This is getting very busy. Introduce the following notation:

$$\frac{\partial Jbar}{\partial \bar{\sigma}} = \frac{\partial}{\partial \bar{\sigma}} \frac{1}{2}[A + B - C + D]$$

Evaluate A:

$$\frac{\partial}{\partial \bar{\sigma}} A = \frac{\partial}{\partial \bar{\sigma}} g_0^t(\bar{\sigma}) J_0$$

By the chain rule, this is equivalent to:

$$\frac{\partial}{\partial \bar{\sigma}} A = J_0 \frac{\partial g_0^t}{\partial \bar{\sigma}}$$

The remaining partial derivative is:

$$\frac{\partial g_0^t}{\partial \bar{\sigma}} = \frac{\partial}{\partial \bar{\sigma}}[(1 + g0i(1)\bar{\sigma} - g0i(1)\sigma_0 + g0i(2)\bar{\sigma}^2 - 2g0i(2)\bar{\sigma}\sigma_0 + g0i(2){\sigma_0}^2)]$$

$$\frac{\partial g_0^t}{\partial \bar{\sigma}} = g0i(1) - 2g0i(2)\sigma_0 + 2g0i(2)\bar{\sigma}$$

$$\frac{\partial g_0^t}{\partial \bar{\sigma}} = \left(g0i(1) + 2g0i(2)(\bar{\sigma} - \sigma_0)\right)$$

Now, term B:

$$\frac{\partial}{\partial \bar{\sigma}} B = \frac{\partial}{\partial \bar{\sigma}} g_1^t(\bar{\sigma}) g_2^t(\bar{\sigma}) \sum_{n=1}^{N} J_n$$

$$\frac{\partial}{\partial \bar{\sigma}} B = g_2^t(\bar{\sigma}) \sum_{n=1}^{N} J_n \frac{\partial}{\partial \bar{\sigma}} g_1^t(\bar{\sigma}) + g_1^t(\bar{\sigma}) \sum_{n=1}^{N} J_n \frac{\partial}{\partial \bar{\sigma}} g_2^t(\bar{\sigma})$$

$$\frac{\partial}{\partial \bar{\sigma}} B = \left(\frac{\partial g_1^t}{\partial \bar{\sigma}} g2 + g1 \frac{\partial g_2^t}{\partial \bar{\sigma}}\right) \sum_{n=1}^{N} J_n$$

And term C:

$$\frac{\partial}{\partial\bar{\sigma}}C=\frac{\partial}{\partial\bar{\sigma}}g_1^t(\bar{\sigma})g_2^t(\bar{\sigma})\sum_{n=1}^{N}J_n\frac{\tau_n a_\sigma(\bar{\sigma})}{\Delta t}$$

$$\frac{\partial}{\partial\bar{\sigma}}C=\left(\frac{\partial g_1^t}{\partial\bar{\sigma}}g2a_\sigma+g1\frac{\partial g_2^t}{\partial\bar{\sigma}}a_\sigma+g1g2\frac{\partial a_\sigma}{\partial\bar{\sigma}}\right)\sum_{n=1}^{N}J_n\frac{\tau_n}{\Delta t}$$

And term D:

$$\frac{\partial}{\partial\bar{\sigma}}D=\frac{\partial}{\partial\bar{\sigma}}g_1^t(\bar{\sigma})g_2^t(\bar{\sigma})\sum_{n=1}^{N}J_n\frac{\tau_n a_\sigma(\bar{\sigma})}{\Delta t}\exp\left(-{}^{\Delta t}/_{\tau_n a_\sigma(\bar{\sigma})}\right)$$

$$\begin{aligned}\frac{\partial}{\partial\bar{\sigma}}D=\sum_{n=1}^{N}J_n\frac{\tau_n}{\Delta t}\Bigg(&\frac{\partial g_1^t}{\partial\bar{\sigma}}g2a_\sigma\exp\left(-{}^{\Delta t}/_{\tau_n a_\sigma(\bar{\sigma})}\right)\\&+g1\frac{\partial g_2^t}{\partial\bar{\sigma}}a_\sigma\exp\left(-{}^{\Delta t}/_{\tau_n a_\sigma(\bar{\sigma})}\right)+g1g2\frac{\partial a_\sigma}{\partial\bar{\sigma}}\exp\left(-{}^{\Delta t}/_{\tau_n a_\sigma(\bar{\sigma})}\right)\\&+g1g2a_\sigma\frac{\partial a_\sigma}{\partial\bar{\sigma}}\left({}^{\Delta t}/_{\tau_n a_\sigma(\bar{\sigma})a_\sigma(\bar{\sigma})}\right)\exp\left(-{}^{\Delta t}/_{\tau_n a_\sigma(\bar{\sigma})}\right)\Bigg)\end{aligned}$$

3.1.1.c $\frac{\partial JHSum1}{\partial\bar{\sigma}}$:

$$\frac{\partial JHSum1}{\partial\bar{\sigma}}=\frac{\partial}{\partial\bar{\sigma}}\left(\frac{1}{2}\sum_{n=1}^{N}J_n\left(g_1^t\exp(-\Delta\varphi\lambda_n)-g_1^{t-\Delta t}\right)q_{nij}^{t-\Delta t}\right)$$

$$\frac{\partial JHSum1}{\partial\bar{\sigma}}=\frac{1}{2}\left(\sum_{n=1}^{N}J_n q_{nij}^{t-\Delta t}\left(\frac{\partial}{\partial\bar{\sigma}}g_1^t\exp(-\Delta\varphi\lambda_n)-\frac{\partial}{\partial\bar{\sigma}}g_1^{t-\Delta t}\right)\right)$$

$$\frac{\partial JHSum1}{\partial\bar{\sigma}}=\frac{1}{2}\left(\sum_{n=1}^{N}J_n q_{nij}^{t-\Delta t}\left(\frac{\partial g_1^t}{\partial\bar{\sigma}}\exp(-\Delta\varphi\lambda_n)+g_1^t\frac{\partial a_\sigma}{\partial\bar{\sigma}}\left({}^{\Delta t}/_{\tau_n a_\sigma(\bar{\sigma})a_\sigma(\bar{\sigma})}\right)\exp\left(-{}^{\Delta t}/_{\tau_n a_\sigma(\bar{\sigma})}\right)\right)\right)$$

3.1.1.d $\frac{\partial JHSum2}{\partial\bar{\sigma}}$:

$$\frac{\partial JHSum2}{\partial\bar{\sigma}}=\frac{\partial}{\partial\bar{\sigma}}\left(\frac{1}{2}g_2^{t-\Delta t}\sum_{n=1}^{N}J_n\left[g_1^{t-\Delta t}\frac{1-\exp\left(-\Delta\varphi^{t-\Delta t}\lambda_n\right)}{\Delta\varphi^{t-\Delta t}\lambda_n}-g_1^t\frac{1-\exp(-\Delta\varphi\lambda_n)}{\Delta\varphi\lambda_n}\right]s_{ij}^{t-\Delta t}\right)$$

$$\frac{\partial JHSum2}{\partial\bar{\sigma}}=\frac{1}{2}g_2^{t-\Delta t}s_{ij}^{t-\Delta t}\left(\sum_{n=1}^{N}J_n\left[\frac{\partial}{\partial\bar{\sigma}}g_1^{t-\Delta t}\frac{1-\exp\left(-\Delta\varphi^{t-\Delta t}\lambda_n\right)}{\Delta\varphi^{t-\Delta t}\lambda_n}-\frac{\partial}{\partial\bar{\sigma}}g_1^t\frac{1-\exp(-\Delta\varphi\lambda_n)}{\Delta\varphi\lambda_n}\right]\right)$$

$$\frac{\partial JHSum2}{\partial\bar{\sigma}}=\frac{1}{2}g_2^{t-\Delta t}s_{ij}^{t-\Delta t}\left(\sum_{n=1}^{N}J_n\left[-\frac{\partial}{\partial\bar{\sigma}}g_1^t(\Delta\varphi\lambda_n)^{-1}+\frac{\partial}{\partial\bar{\sigma}}g_1^t(\Delta\varphi\lambda_n)^{-1}\exp(-\Delta\varphi\lambda_n)\right]\right)$$

$$\frac{\partial JHSum2}{\partial \bar{\sigma}} = \frac{1}{2} g_2^{t-\Delta t} s_{ij}^{t-\Delta t} \left(\sum_{n=1}^{N} J_n \left[-\frac{\partial}{\partial \bar{\sigma}} g_1^t \frac{\tau_n a_\sigma(\bar{\sigma})}{\Delta t} + \frac{\partial}{\partial \bar{\sigma}} g_1^t \frac{\tau_n a_\sigma(\bar{\sigma})}{\Delta t} \exp\left(-\frac{\Delta t}{\tau_n a_\sigma(\bar{\sigma})} \right) \right] \right)$$

$$\frac{\partial JHSum2}{\partial \bar{\sigma}} = \frac{1}{2} g_2^{t-\Delta t} s_{ij}^{t-\Delta t} \left(\sum_{n=1}^{N} J_n \left[-\frac{\tau_n}{\Delta t} \frac{\partial}{\partial \bar{\sigma}} g_1^t a_\sigma(\bar{\sigma}) + \frac{\tau_n}{\Delta t} \frac{\partial}{\partial \bar{\sigma}} g_1^t a_\sigma(\bar{\sigma}) \exp\left(-\frac{\Delta t}{\tau_n a_\sigma(\bar{\sigma})} \right) \right] \right)$$

$$\begin{aligned} \frac{\partial JHSum2}{\partial \bar{\sigma}} = \frac{1}{2} g_2^{t-\Delta t} s_{ij}^{t-\Delta t} \Bigg(\sum_{n=1}^{N} J_n \Bigg[& -\frac{\tau_n}{\Delta t} \left(\frac{\partial g_1^t}{\partial \bar{\sigma}} a_\sigma(\bar{\sigma}) + g_1^t \frac{\partial a_\sigma(\bar{\sigma})}{\partial \bar{\sigma}} \right) \\ & + \frac{\tau_n}{\Delta t} \left(\frac{\partial g_1^t}{\partial \bar{\sigma}} a_\sigma(\bar{\sigma}) \exp\left(-\frac{\Delta t}{\tau_n a_\sigma(\bar{\sigma})} \right) + g_1^t \frac{\partial a_\sigma(\bar{\sigma})}{\partial \bar{\sigma}} \exp\left(-\frac{\Delta t}{\tau_n a_\sigma(\bar{\sigma})} \right) \right. \\ & \left. + g_1^t a_\sigma(\bar{\sigma}) \frac{\partial a_\sigma}{\partial \bar{\sigma}} \left({}^{\Delta t}/_{\tau_n a_\sigma(\bar{\sigma}) a_\sigma(\bar{\sigma})} \right) \exp\left(-{}^{\Delta t}/_{\tau_n a_\sigma(\bar{\sigma})} \right) \right) \Bigg] \Bigg) \end{aligned}$$

$$\begin{aligned} \frac{\partial JHSum2}{\partial \bar{\sigma}} = \frac{1}{2} g_2^{t-\Delta t} s_{ij}^{t-\Delta t} \Bigg(\sum_{n=1}^{N} J_n \frac{\tau_n}{\Delta t} \Bigg[& -\left(\frac{\partial g_1^t}{\partial \bar{\sigma}} a_\sigma(\bar{\sigma}) + g_1^t \frac{\partial a_\sigma(\bar{\sigma})}{\partial \bar{\sigma}} \right) \\ & + \left(\frac{\partial g_1^t}{\partial \bar{\sigma}} a_\sigma(\bar{\sigma}) \exp\left(-\frac{\Delta t}{\tau_n a_\sigma(\bar{\sigma})} \right) + g_1^t \frac{\partial a_\sigma(\bar{\sigma})}{\partial \bar{\sigma}} \exp\left(-\frac{\Delta t}{\tau_n a_\sigma(\bar{\sigma})} \right) \right. \\ & \left. + g_1^t a_\sigma(\bar{\sigma}) \frac{\partial a_\sigma}{\partial \bar{\sigma}} \left({}^{\Delta t}/_{\tau_n a_\sigma(\bar{\sigma}) a_\sigma(\bar{\sigma})} \right) \exp\left(-{}^{\Delta t}/_{\tau_n a_\sigma(\bar{\sigma})} \right) \right) \Bigg] \Bigg) \end{aligned}$$

3.1.2 Dilatational component of S11

Now, back to the total strain equation. The partial derivative of the dilatational component is also need and is evaluated analogously to the deviatoric term

$$\frac{\partial \Delta \varepsilon_{kk}^t}{\partial \Delta \sigma_x^t} = \frac{\partial}{\partial \Delta \sigma_x^t} \left(Bbar \sigma_{kk}^t - Bbar^{old} \sigma_{kk}^{t-\Delta t} - BHSum1 - BHSum2 \right)$$

recognizing that the new stress increment has no effect on the results of previous increments:

$$\frac{\partial \Delta \varepsilon_{kk}^t}{\partial \Delta \sigma_x^t} = Bbar \frac{\partial}{\partial \Delta \sigma_x^t} \sigma_{kk}^t + \sigma_{kk}^t \frac{\partial}{\partial \Delta \sigma_x^t} Bbar - \frac{\partial}{\partial \Delta \sigma_x^t} BHSum1 - \frac{\partial}{\partial \Delta \sigma_x^t} BHSum2$$

3.1.2.a $\frac{\partial \sigma_{kk}^t}{\partial \Delta \sigma_x^t}$

Using the definition of the current stress as a function of the stress increment :

$$\sigma_x^t = \sigma_x^{t-\Delta t} + \Delta \sigma_x^t$$

And the definition of deviatoric stress:

$$\sigma_{kk}^t = \sigma_x^{t-\Delta t} + \Delta \sigma_x^t + \sigma_y^t$$

$$\frac{\partial \sigma_{kk}^t}{\partial \Delta \sigma_x^t} = \frac{\partial}{\partial \Delta \sigma_x^t}\left(\sigma_x^{t-\Delta t} + \Delta \sigma_x^t + \sigma_y^t\right)$$

$$\frac{\partial \sigma_{kk}^t}{\partial \Delta \sigma_x^t} = 1$$

and recognizing that the partial derivative of this equation is simply 1 gives:

$$\frac{\partial \Delta \varepsilon_{kk}^t}{\partial \Delta \sigma_x^t} = Bbar + \sigma_{kk}^t \frac{\partial Bbar}{\partial \Delta \sigma_x^t} - \frac{\partial BHSum1}{\partial \Delta \sigma_x^t} - \frac{\partial BHSum2}{\partial \Delta \sigma_x^t}$$

$$\frac{\partial \Delta \varepsilon_{kk}^t}{\partial \Delta \sigma_x^t} = Bbar + \frac{\partial \bar{\sigma}}{\partial \Delta \sigma_x^t}\left(\sigma_{kk}^t \frac{\partial Bbar}{\partial \bar{\sigma}} - \frac{\partial BHSum1}{\partial \bar{\sigma}} - \frac{\partial BHSum2}{\partial \bar{\sigma}}\right)$$

Now consider the remaining terms individually.

3.1.2.b $\partial Bbar$:

$$\frac{\partial Bbar}{\partial \bar{\sigma}} = \frac{1}{3}\frac{\partial}{\partial \bar{\sigma}}\left(g_0^t B_0 + g_1^t g_2^t \sum_{n=1}^{N} B_n \left(1 - \frac{1 - \exp(-\Delta \varphi \lambda_n)}{\Delta \varphi \lambda_n}\right)\right)$$

For clarity, write each nonlinear parameter explicitly in terms of the octahedral shear stress and expand:

$$\frac{\partial Bbar}{\partial \bar{\sigma}} = \frac{1}{3}\left[\frac{\partial}{\partial \bar{\sigma}} g_0^t(\bar{\sigma}) B_0 + \frac{\partial}{\partial \bar{\sigma}} g_1^t(\bar{\sigma}) g_2^t(\bar{\sigma}) \sum_{n=1}^{N} B_n - \frac{\partial}{\partial \bar{\sigma}} g_1^t(\bar{\sigma}) g_2^t(\bar{\sigma}) \sum_{n=1}^{N} B_n \frac{\tau_n a_\sigma(\bar{\sigma})}{\Delta t} + \frac{\partial}{\partial \bar{\sigma}} g_1^t(\bar{\sigma}) g_2^t(\bar{\sigma}) \sum_{n=1}^{N} B_n \frac{\tau_n a_\sigma(\bar{\sigma})}{\Delta t} \exp\left(-\Delta t / \tau_n a_\sigma(\bar{\sigma})\right)\right]$$

This is getting very busy. Introduce the following notation:

$$\frac{\partial Bbar}{\partial \bar{\sigma}} = \frac{1}{3}\frac{\partial}{\partial \bar{\sigma}}[E + F - G + H]$$

Evaluate E:

$$\frac{\partial}{\partial \bar{\sigma}} E = \frac{\partial}{\partial \bar{\sigma}} g_0^t(\bar{\sigma}) B_0$$

By the chain rule, this is equivalent to:

$$\frac{\partial}{\partial \bar{\sigma}} E = B_0 \frac{\partial g_0^t}{\partial \bar{\sigma}}$$

The two remaining partial derivatives are evaluated in 3.1.1

$$\frac{\partial g_0^t}{\partial \bar{\sigma}} = \left(g0i(1) + 2g0i(2)(\bar{\sigma} - \sigma_0)\right)$$

Appendix E

$$\frac{\partial \bar{\sigma}}{\partial \Delta \sigma_x^t} = \frac{1}{2\bar{\sigma}}\left(2\sigma_x - \sigma_y\right)$$

Now, term F:

$$\frac{\partial}{\partial \bar{\sigma}} F = \frac{\partial}{\partial \bar{\sigma}} g_1^t(\bar{\sigma}) g_2^t(\bar{\sigma}) \sum_{n=1}^{N} B_n$$

$$\frac{\partial}{\partial \bar{\sigma}} F = \left(\frac{\partial g_1^t}{\partial \bar{\sigma}} g2 + g1 \frac{\partial g_2^t}{\partial \bar{\sigma}}\right) \sum_{n=1}^{N} B_n$$

And term G:

$$\frac{\partial}{\partial \bar{\sigma}} G = \frac{\partial}{\partial \bar{\sigma}} g_1^t(\bar{\sigma}) g_2^t(\bar{\sigma}) \sum_{n=1}^{N} B_n \frac{\tau_n a_\sigma(\bar{\sigma})}{\Delta t}$$

$$\frac{\partial}{\partial \bar{\sigma}} G = \left(\frac{\partial g_1^t}{\partial \bar{\sigma}} g2 a_\sigma + g1 \frac{\partial g_2^t}{\partial \bar{\sigma}} a_\sigma + g1 g2 \frac{\partial a_\sigma}{\partial \bar{\sigma}}\right) \sum_{n=1}^{N} B_n \frac{\tau_n}{\Delta t}$$

And term H:

$$\frac{\partial}{\partial \bar{\sigma}} H = \frac{\partial}{\partial \bar{\sigma}} g_1^t(\bar{\sigma}) g_2^t(\bar{\sigma}) \sum_{n=1}^{N} B_n \frac{\tau_n a_\sigma(\bar{\sigma})}{\Delta t} \exp\left(-{}^{\Delta t}/_{\tau_n a_\sigma(\bar{\sigma})}\right)$$

$$\begin{aligned}\frac{\partial}{\partial \bar{\sigma}} H = \sum_{n=1}^{N} B_n \frac{\tau_n}{\Delta t} \Bigg(& \frac{\partial g_1^t}{\partial \bar{\sigma}} g2 a_\sigma \exp\left(-{}^{\Delta t}/_{\tau_n a_\sigma(\bar{\sigma})}\right) \\ & + g1 \frac{\partial g_2^t}{\partial \bar{\sigma}} a_\sigma \exp\left(-{}^{\Delta t}/_{\tau_n a_\sigma(\bar{\sigma})}\right) + g1 g2 \frac{\partial a_\sigma}{\partial \bar{\sigma}} \exp\left(-{}^{\Delta t}/_{\tau_n a_\sigma(\bar{\sigma})}\right) \\ & + g1 g2 a_\sigma \frac{\partial a_\sigma}{\partial \bar{\sigma}} \left({}^{\Delta t}/_{\tau_n a_\sigma(\bar{\sigma}) a_\sigma(\bar{\sigma})}\right) \exp\left(-{}^{\Delta t}/_{\tau_n a_\sigma(\bar{\sigma})}\right)\Bigg)\end{aligned}$$

3.1.2.c $\frac{\partial BHSum1}{\partial \bar{\sigma}}$:

$$\frac{\partial BHSum1}{\partial \bar{\sigma}} = \frac{\partial}{\partial \bar{\sigma}}\left(\frac{1}{3}\sum_{n=1}^{N} B_n\left(g_1^t \exp(-\Delta\varphi\lambda_n) - g_1^{t-\Delta t}\right) q_{nij}^{t-\Delta t}\right)$$

$$\frac{\partial BHSum1}{\partial \bar{\sigma}} = \frac{1}{3}\left(\sum_{n=1}^{N} B_n q_{nij}^{t-\Delta t}\left(\frac{\partial g_1^t}{\partial \bar{\sigma}} \exp(-\Delta\varphi\lambda_n) + g_1^t \frac{\partial a_\sigma}{\partial \bar{\sigma}}\left({}^{\Delta t}/_{\tau_n a_\sigma(\bar{\sigma}) a_\sigma(\bar{\sigma})}\right) \exp\left(-{}^{\Delta t}/_{\tau_n a_\sigma(\bar{\sigma})}\right)\right)\right)$$

3.1.2.d $\frac{\partial BHSum2}{\partial \bar{\sigma}}$:

$$\frac{\partial BHSum2}{\partial \bar{\sigma}} = \frac{\partial}{\partial \bar{\sigma}}\left(\frac{1}{3} g_2^{t-\Delta t} \sum_{n=1}^{N} B_n \left[g_1^{t-\Delta t} \frac{1-\exp\left(-\Delta\varphi^{t-\Delta t}\lambda_n\right)}{\Delta\varphi^{t-\Delta t}\lambda_n} - g_1^t \frac{1-\exp(-\Delta\varphi\lambda_n)}{\Delta\varphi\lambda_n} \right] s_{ij}^{t-\Delta t}\right)$$

$$\begin{aligned}\frac{\partial BHSum2}{\partial \bar{\sigma}} = \frac{1}{3} g_2^{t-\Delta t} s_{ij}^{t-\Delta t} \Bigg(\sum_{n=1}^{N} B_n \Bigg[& -\frac{\tau_n}{\Delta t}\left(\frac{\partial g_1^t}{\partial \bar{\sigma}} a_\sigma(\bar{\sigma}) + g_1^t \frac{\partial a_\sigma(\bar{\sigma})}{\partial \bar{\sigma}}\right) \\ & + \frac{\tau_n}{\Delta t}\left(\frac{\partial g_1^t}{\partial \bar{\sigma}} a_\sigma(\bar{\sigma}) \exp\left(-\frac{\Delta t}{\tau_n a_\sigma(\bar{\sigma})}\right) + g_1^t \frac{\partial a_\sigma(\bar{\sigma})}{\partial \bar{\sigma}} \exp\left(-\frac{\Delta t}{\tau_n a_\sigma(\bar{\sigma})}\right)\right. \\ & \left. + g_1^t a_\sigma(\bar{\sigma}) \frac{\partial a_\sigma}{\partial \bar{\sigma}} \left({\Delta t}/{\tau_n a_\sigma(\bar{\sigma}) a_\sigma(\bar{\sigma})}\right) \exp\left(-{\Delta t}/{\tau_n a_\sigma(\bar{\sigma})}\right)\right)\Bigg]\Bigg)\end{aligned}$$

At this point, we now have all of the terms needed to compute S11.

3.2 S22

S22 is very similar to S11, as it is the influence of the y stress on the y strain:

$$S22 = \frac{\partial \Delta\varepsilon_y^t}{\partial \Delta\sigma_y^t} = Jbar \frac{\partial s_y^t}{\partial \Delta\sigma_y^t} + s_y^t \frac{\partial Jbar}{\partial \Delta\sigma_y^t} - \frac{\partial JHSum1}{\Delta\sigma_y^t} - \frac{\partial JHSum2}{\Delta\sigma_y^t}$$

In fact, the equations for S22 are identical to those for S11 (substituting σ_y in for σ_x as appropriate) with two exceptions.

First , $\frac{\partial s_y^t}{\partial \Delta\sigma_y^t}$:

Using the definition of the current stress as a function of the stress increment :

$$\sigma_y^t = \sigma_y^{t-\Delta t} + \Delta\sigma_y^t$$

And the definition of deviatoric stress:

$$s_y^t = \sigma_y^t - \frac{1}{3}\sigma_{kk}^t = \sigma_y^t - \frac{1}{3}\left(\sigma_x^t + \sigma_y^t\right)$$

$$s_y^t = \frac{2}{3}\sigma_y^t - \frac{1}{3}\sigma_x^t$$

$$\frac{\partial s_y^t}{\partial \Delta\sigma_y^t} = \frac{2}{3}$$

Second:

$$\frac{\partial \bar{\sigma}}{\partial \Delta\sigma_y^t} = \frac{\partial}{\partial \Delta\sigma_y^t}\sqrt{\frac{\left(\sigma_x - \sigma_y\right)^2 + (\sigma_x)^2 + \left(\sigma_y\right)^2 + 6\left(\tau_{xy}\right)^2}{2}}$$

$$\frac{\partial \bar{\sigma}}{\partial \Delta \sigma_y^t} = \frac{1}{2\bar{\sigma}}\left(2\sigma_y - \sigma_x\right)$$

3.3 S12

The off-diagonal terms of the Jacobian require independent consideration. First consider the effect of y stress on x strain:

$$S12 = \frac{\partial \Delta \varepsilon_1^t}{\partial \Delta \sigma_y^t} = \frac{\partial \Delta e_x^t}{\partial \Delta \sigma_y^t} + \frac{1}{3}\frac{\partial \Delta \varepsilon_{kk}^t}{\partial \Delta \sigma_y^t}$$

3.3.1 Deviatoric component of S12

$$\frac{\partial \Delta e_x^t}{\partial \Delta \sigma_y^t} = \frac{\partial}{\partial \Delta \sigma_y^t}\left(Jbars_x^t - Jbar^{old}s_x^{t-\Delta t} - JHSum1 - JHSum2\right)$$

$$\frac{\partial \Delta e_x^t}{\partial \Delta \sigma_y^t} = Jbar\frac{\partial s_x^t}{\partial \Delta \sigma_y^t} + \frac{\partial \bar{\sigma}}{\partial \Delta \sigma_y^t}\left(s_x^t\frac{\partial Jbar}{\partial \bar{\sigma}} - \frac{\partial JHSum1}{\partial \bar{\sigma}} - \frac{\partial JHSum2}{\partial \bar{\sigma}}\right)$$

3.3.1.a $\frac{\partial s_x^t}{\partial \Delta \sigma_y^t}$

Using the definition of the current stress as a function of the stress increment :

$$\sigma_x^t = \sigma_x^{t-\Delta t} + \Delta \sigma_x^t$$

And the definition of deviatoric stress:

$$s_x^t = \sigma_x^t - \frac{1}{3}\sigma_{kk}^t = \sigma_x^t - \frac{1}{3}\left(\sigma_x^t + \sigma_y^t\right)$$

$$s_x^t = \frac{2}{3}\sigma_x^t - \frac{1}{3}\sigma_y^t$$

$$s_x^t = \frac{2}{3}\sigma_x^t - \frac{1}{3}\sigma_y^{t-\Delta t} - \frac{1}{3}\Delta \sigma_y^t$$

$$\frac{\partial s_x^t}{\partial \Delta \sigma_y^t} = \frac{\partial}{\partial \Delta \sigma_y^t}\left(\frac{2}{3}\sigma_x^t - \frac{1}{3}\sigma_y^{t-\Delta t} - \frac{1}{3}\Delta \sigma_y^t\right)$$

$$\frac{\partial s_x^t}{\partial \Delta \sigma_x^t} = -\frac{1}{3}$$

3.3.1.b $\frac{\partial Jbar}{\partial \bar{\sigma}}$

Because we previously calculated $\frac{\partial Jbar}{\partial \Delta \sigma_x^t}$ in terms of the octahedral shear stress:

$$\frac{\partial Jbar}{\partial \Delta\sigma_x^t} = \frac{\partial Jbar}{\partial \bar{\sigma}} \frac{\partial \bar{\sigma}}{\partial \Delta\sigma_x^t}$$

We can use the same formulation for $\frac{\partial Jbar}{\partial \Delta\sigma_y^t}$, and the previous result for $\frac{\partial Jbar}{\partial \bar{\sigma}}$

$$\frac{\partial Jbar}{\partial \Delta\sigma_y^t} = \frac{\partial Jbar}{\partial \bar{\sigma}} \frac{\partial \bar{\sigma}}{\partial \Delta\sigma_y^t}$$

3.3.1.c $\frac{\partial JHSum1}{\partial \Delta\sigma_y^t}$

$$\frac{\partial JHSum1}{\partial \Delta\sigma_y^t} = \frac{\partial \bar{\sigma}}{\partial \Delta\sigma_y^t} \frac{\partial JHSum1}{\partial \bar{\sigma}}$$

Use the result from S11 for $\frac{\partial JHSum1}{\partial \bar{\sigma}}$

3.3.1.d $\frac{\partial JHSum2}{\partial \Delta\sigma_y^t}$

$$\frac{\partial JHSum2}{\partial \Delta\sigma_y^t} = \frac{\partial \bar{\sigma}}{\partial \Delta\sigma_y^t} \frac{\partial JHSum2}{\partial \bar{\sigma}}$$

Use the result from S11 for $\frac{\partial JHSum2}{\partial \bar{\sigma}}$

3.3.2 Dilatational component of S12

$$\frac{\partial \Delta\varepsilon_{kk}^t}{\partial \Delta\sigma_y^t} = \frac{\partial}{\partial \Delta\sigma_y^t}\left(Bbar\sigma_{kk}^t - Bbar^{old}\sigma_{kk}^{t-\Delta t} - BHSum1 - BHSum2\right)$$

$$\frac{\partial \Delta\varepsilon_{kk}^t}{\partial \Delta\sigma_y^t} = Bbar\frac{\partial}{\partial \Delta\sigma_y^t}\sigma_{kk}^t + \sigma_{kk}^t\frac{\partial}{\partial \Delta\sigma_y^t}Bbar - \frac{\partial}{\partial \Delta\sigma_y^t}BHSum1 - \frac{\partial}{\partial \Delta\sigma_y^t}\,BHSum2$$

$$\frac{\partial \Delta\varepsilon_{kk}^t}{\partial \Delta\sigma_y^t} = Bbar\frac{\partial \sigma_{kk}^t}{\partial \Delta\sigma_y^t} + \frac{\partial \bar{\sigma}}{\partial \Delta\sigma_y^t}\left(\sigma_{kk}^t\frac{\partial Bbar}{\partial \bar{\sigma}} - \frac{\partial BHSum1}{\partial \bar{\sigma}} - \frac{\partial BHSum2}{\partial \bar{\sigma}}\right)$$

3.3.2.a $\frac{\partial \sigma_{kk}^t}{\partial \Delta\sigma_y^t}$

Using the definition of the current stress as a function of the stress increment :

$$\sigma_y^t = \sigma_y^{t-\Delta t} + \Delta\sigma_y^t$$

And the definition of deviatoric stress:

$$\sigma_{kk}^t = \sigma_y^{t-\Delta t} + \Delta\sigma_y^t + \sigma_x^t$$

$$\frac{\partial \sigma_{kk}^t}{\partial \Delta \sigma_y^t} = \frac{\partial}{\partial \Delta \sigma_y^t}\left(\sigma_y^{t-\Delta t} + \Delta \sigma_y^t + \sigma_x^t\right)$$

$$\frac{\partial \sigma_{kk}^t}{\partial \Delta \sigma_y^t} = 1$$

3.3.2.b $\frac{\partial Bbar}{\partial \bar{\sigma}}$

From S11 calculation this term is already known:

$$\frac{\partial Bbar}{\partial \bar{\sigma}} = \frac{1}{3}\frac{\partial}{\partial \bar{\sigma}}[E + F - G + H]$$

3.3.2.c $\frac{\partial BHSum1}{\partial \bar{\sigma}}$:

From S11:

$$\frac{\partial BHSum1}{\partial \bar{\sigma}} = \frac{1}{3}\left(\sum_{n=1}^{N} B_n q_{nij}^{t-\Delta t}\left(\frac{\partial g_1^t}{\partial \bar{\sigma}}\exp(-\Delta\varphi\lambda_n) + g_1^t \frac{\partial a_\sigma}{\partial \bar{\sigma}}\left({}^{\Delta t}/_{\tau_n a_\sigma(\bar{\sigma}) a_\sigma(\bar{\sigma})}\right)\exp\left(-{}^{\Delta t}/_{\tau_n a_\sigma(\bar{\sigma})}\right)\right)\right)$$

3.3.2.d $\frac{\partial BHSum2}{\partial \bar{\sigma}}$:

From S11:

$$\begin{aligned}\frac{\partial BHSum2}{\partial \bar{\sigma}} = \frac{1}{3} g_2^{t-\Delta t} s_{ij}^{t-\Delta t}\Bigg(\sum_{n=1}^{N} B_n \Bigg[& -\frac{\tau_n}{\Delta t}\left(\frac{\partial g_1^t}{\partial \bar{\sigma}} a_\sigma(\bar{\sigma}) + g_1^t \frac{\partial a_\sigma(\bar{\sigma})}{\partial \bar{\sigma}}\right) \\ & + \frac{\tau_n}{\Delta t}\left(\frac{\partial g_1^t}{\partial \bar{\sigma}} a_\sigma(\bar{\sigma}) \exp\left(-\frac{\Delta t}{\tau_n a_\sigma(\bar{\sigma})}\right) + g_1^t \frac{\partial a_\sigma(\bar{\sigma})}{\partial \bar{\sigma}} \exp\left(-\frac{\Delta t}{\tau_n a_\sigma(\bar{\sigma})}\right)\right. \\ & \left. + g_1^t a_\sigma(\bar{\sigma}) \frac{\partial a_\sigma}{\partial \bar{\sigma}}\left({}^{\Delta t}/_{\tau_n a_\sigma(\bar{\sigma}) a_\sigma(\bar{\sigma})}\right)\exp\left(-{}^{\Delta t}/_{\tau_n a_\sigma(\bar{\sigma})}\right)\right)\Bigg]\Bigg)\end{aligned}$$

3.4 S21

Now consider the effect of x stress on y strain:

$$S21 = \frac{\partial \Delta \varepsilon_2^t}{\partial \Delta \sigma_1^t} = \frac{\partial \Delta e_y^t}{\partial \Delta \sigma_x^t} + \frac{1}{3}\frac{\partial \Delta \varepsilon_{kk}^t}{\partial \Delta \sigma_x^t}$$

3.4.1 Deviatoric component of S21

$$\frac{\partial \Delta e_y^t}{\partial \Delta \sigma_x^t} = \frac{\partial}{\partial \Delta \sigma_x^t}\left(Jbar s_y^t - Jbar^{old} s_y^{t-\Delta t} - JHSum1 - JHSum2\right)$$

$$\frac{\partial \Delta e_y^t}{\partial \Delta \sigma_x^t} = Jbar\frac{\partial s_y^t}{\partial \Delta \sigma_x^t} + \frac{\partial \bar{\sigma}}{\partial \Delta \sigma_x^t}\left(s_y^t \frac{\partial Jbar}{\partial \bar{\sigma}} - \frac{\partial JHSum1}{\partial \bar{\sigma}} - \frac{\partial JHSum2}{\partial \bar{\sigma}}\right)$$

Appendix E

3.4.1.a$\frac{\partial s_y^t}{\partial \Delta \sigma_x^t}$

Using the definition of the current stress as a function of the stress increment :

$$\sigma_x^t = \sigma_x^{t-\Delta t} + \Delta\sigma_x^t$$

And the definition of deviatoric stress:

$$s_y^t = \sigma_y^t - \frac{1}{3}\sigma_{kk}^t = \sigma_y^t - \frac{1}{3}\left(\sigma_x^t + \sigma_y^t\right)$$

$$s_y^t = \frac{2}{3}\sigma_y^t - \frac{1}{3}\sigma_x^t$$

$$s_y^t = \frac{2}{3}\sigma_y^t - \frac{1}{3}\left(\sigma_x^{t-\Delta t} + \Delta\sigma_x^t\right)$$

$$\frac{\partial s_y^t}{\partial \Delta \sigma_x^t} = \frac{\partial}{\partial \Delta \sigma_x^t}\left(\frac{2}{3}\sigma_y^t - \frac{1}{3}\left(\sigma_x^{t-\Delta t} + \Delta\sigma_x^t\right)\right)$$

$$\frac{\partial s_y^t}{\partial \Delta \sigma_x^t} = -\frac{1}{3}$$

3.4.1.b $\frac{\partial Jbar}{\partial \bar{\sigma}}$

Because we previously calculated $\frac{\partial Jbar}{\partial \Delta \sigma_x^t}$ in terms of the octahedral shear stress:

$$\frac{\partial Jbar}{\partial \Delta \sigma_x^t} = \frac{\partial Jbar}{\partial \bar{\sigma}}\frac{\partial \bar{\sigma}}{\partial \Delta \sigma_x^t}$$

We can use the same formulation for $\frac{\partial Jbar}{\partial \Delta \sigma_x^t}$, and the previous result for $\frac{\partial Jbar}{\partial \bar{\sigma}}$

$$\frac{\partial Jbar}{\partial \Delta \sigma_x^t} = \frac{\partial Jbar}{\partial \bar{\sigma}}\frac{\partial \bar{\sigma}}{\partial \Delta \sigma_x^t}$$

3.3.1.c $\frac{\partial JHSum1}{\partial \Delta \sigma_x^t}$

$$\frac{\partial JHSum1}{\partial \Delta \sigma_x^t} = \frac{\partial \bar{\sigma}}{\partial \Delta \sigma_x^t}\frac{\partial JHSum1}{\partial \bar{\sigma}}$$

Use the result from S11 for $\frac{\partial JHSum1}{\partial \bar{\sigma}}$

3.4.1.d $\frac{\partial JHSum2}{\partial \Delta \sigma_x^t}$

$$\frac{\partial JHSum2}{\partial \Delta \sigma_x^t} = \frac{\partial \bar{\sigma}}{\partial \Delta \sigma_x^t}\frac{\partial JHSum2}{\partial \bar{\sigma}}$$

Use the result from S11 for $\frac{\partial JHSum2}{\partial \bar{\sigma}}$

3.4.2 Dilatational component of S12

$$\frac{\partial \Delta\varepsilon_{kk}^{t}}{\partial \Delta\sigma_{x}^{t}} = \frac{\partial}{\partial \Delta\sigma_{x}^{t}}\left(Bbar\sigma_{kk}^{t} - Bbar^{old}\sigma_{kk}^{t-\Delta t} - BHSum1 - BHSum2\right)$$

$$\frac{\partial \Delta\varepsilon_{kk}^{t}}{\partial \Delta\sigma_{x}^{t}} = Bbar\frac{\partial \sigma_{kk}^{t}}{\partial \Delta\sigma_{x}^{t}} + \frac{\partial \bar{\sigma}}{\partial \Delta\sigma_{x}^{t}}\left(\sigma_{kk}^{t}\frac{\partial Bbar}{\partial \bar{\sigma}} - \frac{\partial BHSum1}{\partial \bar{\sigma}} - \frac{\partial BHSum2}{\partial \bar{\sigma}}\right)$$

3.4.2.a $\frac{\partial \sigma_{kk}^{t}}{\partial \Delta\sigma_{x}^{t}}$

Calculated previously:

$$\frac{\partial \sigma_{kk}^{t}}{\partial \Delta\sigma_{x}^{t}} = 1$$

3.4.2.b $\frac{\partial Bbar}{\partial \bar{\sigma}}$

From S11 calculation this term is already known:

$$\frac{\partial Bbar}{\partial \bar{\sigma}} = \frac{1}{3}\frac{\partial}{\partial \bar{\sigma}}[E + F - G + H]$$

3.4.2.c $\frac{\partial BHSum1}{\partial \bar{\sigma}}$:

From S11:

$$\frac{\partial BHSum1}{\partial \bar{\sigma}} = \frac{1}{3}\left(\sum_{n=1}^{N} B_n q_{nij}^{t-\Delta t}\left(\frac{\partial g_1^t}{\partial \bar{\sigma}}\exp(-\Delta\varphi\lambda_n) + g_1^t\frac{\partial a_\sigma}{\partial \bar{\sigma}}\left({}^{\Delta t}/_{\tau_n a_\sigma(\bar{\sigma})a_\sigma(\bar{\sigma})}\right)\exp\left(-{}^{\Delta t}/_{\tau_n a_\sigma(\bar{\sigma})}\right)\right)\right)$$

3.4.2.d $\frac{\partial BHSum2}{\partial \bar{\sigma}}$:

From S11:

$$\begin{aligned}\frac{\partial BHSum2}{\partial \bar{\sigma}} = \frac{1}{3}g_2^{t-\Delta t}s_{ij}^{t-\Delta t}\Bigg(\sum_{n=1}^{N} B_n\Bigg[&-\frac{\tau_n}{\Delta t}\left(\frac{\partial g_1^t}{\partial \bar{\sigma}}a_\sigma(\bar{\sigma}) + g_1^t\frac{\partial a_\sigma(\bar{\sigma})}{\partial \bar{\sigma}}\right)\\ &+\frac{\tau_n}{\Delta t}\left(\frac{\partial g_1^t}{\partial \bar{\sigma}}a_\sigma(\bar{\sigma})\exp\left(-\frac{\Delta t}{\tau_n a_\sigma(\bar{\sigma})}\right) + g_1^t\frac{\partial a_\sigma(\bar{\sigma})}{\partial \bar{\sigma}}\exp\left(-\frac{\Delta t}{\tau_n a_\sigma(\bar{\sigma})}\right)\right.\\ &\left.+ g_1^t a_\sigma(\bar{\sigma})\frac{\partial a_\sigma}{\partial \bar{\sigma}}\left({}^{\Delta t}/_{\tau_n a_\sigma(\bar{\sigma})a_\sigma(\bar{\sigma})}\right)\exp\left(-{}^{\Delta t}/_{\tau_n a_\sigma(\bar{\sigma})}\right)\right)\Bigg]\Bigg)\end{aligned}$$

3.5 S33

Now consider the effect of shear stress on shear strain:

$$S33 = \frac{\partial \Delta \varepsilon_{12}^t}{\partial \Delta \sigma_{12}^t} = \frac{\partial \Delta e_{12}^t}{\partial \Delta \sigma_{12}^t}$$

3.4.1 Deviatoric component of S33

$$\frac{\partial \Delta \varepsilon_s^t}{\partial \Delta \sigma_s^t} = \frac{\partial}{\partial \Delta \sigma_s^t}\left(Jbars_s^t - Jbar^{old} s_s^{t-\Delta t} - JHSum1 - JHSum2\right)$$

$$\frac{\partial \Delta \varepsilon_s^t}{\partial \Delta \sigma_s^t} = Jbar \frac{\partial s_s^t}{\partial \Delta \sigma_s^t} + \frac{\partial \bar{\sigma}}{\partial \Delta \sigma_s^t}\left(s_y^t \frac{\partial Jbar}{\partial \bar{\sigma}} - \frac{\partial JHSum1}{\partial \bar{\sigma}} - \frac{\partial JHSum2}{\partial \bar{\sigma}}\right)$$

The first partial derivative can be evaluated as below: ($\tau_{xy} = \sigma_s^t$)

$$\frac{\partial \bar{\sigma}}{\partial \Delta \sigma_s^t} = \frac{\partial}{\partial \Delta \sigma_s^t} \sqrt{\frac{\left(\sigma_x - \sigma_y\right)^2 + (\sigma_x)^2 + \left(\sigma_y\right)^2 + 6\left(\tau_{xy}\right)^2}{2}}$$

$$\frac{\partial \bar{\sigma}}{\partial \Delta \sigma_s^t} = \frac{\partial}{\partial \Delta \sigma_s^t} \left(\frac{\left(\sigma_x - \sigma_y\right)^2 + (\sigma_x)^2 + \left(\sigma_y\right)^2 + 6\left(\tau_{xy}\right)^2}{2} \right)^{1/2}$$

$$\frac{\partial \bar{\sigma}}{\partial \Delta \sigma_s^t}$$

$$= \frac{1}{2} \left(\frac{\left(\sigma_x - \sigma_y\right)^2 + (\sigma_x)^2 + \left(\sigma_y\right)^2 + 6\left(\tau_{xy}\right)^2}{2} \right)^{-1/2} \frac{\partial}{\partial \Delta \sigma_s^t} \left(\frac{\left(\sigma_x - \sigma_y\right)^2 + (\sigma_x)^2 + \left(\sigma_y\right)^2 + 6\left(\tau_{xy}\right)^2}{2} \right)$$

$$\frac{\partial \bar{\sigma}}{\partial \Delta \sigma_s^t} = \frac{1}{2\bar{\sigma}} \frac{\partial}{\partial \Delta \sigma_s^t} \left(\frac{\left(\sigma_x - \sigma_y\right)^2 + (\sigma_x)^2 + \left(\sigma_y\right)^2 + 6\left(\tau_{xy}\right)^2}{2} \right)$$

$$\frac{\partial \bar{\sigma}}{\partial \Delta \sigma_s^t} = \frac{1}{4\bar{\sigma}} \frac{\partial}{\partial \Delta \sigma_x^t} \left(\left(\sigma_x - \sigma_y\right)^2 + (\sigma_x)^2 + \left(\sigma_y\right)^2 + 6\left(\tau_{xy}\right)^2 \right)$$

$$\frac{\partial \bar{\sigma}}{\partial \Delta \sigma_s^t} = \frac{1}{4\bar{\sigma}} 12\tau_{xy}$$

$$\frac{\partial \bar{\sigma}}{\partial \Delta \sigma_s^t} = \frac{3\tau_{xy}}{\bar{\sigma}}$$

3.5.1.a $\frac{\partial s_s^t}{\partial \Delta \sigma_s^t}$:

Using the definition of the current stress as a function of the stress increment:

$$\sigma_s^t = \sigma_s^{t-\Delta t} + \Delta\sigma_s^t$$

And the definition of deviatoric stress:

$$s_s^t = \sigma_s^t = \sigma_s^{t-\Delta t} + \Delta\sigma_s^t$$

$$\frac{\partial s_s^t}{\partial \Delta\sigma_s^t} = 1$$

3.5.1.b $\frac{\partial Jbar}{\partial \bar{\sigma}}$

Because we previously calculated $\frac{\partial Jbar}{\partial \Delta\sigma_s^t}$ in terms of the octahedral shear stress:

$$\frac{\partial Jbar}{\partial \Delta\sigma_s^t} = \frac{\partial Jbar}{\partial \bar{\sigma}} \frac{\partial \bar{\sigma}}{\partial \Delta\sigma_s^t}$$

We can use the same formulation for $\frac{\partial Jbar}{\partial \Delta\sigma_s^t}$, and the previous result for $\frac{\partial Jbar}{\partial \bar{\sigma}}$

$$\frac{\partial Jbar}{\partial \Delta\sigma_s^t} = \frac{\partial Jbar}{\partial \bar{\sigma}} \frac{\partial \bar{\sigma}}{\partial \partial \Delta\sigma_s^t}$$

3.5.1.c $\frac{\partial JHSum1}{\partial \Delta\sigma_s^t}$

$$\frac{\partial JHSum1}{\partial \Delta\sigma_s^t} = \frac{\partial \bar{\sigma}}{\partial \Delta\sigma_s^t} \frac{\partial JHSum1}{\partial \bar{\sigma}}$$

Use the result from S11 for $\frac{\partial JHSum1}{\partial \bar{\sigma}}$

3.5.1.d $\frac{\partial JHSum2}{\partial \Delta\sigma_s^t}$

$$\frac{\partial JHSum2}{\partial \Delta\sigma_s^t} = \frac{\partial \bar{\sigma}}{\partial \Delta\sigma_s^t} \frac{\partial JHSum2}{\partial \bar{\sigma}}$$

Use the result from S11 for $\frac{\partial JHSum2}{\partial \bar{\sigma}}$

3.5.2 Dilatational component of S12

There is no dilatational component of the shear strain.

3.6 Compile Results

All of the necessary components are now known. In summary, the four terms of the Jacobian matrix are given by:

$$S_{11} = \frac{\partial \Delta e_x^t}{\partial \Delta \sigma_x^t} + \frac{1}{3}\frac{\partial \Delta \varepsilon_{kk}^t}{\partial \Delta \sigma_y^t}$$
$$= \frac{2}{3}Jbar + \frac{\partial \bar{\sigma}}{\partial \Delta \sigma_x^t}\left(s_x^t \frac{\partial Jbar}{\partial \bar{\sigma}} - \frac{\partial JHSum1}{\partial \bar{\sigma}} - \frac{\partial JHSum2}{\partial \bar{\sigma}}\right)$$
$$+ \frac{1}{3}\left(Bbar + \frac{\partial \bar{\sigma}}{\partial \Delta \sigma_x^t}\left(\sigma_{kk}^t \frac{\partial Bbar}{\partial \bar{\sigma}} - \frac{\partial BHSum1}{\partial \bar{\sigma}} - \frac{\partial BHSum2}{\partial \bar{\sigma}}\right)\right)$$

$$S_{22} = \frac{\partial \Delta e_y^t}{\partial \Delta \sigma_y^t} + \frac{1}{3}\frac{\partial \Delta \varepsilon_{kk}^t}{\partial \Delta \sigma_y^t}$$
$$= \frac{2}{3}Jbar + \frac{\partial \bar{\sigma}}{\partial \Delta \sigma_y^t}\left(s_y^t \frac{\partial Jbar}{\partial \bar{\sigma}} - \frac{\partial JHSum1}{\partial \bar{\sigma}} - \frac{\partial JHSum2}{\partial \bar{\sigma}}\right)$$
$$+ \frac{1}{3}\left(Bbar + \frac{\partial \bar{\sigma}}{\partial \Delta \sigma_y^t}\left(\sigma_{kk}^t \frac{\partial Bbar}{\partial \bar{\sigma}} - \frac{\partial BHSum1}{\partial \bar{\sigma}} - \frac{\partial BHSum2}{\partial \bar{\sigma}}\right)\right)$$

$$S_{12} = \frac{\partial \Delta \varepsilon_x^t}{\partial \Delta \sigma_y^t} = \frac{\partial \Delta e_x^t}{\partial \Delta \sigma_y^t} + \frac{1}{3}\frac{\partial \Delta \varepsilon_{kk}^t}{\partial \Delta \sigma_y^t}$$
$$= -\frac{1}{3}Jbar + \frac{\partial \bar{\sigma}}{\partial \Delta \sigma_y^t}\left(s_x^t \frac{\partial Jbar}{\partial \bar{\sigma}} - \frac{\partial JHSum1}{\partial \bar{\sigma}} - \frac{\partial JHSum2}{\partial \bar{\sigma}}\right)$$
$$+ \frac{1}{3}\left(Bbar + \frac{\partial \bar{\sigma}}{\partial \Delta \sigma_y^t}\left(\sigma_{kk}^t \frac{\partial Bbar}{\partial \bar{\sigma}} - \frac{\partial BHSum1}{\partial \bar{\sigma}} - \frac{\partial BHSum2}{\partial \bar{\sigma}}\right)\right)$$

$$S_{21} = \frac{\partial \Delta \varepsilon_2^t}{\partial \Delta \sigma_1^t} = \frac{\partial \Delta e_y^t}{\partial \Delta \sigma_x^t} + \frac{1}{3}\frac{\partial \Delta \varepsilon_{kk}^t}{\partial \Delta \sigma_x^t}$$
$$= -\frac{1}{3}Jbar + \frac{\partial \bar{\sigma}}{\partial \Delta \sigma_x^t}\left(s_y^t \frac{\partial Jbar}{\partial \bar{\sigma}} - \frac{\partial JHSum1}{\partial \bar{\sigma}} - \frac{\partial JHSum2}{\partial \bar{\sigma}}\right)$$
$$+ \frac{1}{3}\left(Bbar + \frac{\partial \bar{\sigma}}{\partial \Delta \sigma_x^t}\left(\sigma_{kk}^t \frac{\partial Bbar}{\partial \bar{\sigma}} - \frac{\partial BHSum1}{\partial \bar{\sigma}} - \frac{\partial BHSum2}{\partial \bar{\sigma}}\right)\right)$$

$$S_{33} = \frac{\partial \Delta \varepsilon_{12}^t}{\partial \Delta \sigma_{12}^t} = \frac{\partial \Delta e_{12}^t}{\partial \Delta \sigma_{12}^t} = Jbar + \frac{\partial \bar{\sigma}}{\partial \Delta \sigma_s^t}\left(s_y^t \frac{\partial Jbar}{\partial \bar{\sigma}} - \frac{\partial JHSum1}{\partial \bar{\sigma}} - \frac{\partial JHSum2}{\partial \bar{\sigma}}\right)$$

Where the various partial derivatives are given by the following equations:

$$\frac{\partial \bar{\sigma}}{\partial \Delta \sigma_x^t} = \frac{1}{2\bar{\sigma}}(2\sigma_x - \sigma_y)$$

$$\frac{\partial \bar{\sigma}}{\partial \Delta \sigma_y^t} = \frac{1}{2\bar{\sigma}}(2\sigma_y - \sigma_x)$$

$$\frac{\partial \bar{\sigma}}{\partial \Delta \sigma_s^t} = \frac{3\tau_{xy}}{\bar{\sigma}}$$

$$\frac{\partial Jbar}{\partial \bar{\sigma}} = \frac{\partial}{\partial \bar{\sigma}} \frac{1}{2}[A + B - C + D] = \frac{1}{2}\left(\frac{\partial}{\partial \bar{\sigma}} A + \frac{\partial}{\partial \bar{\sigma}} B - \frac{\partial}{\partial \bar{\sigma}} C + \frac{\partial}{\partial \bar{\sigma}} D\right)$$

$$\frac{\partial}{\partial \bar{\sigma}} A = J_0 \frac{\partial g_0^t}{\partial \bar{\sigma}}$$

$$\frac{\partial}{\partial \bar{\sigma}} B = \left(\frac{\partial g_1^t}{\partial \bar{\sigma}} g2 + g1 \frac{\partial g_2^t}{\partial \bar{\sigma}}\right) \sum_{n=1}^{N} J_n$$

$$\frac{\partial}{\partial \bar{\sigma}} C = \left(\frac{\partial g_1^t}{\partial \bar{\sigma}} g2 a_\sigma + g1 \frac{\partial g_2^t}{\partial \bar{\sigma}} a_\sigma + g1 g2 \frac{\partial a_\sigma}{\partial \bar{\sigma}}\right) \sum_{n=1}^{N} J_n \frac{\tau_n}{\Delta t}$$

$$\begin{aligned} \frac{\partial}{\partial \bar{\sigma}} D = \sum_{n=1}^{N} J_n \frac{\tau_n}{\Delta t} \Bigg(& \frac{\partial g_1^t}{\partial \bar{\sigma}} g2 a_\sigma \exp\left(-{}^{\Delta t}/_{\tau_n a_\sigma(\bar{\sigma})}\right) \\ & + g1 \frac{\partial g_2^t}{\partial \bar{\sigma}} a_\sigma \exp\left(-{}^{\Delta t}/_{\tau_n a_\sigma(\bar{\sigma})}\right) + g1 g2 \frac{\partial a_\sigma}{\partial \bar{\sigma}} \exp\left(-{}^{\Delta t}/_{\tau_n a_\sigma(\bar{\sigma})}\right) \\ & + g1 g2 a_\sigma \frac{\partial a_\sigma}{\partial \bar{\sigma}} \left({}^{\Delta t}/_{\tau_n a_\sigma(\bar{\sigma}) a_\sigma(\bar{\sigma})}\right) \exp\left(-{}^{\Delta t}/_{\tau_n a_\sigma(\bar{\sigma})}\right) \Bigg) \end{aligned}$$

$$\frac{\partial JHSum1}{\partial \bar{\sigma}} = \frac{1}{2}\left(\sum_{n=1}^{N} J_n q_{nij}^{t-\Delta t} \left(\frac{\partial g_1^t}{\partial \bar{\sigma}} \exp(-\Delta\varphi\lambda_n) + g_1^t \frac{\partial a_\sigma}{\partial \bar{\sigma}} \left({}^{\Delta t}/_{\tau_n a_\sigma(\bar{\sigma}) a_\sigma(\bar{\sigma})}\right) \exp\left(-{}^{\Delta t}/_{\tau_n a_\sigma(\bar{\sigma})}\right)\right)\right)$$

$$\begin{aligned} \frac{\partial JHSum2}{\partial \bar{\sigma}} = \frac{1}{2} g_2^{t-\Delta t} s_{ij}^{t-\Delta t} \Bigg(\sum_{n=1}^{N} J_n \Bigg[& -\frac{\tau_n}{\Delta t}\left(\frac{\partial g_1^t}{\partial \bar{\sigma}} a_\sigma(\bar{\sigma}) + g_1^t \frac{\partial a_\sigma(\bar{\sigma})}{\partial \bar{\sigma}}\right) \\ & + \frac{\tau_n}{\Delta t}\left(\frac{\partial g_1^t}{\partial \bar{\sigma}} a_\sigma(\bar{\sigma}) \exp\left(-\frac{\Delta t}{\tau_n a_\sigma(\bar{\sigma})}\right) + g_1^t \frac{\partial a_\sigma(\bar{\sigma})}{\partial \bar{\sigma}} \exp\left(-\frac{\Delta t}{\tau_n a_\sigma(\bar{\sigma})}\right)\right. \\ & \left. + g_1^t a_\sigma(\bar{\sigma}) \frac{\partial a_\sigma}{\partial \bar{\sigma}} \left({}^{\Delta t}/_{\tau_n a_\sigma(\bar{\sigma}) a_\sigma(\bar{\sigma})}\right) \exp\left(-{}^{\Delta t}/_{\tau_n a_\sigma(\bar{\sigma})}\right)\right) \Bigg] \Bigg) \end{aligned}$$

$$\frac{\partial Bbar}{\partial \bar{\sigma}} = \frac{1}{3} \frac{\partial}{\partial \bar{\sigma}} [E + F - G + H] = \frac{1}{3}\left(\frac{\partial}{\partial \bar{\sigma}} E + \frac{\partial}{\partial \bar{\sigma}} F - \frac{\partial}{\partial \bar{\sigma}} G + \frac{\partial}{\partial \bar{\sigma}} H\right)$$

$$\frac{\partial}{\partial \bar{\sigma}} E = B_0 \frac{\partial g_0^t}{\partial \bar{\sigma}}$$

$$\frac{\partial}{\partial \bar{\sigma}} F = \left(\frac{\partial g_1^t}{\partial \bar{\sigma}} g2 + g1 \frac{\partial g_2^t}{\partial \bar{\sigma}}\right) \sum_{n=1}^{N} B_n$$

$$\frac{\partial}{\partial\bar{\sigma}}G=\left(\frac{\partial g_1^t}{\partial\bar{\sigma}}g2a_\sigma+g1\frac{\partial g_2^t}{\partial\bar{\sigma}}a_\sigma+g1g2\frac{\partial a_\sigma}{\partial\bar{\sigma}}\right)\sum_{n=1}^{N}B_n\frac{\tau_n}{\Delta t}$$

$$\begin{aligned}\frac{\partial}{\partial\bar{\sigma}}H=\sum_{n=1}^{N}B_n\frac{\tau_n}{\Delta t}\Bigg(&\frac{\partial g_1^t}{\partial\bar{\sigma}}g2a_\sigma\exp\left(-{}^{\Delta t}/_{\tau_n a_\sigma(\bar{\sigma})}\right)\\&+g1\frac{\partial g_2^t}{\partial\bar{\sigma}}a_\sigma\exp\left(-{}^{\Delta t}/_{\tau_n a_\sigma(\bar{\sigma})}\right)+g1g2\frac{\partial a_\sigma}{\partial\bar{\sigma}}\exp\left(-{}^{\Delta t}/_{\tau_n a_\sigma(\bar{\sigma})}\right)\\&+g1g2a_\sigma\frac{\partial a_\sigma}{\partial\bar{\sigma}}\left({}^{\Delta t}/_{\tau_n a_\sigma(\bar{\sigma})a_\sigma(\bar{\sigma})}\right)\exp\left(-{}^{\Delta t}/_{\tau_n a_\sigma(\bar{\sigma})}\right)\Bigg)\end{aligned}$$

$$\frac{\partial BHSum1}{\partial\bar{\sigma}}=\frac{1}{3}\left(\sum_{n=1}^{N}B_n q_{nij}^{t-\Delta t}\left(\frac{\partial g_1^t}{\partial\bar{\sigma}}\exp(-\Delta\varphi\lambda_n)+g_1^t\frac{\partial a_\sigma}{\partial\bar{\sigma}}\left({}^{\Delta t}/_{\tau_n a_\sigma(\bar{\sigma})a_\sigma(\bar{\sigma})}\right)\exp\left(-{}^{\Delta t}/_{\tau_n a_\sigma(\bar{\sigma})}\right)\right)\right)$$

$$\begin{aligned}\frac{\partial BHSum2}{\partial\bar{\sigma}}=\frac{1}{3}g_2^{t-\Delta t}s_{ij}^{t-\Delta t}\Bigg(\sum_{n=1}^{N}B_n\Bigg[&-\frac{\tau_n}{\Delta t}\left(\frac{\partial g_1^t}{\partial\bar{\sigma}}a_\sigma(\bar{\sigma})+g_1^t\frac{\partial a_\sigma(\bar{\sigma})}{\partial\bar{\sigma}}\right)\\&+\frac{\tau_n}{\Delta t}\left(\frac{\partial g_1^t}{\partial\bar{\sigma}}a_\sigma(\bar{\sigma})\exp\left(-\frac{\Delta t}{\tau_n a_\sigma(\bar{\sigma})}\right)+g_1^t\frac{\partial a_\sigma(\bar{\sigma})}{\partial\bar{\sigma}}\exp\left(-\frac{\Delta t}{\tau_n a_\sigma(\bar{\sigma})}\right)\right.\\&\left.+g_1^t a_\sigma(\bar{\sigma})\frac{\partial a_\sigma}{\partial\bar{\sigma}}\left({}^{\Delta t}/_{\tau_n a_\sigma(\bar{\sigma})a_\sigma(\bar{\sigma})}\right)\exp\left(-{}^{\Delta t}/_{\tau_n a_\sigma(\bar{\sigma})}\right)\right)\Bigg]\Bigg)\end{aligned}$$

Appendix F. Derivation of Viscoplastic Jacobian Matrix

The derivation of the compliance matrix for the non-linear viscoplastic constitutive equation is outlined below. First the Zapas-Crissman form will be considered and then Tobolsky-Eyring. The Jacobian matrix is equivalent to the inverse of the compliance matrix.

1. Incremental Form of Recursive Equations for Time-Hardening

Begin with the recursive form of the multiaxial viscoplastic constitutive equation. Note that viscoplastic strain has no dilatational component, so only the shear stress and octahedral shear stress are needed.

$$\Delta\varepsilon_{ij}^{VP} = 1.118\Delta\bar{\varepsilon}^{P}\frac{s_{ij}}{\|\boldsymbol{s}\|}$$

$$s_{ij} = \sigma_{ij} - \frac{1}{3}\sigma_{kk}\delta_{ij}$$

$$\|\boldsymbol{s}\| = \sqrt{s_{11}^2 + s_{22}^2 + s_{12}^2} = \frac{1}{3}\sqrt{5\sigma_x^2 - 8\sigma_x\sigma_y + 5\sigma_y^2 + 9\tau_{xy}^2}$$

$$\bar{\sigma} = \sqrt{\frac{\left(\sigma_x - \sigma_y\right)^2 + (\sigma_x)^2 + \left(\sigma_y\right)^2 + 6\left(\tau_{xy}\right)^2}{2}}$$

2. Compliance Matrix for the Zapas-Crissman viscoplastic equation

The Zapas-Crisman Equation for equivalent plastic strain

$$\Delta\bar{\varepsilon}^{P} = A\bar{\sigma}^{b}(t^{c} - (t - \Delta t)^{c})$$

The compliance matrix is defined as:

$$\bar{\bar{S}} = \begin{bmatrix} \frac{\partial\Delta\varepsilon_x^t}{\partial\Delta\sigma_x^t} & \frac{\partial\Delta\varepsilon_x^t}{\partial\Delta\sigma_y^t} & 0 \\ \frac{\partial\Delta\varepsilon_y^t}{\partial\Delta\sigma_x^t} & \frac{\partial\Delta\varepsilon_y^t}{\partial\Delta\sigma_y^t} & 0 \\ 0 & 0 & \frac{\partial\Delta\gamma_{xy}^t}{\partial\Delta\tau_{xy}^t} \end{bmatrix} = \begin{bmatrix} S_{11} & S_{12} & 0 \\ S_{21} & S_{22} & 0 \\ 0 & 0 & S_{33} \end{bmatrix}$$

2.1. Derive S11

To evaluate this matrix, begin with the S_{11} term.

$$S_{11} = \frac{\partial\Delta\varepsilon_x^{VP}}{\partial\Delta\sigma_x} = \frac{\partial}{\partial\Delta\sigma_x}\left(1.118\Delta\bar{\varepsilon}^{P}\frac{s_x}{\|\boldsymbol{s}\|}\right) = \frac{\partial}{\partial\Delta\sigma_x}\left(1.118A\bar{\sigma}^{b}(t^{c} - (t - \Delta t)^{c})s_x\|\boldsymbol{s}\|^{-1}\right)$$

$$S_{11} = 1.118A(t^{c} - (t - \Delta t)^{c})\frac{\partial}{\partial\Delta\sigma_x}\left(\bar{\sigma}^{b}s_x\|\boldsymbol{s}\|^{-1}\right)$$

$$S_{11} = 1.118A(t^c - (t-\Delta t)^c)\left(\frac{\partial \bar{\sigma}^b}{\partial \Delta\sigma_x} s_x \|\boldsymbol{s}\|^{-1} + \bar{\sigma}^b \frac{\partial s_x}{\partial \Delta\sigma_x}\|\boldsymbol{s}\|^{-1} + \bar{\sigma}^b s_x \frac{\partial \|\boldsymbol{s}\|^{-1}}{\partial \Delta\sigma_x}\right)$$

For simplicity, rename the partial derivatives P_1, P_2, and P_3 as follows:

$$S_{11} = 1.118A(t^c - (t-\Delta t)^c)\left(P_1 s_x \|\boldsymbol{s}\|^{-1} + \bar{\sigma}^b P_2 \|\boldsymbol{s}\|^{-1} + \bar{\sigma}^b s_x P_3\right)$$

2.1.1. Solve $P_1 = \frac{\partial \bar{\sigma}^b}{\partial \Delta\sigma_x}$

Using the chain rule, the equation below is found, and the additional partial derivative is re-named P_4. It will be solved later.

$$P_1 = \frac{\partial \bar{\sigma}^b}{\partial \Delta\sigma_x} = \frac{\partial \bar{\sigma}^b}{\partial \bar{\sigma}}\frac{\partial \bar{\sigma}}{\partial \Delta\sigma_x} = \frac{\partial \bar{\sigma}^b}{\partial \bar{\sigma}} P_4$$

$$P_1 = \frac{\partial \bar{\sigma}^b}{\partial \bar{\sigma}} P_4 = b\bar{\sigma}^{b-1} P_4$$

2.1.2. Solve $P_2 = \frac{\partial s_x}{\partial \Delta\sigma_x}$

Recalling the definition of deviatoric stress, and using the fact that the current stress is the sum of the previous stress and the current stress increment:

$$P_2 = \frac{\partial s_x}{\partial \Delta\sigma_x} = \frac{\partial}{\partial \Delta\sigma_x}\left(\sigma_x - \frac{1}{3}(\sigma_x + \sigma_y)\right) = \frac{\partial}{\partial \Delta\sigma_x}\left(\frac{2}{3}\sigma_x - \frac{1}{3}\sigma_y\right)$$

$$P_2 = \frac{\partial}{\partial \Delta\sigma_x}\left(\frac{2}{3}({\sigma_x}^{old} + \Delta\sigma_x) - \frac{1}{3}\sigma_y\right)$$

$$P_2 = \frac{2}{3}$$

2.1.3. Solve $P_3 = \frac{\partial \|\boldsymbol{s}\|^{-1}}{\partial \Delta\sigma_x}$

Use the chain rule to rearrange this yields the following, and again the partial derivative term P_4 appears

$$P_3 = \frac{\partial \|\boldsymbol{s}\|^{-1}}{\partial \Delta\sigma_x} = 3\frac{\partial\left(5\sigma_x^2 - 8\sigma_x\sigma_y + 5\sigma_y^2 + 9\tau_{xy}^2\right)^{-1/2}}{\partial \Delta\sigma_x} = -\frac{3}{2}\|\boldsymbol{s}\|^{-\frac{3}{2}}(10\sigma_x - 8\sigma_y)$$

2.1.4. Solve $P_4 = \frac{\partial \bar{\sigma}}{\partial \Delta\sigma_x}$

Use the definition of octahedral shear stress as a function of current stress, which is related to the stress increment because the current stress is the sum of the previous stress and the current stress increment.

$$\frac{\partial\bar{\sigma}}{\partial\Delta\sigma_x}=\frac{\partial}{\partial\Delta\sigma_x}\sqrt{\frac{\left(\sigma_x-\sigma_y\right)^2+(\sigma_x)^2+\left(\sigma_y\right)^2+6\left(\tau_{xy}\right)^2}{2}}$$

$$=\frac{\partial}{\partial\Delta\sigma_x}\left(\frac{\left(\sigma_x-\sigma_y\right)^2+(\sigma_x)^2+\left(\sigma_y\right)^2+6\left(\tau_{xy}\right)^2}{2}\right)^{1/2}$$

$$\frac{\partial\bar{\sigma}}{\partial\Delta\sigma_x}$$

$$=\frac{1}{2}\left(\frac{\left(\sigma_x-\sigma_y\right)^2+(\sigma_x)^2+\left(\sigma_y\right)^2+6\left(\tau_{xy}\right)^2}{2}\right)^{-1/2}\frac{\partial}{\partial\Delta\sigma_x}\left(\frac{\left(\sigma_x-\sigma_y\right)^2+(\sigma_x)^2+\left(\sigma_y\right)^2+6\left(\tau_{xy}\right)^2}{2}\right)$$

$$\frac{\partial\bar{\sigma}}{\partial\Delta\sigma_x}=\frac{1}{2\bar{\sigma}}\frac{\partial}{\partial\Delta\sigma_x}\left(\frac{\left(\sigma_x-\sigma_y\right)^2+(\sigma_x)^2+\left(\sigma_y\right)^2+6\left(\tau_{xy}\right)^2}{2}\right)$$

$$\frac{\partial\bar{\sigma}}{\partial\Delta\sigma_x}=\frac{1}{4\bar{\sigma}}\frac{\partial}{\partial\Delta\sigma_x}\left(2{\sigma_x}^2-2\sigma_x\sigma_y+2{\sigma_y}^2+6\left(\tau_{xy}\right)^2\right)$$

$$\frac{\partial\bar{\sigma}}{\partial\Delta\sigma_x}=\frac{1}{4\bar{\sigma}}\frac{\partial}{\partial\Delta\sigma_x}\left(2\left({\sigma_x}^{old}+\Delta\sigma_x\right)^2-2\left({\sigma_x}^{old}+\Delta\sigma_x\right)\sigma_y+2{\sigma_y}^2+6\left(\tau_{xy}\right)^2\right)$$

$$\frac{\partial\bar{\sigma}}{\partial\Delta\sigma_x}=\frac{1}{4\bar{\sigma}}\frac{\partial}{\partial\Delta\sigma_x}\left(2\left({\sigma_x}^{old}\right)^2+2\left(2{\sigma_x}^{old}\Delta\sigma_x\right)+2(\Delta\sigma_x)^2-2\left({\sigma_x}^{old}+\Delta\sigma_x\right)\sigma_y+2{\sigma_y}^2+6\left(\tau_{xy}\right)^2\right)$$

$$\frac{\partial\bar{\sigma}}{\partial\Delta\sigma_x}=\frac{1}{4\bar{\sigma}}\left(4{\sigma_x}^{old}+4\Delta\sigma_x-2\sigma_y\right)$$

$$P_4=\frac{\partial\bar{\sigma}}{\partial\Delta\sigma_x}=\frac{2\sigma_x-\sigma_y}{2\bar{\sigma}}$$

2.1.5. Combining terms from above

$$S_{11}=1.118A(t^c-(t-\Delta t)^c)\left(P_1s_x\|\boldsymbol{s}\|^{-1}+\bar{\sigma}^bP_2\|\boldsymbol{s}\|^{-1}+\bar{\sigma}^bs_xP_3\right)$$

$$S_{11}=1.118A(t^c-(t-\Delta t)^c)\left(b\bar{\sigma}^{b-1}P_4s_x\|\boldsymbol{s}\|^{-1}+\bar{\sigma}^b\frac{2}{3}\|\boldsymbol{s}\|^{-1}-\bar{\sigma}^bs_x\frac{3}{2}\|\boldsymbol{s}\|^{-\frac{3}{2}}(10\sigma_x-8\sigma_y)\right)$$

$$S_{11}=1.118A(t^c-(t-\Delta t)^c)\left(b\bar{\sigma}^{b-1}\frac{2\sigma_x-\sigma_y}{2\bar{\sigma}}s_x\|\boldsymbol{s}\|^{-1}+\bar{\sigma}^b\frac{2}{3}\|\boldsymbol{s}\|^{-1}-\bar{\sigma}^bs_x\frac{3}{2}\|\boldsymbol{s}\|^{-\frac{3}{2}}(10\sigma_x-8\sigma_y)\right)$$

2.2. Derive S22

S22 is very similar to S11, as it is the influence of the y stress on the y strain:

$$S22=\frac{\partial\Delta\varepsilon_y^t}{\partial\Delta\sigma_y^t}=1.118A(t^c-(t-\Delta t)^c)\left(\frac{\partial\bar{\sigma}^b}{\partial\Delta\sigma_y}s_y\|\boldsymbol{s}\|^{-1}+\bar{\sigma}^b\frac{\partial s_y}{\partial\Delta\sigma_y}\|\boldsymbol{s}\|^{-1}+\bar{\sigma}^bs_y\frac{\partial\|\boldsymbol{s}\|^{-1}}{\partial\Delta\sigma_y}\right)$$

$$S22 = \frac{\partial \Delta \varepsilon_y^t}{\partial \Delta \sigma_y^t} = 1.118A(t^c - (t-\Delta t)^c)\left(P_5 s_y \|\boldsymbol{s}\|^{-1} + \bar{\sigma}^b P_6 \|\boldsymbol{s}\|^{-1} + \bar{\sigma}^b s_y P_7\right)$$

2.2.1. Solve $P_5 = \frac{\partial \bar{\sigma}^b}{\partial \Delta \sigma_y}$

Using the chain rule, the equation below is found, and the additional partial derivative is re-named P_8. It will be solved later.

$$P_5 = \frac{\partial \bar{\sigma}^b}{\partial \Delta \sigma_y} = \frac{\partial \bar{\sigma}^b}{\partial \bar{\sigma}} \frac{\partial \bar{\sigma}}{\partial \Delta \sigma_y} = \frac{\partial \bar{\sigma}^b}{\partial \bar{\sigma}} P_8$$

$$P_5 = \frac{\partial \bar{\sigma}^b}{\partial \bar{\sigma}} P_8 = b\bar{\sigma}^{b-1} P_8$$

2.2.2. Solve $P_6 = \frac{\partial s_y}{\partial \Delta \sigma_y}$

Recalling the definition of deviatoric stress, and using the fact that the current stress is the sum of the previous stress and the current stress increment:

$$P_6 = \frac{\partial s_y}{\partial \Delta \sigma_y} = \frac{\partial}{\partial \Delta \sigma_y}\left(\sigma_y - \frac{1}{3}(\sigma_x + \sigma_y)\right) = \frac{\partial}{\partial \Delta \sigma_y}\left(\frac{2}{3}\sigma_y - \frac{1}{3}\sigma_x\right)$$

$$P_6 = \frac{\partial}{\partial \Delta \sigma_y}\left(\frac{2}{3}\left({\sigma_y}^{old} + \Delta \sigma_x\right) - \frac{1}{3}\sigma_x\right)$$

$$P_6 = \frac{2}{3}$$

2.2.3. Solve $P_7 = \frac{\partial \|\boldsymbol{s}\|^{-1}}{\partial \Delta \sigma_y}$

Use the chain rule to rearrange this yields the following, and again the partial derivative term P_8 appears

$$P_7 = \frac{\partial \|\boldsymbol{s}\|^{-1}}{\partial \Delta \sigma_y} = 3\frac{\partial\left(5\sigma_x^2 - 8\sigma_x\sigma_y + 5\sigma_y^2 + 9\tau_{xy}^2\right)^{-1/2}}{\partial \Delta \sigma_y} = -\frac{3}{2}\|\boldsymbol{s}\|^{-\frac{3}{2}}(10\sigma_y - 8\sigma_x)$$

2.2.4. Solve $P_8 = \frac{\partial \bar{\sigma}}{\partial \Delta \sigma_y}$

This solution follows the process of 2.1.4 very closely, except that the current y stress is expressed in terms of old y stress and current y increment instead of making that expansion on the x stress. This yields the following result.

$$P_8 = \frac{\partial \bar{\sigma}}{\partial \Delta \sigma_y} = \frac{2\sigma_y - \sigma_x}{2\bar{\sigma}}$$

2.2.5. Combining terms from above

$$S_{22} = 1.118A(t^c - (t-\Delta t)^c)\left(P_5 s_y \|\boldsymbol{s}\|^{-1} + \bar{\sigma}^b P_6 \|\boldsymbol{s}\|^{-1} + \bar{\sigma}^b s_y P_7\right)$$

$$S_{22} = 1.118A(t^c - (t-\Delta t)^c)\left(b\bar{\sigma}^{b-1}\frac{2\sigma_y - \sigma_x}{2\bar{\sigma}} s_y \|\boldsymbol{s}\|^{-1} + \bar{\sigma}^b \frac{2}{3}\|\boldsymbol{s}\|^{-1} - \bar{\sigma}^b s_y \frac{3}{2}\|\boldsymbol{s}\|^{-\frac{3}{2}}(10\sigma_y - 8\sigma_x)\right)$$

2.3. Derive S12

This off-diagonal term represents the effect a change in y stress has on the x-directional strain.

$$S_{12} = \frac{\partial \Delta\varepsilon_x^{VP}}{\partial \Delta\sigma_y} = \frac{\partial}{\partial \Delta\sigma_y}\left(1.118\Delta\bar{\varepsilon}^P \frac{s_x}{\|\boldsymbol{s}\|}\right) = \frac{\partial}{\partial \Delta\sigma_y}\left(1.118A\bar{\sigma}^b (t^c - (t-\Delta t)^c) s_x \|\boldsymbol{s}\|^{-1}\right)$$

$$S_{12} = 1.118A(t^c - (t-\Delta t)^c)\frac{\partial}{\partial \Delta\sigma_y}\left(\bar{\sigma}^b s_x \|\boldsymbol{s}\|^{-1}\right)$$

$$S_{12} = 1.118A(t^c - (t-\Delta t)^c)\left(\frac{\partial \bar{\sigma}^b}{\partial \Delta\sigma_y} s_x \|\boldsymbol{s}\|^{-1} + \bar{\sigma}^b \frac{\partial s_x}{\partial \Delta\sigma_y}\|\boldsymbol{s}\|^{-1} + \bar{\sigma}^b s_x \frac{\partial \|\boldsymbol{s}\|^{-1}}{\partial \Delta\sigma_y}\right)$$

For simplicity, rename the partial derivatives P_9, P_{10}, and P_{11} as follows:

$$S_{12} = 1.118A(t^c - (t-\Delta t)^c)\left(P_9 s_x \|\boldsymbol{s}\|^{-1} + \bar{\sigma}^b P_{10} \|\boldsymbol{s}\|^{-1} + \bar{\sigma}^b s_x P_{11}\right)$$

2.3.1. Solve $P_9 = \frac{\partial \bar{\sigma}^b}{\partial \Delta\sigma_y}$

This partial derivate was solved previously in 2.2.1. The solution is repeated below.

$$P_9 = P_5 = \frac{\partial \bar{\sigma}^b}{\partial \bar{\sigma}} P_8 = b\bar{\sigma}^{b-1} P_8$$

2.3.2. Solve $P_{10} = \frac{\partial s_x}{\partial \Delta\sigma_y}$

Recalling the definition of deviatoric stress, and using the fact that the current stress is the sum of the previous stress and the current stress increment:

$$P_{10} = \frac{\partial s_x}{\partial \Delta\sigma_y} = \frac{\partial}{\partial \Delta\sigma_y}\left(\sigma_x - \frac{1}{3}(\sigma_x + \sigma_y)\right) = \frac{\partial}{\partial \Delta\sigma_y}\left(\frac{2}{3}\sigma_x - \frac{1}{3}\sigma_y\right)$$

$$P_2 = \frac{\partial}{\partial \Delta\sigma_x}\left(\frac{2}{3}\left({\sigma_x}^{old} + \Delta\sigma_x\right) - \frac{1}{3}\sigma_y\right)$$

$$P_{10} = -\frac{1}{3}$$

2.3.3. Solve $P_{11} = \frac{\partial \|\boldsymbol{s}\|^{-1}}{\partial \Delta\sigma_y}$

This partial derivate was solved previously in 2.2.3. The solution is repeated below.

$$P_{11} = P_7 = -\frac{3}{2}\|\boldsymbol{s}\|^{-\frac{3}{2}}(10\sigma_y - 8\sigma_x)$$

2.3.4. Combining terms from above

$$S_{12} = 1.118A(t^c - (t-\Delta t)^c)\left(P_9 s_x\|\boldsymbol{s}\|^{-1} + \bar{\sigma}^b P_{10}\|\boldsymbol{s}\|^{-1} + \bar{\sigma}^b s_x P_{11}\right)$$

$$S_{12} = 1.118A(t^c - (t-\Delta t)^c)\left(b\bar{\sigma}^{b-1}\frac{2\sigma_y - \sigma_x}{2\bar{\sigma}}s_x\|\boldsymbol{s}\|^{-1} - \bar{\sigma}^b\frac{1}{3}\|\boldsymbol{s}\|^{-1} - \bar{\sigma}^b s_x\frac{3}{2}\|\boldsymbol{s}\|^{-\frac{3}{2}}(10\sigma_y - 8\sigma_x)\right)$$

2.4. Derive S21

This off-diagonal term represents the effect a change in x stress has on the y-directional strain.

$$S_{21} = \frac{\partial \Delta\varepsilon_y^{VP}}{\partial \Delta\sigma_x} = \frac{\partial}{\partial \Delta\sigma_x}\left(1.118\Delta\bar{\varepsilon}^P\frac{s_y}{\|\boldsymbol{s}\|}\right) = \frac{\partial}{\partial \Delta\sigma_x}\left(1.118A\bar{\sigma}^b(t^c - (t-\Delta t)^c)s_y\|\boldsymbol{s}\|^{-1}\right)$$

$$S_{21} = 1.118A(t^c - (t-\Delta t)^c)\frac{\partial}{\partial \Delta\sigma_x}\left(\bar{\sigma}^b s_y\|\boldsymbol{s}\|^{-1}\right)$$

$$S_{21} = 1.118A(t^c - (t-\Delta t)^c)\left(\frac{\partial \bar{\sigma}^b}{\partial \Delta\sigma_x}s_y\|\boldsymbol{s}\|^{-1} + \bar{\sigma}^b\frac{\partial s_y}{\partial \Delta\sigma_x}\|\boldsymbol{s}\|^{-1} + \bar{\sigma}^b s_y\frac{\partial \|\boldsymbol{s}\|^{-1}}{\partial \Delta\sigma_x}\right)$$

For simplicity, rename the partial derivatives P_{12}, P_{13}, and P_{14} as follows:

$$S_{21} = 1.118A(t^c - (t-\Delta t)^c)\left(P_{12}s_y\|\boldsymbol{s}\|^{-1} + \bar{\sigma}^b P_{13}\|\boldsymbol{s}\|^{-1} + \bar{\sigma}^b s_y P_{14}\right)$$

2.4.1. Solve $P_{12} = \frac{\partial \bar{\sigma}^b}{\partial \Delta\sigma_x}$

This partial derivate was solved previously in 2.2.1. The solution is repeated below.

$$P_{12} = P_1 = \frac{\partial \bar{\sigma}^b}{\partial \Delta\sigma_x} = \frac{\partial \bar{\sigma}^b}{\partial \bar{\sigma}}\frac{\partial \bar{\sigma}}{\partial \Delta\sigma_x} = \frac{\partial \bar{\sigma}^b}{\partial \bar{\sigma}}P_4$$

$$P_{12} = P_1 = b\bar{\sigma}^{b-1}P_4$$

2.4.2. Solve $P_{13} = \frac{\partial s_y}{\partial \Delta\sigma_x}$

Recalling the definition of deviatoric stress, and using the fact that the current stress is the sum of the previous stress and the current stress increment:

$$P_{13} = \frac{\partial s_y}{\partial \Delta\sigma_x} = \frac{\partial}{\partial \Delta\sigma_x}\left(\sigma_y - \frac{1}{3}(\sigma_x + \sigma_y)\right) = \frac{\partial}{\partial \Delta\sigma_x}\left(\frac{2}{3}\sigma_y - \frac{1}{3}\sigma_x\right)$$

$$P_{13} = \frac{\partial}{\partial \Delta\sigma_x}\left(\frac{2}{3}({\sigma_y}^{old} + \Delta\sigma_y) - \frac{1}{3}\sigma_x\right)$$

$$P_{13} = -\frac{1}{3}$$

2.4.3. Solve $P_{14} = \frac{\partial \|\boldsymbol{s}\|^{-1}}{\partial \Delta\sigma_x}$

This partial derivate was solved previously in 2.1.3. The solution is repeated below.

$$P_{14} = -\frac{3}{2}\|\boldsymbol{s}\|^{-\frac{3}{2}}(10\sigma_x - 8\sigma_y)$$

2.4.4. Combining terms from above

$$S_{21} = 1.118A(t^c - (t-\Delta t)^c)\left(P_{12}s_y\|\boldsymbol{s}\|^{-1} + \bar{\sigma}^b P_{13}\|\boldsymbol{s}\|^{-1} + \bar{\sigma}^b s_y P_{14}\right)$$

$$S_{21} = 1.118A(t^c - (t-\Delta t)^c)\left(b\bar{\sigma}^{b-1}\frac{2\sigma_x - \sigma_y}{2\bar{\sigma}}s_y\|\boldsymbol{s}\|^{-1} - \frac{1}{3}\bar{\sigma}^b\|\boldsymbol{s}\|^{-1} - \bar{\sigma}^b s_y\frac{3}{2}\|\boldsymbol{s}\|^{-\frac{3}{2}}(10\sigma_x - 8\sigma_y)\right)$$

2.5. Derive S33

The S33 term describes the impact that shear strain has on shear stress. Thus, it is initially similar to the other diagonal terms in the matrix.

$$S_{33} = \frac{\partial \Delta\varepsilon_s^{VP}}{\partial \Delta\sigma_s} = \frac{\partial}{\partial \Delta\sigma_s}\left(1.118\Delta\bar{\varepsilon}^P\frac{s_s}{\|\boldsymbol{s}\|}\right) = \frac{\partial}{\partial \Delta\sigma_s}\left(1.118A\bar{\sigma}^b(t^c - (t-\Delta t)^c)s_s\|\boldsymbol{s}\|^{-1}\right)$$

$$S_{33} = 1.118A(t^c - (t-\Delta t)^c)\left(\frac{\partial \bar{\sigma}^b}{\partial \Delta\sigma_s}s_s\|\boldsymbol{s}\|^{-1} + \bar{\sigma}^b\frac{\partial s_s}{\partial \Delta\sigma_s}\|\boldsymbol{s}\|^{-1} + \bar{\sigma}^b s_s\frac{\partial \|\boldsymbol{s}\|^{-1}}{\partial \Delta\sigma_s}\right)$$

Here, a simplification may be introduced. Because there is no dilatational component to the shear stress, by definition, the 'deviatoric shear stress' $s_s$is simply the total shear stress. Therefore, the second partial derivative is equivalent to one.

$$S_{33} = 1.118A(t^c - (t-\Delta t)^c)\left(\frac{\partial \bar{\sigma}^b}{\partial \Delta\sigma_s}s_s\|\boldsymbol{s}\|^{-1} + \bar{\sigma}^b\|\boldsymbol{s}\|^{-1} + \bar{\sigma}^b s_s\frac{\partial \|\boldsymbol{s}\|^{-1}}{\partial \Delta\sigma_s}\right)$$

For simplicity, rename the partial derivatives P_{15}, and P_{16} as follows:

$$S_{33} = 1.118A(t^c - (t-\Delta t)^c)\left(P_{15}s_s\|\boldsymbol{s}\|^{-1} + \bar{\sigma}^b\|\boldsymbol{s}\|^{-1} + \bar{\sigma}^b s_s P_{16}\right)$$

2.5.1. Solve $P_{15} = \frac{\partial \bar{\sigma}^b}{\partial \Delta\sigma_s}$

Using the chain rule, the equation below is found, and the additional partial derivative is re-named P_{17}. It will be solved later.

$$P_{15} = \frac{\partial \bar{\sigma}^b}{\partial \Delta\sigma_s} = \frac{\partial \bar{\sigma}^b}{\partial \bar{\sigma}}\frac{\partial \bar{\sigma}}{\partial \Delta\sigma_s} = \frac{\partial \bar{\sigma}^b}{\partial \bar{\sigma}}P_{17}$$

$$P_{15} = b\bar{\sigma}^{b-1}P_{17}$$

2.5.2. Solve $P_{16} = \frac{\partial \|\boldsymbol{s}\|^{-1}}{\partial \Delta\sigma_s}$

Use the chain rule to rearrange this yields the following, and again the partial derivative term P_{17} appears

$$P_{16} = \frac{\partial \|\boldsymbol{s}\|^{-1}}{\partial \Delta\sigma_s} = 3\frac{\partial\left(5\sigma_x^2 - 8\sigma_x\sigma_y + 5\sigma_y^2 + 9\tau_{xy}^2\right)^{-1/2}}{\partial \Delta\sigma_s} = -\frac{3}{2}\|\boldsymbol{s}\|^{-\frac{3}{2}}(18\sigma_s)$$

2.5.3. Solve $P_{17} = \frac{\partial \bar{\sigma}}{\partial \Delta\sigma_s}$

Use the definition of octahedral shear stress as a function of current stress, which is related to the stress increment because the current stress is the sum of the previous stress and the current stress increment.

$$\frac{\partial \bar{\sigma}}{\partial \Delta\sigma_s} = \frac{\partial}{\partial \Delta\sigma_s}\sqrt{\frac{\left(\sigma_x - \sigma_y\right)^2 + (\sigma_x)^2 + \left(\sigma_y\right)^2 + 6\left(\tau_{xy}\right)^2}{2}}$$

$$= \frac{\partial}{\partial \Delta\sigma_s}\left(\frac{\left(\sigma_x - \sigma_y\right)^2 + (\sigma_x)^2 + \left(\sigma_y\right)^2 + 6(\sigma_s)^2}{2}\right)^{1/2}$$

$$\frac{\partial \bar{\sigma}}{\partial \Delta\sigma_s} = \frac{1}{4\bar{\sigma}}\frac{\partial}{\partial \Delta\sigma_s}\left(2{\sigma_x}^2 - 2\sigma_x\sigma_y + 2{\sigma_y}^2 + 6(\sigma_s)^2\right)$$

$$\frac{\partial \bar{\sigma}}{\partial \Delta\sigma_s} = \frac{1}{4\bar{\sigma}}\frac{\partial}{\partial \Delta\sigma_s}\left(2{\sigma_x}^2 - 2\sigma_x\sigma_y + 2{\sigma_y}^2 + 6\left({\sigma_s}^{old} + \Delta\sigma_s\right)^2\right)$$

$$\frac{\partial \bar{\sigma}}{\partial \Delta\sigma_s} = \frac{1}{4\bar{\sigma}}\frac{\partial}{\partial \Delta\sigma_s}\left(2{\sigma_x}^2 - 2\sigma_x\sigma_y + 2{\sigma_y}^2 + 6\left({\sigma_s}^{old}\right)^2 + 12{\sigma_s}^{old}\Delta\sigma_s + 6(\Delta\sigma_s)^2\right)$$

$$\frac{\partial \bar{\sigma}}{\partial \Delta\sigma_s} = \frac{1}{4\bar{\sigma}}\left(12{\sigma_s}^{old} + 12\Delta\sigma_s\right)$$

$$P_{17} = \frac{\partial \bar{\sigma}}{\partial \Delta\sigma_s} = \frac{6\sigma_s}{2\bar{\sigma}}$$

2.5.4. Combining terms from above

$$S_{33} = 1.118A(t^c - (t-\Delta t)^c)\left(P_{15}s_s\|\boldsymbol{s}\|^{-1} + \bar{\sigma}^b\|\boldsymbol{s}\|^{-1} + \bar{\sigma}^b s_s P_{16}\right)$$

$$S_{33} = 1.118A(t^c - (t-\Delta t)^c)\left(b\bar{\sigma}^{b-1}\frac{6\sigma_s}{2\bar{\sigma}}s_s\|\boldsymbol{s}\|^{-1} + \bar{\sigma}^b\|\boldsymbol{s}\|^{-1} - \bar{\sigma}^b s_s\frac{3}{2}\|\boldsymbol{s}\|^{-\frac{3}{2}}(18\sigma_s)\right)$$

3. Compile Results

All of the necessary components are now known. In summary, the four terms of the compliance matrix for the Zapas-Crissman form of the viscoplastic equation are given by:

$$S_{11} = 1.118A(t^c - (t-\Delta t)^c)\left(b\bar{\sigma}^{b-1}\frac{2\sigma_x - \sigma_y}{2\bar{\sigma}}s_x\|\boldsymbol{s}\|^{-1} + \bar{\sigma}^b\frac{2}{3}\|\boldsymbol{s}\|^{-1} - \bar{\sigma}^b s_x\frac{3}{2}\|\boldsymbol{s}\|^{-\frac{3}{2}}(10\sigma_x - 8\sigma_y)\right)$$

$$S_{22} = 1.118A(t^c - (t-\Delta t)^c)\left(b\bar{\sigma}^{b-1}\frac{2\sigma_y - \sigma_x}{2\bar{\sigma}}s_y\|\boldsymbol{s}\|^{-1} + \bar{\sigma}^b\frac{2}{3}\|\boldsymbol{s}\|^{-1} - \bar{\sigma}^b s_y\frac{3}{2}\|\boldsymbol{s}\|^{-\frac{3}{2}}(10\sigma_y - 8\sigma_x)\right)$$

$$S_{12} = 1.118A(t^c - (t-\Delta t)^c)\left(b\bar{\sigma}^{b-1}\frac{2\sigma_y - \sigma_x}{2\bar{\sigma}}s_x\|\boldsymbol{s}\|^{-1} - \bar{\sigma}^b\frac{1}{3}\|\boldsymbol{s}\|^{-1} - \bar{\sigma}^b s_x\frac{3}{2}\|\boldsymbol{s}\|^{-\frac{3}{2}}(10\sigma_y - 8\sigma_x)\right)$$

$$S_{21} = 1.118A(t^c - (t-\Delta t)^c)\left(b\bar{\sigma}^{b-1}\frac{2\sigma_x - \sigma_y}{2\bar{\sigma}}s_y\|\boldsymbol{s}\|^{-1} - \frac{1}{3}\bar{\sigma}^b\|\boldsymbol{s}\|^{-1} - \bar{\sigma}^b s_y\frac{3}{2}\|\boldsymbol{s}\|^{-\frac{3}{2}}(10\sigma_x - 8\sigma_y)\right)$$

$$S_{33} = 1.118A(t^c - (t-\Delta t)^c)\left(b\bar{\sigma}^{b-1}\frac{6\sigma_s}{2\bar{\sigma}}s_s\|\boldsymbol{s}\|^{-1} + \bar{\sigma}^b\|\boldsymbol{s}\|^{-1} - \bar{\sigma}^b s_s\frac{3}{2}\|\boldsymbol{s}\|^{-\frac{3}{2}}(18\sigma_s)\right)$$

4. Compliance matrix for the Tobolsky-Eyring viscoplastic equation.

The derivation of the compliance matrix for the Tobolsky-Eyring form of the viscoplastic constitutive expression follows the same steps outlined above and in fact yields nearly identical results. However, because the constitutive expression for equivalent plastic strain is different, the partial derivatives change slightly. The S11 term is derived below and the other are reported without demonstration.

Tobolsky-Eyring expression for equivalent plastic strain:

$$\Delta\bar{\varepsilon}^P = Aexp(b\sigma)\ (t^c - (t-\Delta t)^c)$$

$$S_{11} = \frac{\partial\Delta\varepsilon_x^{VP}}{\partial\Delta\sigma_x} = \frac{\partial}{\partial\Delta\sigma_x}\left(1.118\Delta\bar{\varepsilon}^P\frac{s_x}{\|\boldsymbol{s}\|}\right) = \frac{\partial}{\partial\Delta\sigma_x}\left(\frac{3}{2}Aexp(b\bar{\sigma})\ (t^c - (t-\Delta t)^c)s_x\|\boldsymbol{s}\|^{-1}\right)$$

$$S_{11} = 1.118A(t^c - (t-\Delta t)^c)\frac{\partial}{\partial\Delta\sigma_x}(exp(b\bar{\sigma})s_x\|\boldsymbol{s}\|^{-1})$$

$$S_{11} = 1.118A(t^c - (t-\Delta t)^c)\left(\frac{\partial exp(b\bar{\sigma})}{\partial\Delta\sigma_x}s_x\|\boldsymbol{s}\|^{-1} + exp(b\bar{\sigma})\frac{\partial s_x}{\partial\Delta\sigma_x}\|\boldsymbol{s}\|^{-1} + exp(b\bar{\sigma})s_x\frac{\partial\|\boldsymbol{s}\|^{-1}}{\partial\Delta\sigma_x}\right)$$

For simplicity, rename the partial derivatives P_{18}, P_{19}, and P_{20} as follows:

$$S_{11} = 1.118A(t^c - (t-\Delta t)^c)(P_{18}s_x\|\boldsymbol{s}\|^{-1} + exp(b\bar{\sigma})P_{19}\|\boldsymbol{s}\|^{-1} + exp(b\bar{\sigma})s_xP_{20})$$

4.1.1. Solve $P_{18} = \frac{\partial exp(b\bar{\sigma})}{\partial \Delta\sigma_x}$

Using the chain rule, the equation below is found, and the additional partial derivative is re-named P_4because it is equivalent to the partial derivate P_4computed for the Zapas-Crissman analysis.

$$P_{18} = \frac{\partial exp(b\bar{\sigma})}{\partial \Delta\sigma_x} = \frac{\partial exp(b\bar{\sigma})}{\partial \bar{\sigma}}\frac{\partial \bar{\sigma}}{\partial \Delta\sigma_x} = \frac{\partial exp(b\bar{\sigma})}{\partial \bar{\sigma}}P_4$$

$$P_{18} = \frac{\partial exp(b\bar{\sigma})}{\partial \bar{\sigma}}P_4 = bexp(b\bar{\sigma})P_4$$

4.1.2. Solve $P_{19} = \frac{\partial s_x}{\partial \Delta\sigma_x}$

This partial derivative was also solved for the Zapas-Crissman analysis. Recalling the definition of deviatoric stress, and using the fact that the current stress is the sum of the previous stress and the current stress increment:

$$P_{19} = P_2 = \frac{\partial s_x}{\partial \Delta\sigma_x} = \frac{\partial}{\partial \Delta\sigma_x}\left(\sigma_x - \frac{1}{3}(\sigma_x + \sigma_y)\right) = \frac{\partial}{\partial \Delta\sigma_x}\left(\frac{2}{3}\sigma_x - \frac{1}{3}\sigma_y\right)$$

$$P_{19} = P_2 = \frac{\partial}{\partial \Delta\sigma_x}\left(\frac{2}{3}({\sigma_x}^{old} + \Delta\sigma_x) - \frac{1}{3}\sigma_y\right)$$

$$P_{19} = P_2 = \frac{2}{3}$$

4.1.3. Solve $P_{20} = \frac{\partial \|\boldsymbol{s}\|^{-1}}{\partial \Delta\sigma_x}$

This partial derivative was also solved for the Zapas-Crissman analysis. Use the chain rule to rearrange this yields the following, and again the partial derivative term P_4 appears

$$P_{20} = P_3 = -\frac{3}{2}\|\boldsymbol{s}\|^{-\frac{3}{2}}(10\sigma_x - 8\sigma_y)$$

4.1.4. Solve $P_4 = \frac{\partial \bar{\sigma}}{\partial \Delta\sigma_x}$

This partial derivative was also solved for the Zapas-Crissman analysis. From above,

$$P_4 = \frac{\partial \bar{\sigma}}{\partial \Delta\sigma_x} = \frac{2\sigma_x - \sigma_y}{2\bar{\sigma}}$$

4.1.5. Combining terms from abov

$$S_{11} = 1.118A(t^c - (t-\Delta t)^c)(P_{18}s_x\|\boldsymbol{s}\|^{-1} + exp(b\bar{\sigma})P_{19}\|\boldsymbol{s}\|^{-1} + exp(b\bar{\sigma})s_xP_{20})$$

$$S_{11} = 1.118A(t^c - (t-\Delta t)^c)\left(bexp(b\bar{\sigma})\frac{2\sigma_x - \sigma_y}{2\bar{\sigma}}s_x\|\boldsymbol{s}\|^{-1} + exp(b\bar{\sigma})\frac{2}{3}\|\boldsymbol{s}\|^{-1} - exp(b\bar{\sigma})s_x\frac{3}{2}\|\boldsymbol{s}\|^{-\frac{3}{2}}(10\sigma_x - 8\sigma_y)\right)$$

Comparison of this equation with the S11 equation derived for the Zapas-Crissman definition reveals that this compliance terms for the Tobolsky-Eyring constitutive equation is identical to that of the Zapas-Crissman equation with the exception of the definition of viscoplastic strain. That is, the Zapas-Crissman compliance equations can be used for the Tobolsky-Eyring form by replacing each $\bar{\sigma}^b$ with $exp(b\bar{\sigma})$.

$$S_{11} = 1.118A(t^c - (t-\Delta t)^c)\left(bexp(b\bar{\sigma})\frac{2\sigma_x - \sigma_y}{2\bar{\sigma}}s_x\|\boldsymbol{s}\|^{-1} + exp(b\bar{\sigma})\frac{2}{3}\|\boldsymbol{s}\|^{-1} - exp(b\bar{\sigma})s_x\frac{3}{2}\|\boldsymbol{s}\|^{-\frac{3}{2}}(10\sigma_x - 8\sigma_y)\right)$$

$$S_{22} = 1.118A(t^c - (t-\Delta t)^c)\left(bexp(b\bar{\sigma})\frac{2\sigma_y - \sigma_x}{2\bar{\sigma}}s_y\|\boldsymbol{s}\|^{-1} + exp(b\bar{\sigma})\frac{2}{3}\|\boldsymbol{s}\|^{-1} - exp(b\bar{\sigma})s_y\frac{3}{2}\|\boldsymbol{s}\|^{-\frac{3}{2}}(10\sigma_y - 8\sigma_x)\right)$$

$$S_{12} = 1.118A(t^c - (t-\Delta t)^c)\left(bexp(b\bar{\sigma})\frac{2\sigma_y - \sigma_x}{2\bar{\sigma}}s_x\|\boldsymbol{s}\|^{-1} - exp(b\bar{\sigma})\frac{1}{3}\|\boldsymbol{s}\|^{-1} - exp(b\bar{\sigma})s_x\frac{3}{2}\|\boldsymbol{s}\|^{-\frac{3}{2}}(10\sigma_y - 8\sigma_x)\right)$$

$$S_{21} = 1.118A(t^c - (t-\Delta t)^c)\left(bexp(b\bar{\sigma})\frac{2\sigma_x - \sigma_y}{2\bar{\sigma}}s_y\|\boldsymbol{s}\|^{-1} - \frac{1}{3}exp(b\bar{\sigma})\|\boldsymbol{s}\|^{-1} - exp(b\bar{\sigma})s_y\frac{3}{2}\|\boldsymbol{s}\|^{-\frac{3}{2}}(10\sigma_x - 8\sigma_y)\right)$$

$$S_{33} = 1.118A(t^c - (t-\Delta t)^c)$$

Appendix G. Attempts to Resolve Discrepancy in Biaxial Results

1. Experimental Technique and Results

After performing the blister experiments, surface strain and radius of curvature are exported from the DIC. For each experiment, a region near the center of the deformed blister is selected and the average x- and y- strains are computed over this region. (Ideally, this region is near enough to the center that the stress and strain states are equal-biaxial, so only the x-strain is exported for analysis.) The software uses this same region to compute the radius of curvature with a built-in algorithm. The average strain and radius of curvature are computed for each pair of images (each time step has left and right images which are combined for 3D deformation results) for the entire experiment and exported to Excel.

Within Excel, this data is processed. Stress is calculated from the applied pressure, *p*, the radius of curvature, *R*, and the blister thickness, *t*, by the Equation G 1, which is obtained from thin-wall pressure-vessel theory. The thickness of each blister sample is the average of the thickness measured in nine places on the surface with a drop-gage micrometer prior to testing.

$$\sigma_{ENGR} = \frac{pR}{2t} \qquad \textbf{G 1}$$

This equation yields engineering stress. However, the simulations performed in Abaqus will be expressed in a true stress measure. For correct comparison, the experimental surface strains and calculated stresses are converted using the following equations, in which γ represents the in-plane stretch at the center of the blister and θ is the through-plane stretch in the same region. Poisson's ratio, *v*, is assumed to be 0.5 and is used to convert between γ and θ. (Note that the strains must be expressed as mm/mm rather than % strains for these computations.)

$$\varepsilon = \frac{1}{2}\left(1 - \frac{1}{\gamma^2}\right) \qquad \textbf{G 2}$$

$$\sigma = \frac{\sigma_{ENGR}}{\gamma\theta} = \frac{\sigma_{ENGR}}{\gamma\frac{1}{\gamma^2}} = \gamma * \sigma_{ENGR} \qquad \textbf{G 3}$$

This yields the following figures which summarize the experimental results at all pressure levels.

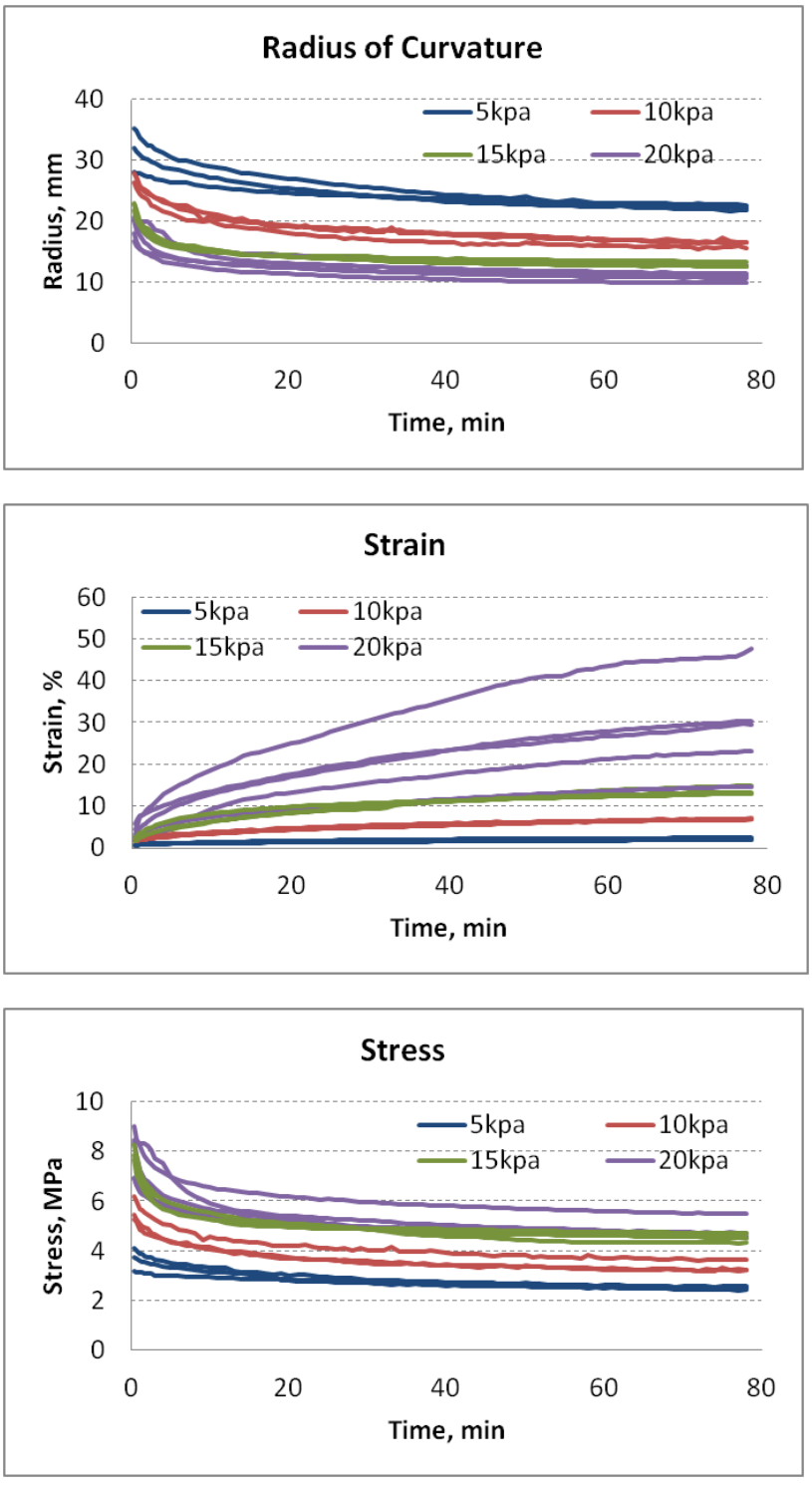

Figure G 1. Experimental results from DIC near the center of the blister: (top) radius of curvature fit, (center) Almansi-Hamel strain, (bottom) Cauchy stress.

2. Simulation Technique and Results

The first simulations performed used the UMAT which was validated against uniaxial experiments. For the uniaxial case, viscoplastic strains develop only in the direction of loading. The constitutive equation selected for viscoplastic strains is a function of the octahedral shear stress. As an example, consider Equation G 4, which expresses the increment of viscoplastic strain which develops during a specified time increment under a uniaxial stress application.

$$\Delta\varepsilon^{VP} = A(\bar{\sigma})^b(t^c - (t-\Delta t)^c) \qquad \text{G 4}$$

For uniaxial loading, the octahedral stress reduces to the axial stress, as demonstrated in Equation

G 5.

$$\bar{\sigma} = \sqrt{\frac{1}{2}((\sigma_{11}-\sigma_{22})^2 + {\sigma_{11}}^2 + {\sigma_{22}}^2 + 6{\sigma_{12}}^2)} = \sigma_{22} \qquad \text{G 5}$$

Thus, the increment of viscoplastic strain that develops in the axial (22) direction can be expressed by Equation G 6**Error! Reference source not found.** instead of Equation G 4.

$$\Delta\varepsilon^{VP} = A(\sigma_{22})^b(t^c - (t-\Delta t)^c) \qquad \text{G 6}$$

These equations are applicable to uniaxial simulations. For biaxial simulations, a technique is required to properly account for how the strain increment which develops from the equivalent (octahedral) shear stress is divided among the material directions. This analysis uses equivalent plastic strain theory, which uses Equation G 4 to compute the total strain increment, as for the uniaxial case. However, an additional equation is needed to compute the directional viscoplastic strains.

It is reasonable to suggest that the magnitude of the directional viscoplastic increments scales with the magnitude of the directional stresses. Thus, for the present analysis, the ratio of the directional deviatoric stress s_{ij} to the magnitude of the stress deviator tensor $\|s_{ij}\|$ is used to separate the total viscoplastic strain increment into directional increments. Equation G 7 expresses this technique. The parameter K will be defined below.

$$\Delta\varepsilon_{ij}^{VP} = K\frac{s_{ij}}{\|s_{ij}\|}\Delta\varepsilon^{VP} = K\frac{s_{ij}}{\|s_{ij}\|}A(\bar{\sigma})^b(t^c - (t-\Delta t)^c) \qquad \text{G 7}$$

Equation G 7 must reduce to Equation G 6 for the case of uniaxial loading. In other words, the parameter K must be determined such that Equation G 8 is true.

$$\Delta\varepsilon_{22}^{VP} = K\frac{s_{22}}{\|s_{ij}\|}A(\bar{\sigma})^b(t^c - (t-\Delta t)^c) = A(\bar{\sigma})^b(t^c - (t-\Delta t)^c) \qquad \text{G 8}$$

$$K\frac{s_{22}}{\|s_{ij}\|} = 1 \qquad \text{G 9}$$

$$K = \frac{\|s_{ij}\|}{s_{22}} \quad \text{G 10}$$

The magnitude of the stress deviator tensor is given by Equation G 9.

$$\|s_{ij}\| = \sqrt{(s_{11})^2 + (s_{22})^2 + (s_{12})^2} \quad \text{G 11}$$

The deviatoric stresses are defined as:

$$s_{11} = \sigma_{11} - \frac{1}{3}({\sigma_{11}}^2 + {\sigma_{22}}^2) = \frac{2}{3}\sigma_{11} - \frac{1}{3}\sigma_{22} \quad \text{G 12}$$

$$s_{22} = \sigma_{22} - \frac{1}{3}({\sigma_{11}}^2 + {\sigma_{22}}^2) = \frac{2}{3}\sigma_{22} - \frac{1}{3}\sigma_{11} \quad \text{G 13}$$

$$s_{12} = \sigma_{12} \quad \text{G 14}$$

For uniaxial loading, Equations G 12 through G 14 further reduce to Equations G 15 through G 17 since σ_{22} is the only non-zero stress component.

$$s_{11} = -\frac{1}{3}\sigma_{22} \quad \text{G 15}$$

$$s_{22} = \frac{2}{3}\sigma_{22} \quad \text{G 16}$$

$$s_{12} = 0 \quad \text{G 17}$$

Substituting Equations G 15 through G 17 into Equation G 11 yields Equation G 18.

$$\|s_{ij}\| = \sqrt{\left(\frac{1}{3}\sigma_{22}\right)^2 + \left(\frac{2}{3}\sigma_{22}\right)^2 + (0)^2} = \sqrt{\frac{5}{9}(\sigma_{22})^2} = 0.745356 * \sigma_{22} \quad \text{G 18}$$

Substituting Equation G 18 back into Equation G 10 yields Equation G 19.

$$K = \frac{\|s_{ij}\|}{s_{22}} = \frac{0.745356 * \sigma_{22}}{\frac{2}{3}\sigma_{22}} = 1.118 \quad \text{G 19}$$

Therefore, in the UMAT used for biaxial simulations, Equation G 20 is used to compute viscoplastic strain increments.

$$\Delta\varepsilon_{ij}^{VP} = 1.118\frac{s_{ij}}{\|s_{ij}\|}A(\bar{\sigma})^b(t^c - (t - \Delta t)^c) \quad \text{G 20}$$

Equation **Error! Reference source not found.** for viscoplastic strain increments yielded the simulated stresses shown in Figure G 2. In this figure, the experimental stresses are represented by the data points with error bars, which represent the 95% confidence interval calculated from the replicates at each pressure level. The simulations predict much greater stresses than are observed experimentally at all pressure levels.

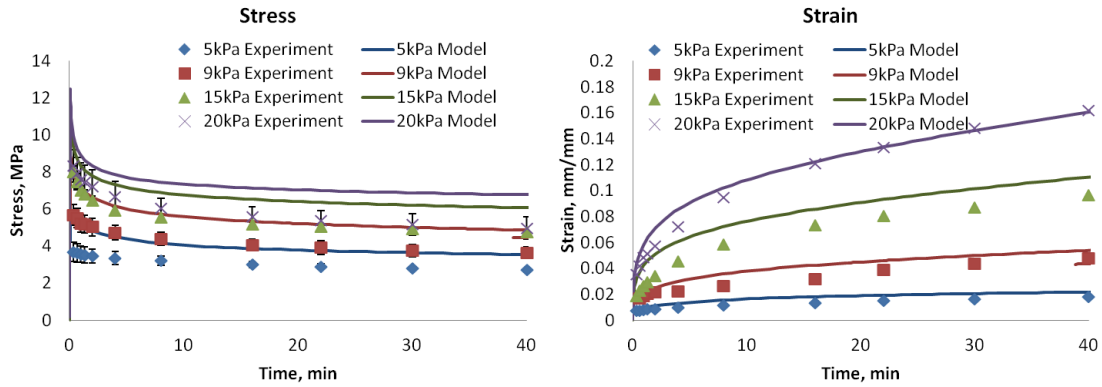

Figure G 2. Simulated vs. experimental results. Poor agreement is observed.

3. Attempts to Correct Discrepancy

The following figures demonstrate various attempts to address the discrepancy between the experimental and simulated stresses. The first set of figures addresses potential problems with the experimental side of the analysis and the second set explores how changes in the model affect the simulated stresses. Rather than demonstrating each effect at all the pressure levels, a single pressure level was chosen for each study and is presented here.

3.1. Experimental Factors

3.1.1. Area used for radius of curvature fit

Recall that the radius of curvature for each experiment is computed over a user-selected area near the center of the blister. A potential source of error is sensitivity to that selected region. To explore this effect, the stresses from a sphere fit to the central region are compared with those from a sphere fit to the entire blister from a 10kpa experiment. Figure G 3 demonstrates that the stress results, which vary linearly with radius of curvature, are not sensitive to the region selected.

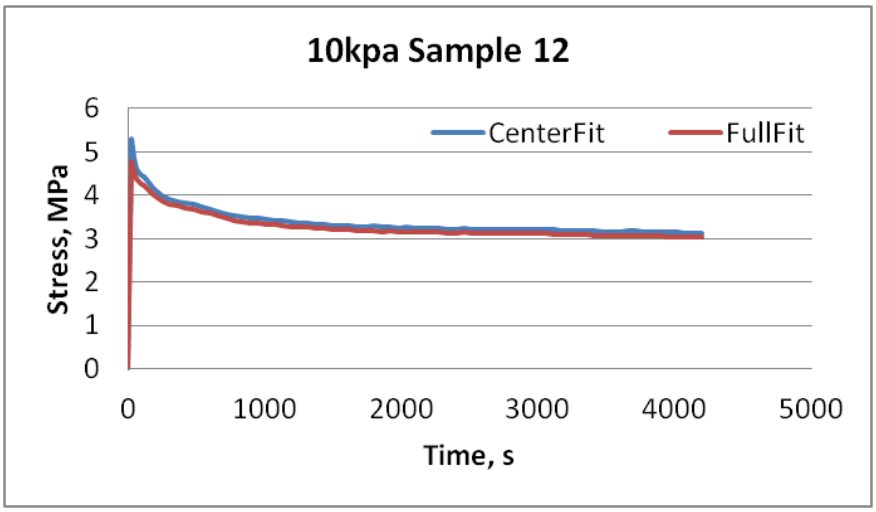

Figure G 3. Comparison of the stresses calculated from a single experiment using two techniques to find the radius of curvature. 'CenterFit' uses only the central portion of the blister, where the stress and strain states are equal-biaxial. 'Fullfit' uses the entire blister surface resolved by the DIC. This figure demonstrates that the stress calculation is not sensitive to the region over which the radius of curvature is calculated.

3.1.2. Uncertainty in out-of-plane displacement measurement

The out-of-plane (z-direction) displacement of the blister specimen is used to compute the radius of curvature of the deforming blister. From geometry, it can be shown that the radius of curvature, R, of a spherical cap is a function of the height of the cap, h, and the free radius, a, as in Figure G 4.

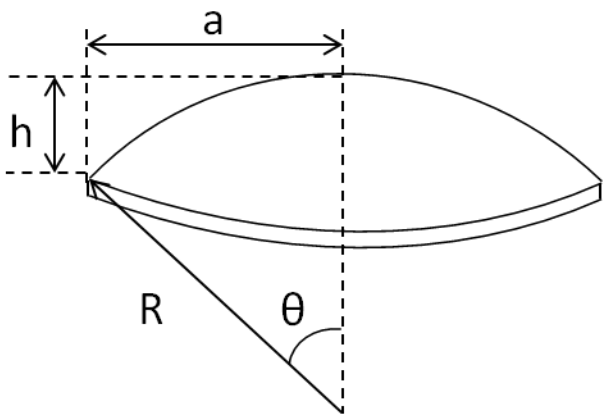

$$R = \frac{h}{2} + \frac{a^2}{2h}$$

Figure G 4. Geometry of spherical cap.

During the experiments, the noise floor of the in-plane displacement measurement was established by comparing two sets of images which should have been identical (no deformation or displacement was applied to the blister specimen between the two sets of images). This analysis demonstrated that, in the absence of any applied deformation, 'ghost' deformations of approximately 6 µm were observed in the out-of-plane measurement. The effect of this out-of-plane uncertainty u_h in the height measurement on the radius of curvature measurement may be computed by considering the partial derivative of the radius of curvature with respect to blister height. (This is the propagation of uncertainty technique.) The free radius a is a constant of 9.525 mm, so no uncertainty results from that parameter.

$$u_R = \sqrt{\left(\frac{\partial R}{\partial h}\right)^2 (u_h)^2} \quad \text{G 21}$$

$$u_R = \sqrt{\left(\frac{1}{2} - \frac{a^2}{2h^2}\right)^2 (u_h)^2} \quad \text{G 22}$$

The radius of curvature in the blister is generally between 40 mm and 10 mm. The uncertainty in the radius of curvature, as computed by Equation G 22, is 0.2 mm for a 40 mm blister and 0.3 µm for a 10 mm blister, as shown through the calculations in Table G 1. In both cases, accounting for the uncertainty in the z-displacement measurement affects the radius of curvature value, and thus the stress value, by less than 1%.

Table G 1. Computation of uncertainty in blister radius of curvature from height measurement uncertainty.

R, mm	a, mm	h, mm	u_h, mm	dR/dh	u_R, mm
41.7889	9.525	1.1	0.006	-36.9899	0.2219
9.5363	9.525	10	0.006	0.0464	0.0003

3.1.3. Uncertainty in applied pressure

Because the stress is a function of applied pressure, any error in the pressure measurement would cause an error in the stress calculation. A low-pressure gage with NIST-traceable calibration was used to verify the accuracy of the experimental pressure measurement. Figure G 5 demonstrates the software pressure measurement and the pressure indicated by the gage for increasing and decreasing stresses. At each point, the pressure setting was allowed to equilibrate for 60 seconds before the results were recorded. No error was observed in the pressure measurement over the range of relevant experimental pressures.

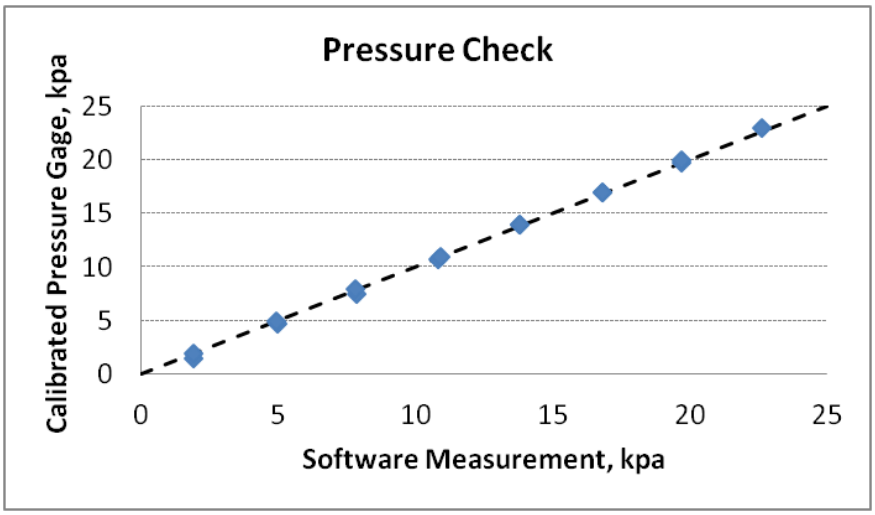

Figure G 5. Correlation between pressure level indicated by software controlling the blister fixture and a calibrated gage attached where the blister is during experiments. This figure demonstrates that there is not an error with the pressure measurement which could affect the stress calculation.

3.1.4. Thickness of blister specimens

The thickness of the material sheets provided is nominally 18 µm. However, because the stress calculation depends directly on thickness, the thickness of each individual sample was recorded prior to testing. Most samples were between 20.5 µm and 24 µm thick. The following figure demonstrates the potential error resulting from incorrect thickness in the stress calculations. This figure was generated by taking the radius of curvature from a 10 kpa experiment (where the specimen was actually 21 µm thick) and calculating the stresses if the sample were 20, 22 or 24 µm thick. Although the effect is significant, the thickness of each specimen was already included in the stress calculations in Figure 2. Therefore, this figure demonstrates the importance of knowing the actual sample thickness, but does not address the discrepancy observed between the model and experiments.

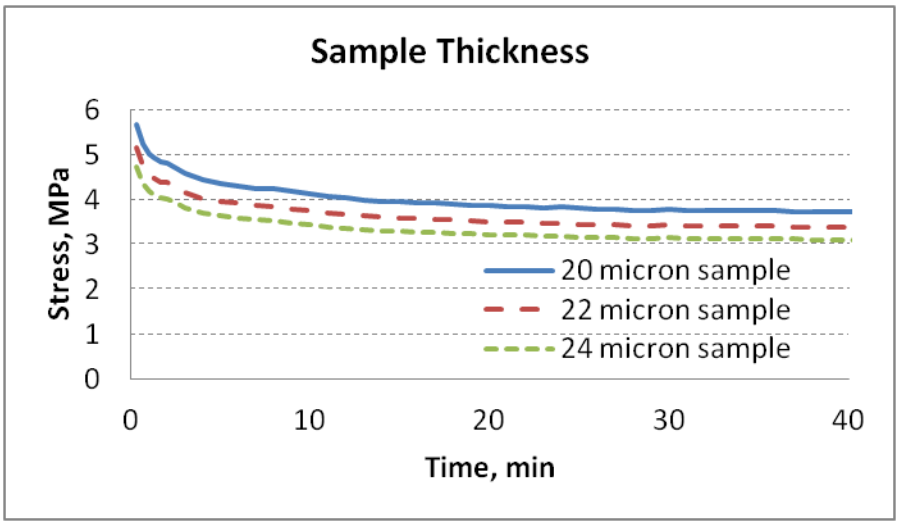

Figure G 6. Influence of specimen thickness on the experimental stress calculation. This figure demonstrates that knowing the actual thickness of each sample is important in performing the stress computation. However, this information has already been incorporated into the analysis.

A second attempt to address the influence of sample thickness was to report the membrane force resultants instead of the stresses. Membrane forces resultant is obtained by integrating the stress through the thickness of the sample, as defined by Equation G 23. In this equation, t is the sample thickness, σ_{ij} is the stress through the sample and z is the through-plane displacement variable.

$$N_{ij} = \int_{-t/2}^{t/2} \sigma_{ij}\, dz \qquad \text{G 23}$$

Substituting Equation G 3 in for the stress in Equation G 23 and recognizing the equal biaxial stress state at the center of the blister yields:

$$N_{11} = N_{22} = \int_{-t/2}^{t/2} \sigma_{22}\, dz = \int_{-t/2}^{t/2} \frac{pR}{2t}\, dz = \frac{pR}{2} \qquad \text{G 24}$$

This result is easily obtained from the experimental results. For the simulated results, the radius of curvature is determined by fitting a circle between the deflection at the center of the simulated geometry and the fixed edge. These results are shown in Figure G 7.

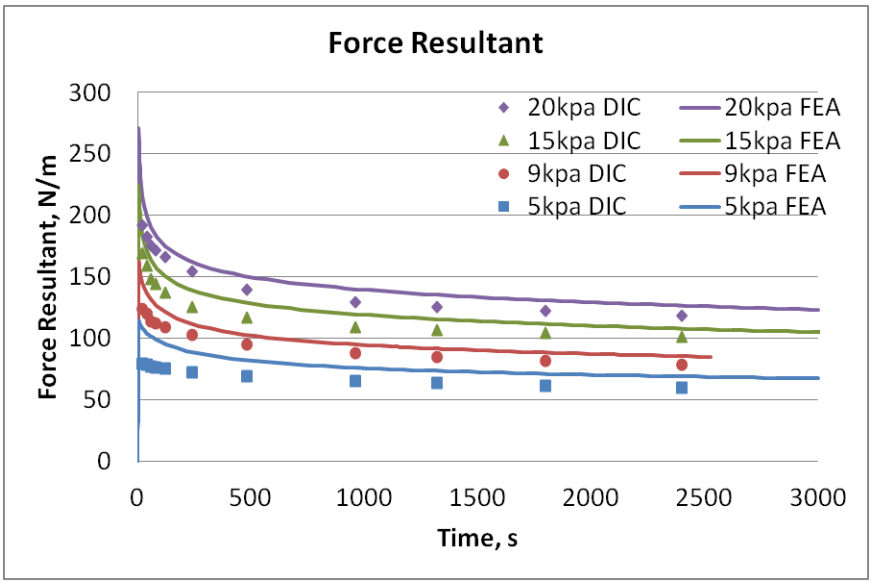

Figure G 7. Experimental vs. simulation membrane force resultants for blister tests. The discrepancy observed between the experiments and simulations is similar to that seen in the stress results.

3.1.5. Effect of ink used for speckling DIC samples

Another potential source of error is the effect that the ink used to speckle the blister specimens might have on the material properties. To explore this possibility, stress relaxation experiments were performed on both speckled and unspeckled samples. Figure G 8 shows that there is no noticeable difference in the relaxation modulus of the samples.

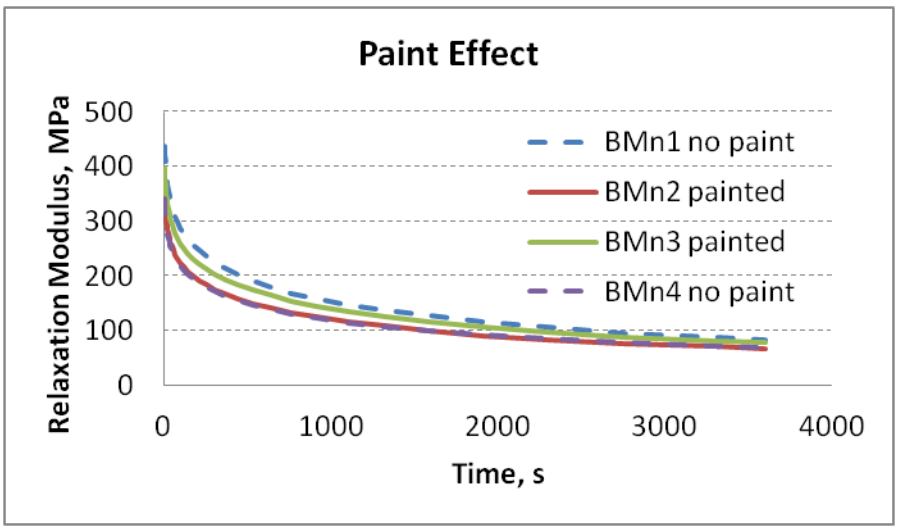

Figure G 8. Relaxation modulus of speckled and unspeckled uniaxial samples from DMA experiments. This demonstrates that the painting procedure does not significantly influence the material properties of the blister.

3.2. Simulation Factors

Thus far, no significant error has been indicated in the experimental stress calculation. Therefore, the attention now turns toward the model. Some of the following simulations were performed with different parameter sets, meaning the degree of non-linearity may differ slightly between different simulations. However, it will be demonstrated that changing the non-linear parameters does not affect the stress results in a way that would obstruct the purpose of this demonstration

3.2.1. Geometry thickness

Just as the sample thickness affects the stress calculation with the experimental results, so also the model thickness influences the simulation stresses. Therefore, care was taken to make the model thickness the average thickness of the samples run at each stress level. No figure is included here for demonstration because the effect is similar to that observed in the experimental stresses in Figure 5.

3.2.2. Length of pressure ramp

To examine the effect of how quickly the pressure is applied on the simulation results, 15 kpa simulations were performed with 1 second and 5 second pressure ramps. The first 30 seconds of both simulations are shown in Figure G 9. Although the 1 second ramp results in slightly higher peak stresses than the 5 second ramp, any difference in the two simulations has disappeared after 30 seconds.

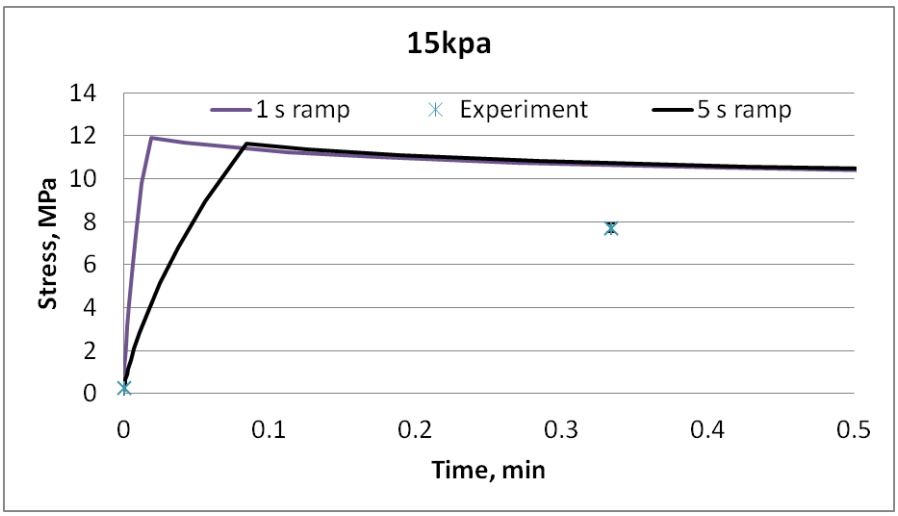

Figure G 9. Comparison of two pressure ramp rates for the 15kpa simulations. The ramp rate does not affect the long-term stress response of the simulation.

3.2.3. In-plane Poisson's ratio

Another parameter that may influence the simulated stress is Poisson's ratio. At the time of this analysis, the in-plane material Poisson's ratio had not been experimentally measured, so the proper value for use in the model was unknown. Therefore, the model was run with two values of Poisson's ratio expected to bracket the actual value. Experiments later showed that Poisson's ratio of the material is initially 0.35 and increases toward 0.5 as time goes on. Figure G 10 shows that changing the in-plane Poisson's ratio does not significantly alter the simulated stresses.

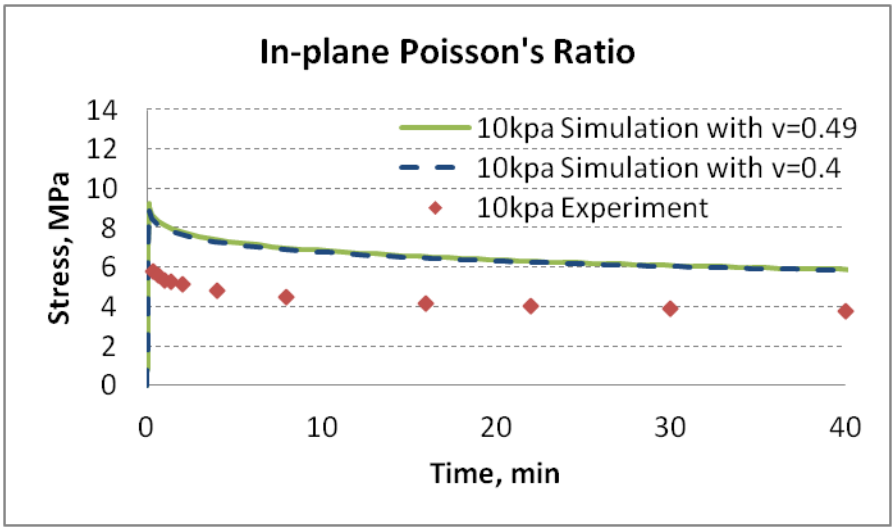

Figure G 10. Experimental results at 10kpa and simulations with two values of in-plane Poisson's ratio. The assumed value of Poisson's ratio in the plane of the material does not significantly affect the value of the simulated stresses.

3.2.4. Through-plane Poisson's ratio

Although the material is essentially isotropic in-plane, some of the out-of-plane properties vary significantly from the in-plane properties. Therefore, it is also important to consider the effect of the

through-plane Poisson's ratio. Like the previous example, simulations were performed with several values of through-plane Poisson's ratio. The results Figure G 11 demonstrate that the through-plane Poisson's ratio does not resolve the discrepancy between the experimental and simulation stresses.

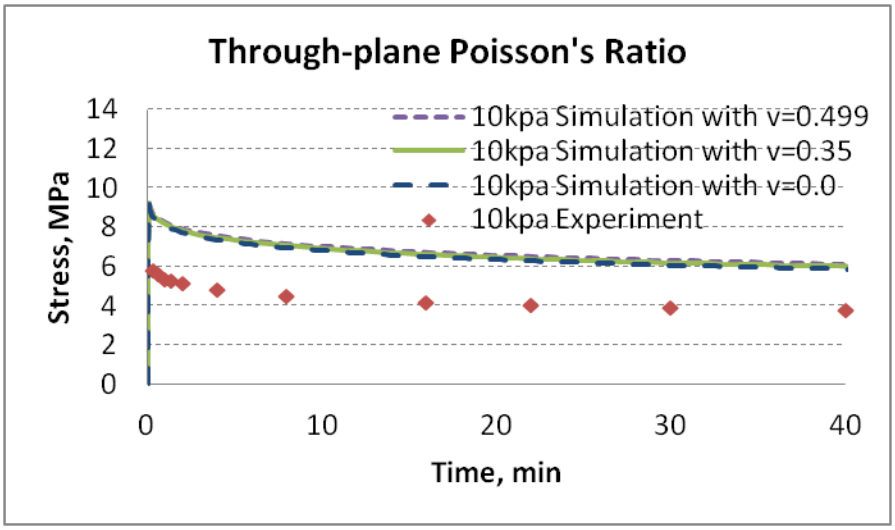

Figure G 11. Experimental results at 10kpa and simulations with three values of through-plane Poisson's ratio. The assumed value of Poisson's ratio through the plane of the material does not significantly affect the value of the simulated stresses.

3.2.5. Effect of non-linear parameters

It was mentioned previously that the non-linear parameters are also unable to address the discrepancy between the experimental stresses and model stresses. Figure G 12 shows the effect of the adjusting the non-linear elastic parameter, g_0. For this figure, three values of g_0 were considered; the original value from parameter estimation of the uniaxial results, and half and twice that value. Although g_0 does affect the simulated stresses, it is not significant enough to address the full discrepancy. Additionally, if the half and double values of g_0 are used for uniaxial simulations, the results are much worse than with the original value of g_0.

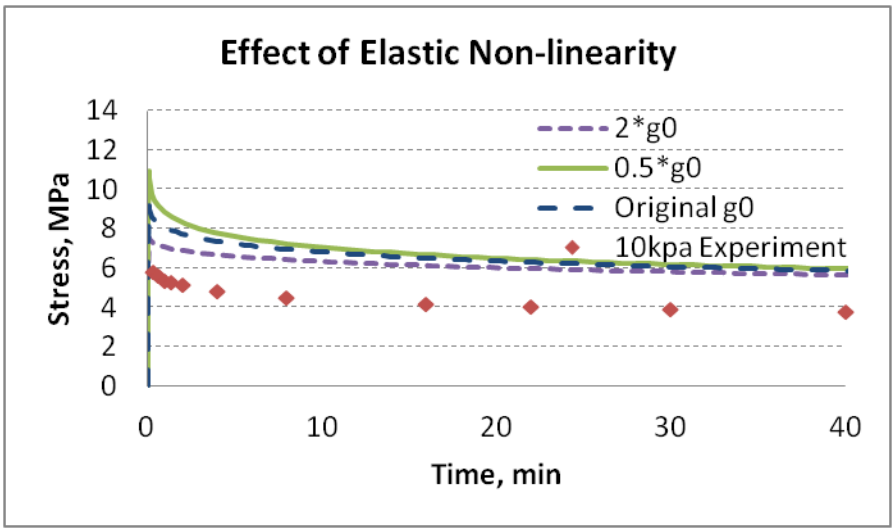

Figure G 12. Experiment results at 10 kpa and the effect of elastic non-linearity on the simulated stresses. This figure demonstrates that adjusting g_0 is not sufficient to bring the experiments and results into agreement.

In addition to the elastic non-linearity, the non-linear response to loading, characterized by g_2, was also examined for its effect on simulation stresses. This parameter appears with applied stress inside the convolution integral in the non-linear viscoelastic constitutive equation. In the original simulation, the parameter was not active, but two stress-dependent trends were used to run the simulation. The results are shown in Figure G 13.

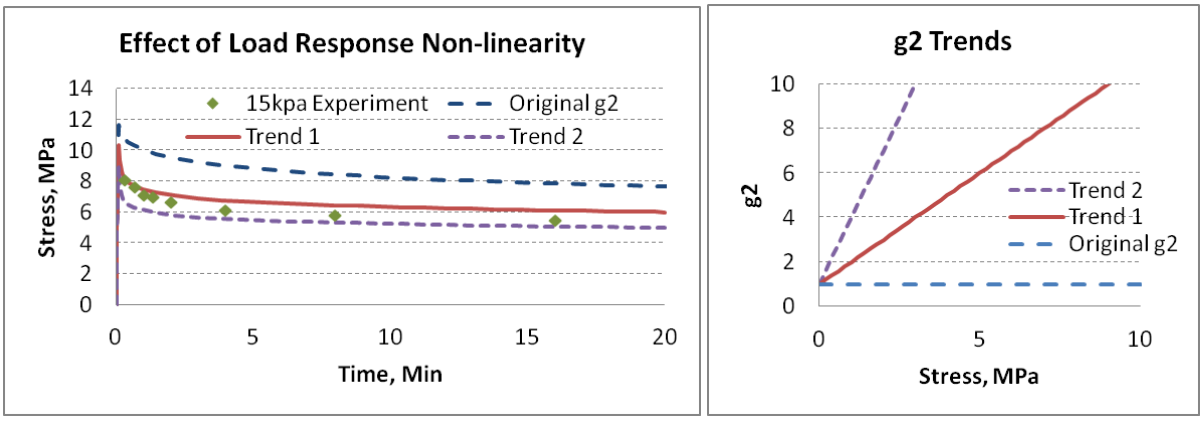

Figure G 13. Experimental results at 15 kpa and simulations with three trends for g_2. It appears that allowing g_2 to increase as stress increases moves the simulated stresses closer to the experimental stresses.

This figure is encouraging – the attempted g_2 trends bracket the experimental stresses when used in the simulation. Unfortunately, this improvement is only observed in the biaxial simulation. If either of these trends is assumed during parameter estimation (which is performed with uniaxial tensile experiments), a valid set of parameters cannot be found. That is, there is no combination of the other model parameters which allows these definitions of g_2. Therefore, altering g_2 is not a solution for bringing the biaxial simulation into agreement with the experimentally observed stresses.

The other non-linear viscoelastic parameter, g_1 and a_σ, are also unable to improve the biaxial simulations without having a significant negative impact on the quality of the uniaxial calculations. The same is true of the viscoplastic parameters.

3.2.6. Effect of initial slack in blister specimen

When the blister experiments are conducted, the specimen is loaded into the fixture at room conditions and then allowed to equilibrate at the test condition, 70C 30%RH, for an hour. During this time, the sample dimensions change due to hygral and thermal expansion. The following figures demonstrate the effect of having the blister geometry slightly 'buckled' when pressure is applied during the simulation. Figure G 14 demonstrates the effect of having an initial blister height of 0.57 mm, even before the pressure is applied, for both the 9 kpa and 15 kpa pressure loads. Figure G 15 demonstrated the effect of having in initial blister height of 1.82 mm for a pressure loading of 9 kpa. Neither example results in significant improvement over the original simulations, which are included in Figure G 16 for comparison. Thus, it appears that the effect of initial slack in the blister does not explain the discrepancy in the stress results.

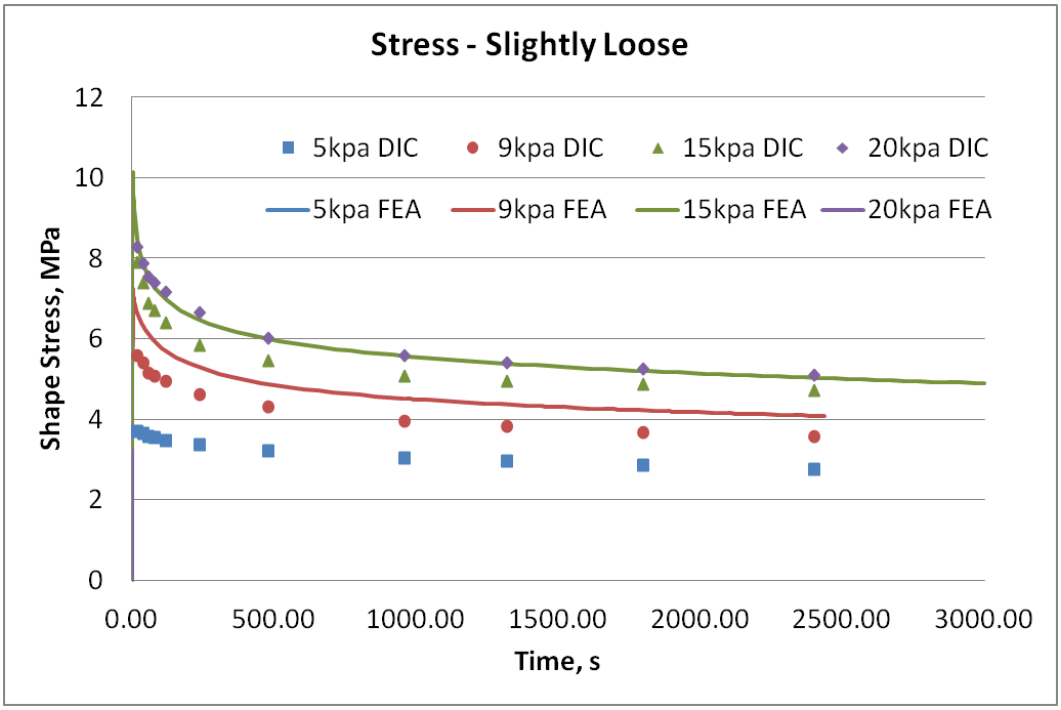

Figure G 14. 9 kpa and 15 kpa simulations of a blister with slight initial slack compared to experimental results.

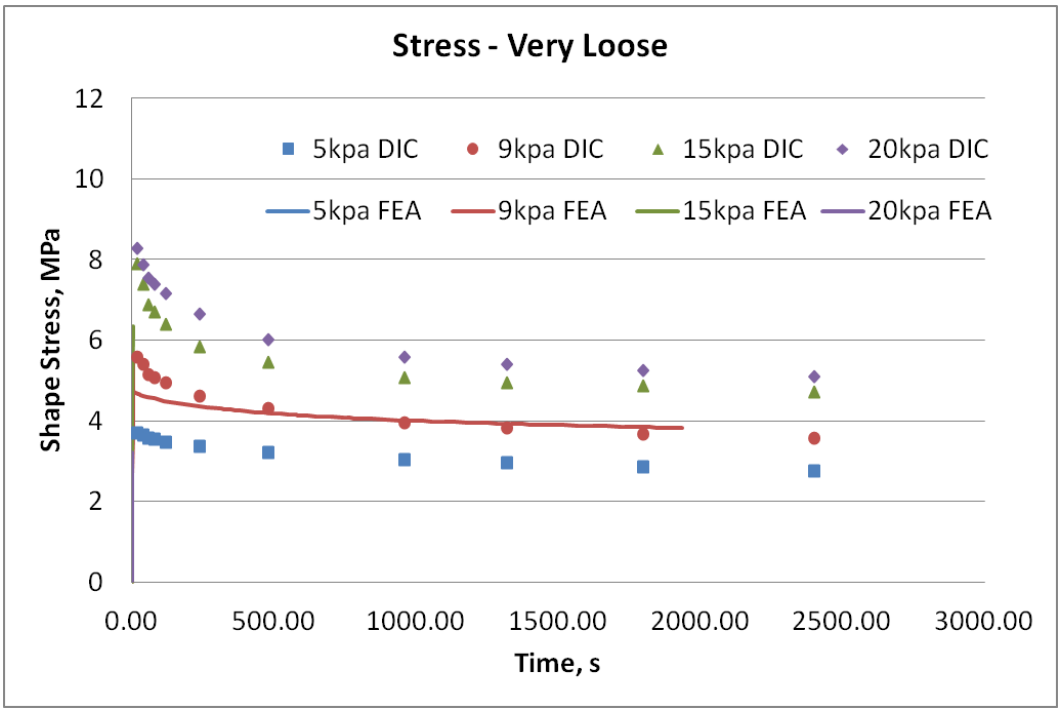

Figure G 15. 9 kpa simulations of a blister with significant initial slack compared to experimental results.

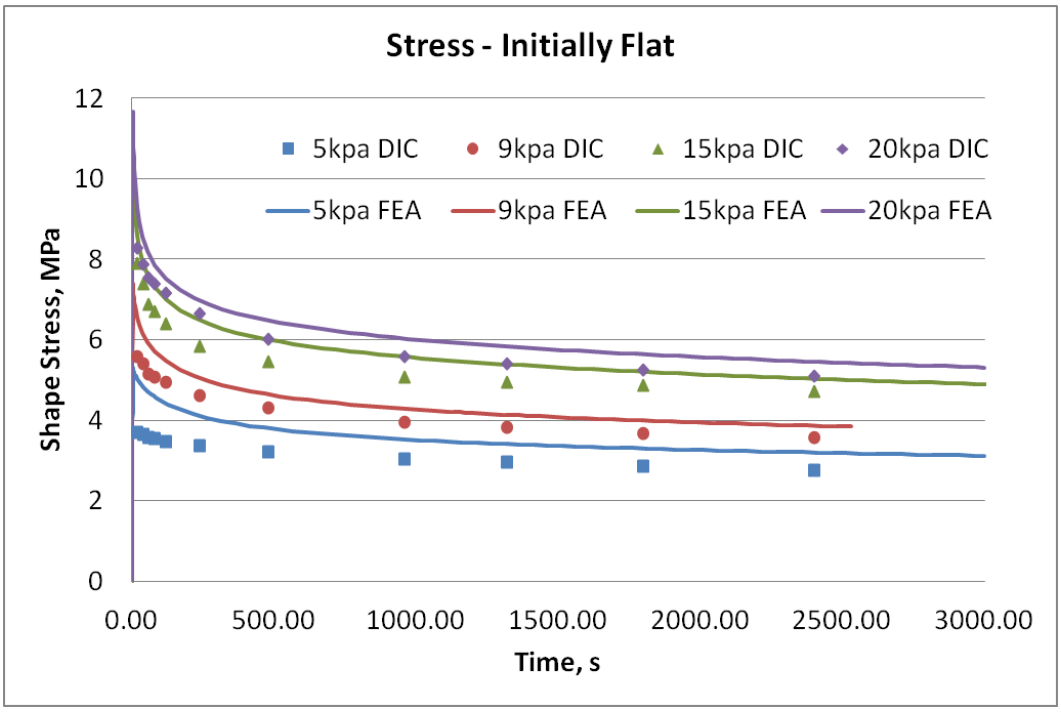

Figure G 16. Simulations of a blister with no initial slack compared to experimental results.

4. Proposed Source of Discrepancy

After ruling out various potential sources of discrepancy as demonstrated in the previous pages, there are few places left to search. The source of the discrepancy does not appear to be experimental, as the pressure level, radius of curvature, and thickness of the blister are all confidently reported. From a simulation standpoint, the geometric model used to perform simulations does not appear to be the source of the issue. This leaves the constitutive expression as one of the few remaining places for the discrepancy to occur.

Recall that equivalent plastic strain theory is used to compute the directional viscoplastic strain increments. This expression was developed from and validated against uniaxial experiments, and uniaxial simulations do a good job predicting uniaxial experimental results. However, it is possible that the expression used for equivalent plastic strain does not appropriately capture the effects of multiaxial loading, for instance through the use of octahedral shear stress as the equivalent stress measure. Without using multiaxial experimental data, an appropriate expression for equivalent plastic strain theory cannot be confidently identified. This is the most likely source of the error in the blister results.